

## Rheology and Setting Behaviour of Alkali-Activated Cements

**Xiaodi Dai**

Doctoral dissertation submitted to obtain the academic degree of  
Doctor of Civil Engineering

### Supervisors

Prof. Geert De Schutter, PhD - Karel Lesage, PhD

Department of Structural Engineering and Building Materials  
Faculty of Engineering and Architecture, Ghent University

November 2022





## **Rheology and Setting Behaviour of Alkali-Activated Cements**

**Xiaodi Dai**

Doctoral dissertation submitted to obtain the academic degree of  
Doctor of Civil Engineering

### **Supervisors**

Prof. Geert De Schutter, PhD - Karel Lesage, PhD  
Department of Structural Engineering and Building Materials  
Faculty of Engineering and Architecture, Ghent University

November 2022



ISBN 978-94-6355-649-1

NUR 956, 971

Wettelijk depot: D/2022/10.500/90

## **Members of the Examination Board**

### **Chair**

Prof. Filip De Turck, PhD, Ghent University

### **Other members entitled to vote**

Prof. Serdar Aydin, PhD, Dokuz Eylül University, Turkey

Prof. Flavio Marchesini de Oliveira, PhD, Ghent University

Prof. Stijn Matthys, PhD, Ghent University

Prof. Stéphanie Staquet, PhD, Université libre de Bruxelles

### **Supervisors**

Prof. Geert De Schutter, PhD, Ghent University

Karel Lesage, PhD, Ghent University



# **Rheology and setting behaviour of alkali-activated cements**

---



## Acknowledgement

Before I start presenting my thesis, please allow me to express my gratitude to all those who have helped me during my PhD career.

Firstly, I would like to appreciate the financial support from FWO Excellence of Science project “INTERACT”. The financial support of the project allows me to successfully complete my study and research.

I would like to give my greatest thanks to my supervisor Prof. Geert De Schutter. When I first came to gent, I knew nothing about cement-based materials, and I could not even do a complete presentation. But you gave me enough encouragement and patience. It allowed me to gradually get familiar with the project, gradually became interested in scientific research, and qualified to complete my tasks during the doctoral period. It is my greatest honor and luck to join your group. I wish you every success in your further career and life. I would like to also appreciate my co-promoter Karel who trained me how to use rheometer, gave lots of suggestions on my study and thesis and encouraged me a lot after my first presentation in the EOS meeting.

I would also like to give my great gratitude to my colleagues Serdar and Mert in the project. Thank you for your training, let me know the research background, know how to use a variety of instruments, and learn to develop my own experimental plan. Thank you for your discussions again and again, I benefited a lot from each discussion. You are rigorous and serious in academics, optimistic and humorous in life, these have deeply influenced me. It is great to work and study with you.

Special thanks to examination board, with your valuable and insightful suggestions, the thesis was significantly improved. Thanks for your time for reviewing this thesis.

Many thanks to our secretaries at Magnel-Vandepitte lab, Marijke, Christel and Jens for managing travelling and ordering different kinds of experimental materials and also thank all technicians for helping me conduct research during the last four years.

My friends and colleagues at Magenl-Vandepitte lab also helped me a lot. I would like to give my gratitude to Branda, Beibei and Xuejiao who shared the office room during my PhD career. Many thanks to my small fantasy group, Qiang, Luchuan, Dengwu, Yaxin, Weixi, Changyuan, Tianlong, Yubo, Zhiyuan, Xiujiào, Kai, Jinbing, Yiyuan, Yi, Xiaoyun, Guo, Bo, Yicheng and Yilin. Thank you for inviting me to your apartment to enjoy your delicious food! Thanks Natalia, Jolien and Sandra who helped me carry out the SEM measurement. Thanks Philp for training me how to use MIP. Thanks Manu and Rahul for discussing the 3D printing and rheological issues. Thanks Didier for training me how to use UPV and analyze data.

I never thought that I would become a Ph.D. one day, but I did, and I want to thank myself for my persistence and struggle. Failure is the main theme of life. This journey has given me enough happiness and wealth. I hope each of us can go from failure to success.

Lastly, I would like to thank my beloved family. The most important meaning of life is always to be with my family, I hope I can spend more time with my family in the future. I also thank my grandfather in heaven for supporting me all the way in my studies.

Now, I would say the times I was told no or wasn't included, wasn't chosen, didn't win, didn't make the cut, but looking back, it really feels like those moments were as important, if not more crucial, than the moments I was told 'yes'. I am super agree with that losing things doesn't just mean losing. I am about to graduate, quoting Taylor Swift's words: "Scary news is: you're on your own now; Cool news is: You're on your own now."

May those I love and those who love me be happy forever in their lives, this thesis is dedicated to my family and friends for their love and support.

Xiaodi DAI  
Gent, Belgium  
Nov 2022



---

## Table of contents

<b>Rheology and setting behaviour of alkali-activated cements .....</b>	<b>I</b>
<b>Notation index .....</b>	<b>XII</b>
<b>Summary .....</b>	<b>XVI</b>
<b>Samenvatting.....</b>	<b>XXI</b>
<b>Part I.....</b>	<b>1</b>
<b>Chapter 1 Introduction.....</b>	<b>3</b>
1. Research background.....	4
2. Scope and objectives.....	5
3. Outline of the PhD thesis .....	6
<b>Chapter 2 State-of-the-art.....</b>	<b>8</b>
1. Rheology and structural build-up of AACs.....	9
1.1 Introduction .....	9
1.2 The evaluation method for rheological properties of AACs .....	9
1.2.1 Dynamic yield stress and plastic viscosity determined by flow curves ..	9
1.2.2 Static yield stress .....	10
1.3 The characterization of early structural formation of AAC with various evaluation methods .....	11
1.3.1 The Vicat apparatus for determination of setting time of AAC.....	11
1.3.2 Ultrasonic pulse wave velocity (UPV) for reaction process of AAC ...	12
1.3.3. Small amplitude oscillation shear tests (SAOS) for structural build-up of AAC .....	13
1.3.4. Isothermal calorimetric heat .....	15
1.3.5. Summary of the evaluation method .....	16
1.4 The correlation between early gel formation with rheology of AAC by various evaluation methods .....	17
1.4.1 Small angle X-ray scattering (SAXS) technique .....	17
1.4.2 In-situ X-ray diffraction technique .....	18
1.4.3 In-situ Fourier-Transform Infrared Spectroscopy-Attenuated Total Reflection (FTIR-ATR).....	20
1.4.5 Method to stop the reaction of AAC.....	21
1.4.6 Nuclear magnetic resonance (NMR) .....	23
1.4.7 Scanning electron microscopy (SEM) .....	24
1.4.8 Thermodynamic modeling approaches .....	26
1.5 The origins of the thixotropic structural build-up of AAC.....	27
1.6 Various influencing factors on the rheology and setting behaviour of AAC.....	29
1.6.1 Precursors .....	29
1.6.2 Activators .....	31
1.6.3 Mineral additions.....	37
1.6.4 Chemical admixtures .....	38
1.6.5 External factors.....	40

<b>Part II .....</b>	<b>43</b>
<b>Chapter 3 Materials and methods .....</b>	<b>45</b>
1. Materials properties .....	46
1.1 Precursors and mineral additions properties .....	46
1.2 Activator properties .....	47
2. Testing methods .....	47
2.1 Fresh properties testing methods .....	47
2.1.1 Mini slump tests .....	47
2.1.2 Setting times .....	47
2.1.3 Flow curves .....	47
2.1.4 Small amplitude oscillation shear tests (SAOS) .....	48
2.1.5 Ultrasonic pulse velocity (UPV).....	49
2.2 Mechanical properties and drying shrinkage testing methods .....	49
2.2.1 Mechanical performance .....	49
2.2.2 Mercury intrusion porosimetry (MIP) .....	49
2.2.3 Drying shrinkage .....	50
2.3 Microstructure analysis.....	50
2.3.1 Pore solution chemistry .....	50
2.3.2 X-ray diffraction (XRD).....	50
2.3.3 Fourier transform infrared spectroscopy (FTIR) .....	51
2.3.4 Scanning electron microscopy (SEM) and Image analysis (IA).....	51
2.3.5 Isothermal calorimetry.....	52
2.3.6 Nuclear magnetic resonance (NMR) .....	53
<b>Part III .....</b>	<b>54</b>
<b>Chapter 4 Sodium hydroxide activator.....</b>	<b>56</b>
1. Introduction.....	57
2. Experimental program .....	57
2.1 Mixture design .....	57
2.2 Sample preparation .....	58
2.3 Protocol for flow curves .....	58
2.4 Thermodynamic modeling .....	59
3. Results and discussions.....	60
3.1 Comparison between UPV and Vicat setting results.....	60
3.2 Comparison between UPV and calorimetric results .....	62
3.3 Rheological test results .....	64
3.4 Pore solution chemistry .....	69
3.5 Pore solution thermodynamic modelling .....	72
3.6 Compressive strength of AAC mixtures .....	75
4. Conclusion .....	77
<b>Chapter 5 Sodium silicate activator .....</b>	<b>78</b>
1. Introduction.....	79
2. Experimental program .....	80
2.1 Mixture design.....	80
2.2 Sample preparation .....	81

2.3 Protocol for flow curves .....	82
3. Results and discussions.....	82
3.1 Setting times .....	82
3.2 Critical strain of AAC mixtures .....	84
3.3 Structural build-up of AAC mixtures.....	86
3.4 Rheological parameters (flow curve).....	93
3.5 Chemistry of pore solution .....	96
3.6 Microstructure analysis of AAC .....	101
3.7 Mechanical properties.....	102
4. Conclusion .....	104
<b>Chapter 6 Possibilities of using silica fume activator .....</b>	<b>105</b>
1. Introduction.....	106
2. Experimental program .....	107
2.1 Mixture design .....	107
2.2 Dissolution ratio of silica fume.....	107
2.3 Sample preparation .....	108
2.4 Protocol for flow curves and constant shear rate .....	108
3. Results and discussions.....	109
3.1 Activator solution characterization from FTIR spectroscopy .....	109
3.2 Rheology of AAS made with SFA and SSA .....	111
3.2.1 Structural build-up.....	111
3.2.2 Behaviour under high constant shear rate.....	114
3.2.3 Behaviour under shear cycles (Yield stress).....	115
3.3 Setting times of AAS .....	116
3.4 Mechanical properties, reaction kinetics and drying shrinkage .....	117
3.4.1 Mechanical properties.....	118
3.4.2 Reaction kinetics .....	118
3.4.3 Drying shrinkage of AAC mixtures.....	120
3.5 Microstructure of AAS.....	121
3.6 Comparison of carbon dioxide emission and cost of activator solutions .	124
4. Conclusion .....	126
<b>Part IV .....</b>	<b>127</b>
<b>Chapter 7 Effects of mineral addition on rheology in a binary system .....</b>	<b>129</b>
1. Introduction.....	130
2. Experimental program .....	130
2.1 Mixture design .....	130
2.2 Sample preparation .....	132
2.3 Protocol for flow curves .....	132
3. Results and discussions.....	133
3.1 Isothermal Calorimetric results of AAC pastes.....	133
3.2 Ultrasonic pulse velocity of AAC pastes and its correlation with heat evolution and Vicat setting times.....	138
3.2.1 Comparison between ultrasonic pulse velocity and heat evolution ....	138

3.2.2 Comparison between Vicat setting times and cumulative heat release	144
3.3 Flow curves and very early structural build-up of AAC pastes	145
3.4 Microstructure and chemical composition of reaction products of AAC pastes	148
4. Conclusion	152
<b>Part V</b>	<b>153</b>
<b>Chapter 8 Influence of retarders on the rheological and setting behaviour of AACs</b>	<b>155</b>
1. Introduction	156
2. Experimental program	157
2.1 Mixture design	157
2.2 Sample preparation	158
3. Results and discussions	158
3.1 Workability loss, setting times and mechanical performance	158
3.2 Reaction kinetics of AAS pastes	162
3.3 FTIR-ATR and pH value analysis of activator solutions	165
3.4 Structural build-up of AAS pastes	167
3.5 Pore solution chemistry and its relation to the structural build-up of AAS pastes	169
3.6 X-ray diffraction of AAS pastes	173
3.7 Porosity of AAS pastes	174
3.8 SEM/EDX of AAS pastes	175
4. Conclusion	179
<b>Part VI</b>	<b>180</b>
<b>Chapter 9 Setting mechanism of AAS mixtures from rheological point of view</b>	<b>182</b>
1. Introduction	183
2. Experimental program	183
2.1 Materials and mixture design	183
2.2 Sample preparation	185
2.3 Protocol for flow curves and SAOS tests	185
3. Results and discussions	186
3.1 Rheological properties of AAS and PC pastes	186
3.1.1 Yield stress and plastic viscosity	186
3.1.2 Shear thickening and shear thinning behaviour	188
3.1.3 The effect of activator on the yield stress of AAS pastes	189
3.1.4 The effect of activator on the viscosity of AAS pastes	191
3.2 Time-dependend properties of AAS pastes	192
3.2.1 Vicat setting times and reaction kinetics of AAS pastes	192
3.2.2 Structural build-up of AAS and PC pastes	194
4. Conclusion	199
<b>Chapter 10 Nanostructure of AAS at initial setting times</b>	<b>200</b>
1. Introduction	201

2. Experimental program .....	201
2.1 Mixture design .....	201
2.2 Sample preparation .....	202
3. Results and discussions.....	202
3.1 Structural build-up behaviour, initial setting times and heat evolution of AAS pastes.....	202
3.2 NMR analysis of AAS pastes.....	205
3.2.1 NMR analysis at initial setting times.....	205
3.2.2 NMR analysis of SS-AAS pastes based on calorimetric curves.....	212
3.2.3 Quantitative assessment of C-A-S-H/C-(N-)A-S-H and N-A-S-H.....	216
3.3 FTIR analysis of AAS pastes .....	217
3.4 SEM/EDX analysis of AAS pastes .....	218
4. Conclusion .....	222
<b>Part VII.....</b>	<b>223</b>
<b>Chapter 11 Conclusions and perspectives.....</b>	<b>225</b>
1. General conclusions .....	226
2. Main contributions .....	228
3. Perspectives .....	228
<b>References.....</b>	<b>230</b>
<b>Curriculum Vitae .....</b>	<b>260</b>
Personal information .....	260
Education .....	260
Research experience .....	260
Honors & Awards.....	261
Publication list .....	261



## Notation index

---

### Abbreviations

AAC	Alkali-activated cement
AAS	Alkali-activated slag
BSE	Backscattered electron
CP	Cross polarization
EDX	Energy dispersive X-ray
ESI	Effective saturation index
FA	Fly ash
FTIR-ATR	Fourier-transform infrared spectroscopy-Attenuated total reflection
GGBFS	Ground granulated blast furnace slag
IA	Image analysis
IAP	Ion activity product
ICP-OES	Inductively coupled plasma optical emission spectrometer
LOI	Loss on ignition
LSP	Limestone powder
LVER	Linear viscoelastic region
MAS	Magic angle spinning
MIP	Mercury intrusion porosimetry
Ms	Silicate modulus ( $[\text{SiO}_2]/[\text{Na}_2\text{O}]$ )
NMR	Nuclear magnetic resonance
PC	Portland cement
SAOS	Small amplitude oscillatory shear
SAXS	Small angle X-ray scattering
SD	Standard deviation
SE	Secondary electron mode
SEM	Scanning electron microscopy
SF	Silica fume

SFA	Silica fume activator
SI	Saturation index
SSA	Sodium silicate activator
UPV	Ultrasonic pulse wave
w/b	Water-to-binder ratio
XRD	X-ray diffraction
XRF	X-ray fluorescence

### **Roman symbols**

$c$	A parameter for modified Bingham model
$G$	A variable linked to yield stress
$G'$	Storage modulus
$G''$	Loss modulus
$H$	A variable associated with plastic viscosity
$h$	Vane height
$K$	Consistency factor
$K_{s0}$	Equilibrium solubility product of a solid
$N$	Speed of rotation
$n$	Consistency index (power)
$Q_{\infty}$	Ultimate heat release at infinite time
$Q(t)$	Cumulative heat release at time $t$
$R_1$	Vane radius
$R_2$	Inner cup radius
$T$	Torque

## Greek symbols

$\alpha(t)$	Degree of reaction at a certain age
$\dot{\gamma}$	Shear rate
$\gamma_c$	Critical strain
$\delta$	Phase angle
$\mu$	Plastic viscosity
$\rho$	Density of particles
$\tau$	Shear stress
$\tau_0$	Yield stress

The abbreviations of chemistry of cement:

CA	Citric acid
C-A-S-H	Aluminum-modified calcium silicate hydrate
$\text{Na}_2\text{CO}_3$	Sodium carbonate
$\text{Na}_2\text{O} \cdot n\text{SiO}_2$	Sodium silicate
$\text{Na}_2\text{SO}_4$	Sodium sulfate
NaOH	Sodium hydroxide
SB	Sodium tetraborate decahydrate
SP	sodium triphosphate pentabasic
N-A-S-H	Sodium aluminosilicate hydrate



## Summary

---

Over the last century, the manufacturing of Portland cement (PC) consumes around 3 % of primary energy and causes over 9 % of CO<sub>2</sub> emission. For every ton of PC produced, about 0.9 ton of CO<sub>2</sub> are emitted. Therefore, there is a great need to lower the CO<sub>2</sub> footprint of cement production and select alternative cementitious materials for building and infrastructure construction. Alkali-activated cements (AAC) have attracted attention as a promising alternative to PC. This type of cementitious materials can be produced by activating a reactive solid aluminosilicate, such as ground granulated blast furnace slag (GGBFS), fly ash (FA), metakaolin (MK) and other precursors, with an activator solution, such as sodium hydroxide, sodium silicate and sodium carbonate. Properly designed AAC can result in superior engineering properties, such as higher mechanical performance and better durability performance against high temperature, acid and sulfate attacks, than conventional PC. However, to successfully promote the application of AAC, it is important to understand the rheological and setting behaviour of AAC as these information can be effectively used to guide mixture design in terms of flowability, stability, pumpability, pouring and casting processes of fresh concrete.

Typically, the rheological and setting behaviour of AAC were significantly influenced by activator properties. The effects of sodium hydroxide (NaOH) concentration on the rheology and early reaction process of alkali-activated slag (AAS) mixtures were studied. A strong relationship between the Vicat initial setting time and ultrasonic pulse wave (UPV) for NaOH activated slag mixtures identifying the characteristic points or inflection points in the ultrasonic curves and reaching a specific value in the ultrasonic velocity. The early reaction process of the NaOH-activated slag pastes determined by UPV and calorimeter consisted of three stages: dissolution, acceleration/condensation and deceleration stages. The yield stress and apparent viscosity of the pastes increased by the addition of NaOH, and the pastes started to show shear-thickening behaviour when NaOH concentration reached 8 M. It was also revealed that Si, Al and Ca ion concentrations in the pore solution determined by inductively coupled plasma-optical emission spectroscopy (ICP-OES) increased with an increase in NaOH concentration, and the pore solution of the pastes was dominated by Na<sup>+</sup> and OH<sup>-</sup>. No significant influence of NaOH concentrations upon 4 M on the compressive strength of the mortar samples was observed.

The influence of another commonly used activator, sodium silicate, on the rheological and setting behaviour was also investigated. The early rheological response of AAC mixtures was elaborated by small-amplitude oscillatory shear (SAOS) tests. Storage modulus and loss factor were measured to evaluate the structural build-up of AAC. Results showed that the Ms value (SiO<sub>2</sub>/Na<sub>2</sub>O) had significant effect on the structural build-up. A significantly higher initial storage modulus with a low growth rate was observed for the Ms values lower than 0.8. However, for higher Ms values, a sudden increase in storage modulus was observed after a negligible initial structuration. An increase in sodium silicate dosage caused a considerable delay in the abrupt increase

in the structural formation. The pore solution measured by ICP-OES also revealed a lower release of aluminum and calcium into the pore solution of AAC mixtures with lower Ms value.

The effects of silica fume and sodium silicate-based activators (SFA and SSA, respectively) with different Ms values on the setting behaviour, rheological, mechanical, and microstructural properties of AAS were also investigated. The setting time of AAS - activated by SFA - prolonged significantly with an increase of Ms value as opposed to the SSA activation case. From a rheological point of view, SFA-activated mixtures exhibited a slower structural build-up in the early stage and better workability retention than SSA-activated mixtures. In addition, SFA mixtures showed lower drying shrinkage and slightly higher mechanical properties as compared to SSA mixtures. Microstructure analysis revealed that the mixture produced with SFA with a Ms value of 1.2 had less micro-cracks and a well-packed microstructure as compared to the mixtures produced with SSA. The overall evaluation of the test results revealed that SFA could be a more economical and sustainable alternative to SSA with its lower cost, much lower CO<sub>2</sub> emissions and more favorable engineering properties.

The precursor's nature also significantly affects the rheological and setting behaviour. The effects of PC, silica fume (SF), fly ash (FA) and limestone (LSP) on the structural build-up and reaction process of AAS mixtures were investigated. Results indicated that the pastes incorporating PC or SF have a potential to be used in the engineering practice requiring a high structural build-up rate, such as the reduction of formwork pressure, slip form paving, stability and 3D printing concrete. While the lower early structural build-up rate for FA and LSP activated by sodium silicate (Ms1.2) is preferred for the application of multi-layers casting. The reaction products were found to be C-A-S-H with a chain-like structure at later ages, which was determined by scanning electron microscopy/energy dispersive X-ray analysis (SEM/EDX).

As well known, slag mixtures activated by sodium silicate activator show a very quick and uncontrolled setting behaviour. Therefore, the utilization potential of citric acid, sodium tetraborate decahydrate and sodium triphosphate pentabasic to control the fresh state properties of AAS have been studied. The early structural build-up, reaction kinetics, pore solution chemistry, setting behaviour, and hardened properties such as microstructure, pore structure, and mechanical properties of AAS with these chemicals were investigated. Test results showed that early structural build-up, reaction kinetics and setting behaviour of AAS can be well controlled by using these chemicals. The citric acid was found the most effective admixture to prolong the setting times of AAS; however, it caused a dramatic decrease in mechanical properties. On the other hand sodium triphosphate pentabasic could provide a slight delay in setting times, while sodium tetraborate decahydrate prolonged the setting times significantly without any detrimental effect on the mechanical properties.

To find out the setting mechanism behind AAS, a comprehensive and systematic comparison between sodium hydroxide-activated slag mixtures (NH-AAS) and sodium silicate-activated slag mixtures (SS-AAS) was implemented. Flow curves

indicated that the SS-AAS exhibited a lower yield stress and a higher plastic viscosity than NH-AAS mixtures. SAOS tests showed a negligible colloidal interaction between slag particles in the SS-AAS system; therefore, the early increase in structuration was associated with the formation of reaction products due to the interaction between the dissolved calcium ions and the silicates originating from the activator solution. On the other hand, the stiffness and the early increase in structural build-up of NH-AAS were attributed to the formation of a well-percolated network.

The correlation between the nanostructure and early structural build-up of AAS was also investigated. Early structural build-up behaviour was evaluated by SAOS tests, the reaction process was recorded by isothermal calorimeter, and the nanostructure was characterized using  $^1\text{H}$ - $^{29}\text{Si}$  CPMAS and  $^{29}\text{Si}$  MAS nuclear magnetic resonance spectroscopy (NMR), fourier transform infrared spectroscopy (FTIR) and SEM/EDX. Test results showed the distinctive differences in early structural build-up behaviour and nanostructure between NH-AAS and SS-AAS. The C-A-S-H and N-A-S-H gel were the main reaction products for the AAS pastes at the initial setting times. The SS-AAS mixture showed a much higher percentage of N-A-S-H formation as compared to C-A-S-H, while the amount of C-A-S-H was relatively similar to N-A-S-H in NH-AAS mixtures. Furthermore, the N-A-S-H gel gradually degraded to form C-A-S-H during the acceleration period for the SS-AAS.





## Samenvatting

---

De voorbije honderd jaar heeft het productieproces van Portland cement (PC) ongeveer 3% primaire energie gekost en ongeveer 9% van de mondiale CO<sub>2</sub> uitgestoten. Elke ton PC kostte ongeveer 0.9 ton CO<sub>2</sub>. Er is dus een grote nood aan ofwel een verlaagde CO<sub>2</sub>-voetafdruk van de cementproductie ofwel aan het vaker inzetten van cementalternatieven in het bouwproces. Alkali-geactiveerde cementen (AAC) zijn in dat opzicht beloftevolle alternatieven. Dit type cementen wordt namelijk geproduceerd door een reactief aluminosilicaat, zoals gemalen hoogovenslakken (GGBFS), vliegassen (FA), metakaolin (MK) of andere precursoren, te activeren met een activator-oplossing, zoals natriumhydroxide, natriumsilicaat of natriumcarbonaat. Goed ontworpen AAC kunnen prima kwaliteiten vertonen zoals een hogere mechanische sterkte dan PC en een betere duurzaamheidsweerstand tegen hoge temperaturen, zuur- en sulfaataantasting. Desalniettemin is het belangrijk om ook een beter begrip op te bouwen over hoe de verwerkbaarheid en uitharding zich ontwikkelt om het gebruik van AAC verder te promoten. Een beter begrip zou toelaten om ook mengsels samen te stellen met een geschikte vloeï, stabiliteit, verpompbaarheid, etc. ten behoeve van het plaatsingsproces van vers alkali-geactiveerd beton.

De activatoreigenschappen hebben gewoonlijk een grote invloed op de reologie en het uithardingsgedrag van AAC. In dit onderzoek werden dan ook de effecten van natriumhydroxide (NaOH) concentratie op de reologie en de reactiekinetiek in alkali-geactiveerde slak (AAS) mengsels onderzocht. Een sterke correlatie tussen de Vicat initiële uithardingstijd en de ultrasone pulsgolf (UPV) werd gevonden voor NaOH geactiveerde mengsels, waarbij karakteristieke punten en buigpunten in het ultrasoon signaal een specifieke waarde in ultrasone snelheid aannamen. De initiële reacties werden met UPV en calorimetrie bepaald : De oplossingsfase, de versnellings-/condensatiefase en de afremmingsfase. De vloedrempel en de schijnbare viscositeit van de pasta's steeg door toevoeging van NaOH en de pasta's begonnen dilatantie te vertonen van zodra de NaOH concentratie 8M bedroeg. Er werd ook ontdekt dat de concentratie van Si, Al en Ca ionen - bepaald door *inductively coupled plasma-optical emission spectroscopy* (ICP-OES) – steeg met een toename in NaOH concentratie en dat het interstitiële medium gedomineerd werd door Na en OH<sup>-</sup>. Er werd geen significante invloed gevonden op de druksterkte van mortels voor NaOH concentraties onder 4M.

Ook de invloed van een andere gebruikelijke activator, natriumsilicaat, op het reologisch en uithardingsgedrag werd onderzocht. De initiële reologische respons van AAC mengsels werd verhelderd aan de hand van *small-amplitude oscillatory shear* (SAOS) experimenten. De *storage modulus* en *loss factor* werden gemeten om de structuuropbouw in AAC te evalueren. Resultaten toonden aan dat een hogere Ms waarde (SiO<sub>2</sub>/Na<sub>2</sub>O) een significant effect had op de structuuropbouw. Een hogere initiële *storage modulus* met een lage groeisnelheid werd gevonden voor Ms waarden lager dan 0.8. Voor hogere Ms waarden werd een plotse stijging in de *storage modulus*

gevonden na verwaarloosbare initiële structuuropbouw. Een toename in de natriumsilicaatconcentratie veroorzaakte een aanzienlijke vertraging in die abrupte stijging. In de poriënoplossing werd tevens een lagere concentratie aluminium and calcium gevonden voor AAC mengsels met een lagere Ms waarde.

Voor silica fume en natriumsilicaat gebaseerde activators (resp. SFA en SSA) met verschillende Ms waarden werden de effecten op het uithardingsgedrag, de reologische, mechanische en microstructurele eigenschappen van AAS ook onderzocht. De uithardingstijd van AAS – geactiveerd door SFA – werd aanzienlijk verlengd door een toename in Ms waarde in tegenstelling tot activering door SSA. Reologisch gezien, vertoonden SFA-geactiveerde mengsels een tragere structuuropbouw in het vroege stadium en een langer behoud van verwerkbaarheid dan SSA-geactiveerde mengsels. Bovendien vertoonden SFA mengsels een kleinere drogingskrimp en een ietwat grotere mechanische weerstand vergeleken met SSA mengsels. De analyse van de microstructuur liet zien dat een mengsel geproduceerd met SFA en een Ms waarde van 1.2 minder microscheuren en een dicht gepakte microstructuur had vergeleken met de SSA mengsels. Over het algemeen toonden de testresultaten aan dat SFA een economischer en duurzamer alternatief kan zijn voor SSA, met ook nog eens een lagere kostprijs, veel lagere CO<sub>2</sub>-voetafdruk en andere gunstige eigenschappen.

Ook de aard van de precursor beïnvloedt het reologische en uithardingsgedrag in significante mate. Daartoe werden de effecten van PC, silica fume (SF), vliegassen (FA) en kalksteenmeel (LSP) op de structuuropbouw en het reactieproces van de AAS mengsels onderzocht. De resultaten toonden aan dat de pasta's met PC of SF een groter potentieel hebben in een bouw materiaal met een verhoogde structuuropbouw zoals voor *slip form paving*, mengsels met verhoogde stabiliteit, 3D printen of ter reductie van de bekistingsdruk. Daarentegen, kan de lagere structuuropbouw van FA en LSP – geactiveerd met natriumsilicaat (Ms 1.2) – geprefereerd worden voor bekistingen die gevuld worden in meerdere lagen met aanzienlijke tijdsintervallen. Als reactieproduct werd C-A-S-H met een kettingvormige structuur gevonden op gevorderde leeftijd gebruik makend van *scanning electron microscopy/energy dispersive X-ray analysis* (SEM/EDX).

Slakmengsels geactiveerd door natriumsilicaat vertonen een erg snelle en ongecontroleerde uitharding. Daarom werd ook het potentieel gebruik van citroenzuur, natrium tetraboraat decahydraat en natrium trifosfaat pentabasic onderzocht om de verse eigenschappen beter te controleren. De initiële structuuropbouw, reactiekinetiek, chemie van de poriënoplossing, uithardingsgedrag en verharde eigenschappen zoals microstructuur, poriënstructuur en mechanische eigenschappen van AAS werden onderzocht in aanwezigheid van deze chemicaliën. Testresultaten toonden aan dat initiële structuuropbouw, reactiekinetiek en uithardingsgedrag van AAS goed gecontroleerd kan worden door deze chemicaliën. Het citroenzuur werd het meest effectief bevonden in het verlengen van de uithardingstijd van AAS, alhoewel het ook een dramatisch daling van de mechanische eigenschappen veroorzaakte. Natrium

trifosfaat kon een kleinere vertraging in de uitharding voorzien terwijl natrium tetraboraat decahydraat de uitharding significant verlengde zonder enig nadelig effect op de mechanische eigenschappen.

Om het uithardingsmechanisme in AAS te achterhalen werd een systematische vergelijking uitgewerkt tussen natrium hydroxide geactiveerde slakmengsels (NH-AAS) en natrium silicaat geactiveerde slakmengsels (SS-AAS). Vloeicurven toonden aan dat de SS-AAS mengsels een hogere vloedrempel en een hogere viscositeit hadden dan NH-AAS mengsels. SAOS experimenten demonstreerden een verwaarloosbare colloïdale interactie tussen slakpartikels in het SS-AAS systeem. Daarom werd de vroege stijging in structuuropbouw geassocieerd met de vorming van reactieproducten ten gevolge van de interactie tussen opgeloste calcium ionen en silicaten vanuit de activatoroplossing. Anderzijds werd de stijfheid en de vroege stijging in structuuropbouw van NH-AAS toegekend aan de vorming van een goed ontwikkeld netwerk.

De correlatie tussen de nanostructuur en de initiële structuuropbouw van AAS werd ook onderzocht. De initiële structuuropbouw werd geëvalueerd met SAOS experimenten, het reactieproces werd gemonitord met isotherme calorimetrie en de nanostructuur werd gekarakteriseerd door  $^1\text{H}$ - $^{29}\text{Si}$  CPMAS en  $^{29}\text{Si}$  MAS *nuclear magnetic resonance spectroscopy* (NMR), *fourier transform infrared spectroscopy* (FTIR) en SEM/EDX. Testresultaten toonden de verschillen in initiële structuuropbouw en nanostructuur tussen NH-AAS en SS-AAS. De C-A-S-H en N-A-S-H gel waren de voornaamste reactieproducten voor de AAS pasta's op het moment van initiële uitharding. Het SS-AAS mengsel vertoonde een veel hoger percentage N-A-S-H in vergelijking met C-A-S-H, terwijl de hoeveelheid C-A-S-H relatief gelijkaardig was aan N-A-S-H in NH-AAS mengsels. Verder degradeerde de N-A-S-H gel geleidelijk tot C-A-S-H gedurende de versnellingsperiode van de SS-AAS mengsels.



## **Part I**

---

# **GENERAL INFORMATION**



## **Chapter 1 Introduction**

---

In this chapter, the research background, scope and objective, as well as the outline of this PhD thesis is given.

## 1. Research background

---

Due to its simplicity of manufacture and use, local availability, relative resilience, diversity, and low cost, concrete is the most frequently used building material in the world. Portland cement (PC) is the most critical component of concrete, accounting for 4.6 billion tons of global yearly production and accounting for 8% of global anthropogenic CO<sub>2</sub> emissions [1]. Around 60% of CO<sub>2</sub> emissions are caused by the calcination of limestone during the clinker manufacturing process, while 40% are caused by the fuels needed to fire cement kilns and electricity used for milling. By 2050, the percentage of CO<sub>2</sub> emissions attributable to cement manufacturing is expected to grow to 16-24%, highlighting the critical need to enhance sustainability of concrete. In this context, clinker-free alternative binders with a reduced CO<sub>2</sub> emission [2]–[4], including the binder class of alkali-activated cements (AACs), have emerged as a viable and necessary alternative to conventional Portland binders. These binders are manufactured mostly or exclusively from industrial by-products (e.g. blast furnace slag from steel manufacturing, fly ash from coal combustion). They normally do not require additional thermal processing and are naturally rich in reactive calcium silicates and aluminosilicates capable of forming an insoluble binder phase with the addition of an alkaline activator at elevated temperatures. As a result, alkali-activated binders have been discovered as a potential source of CO<sub>2</sub> emission reductions of up to 70% when compared to PC [5].

AACs are normally produced from an alkali metal source (solid or dissolved) and calcium silicate or aluminosilicate-rich solid precursors, such as coal combustion fly ash (FA), calcined clays (e.g. metakaolin), metallurgical slag (e.g. ground granulated blast furnace slag – GGBFS, stainless steel slag), mine tailings and even some natural pozzolans [5]–[7]. The chemical composition of solid reactant, the type and concentration of the alkaline solution, and the curing temperature all influence the reaction processes and microstructural features of AACs [5], [8], [9]. The aluminosilicate-rich materials react by means of dissolution, gelation and polycondensation to form inorganic N-A-S-H gel where sodium is integrated in the gel structure, as well as networks of zeolites which form via polycondensation [5], [10]–[12]. Calcium silicate hydrate gels, generally including aluminum, are the primary reaction products in calcium-rich materials and are hence referred to as C-A-S-H gel [5], [6], [13].

AACs have various potential benefits to PC materials due to their chemical and microstructural features, including better mechanical properties such as a faster rate of compressive strength growth [14] and much greater tensile strength [15]. When considering durability, the potential of AACs is evident. Better durability of AACs is demonstrated by their resistance to chemical attacks (acid and sulphate) [12], [16], chloride penetration [17], fire [18], and freeze-thaw cycles [19]. Despite these benefits, AACs have a critical disadvantage: quick hardening, which results in extremely short setting times and significant shrinkage deformations [16], [20]–[22]. The former results in significant and rapid rheological changes, resulting in poor workability. The

latter results from physicochemical events that occur during AACs solidification and can be up to four times greater than those seen in PC [23], [24]. It is very urgent to understand the rheological behaviour and setting process of AACs in order to provide a better mixture design concerning flowability, stability, pumpability, pouring and casting process of fresh AACs concrete.

Cementitious materials generally are described as Bingham fluid with a plastic viscosity [25]. This behaviour is the outcome of a complicated interaction between a variety of physical processes [26]. It is worth noting that the extensive poly-dispersity of concrete components suggests the presence of at least four distinct types of interactions (surface forces (or colloidal interactions), Brownian forces, hydrodynamic forces, and different contact forces between particles). Depending on the particle size, the volume fraction of the particles in the mixture, and external influences (e.g. the magnitude of the applied stress or strain rate), one or more of these interactions may predominate [26]. However, the mechanism of interaction between precursor particles of the AACs prepared with various activators is still unknown, more deeply understanding on the relationship between composition factors and inter-particle forces is needed. Besides, structural build-up of cementitious materials is another important index to evaluate the fresh performance of concrete during different steps in the production operation process. For instance, the higher structural build-up rates are preferred in many concrete applications, such as reduction of formwork pressure, slip form paving, fresh state stability, and 3D printing concrete, while lower structural build-up rates are generally desired in some cases, such as multi-layer casting applications to increase the bond strength between the layers [27], [28]. Therefore, to promote the application of AACs, the control of early structural build-up and setting behaviour should be paid more attention.

From the aforementioned statements, the AACs have a great potential to be an alternative to PC due to the significant reduction of greenhouse gas emission. However, there is still a huge gap from research to practical engineering as AACs still present some shortcomings, such as rapid and uncontrolled setting. This becomes a huge barrier to improve the application of AACs. A deeper understanding on the rheological and setting behaviour of AACs is needed.

## **2. Scope and objectives**

---

The first purpose of this thesis is to understand the rheological and setting behaviour of AACs pastes influenced by various composition factors including activators, precursors, admixtures, etc. This is explored by evaluation of rheological behaviour, calorimetric heat release, pore solution chemistry and further microstructure tests. This provides fundamental knowledge of the effects of mixture design on fresh properties of AACs pastes.

Another important objective is to understand the setting mechanism and the relationship between nanostructure and rheological properties of AACs. Nuclear magnetic resonance (NMR) was applied to reveal the early nanostructure of AACs

prepared with different alkaline solutions. The setting mechanism of AACs was investigated by coupling the nanostructure found by NMR with rheological behaviour. Based on the fundamental understanding of the early nanostructure of AACs, more attempts to control the rheology and setting process by adjusting the mixture design are made. This new scientific understanding on the setting of AACs will enable researchers in the future to develop new strategies to extend the workability of AACs.

### **3. Outline of the PhD thesis**

---

This thesis consists of seven parts with 11 Chapters.

Part I presents a general information of this thesis. In Chapter 1, the research background, scope and objectives of this thesis are given. Chapter 2 gives a state-of-the-art about rheological and setting behaviour of AACs.

Part II, material and testing methods are presented (Chapter 3).

Part III, including three chapters, exhibits the rheological properties and structural build-up of AACs prepared with various alkaline activators, precursors, mineral addition and chemical retarders. In Chapter 4, the effects of concentration and solution to binder ratio of sodium hydroxide on the structural build-up and rheological properties of slag mixtures are discussed. Thermodynamic modeling based on the pore solution results was also applied to investigate the phases and presence of early reaction products. Chapter 5 presents the effects of sodium silicate activator properties, water to solid binder ratio,  $\text{SiO}_2/\text{Na}_2\text{O}$  ratio (Ms value) and  $\text{Na}_2\text{O}$  content, on the structural formation of alkali-activated slag/fly ash mixtures. The relationship between the structural build-up and pore solution chemistry were established. The reaction process of sodium silicate-based mixtures were also investigated by means of ultrasonic wave. In Chapter 6, the possibilities of using the silica fume activators are also investigated, which can be a more sustainable activator in the future. The rheological and mechanical performance between silica fume activator and sodium silicate activator are compared.

Part IV has one Chapter and presents the effects of mineral addition on the rheology and structural build-up behaviour of AACs. Chapter 7 shows the influence of binary precursor usage (slag-fly ash, slag-silica fume, slag-limestone and slag-Portland cement) on the rheological and setting behaviour of AACs.

Part V includes Chapter 8 and presents the effects of different types of chemical retarders on the AACs for extending the setting times. Meanwhile, the rheological and mechanical performance of AACs in the presence of chemical retarders also are discussed.

Part VI, including two chapters, presents the setting mechanism behind sodium hydroxide and sodium silicate-activated slag mixtures from the rheological point of view in Chapter 9. In Chapter 10, the early nanostructure of AACs is evaluated by NMR technique, and the relationship between structural build-up and nanostructure

is found.

In conclusion, Part VII (Chapter 11) provides the main findings of this thesis and perspectives for future research.

## **Chapter 2 State-of-the-art**

---

This chapter presents a state-of-the-art regarding rheology and structural build-up of AACs. Various structural characterizations to reveal the reaction process are also presented.

## 1. Rheology and structural build-up of AACs

---

### 1.1 Introduction

---

Rheology is the science of flow and deformation of matter and describes the interrelation between force, deformation and time. Cementitious materials, including AACs suspensions, have been described as a Bingham fluid with plastic viscosity. The yield stress and plastic viscosity originating from a Bingham fluid have a significance in terms of guiding engineering applications of concrete, such as, concrete mixture design, evaluating workability, predicting the flow behaviour and stability. Other rheological parameters, such as viscoelastic properties (i.e., storage and loss modulus), can be used to characterize the structural build-up and setting times of cementitious materials.

In this chapter, the common methods to evaluate the fresh properties of cementitious materials are introduced. Regarding the AAC suspensions, lots of composition factors, such as the activator, precursors, chemical retarders, influenced the rheological performance of AACs and are introduced in this chapter. Many characterization methods to reveal the early structural formation of AACs are also introduced.

### 1.2 The evaluation method for rheological properties of AACs

---

#### 1.2.1 Dynamic yield stress and plastic viscosity determined by flow curves

In the rheological measurements by a rotational rheometer, the fundamental rheological parameters plastic viscosity and dynamic yield stress measure the material resistance to flow after it begins to flow and the shear stress required to initiate flow, respectively. The Bingham model Eq. (2-1) describe the relationship between shear stress ( $\tau$ ) and shear strain rate ( $\dot{\gamma}$ ), which is the common rheological model used to evaluate the rheological behaviour of cementitious materials.

$$\tau = \tau_0 + \mu\dot{\gamma} \quad (2-1)$$

Where  $\tau_0$  is the dynamic yield stress and  $\mu$  denotes the plastic viscosity. However, some cementitious materials may exhibit non-linear rheological behaviour, the modified Bingham model Eq. (2-2) can be applied and does not increase the complexity as it uses three parameters.

$$\tau = \tau_0 + \mu\dot{\gamma} + c \cdot \dot{\gamma}^2 \quad (2-2)$$

In comparison to the Bingham model, the modified Bingham model [29] includes a quadratic term related to shear rate, with the pseudoplastic constant as its coefficient  $c$ . Furthermore, Herschel-Bulkley model Eq. (2-3) also can be used to describe non-linear behaviour.

$$\tau = \tau_0 + K \cdot \dot{\gamma}^n \quad (2-3)$$

Where  $K$  is the consistency index,  $n$  denotes the power-law index. The Herschel-Bulkley model can be employed to indicate the shear-thickening ( $n > 1$ ) and shear

thinning ( $n < 1$ ) behaviour.

Previous studies [30]–[32] have shown that the sodium hydroxide-activated pastes are more fitted with Bingham model, while the Herschel-Bulkley are more suitable for sodium silicate-activated pastes. For example, Fig. 2-1 shows the flow curves for AAC pastes activated by sodium hydroxide (A) and sodium silicate (B), as shown in Fig. 2-1A, the downward curve for the pastes activated by sodium hydroxide is a straight line that fits the Bingham model, while the pastes activated by sodium silicate solution did not form a straight line for the downward curve, which is better fitted with the Herschel-Bulkley model. It should be noted that an accurate flow curve is built from steady state data, which means that the upper and lower curves as shown in Fig. 2-1A should coincide. However, In the case of Fig. 2-1B, the data is clearly affected by the time dependency of the measurements and therefore cannot be considered as an accurate flow curve of the material. This is an inherent difficulty of studying cement systems as the chemical reactions are progressing and the material is evolving with time. When there is a dormant period, then the flow curve can be built from quasi-steady data, but when the reactions progress in a fast rate, then there will be always uncertainty on the measurements.

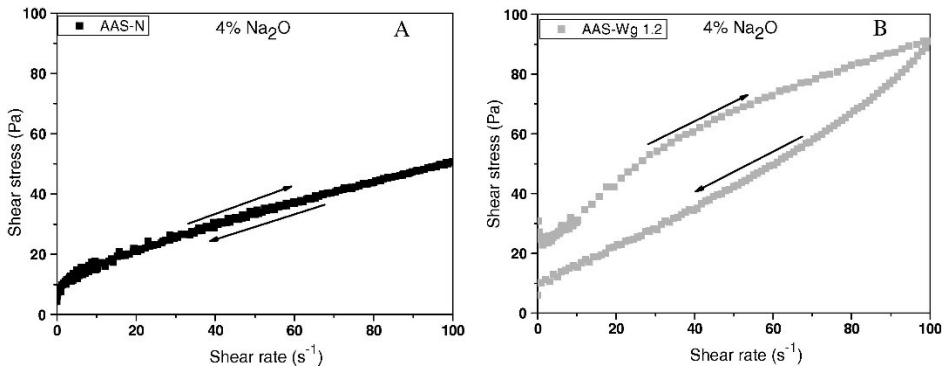


Fig. 2-1 Flow curves for AAC pastes activated by sodium hydroxide (A) and sodium silicate solution (B) [31].

### 1.2.2 Static yield stress

As aforementioned, the dynamic yield stress determined through the equilibrium flow curve is considered as the shear stress when the shear rate is zero, which is the minimum stress required to maintain or terminate the flow of the materials. Meanwhile, a yield stress exists that corresponds to the state before the structure is broken down, so the stress necessary to initiate flow, corresponding to a well-connected undisturbed microstructure [26], [33]. This is considered as the static yield stress. There are many methods to evaluate and determine the static yield stress. One

approach for determining static yield stress is by the use of creep-recovery [34]. This is a stress-controlled test in which the material does not flow until the applied creep stress exceeds the static yield stress. Another common used method is the shear growth tests. Static yield stress is determined by shearing the sample at a very low and constant shear rate and a peak value or a plateau of stress is obtained before the flow.

### **1.3 The characterization of early structural formation of AAC with various evaluation methods**

---

The structural build-up is a very important feature that determines the macroscopic behaviour of cement-based materials during casting [35]–[37]. Indeed, when casting tall wall parts, it is preferable to utilize concrete with high structural build-up kinetics in order to decrease lateral pressure on the formwork and allow for quicker pressure decline following casting [38]. Additionally, while 3D-printing cement-based materials is layer by layer, it is critical to optimize the degree of structural build-up to enable proper casting [36]. Indeed, rapid build-up can have an effect on the binding between cast layers inside a printed structure [35]. Meanwhile, an appropriate structure is necessary to achieve a strength level capable of supporting the weight of succeeding extruded layers [39]. Therefore, understanding the structural build-up and setting times is critical for transportation, placing and compaction of cement concrete. In the following section, various methods to evaluate the structural build-up have been introduced.

#### 1.3.1 The Vicat apparatus for determination of setting time of AAC

In Portland cement, there are many standards elucidating how to determine the setting times of PC pastes by using a Vicat apparatus. For example, as shown in EN196-3 [40], the initial setting of PC pastes is determined by measuring from zero to the time which the distance between the needle and the base-plate is  $(6 \pm 3)$  mm, while the final setting time is when the penetration of the needle into the specimen first reaches to 0.5 mm. While standard ASTM C191-08 [41] elucidates that Vicat initial time of setting is the time elapsed between the initial contact of cement and water and the time when the penetration is measured to be 25 mm. The Vicat final time of setting is the time elapsed between initial contact of cement and water and the time when the needle does not leave a complete circular impression in the paste surface.

However, as the mixture design of AAC is quite complex and influenced by numerous factors (i.e. activator type and precursor nature), it is difficult to determine the standard consistency of AAC and almost all studies relied on the PC standard to determine the setting time of AAC.

### 1.3.2 Ultrasonic pulse wave velocity (UPV) for reaction process of AAC

Similar to Portland cement pastes, AAC are transformed progressively from a liquid phase to a solid gel as a result of complex physical-chemical reaction composed of dissolution, gelation, polycondensation and densification [9]. Ultrasonic wave technology can be used as a non-destructive test method to monitor the reaction process of cementitious materials [42]–[44], the development of compressive strength, internal defects and porosity, and the propagation of cracks in concrete structures. Therefore, ultrasonic wave technology can be developed/adopted to monitor the early-age reaction and structure development of AAC.

In Fig. 2-2, Cao et al. [43] has applied the embedded ultrasonic measurement to observe the structural development of AAC in terms of sodium hydroxide- (SH-) and sodium silicate- (SS-) activated slag mixtures. According to UPV curves, three distinct stages are observed during the early-age reaction process of the AAS activated with sodium hydroxide, whereas five stages are observed for the AAS made with sodium silicate, including (I) dormant period, (II) acceleration period, (III) deceleration period, (IV) second acceleration period, and (V) second deceleration period. Additionally, stages II and IV are diffusion-controlled, whereas stage III is a dissolution-controlled stage. With the observation of UPV, the early-age reaction process is quite straightforward for the SH-activated AAC pastes. Stage I shows substantially lower velocity due to the energy attenuation of the ultrasonic wave signals caused by interfaces scattering, reflection and absorption and air bubbles in the initial suspended mixture. In stage II, the increase of UPV is related to the formation of reaction products and their connections between GGBFS particles, and these reaction products are formed due to the interaction between dissolved silicates, aluminum and calcium from GGBFS particles. Once the capillary pores in the compact matrix start to be filled with further reaction products, the UPV increases slowly and tends to be stable in stage III. While the situation is more complex for the SS-activated AAC pastes. The silicates ions used to form the preliminary gel products at stages I and II are derived primarily from sodium silicate solution, resulting in the fast increase in UPV, whereas the C-(N)-A-S-H gels generated at stages IV and V are derived primarily from GGBS particles.

Siva et al. [44] also tried to correlate the UPV with the vicat setting times, they found that UPV of around 1450–1550 m/s and 1650–1750 m/s correspond to the initial and final settings, respectively. Hertwig et al. [45] reported that there is a strong correlation between setting time as determined by the Vicat needle test and ultrasonic curves. The initial and final setting times are quite close to the duration of the induction phase and the time required to reach maximum acceleration, respectively. Additionally, both setting times are shown to be highly correlated with the maximum acceleration value.

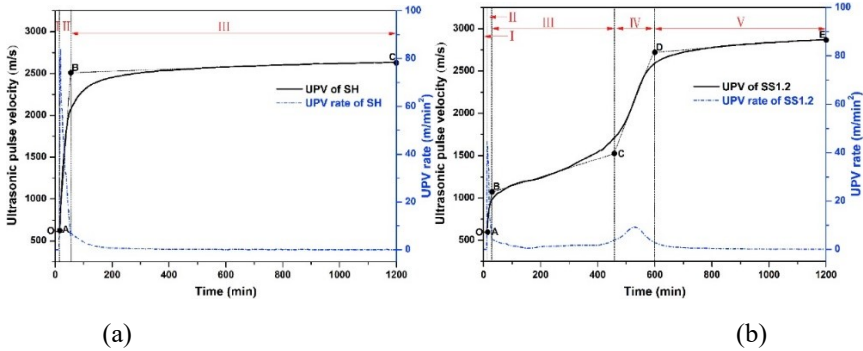


Fig. 2-2 The evolution of UPV and UPV rate curves of AAS pastes, (a) Sodium hydroxide-activated slag pastes, (b) Sodium silicate-activated slag pastes [43].

### 1.3.3. Small amplitude oscillation shear tests (SAOS) for structural build-up of AAC

Dynamic shear rheometers with controlled shear oscillation can be used to investigate the temporal changes in the viscoelastic behaviour [27]. As an in-situ testing tool, the small amplitude oscillatory shear (SAOS) test is generally used to provide a full understanding of the structural build-up throughout the early times. This technique permits the monitoring of the rheological changes that occur during the transformation of solid aluminates and silicates in the precursors into a synthetic aluminosilicate gel. The SAOS test subjects the sample to a very tiny sinusoidal deformation, the response of the material such as storage modulus ( $G'$ ), loss modulus ( $G''$ ) and phase angle ( $\delta$ ) as shown in Eq. (2-4) can be obtained, which enables an in-depth assessment of the sample within linear viscoelastic properties. These three parameters follow the relation:

$$\tan(\delta) = \frac{G''}{G'} \quad (2-4)$$

Where  $G'$  denotes the solid-like (or elastic) behaviour and  $G''$  indicates the liquid-like (or viscous) property. The materials with a higher storage modulus and a lower phase angle reflect higher solid-like behaviour. Prior to the time-sweep SAOS measurement, it is important to determine the linear viscoelastic region (LVER). Yuan et al. [27] reported that the upper limit of LVER for cementitious paste is commonly regarded to be in the order of  $10^{-4}$ , and hence the shear strain is generally between  $10^{-6}$  and  $10^{-4}$  at constant frequency during the time-sweep tests (i.e. 1Hz). Therefore the SAOS test can be deemed as a non-destructive method as the small shear strain preserves the integrity of the internal microstructure.

Although the SAOS test has been effectively used to explore the viscoelastic properties and structural build-up of cementitious pastes [46], relatively little research has used it to investigate AAC. For example, previous researchers [47] investigated the activator type and concentration on the structural build-up of AAC. They found a

more rapid increase in structuration when using lower  $\text{SiO}_2/\text{Na}_2\text{O}$  (Ms) ratio or lower  $\text{Na}_2\text{O}\%$  concentration in the sodium silicate solution. Riffai et al. [48] reported that no enhancement in the structural build-up was observed once the sodium hydroxide concentration reached to 7 mol/L for alkali-activated fly ash pastes.

Recently, some studies also aim to correlate the structural formation measured by SAOS with the initial setting times determined by Vicat needle tests. Alnahhal et al [49]. reported that the evolution of early viscoelastic behaviour can be divided into four stages for alkali-activated slag/fly ash pastes as shown in Fig. 2-3. In stage I, the loss modulus  $G''$  that represents the viscous portion of the materials are higher than storage modulus  $G'$ , which denotes the elastic portion of the materials. This shows the liquid-like behaviour is more dominated in this stage. During stage II, the increasing rate of  $G'$  is higher than  $G''$ , resulting in a decrease in phase angle. However, in this stage, the magnitude of  $G'$  is still very low, indicating a weak attractive interaction between particles. Stage III is a transient stage, which is characterized by a faster increase in  $G''$  relative to  $G'$ , hence increasing the phase angle. This means that some of the stored energy has been dissipated. Although the basic reason(s) for the formation of this phase are unknown, it could be related to the partial dissipation of stored energy during the start of geopolymerisation [50]. Other authors [51], [52] also elucidated that this stage related to the polycondensation process in which water is released into the matrix leading to the dominance of viscous behaviour over elastic behaviour. Finally in the last stage (IV),  $G'$  inclines rapidly due to the weak attractive interactions transfers to the rigid interactions. The massive formation of reaction products starts to fill the matrix, resulting in the initial set of the materials. It is found that the initial setting occurred at the end of stage III and the start of the stage IV. Therefore, it is also useful to use SAOS measurement to monitor the setting process of AAC pastes, and it can give lots of information in terms of the viscoelastic behaviour of materials.

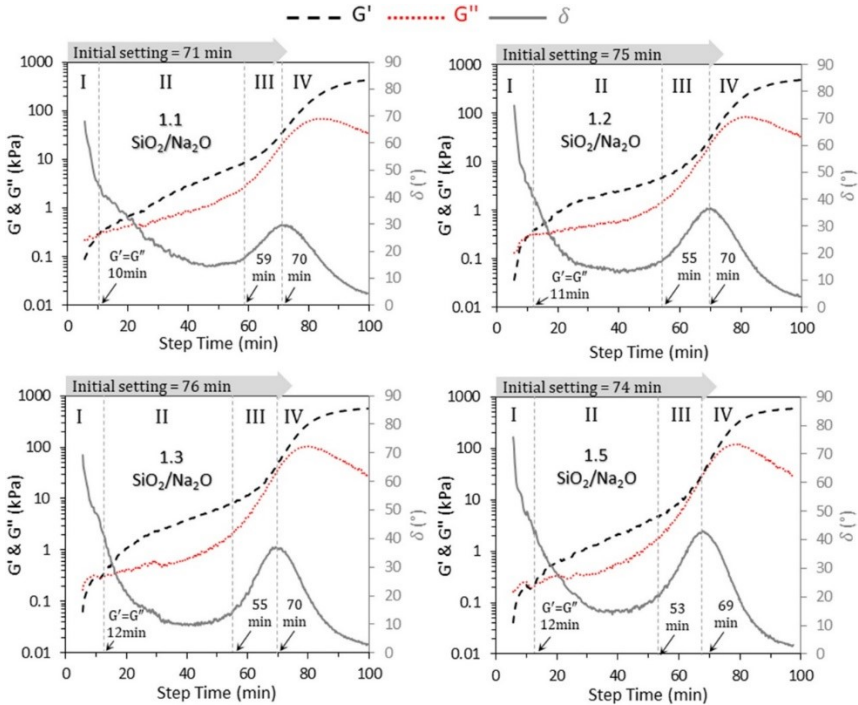


Fig. 2-3 Evolution of viscoelastic parameters as a function of time at different  $\text{SiO}_2/\text{Na}_2\text{O}$  ratios. Strain amplitude = 0.01% and frequency = 1Hz. Initial setting times determined by the Vicat needle test are shown in the scaled grey arrow on the top of each plot [49].

#### 1.3.4. Isothermal calorimetric heat

As well known, with the advantage of real-time data over other intermittently recorded techniques, isothermal calorimetric characterization has developed into a highly effective methodology for analyzing cement hydration kinetics [53], [54]. Calorimetric measurements of alkali-metakaolin and alkali-slag reaction systems have proved their utility in acquiring the information required to describe alkali activation [55]–[57].

However, this method cannot provide structural evolution of materials. Therefore, a few researchers started to correlate the calorimetric data with UPV and setting times results, expecting to understand the reaction process of AAC pastes. Uppalapati et al. [44] found that the heat flow curves closely match the first derivative P-wave velocity curve and temperature measurements made by the ultrasonic device. Based on the calorimetric findings, the authors also divided the reaction process into four stages as dissolution-hydrolysis, precipitation-condensation, polycondensation and further

reaction with increasing time of curing. Buchwald et al. [58] analyzed the relationship between reaction degree determined by isothermal calorimetry and P-wave velocity, and found that a characteristic bend at reaction degree around 0.1 that seems to be matched with the initial setting times determined by penetration tests for alkali-activated metakaolin-GGBFS pastes.

Furthermore, Zuo et al. [59] also investigated the activator nature (sodium silicate or sodium hydroxide) on the isothermal calorimetric heat of AAC pastes as shown in Fig. 2-4. It was found that the heat flow curves from alkali-activated slag paste was shown to be dependent on the presence of soluble Si in the alkaline activator. Three reaction phases were determined for NaOH activated slag paste based on dissolution peak and acceleration peak. Between dissolution peak and acceleration peak, for sodium silicate activated slag paste, an additional reaction phase, referred to as the induction period, was discovered.

The authors proposed a dissolution theory-based mechanism and applied it to interpret the reaction process and origin of the induction period. In sodium hydroxide-activated slag paste, a high degree of undersaturation resulted in quick slag dissolution, resulting in no discernible induction period. The undersaturation of sodium silicate activated slag paste with respect to Si was so low that it was unable to provide sufficient energy to overcome the activation energy barriers required for the creation of vacancy islands and etch pits [60]–[62] on the slag surface. This slowed the dissolving of slag, resulting in an induction time.

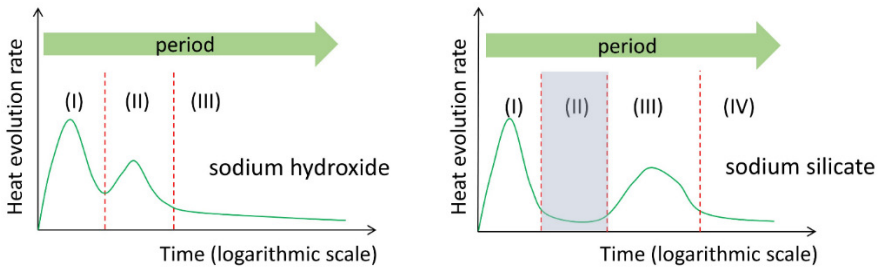


Fig. 2-4 Schematic representation of the heat evolution curves of AAC activated by sodium hydroxide or sodium silicate solution [59].

### 1.3.5. Summary of the evaluation method

As aforementioned, different evaluation methods give different information in terms of structural formation of AAC.

Table 2-1 summaries the advantages and disadvantages of different methods to investigate the structural formation of AAC.

Table 2-1 Comparison of different evaluation methods.

Evaluation methods	Advantages	Disadvantages
Vicat setting time	Give a standard index that can be compared with Portland cement; easy to conduct;	Lost information about structural formation in the very early time
UPV	Provide microstructure change with time;	The early structural formation may be influenced by air void
SAOS	Provide viscoelastic data to describe the structural formation;  Can identify the liquid/solid state of pastes;	Results are influenced by geometry of rheometer; Cannot isolate the chemical and physical effects
Calorimetry	Provide chemical reaction information	No structural formation data

#### 1.4 The correlation between early gel formation with rheology of AAC by various evaluation methods

Due to the complexity of gel formation and its dependence on a number of compositional and processing parameters, a variety of state-of-the-art methods have been used to examine the early stage reaction behaviours. Some authors also tried to correlate the early gel formation with the rheological behaviour.

##### 1.4.1 Small angle X-ray scattering (SAXS) technique

Recently, it has been reported that scattering methods are also quite suitable to characterize the structure of a disordered system such as geopolymer [63]. Small-angle X-ray scattering (SAXS) is a technique for quantifying nanoscale density changes in a sample. This means that it may be used to determine the size distributions of nanoparticles, the size and shape of (monodisperse) macromolecules, pore diameters, and the characteristic distances of partially ordered materials, among other things. Rouyer and Poulesquen [52] investigated the scattering intensities of the oligomers formed by reactions between dissolution products and the silica initially originated from the activator solution as shown in Fig. 2-5. In general, the intensity of

the scattering rises with time, implying an increase in volume fraction of entities in the solution. As shown in Fig. 2-5, the authors found that after the gel point of alkali-activated metakaolin pastes (observed by rheological measurements), the slope grew rapidly, indicating that a percolated network had occurred with a process of densification. Throughout the evolution of the network from a viscoelastic to a solid-like state, the oligomerization process continued in the interstitial region. After 10 hours, the slope of the scattering intensities further increases, which reveals that the presence of a surface fractal dimension, implying that mesoporous network formed after the mechanical strengthening. The increase in the storage modulus measured by the rheometer is perfectly correlated with the increase in scattering intensity, and both of these increases are due to the densification of the percolated network.

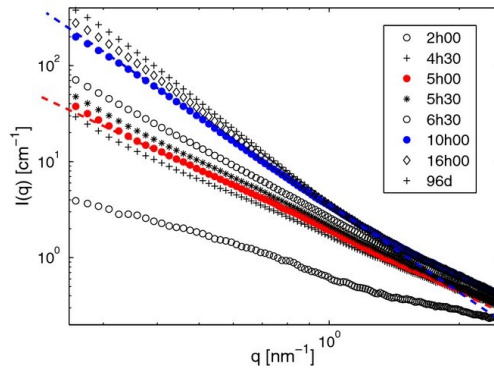


Fig. 2-5 The early age SAXS spectra ranging between 0.25 and 1.25 nm<sup>-1</sup>. Herein, the red dots denote the percolation time determined by rheological test and the blue dots indicate the onset of the mesoporous network [52].

#### 1.4.2 In-situ X-ray diffraction technique

X-ray diffraction (XRD) is another analytical technique that is frequently used to characterize cementitious systems. To obtain insights into time-resolved chemical reactions and change in reaction products, in-situ XRD analysis enables the determination of mineral phase dissolution and formation during reaction. The success of XRD in recent years has been attributed to a variety of quantification techniques, including the Rietveld refinement and the Partial Or No Known Crystal Structure (PONKCS) methods [64]. Rietveld refinement has been used to measure mineral and total amorphous phases using internal or external standards. PONKCS, a method that combines profile summation and the Rietveld method, enables the classification and measurement of various amorphous phases. Recent research has focused on determining the degree of reactivity between supplemental cementitious components in blended cements [65], [66].

Sun et al. [67] investigated the heat and mineral evolution of sodium hydroxide activated GGBFS by means of isothermal calorimeter and in-situ XRD technique. They reported that the main reaction product for the sodium hydroxide-activated GGBFS is C-A-S-H, no or limited secondary reaction products have been found at early ages as shown in Fig. 2-6. They also found that the reaction product formation correlates well with the heat evolution, indicating that the combination of isothermal calorimeter and in-situ XRD can significantly enhance the quantitative analysis for alkaline activation.

The combination of in-situ XRD measurements and the PONKCS approach enables quantification of the production of N-A-S-H and C-A-S-H gels of AAC at very early ages. However, additional cross-checking work is necessary to optimize the analysis processes. Additionally, advanced approaches are required, particularly for a better understanding of medium- or long-term geopolymerization.

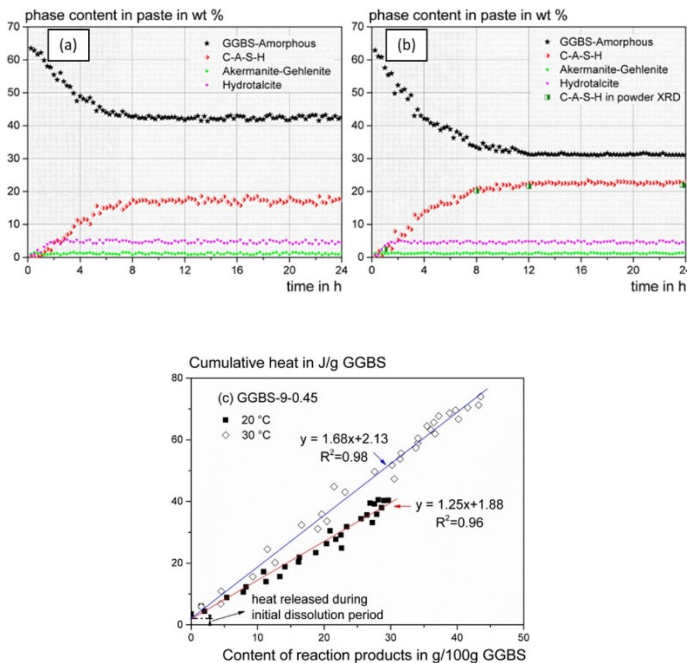


Fig. 2-6 Phase assemblage of sodium hydroxide-activated GGBFS mixture at 20 °C (a) and 30 °C (b), and the correlation of calorimetry results with XRD measurements (c).

### 1.4.3 In-situ Fourier-Transform Infrared Spectroscopy-Attenuated Total Reflection (FTIR-ATR)

In-situ FTIR-ATR is a sampling technique used alongside traditional infrared spectroscopy, which ultimately qualifies samples to be observed directly in either solid or liquid state, without additional preparation. Alnahhal et al. [49] carried out in-situ FTIR-ATR tests to investigate the early age gel formation of sodium silicate-activated slag/fly ash pastes ( $M_s = 1.0$ ,  $Na_2O \% = 7.5\%$ ). The authors reported that the correlation between the polycondensation rate and the evolution of viscoelastic parameters of the paste from mixing to setting as shown in Fig. 2-7. They found that the intensity of the water bending vibration ( $1643\text{ cm}^{-1}$ ) generally decreased with time elapsing, indicating that the paste was transferred from a liquid-state to a solid-state as presented by SAOS measurements, due to the consumption of water in reaction [68]. Besides, the intensity of the developing peak of the Si-O-(Si or Al) bonds were also correlated with viscoelastic parameters. As the reaction progresses, the intensity of the shift band of the Si-O-(Si or Al) bonds ( $979\text{-}967\text{ cm}^{-1}$ ) increased, which coincided with the decrease of phase angle. Although in-situ FTIR tests do not require further sample preparation and give information related to polycondensation rate, it cannot provide further accurate crosslinking degree of reaction products and the nanostructure of AAC.

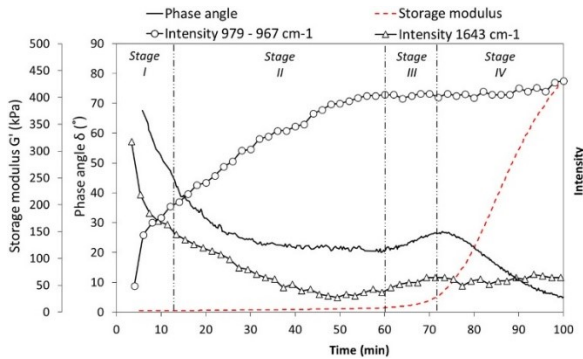


Fig. 2-7 Comparison between the evolution of the intensity of FTIR bonds for free water and Si-O-(Si or Al) and the evolution of viscoelastic parameters [49].

### 1.4.4 Inductively Coupled Plasma Optical Emission Spectrometer (ICP-OES)

ICP-OES is a technique that uses plasma and a spectrometer to detect the composition of elements in (mainly water-dissolved) samples. Therefore, many researchers used this technique to investigate the element composition in pore solution of AAC. Song and Jennings [69] investigated the pore solution chemistry of alkali-activated slag and discovered that increasing the alkalinity of the pore solution resulted in increased Si

and Al concentrations and decreased Ca and Mg concentrations. Zuo and Ye [70] pointed out that increasing temperature (from 40 °C to 60 °C) resulted in decreases in the concentration of Si, Al, Ca, Na, OH<sup>-</sup>, K, Fe and Mg in the pore solutions of alkali-activated fly ash pastes, whereas the soluble silicate in the activator solution led to an increase in the above element concentrations.

Some authors [20], [70] also used thermodynamic modelling and the pore solution chemistry results to calculate the effective saturation index to predict the possible formation of solid reaction products for the sodium silicate-activated slag mixtures ( $M_s = 1.5$ ,  $Na_2O \% = 4\%$ ) at early ages as shown in Fig. 2-8. Palacios et al. [20] reported that the positive effective saturation index showed that the pore solution were always oversaturated with M-S-H, C-N-A-S-H, and numerous Na-containing zeolites. Additionally, the solutions were also oversaturated with brucite, hydrotalcite, and siliceous hydrogarnet. The positive effective saturation indices also indicate that precipitation of stratlingite during the first hours when Al concentrations are relatively high, however the stratlingite would be destabilized once the solutions became undersaturated (negative effective saturation index).

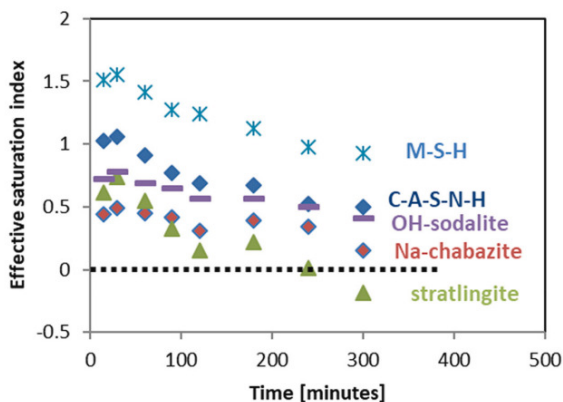


Fig. 2-8 Calculated effective saturation indices as a function of hydration time. A positive saturation index indicates oversaturation, a negative value undersaturation.

#### 1.4.5 Method to stop the reaction of AAC

Most of the aforementioned characterization measurements are in-situ methods, which can provide real-time information. There are other intermittently recording methods, such as Scanning electron microscopy (SEM) and Nuclear Magnetic Resonance (NMR), which also can provide important information. However, for those test methods, sample preparation is particularly important.

For the hardened samples, RILEM TC-238 [72] has provided an effective method to arrest the hydration of cementitious materials by using solvent exchange. However, to

study the early reaction process of AAC, it is important to find an appropriate method to arrest the reaction of AAC at fresh state.

In general, it is easy to stop the reaction of sodium hydroxide-activated materials at fresh state because there is no high amount of soluble silicates in the activator solution. While the key problem to arrest the reaction of sodium silicate-activated materials is to remove the soluble silicates in the pastes at fresh state, which will influence the further microstructural analysis, such as NMR and FTIR, etc. Table 2-2 summaries advantages and disadvantages of different methods to stop the reaction of AAC.

Table 2-2 Different methods to stop the reaction of AAC

Method	Order of operation	Advantages	Disadvantages
Solvent replacement with acetone and ethanol [20]	<ol style="list-style-type: none"> <li>1. The paste is treated with acetone;</li> <li>2. The solvent is vacuum filtered and the acetone treatment is repeated once</li> <li>3. The solid is treated with ethanol, then the solid is vacuum filtered and dried in a desiccator</li> </ol>	<ol style="list-style-type: none"> <li>1. Easy and quick to operate</li> </ol>	<ol style="list-style-type: none"> <li>1. Cannot remove the soluble silicates</li> <li>2. Sample has high weight loss</li> </ol>
Freeze-drying [20]	<ol style="list-style-type: none"> <li>1. The paste is submerged into liquid nitrogen and after 1h introduced in a freeze dryer device for 24 h.</li> </ol>	<ol style="list-style-type: none"> <li>1. The simplest method.</li> <li>2. No chemical influence</li> </ol>	<ol style="list-style-type: none"> <li>1. Cannot remove the soluble silicates, and an unknown product is on the precursor surface, which may influence the results.</li> <li>2. Sample has high weight loss</li> </ol>
Water and isopropanol treatment [20]	<ol style="list-style-type: none"> <li>1. The paste is mixed with ultrapure water.</li> <li>2. The solid is vacuum filtrated and water treatment repeated.</li> <li>3. The solid is washed with isopropanol, filtered and transferred to a desiccator.</li> </ol>	<ol style="list-style-type: none"> <li>1. Sample has very small weight loss that fits with the early studied hydration time.</li> <li>2. No precipitation is identified in samples surfaces</li> </ol>	<ol style="list-style-type: none"> <li>1. Complex procedures</li> <li>2. Difficult to confirm if all the soluble silicates have been removed</li> </ol>
Centrifugation and treatment with water and methanol/Acetone [73]	<ol style="list-style-type: none"> <li>1. The paste is mixed with ultrapure water.</li> <li>2. The suspension is centrifuged and the upper liquid is mixed with methanol to check if all the silicates have been removed (because the alcohol reduces the solubility of silicate species).</li> <li>3. After all the soluble silicate silicates have been removed, the solid is washed with methanol/Acetone, filtrated and transferred to a desiccator.</li> </ol>	<ol style="list-style-type: none"> <li>1. Remove all the soluble silicates.</li> <li>2. Easy to confirm whether all soluble silicates have been removed or not.</li> </ol>	<ol style="list-style-type: none"> <li>1. Complex procedures</li> </ol>

Furthermore, to further distinguish the early reaction products of alkali-activated



20%, the development of ill ordered N-A-S-H and C-A-S-H gel can be expected to dominate the hydrates formed and thus the rheological properties.

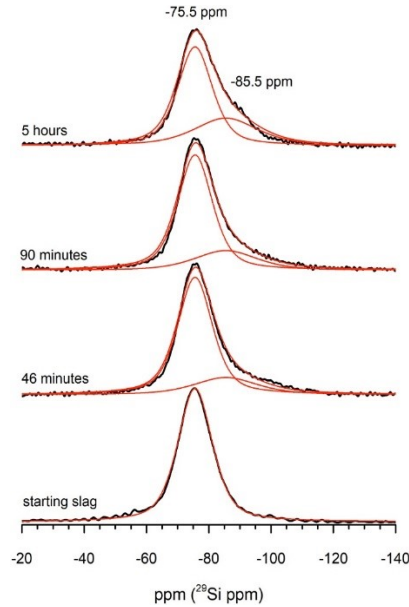


Fig. 2-10  $^{29}\text{Si}$  MAS NMR spectra of the starting slag and SS-AAS pastes across a 5 hour reaction time period. After subtracting the slag contribution from the spectrum, resonances in the range of -85 ppm are revealed that correspond to aluminosilicate gels and C-A-S-H; their intensity increased with time.

#### 1.4.7 Scanning electron microscopy (SEM)

SEM is a type of electron microscope that generate pictures of a material by scanning the surface with a focused beam of electrons. The electrons interact with the atoms in the samples, generating a variety of signals that carry information on the surface topography and composition of the sample. A raster scan pattern is used to scan the electron beam, and the position of the beam is coupled with the intensity of the received signal to create a picture. Certainly, many researchers [20], [79]–[83] have applied SEM to observe the morphology of AAC mixtures. Fig. 2-11 presents the surface morphology of hydration products of sodium silicate-activated slag mixtures at specific reaction stages. Cao et al. [43] observed that the slag particles showed a relatively smooth surface within 50 min (as shown in Fig. 2-11b). The same observation was also reported by Palacios et al. [20], which was also consistent with the storage modulus results showing no significant increase at this stage. With age time reaching to 250 min, the smooth surface faded and impressive eroded traces were revealed (Fig. 2-11c); At 530 min, a number of dense rod gel product were formed and observed in Fig. 2-11d. Afterwards, partly un-hydrated slag particles were

surrounded and strongly bound by thick rod-like gel as shown in Fig. 2-11e and f. It can be seen that SEM images at specific reaction times can be used to reveal the reaction process of AAC.

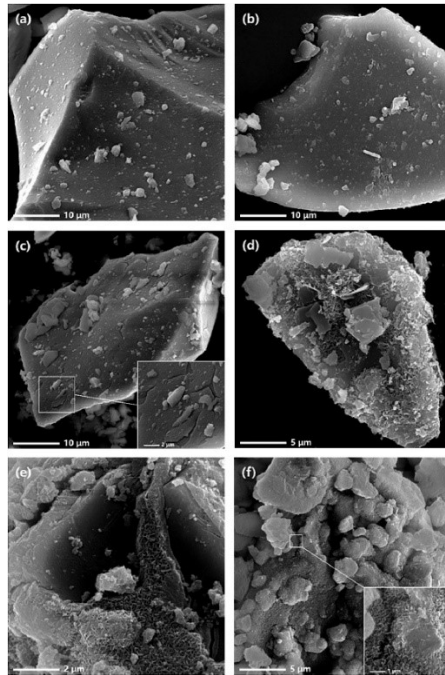


Fig. 2-11 SEM images of sodium silicate-activated slag pastes at different reaction stage (a) 30 min; (b) 50 min; (c) 250 min; (d) 530 min; (e) 600 min; (f) 1200 min, adapted from [43].

Furthermore, recently, Sun et al. [84] has used the cryogenic SEM (cryo-SEM) to observe the early microstructure change in AAC and tried to understand the rheological behaviour of AAC from microstructural perspectives. They reported that at extremely early ages, amorphous reaction products formed on the slag surface in hydroxide-based AAC mixtures. In AAC mixes, the slag particles were linked and bridged together by the reaction products, forming agglomerations, while the free water was trapped in flocs. As a result, a greater and substantial yield stress has been discovered in AAC mixes based on hydroxide. Cryo-SEM pictures revealed a network structure wrapped around the slag particles when silicate was added to the activator. Meanwhile, the pore solution had normal emulsion properties, with water droplets scattered throughout the silicate gels. The yield stress of the silicate-based AAS paste was much lower than that of the hydroxide-based mixtures due to the silicate gels dispersing the slag particles.

#### 1.4.8 Thermodynamic modeling approaches

Thermodynamic modeling of phase assemblages in AAC has seen major advancements in recent year, with the use of a comprehensive ideal solid solution model for the C-(N,K)-A-S-H system [85] and the availability of better solubility data [86] greatly advancing the state of the art. This has resulted in advancements in the prediction of phase assemblages for alkali-activation of slag mixtures [87], [88], including the prediction of phase diagrams over a wide variety of slag and activator compositions [89]. Solubility data for N-A-S-H gels [90], as well as improved data for aqueous species in the N-K-A-S-H-Cl system [91], are enabling modeling of some lower-calcium binder systems [92], although much work remains to be done to develop and validate the necessary range of model constituents to fully describe the phase assemblages in these binders. The library of zeolite phases available for inclusion in models of the (N,K)-A-S-H system, in particular, needs to be expanded, since there are major gaps in the literature, although hampered to some extent by metastability concerns and challenges in defining "solubility" in many instances. Besides, more work should be done to interpret the rheological behaviour of AAC by thermodynamic modeling.

#### 1.4.9 Summary of different structural characterization methods

In this study, a wide variety of testing methods in terms of structural characterization of AAC are presented. Each testing method can give different information to reveal the early reaction process of AAC. Table 2-3 summarize the different structural characterization methods. This can assist researchers to select appropriate methods or the combination of them to better investigate the early age properties of AAC.

Table 2-3 Comparison of different structural characterization method.

Structural characterization method	Information that can be given	Pros	Cons
SAXS	Average size of oligomers; identify the gelation point (coupled with SAOS data)	Simple sample preparation;	Cannot provide nanostructure
In-situ XRD	Phase assemblage of reaction products with time	Simple sample preparation;	Semi-quantitative tests;
FTIR	Si- and Al- bonding	Simple sample preparation; Simple operation; quick data collection;	Water in the sample can interfere with FTIR spectra; low resolution when too many peaks shown, and difficult to interpret.
ICP-OES	The concentration of various ions in pore solution	Simple operation; quick data collection;	When sodium silicate is activator, containing extremely high concentrations of Si and Na, other important elements are hard to be interpreted due to ion's sheltering/masking effect
NMR	Nanostructure ( $Q^n$ environments)	Quantitative tests;	Complex sample preparation; The results was much Sinfluenced by sample preparation; need longer time to collect data;
SEM	Microstructure	Visible results; quick data collection;	Complex sample preparation;
Thermodynamic modeling	Phase assemblage	Quick to obtain information;	Need large data base;

### 1.5 The origins of the thixotropic structural build-up of AAC

Physical and chemical reactions take place in fresh cementitious suspension. At rest, there are different types of force existing in the suspension, including Brownian motion, van der Waals attractive forces, electrostatic double layer forces or steric hindrance forces, gravitational and inertial forces [26], [33], [93], [94]. Brownian motion is the thermal, random, uncontrolled movement of particles in a fluid. The Van der Waals attractive forces, which include Keesom, Debye, and London interactions, are generated from the moment of dipoles of atoms or molecules [95]. Additionally, Brownian effects only play a minor role as compared to the van der Waals attractive interparticle forces [26]. An electrostatic repelling force is generated by the electrical double layer of particles. At large intermolecular distances, the Van der Waals attraction prevails, whereas at small intermolecular distances, the sharp Born repulsion caused by the overlapping electron clouds of molecules dominates [96]. For cementitious pastes with low zeta potentials (usually between 15 and 20 mV [97], [98]), the repulsive electrostatic double layer interaction is insufficient to overcome the attractive van der Waals forces [93].

Roussel et al. [33] elucidated the origins of thixotropic structural build-up of fresh cement particles as shown in Fig. 2-12. After mixing, cement particles are dispersed. Then the flocculation of cement particles is rapidly formed and led to the network

formation due to the colloidal attractive forces, then the suspension starts to resist stress and to display an elastic modulus. In the meantime, although the material is still in the dormant period, nucleation of C-S-H (black and white dots) occurs at the pseudo contact points between particles within the network. This nucleation process converts locally the soft colloidal connections between cement particles into C-S-H bridges, leading to an increase in elastic modulus. If additional shearing is applied now, it can break down the interparticle bridges of the early hydration products, allowing the particles to re-separate. In this circumstance, the un-hydrated cement particles surfaces are exposed to a water environment, resulting in the dissolution of ions and the formation of new hydration products [99], [100]. However, when the shearing state is stopped, cement particles re-flocculate [96]. With time elapsing, all the particles in the percolation path (black particles) are connected by C-S-H bridges, establishing a percolated stiff network in the material; As the size of the C-S-H bridges (black and white dots) increases, the elastic modulus of the mixture continues to grow.

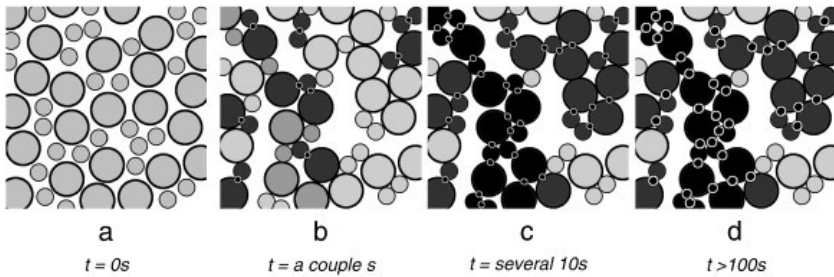


Fig. 2-12 The formation of percolation network of cement particles.

However, in comparison with Portland cement, the origins of thixotropic structural build-up of AAC have similarities and differences. The common activators for AAC are sodium hydroxide and sodium silicate. For sodium hydroxide, it has a viscous nature with high pH value. As reported in [47], the mixture activated by sodium hydroxide normally shows a very high initial storage modulus, this is due to the rapid dissolution of precursors and precipitation of reaction products. It seems that the dispersion effect between precursor particles induced by the viscous nature of activator cannot overcome the flocculation effect caused by the attractive colloidal interaction and rapid alkaline activation. Therefore, a percolated network normally will form for the sodium hydroxide-activated precursors, which is similar to the mechanism behind setting process of Portland cement.

However, the origins of thixotropic structural build-up of sodium silicate-activated mixture seem totally different. Because the sodium silicate-activated material shows the viscous effect and its low pH value cannot induce rapid reaction at early ages, these type of effects of the activator solution led to a significant decrease in the

colloidal interactions between precursors and prevent the formation of the well-percolated network [49], [101]. In the meantime, the soluble silicate in the activator solution shows its plasticizing and deflocculating effects, which will adsorb on the particle surface, increasing the magnitude of the repulsive double layer electric force [102]. Therefore, the sodium silicate-activated mixtures generally are not able to resist stress at early ages. With time elapsing, the continuous dissolution of precursors results in oversaturation of Ca and Al ions, which can interact with Si originating from activator solution to form reaction products [70], [71]. The pastes start to display an elastic modulus, and it should be noted that this structural formation is not easy to break when applying an additional shearing. In comparison between Portland cement and sodium silicate-activated materials, the solid-like nature of cement particles is achieved as a result of the formation of the well-percolated network [33], while sodium silicate-activated material shows the solid-like behaviour due to the result of stiffening [49].

## **1.6 Various influencing factors on the rheology and setting behaviour of AAC**

---

### 1.6.1 Precursors

AAC is produced from an alkali metal source (solid or dissolved) and calcium silicate or aluminosilicate-rich solid precursors such as coal combustion fly ash (FA), calcined clays (e.g. metakaolin), metallurgical slags (i.e. ground granulated blast furnace slag – GGBFS, stainless steel slags), mine tailings and even natural pozzolans [5]–[7]. In general the precursor's nature has a significant influence on the reaction mechanism. The aluminosilicate-rich materials react by means of dissolution, gelation and polycondensation to form inorganic N-A-S-H gel where sodium is integrated in the gel structure [7], [103]–[106], and networks of zeolites which form via polycondensation [5], [6]. Main reaction products in calcium-rich materials include calcium silicate hydrate gels, typically incorporating aluminum [3], [6], which are therefore labelled as C-A-S-H gel.

Generally, ground granulated blast furnace slag, phosphorous slag and Class C fly ash contain high calcium, which can be used as sole precursors in the AAC manufacturing because they contain a high content of reactive components [107]. Previous studies [102] also pointed out that alkali-activated slag mixture showed low workability and quick loss of fluidity due to its higher dissolution and reactivity in the alkaline environment and intricate particle surface chemistry. Puertas et al. [31] reported that a rapid loss of fluidity within 30 min after mixing when the sodium silicate activator has Ms value ( $\text{SiO}_2/\text{Na}_2\text{O}$ ) of 2.0 and its  $\text{Na}_2\text{O}$  content is 5%. Mehdizadeh et al. [108] also pointed out that the shear stress of alkali-activated phosphorous slag quickly increased with time due to higher dissolution rate of phosphorous slag and more gel formation. It was also discovered that increasing the proportion of calcium-rich waste brick powder in a Class C fly ash-waste brick powder blended high-calcium system increased the yield stress and consistency coefficient of Na-silicate activated pastes

[109], owing to more divalent cations ( $\text{Ca}^{2+}$ ) could result the interaction with Si originating from activator solution to form primary gels [71], [110]. Generally, alkali-activated slag mixtures showed an initial setting time ranging from 45 min to 300 min when the Ms ( $\text{SiO}_2/\text{Na}_2\text{O}$ ) decreases from 1.2 to 0.4 [111].

Opposite to high-calcium precursors, the low-calcium precursors, such as class-F fly ash, generally showed very low reactivity when contacting with alkaline solution. Previous study [112] reported that alkali-activated fly ash pastes showed a significant longer setting time as compared to that of alkali-activated slag pastes when using an identical sodium silicate solution due to the low reactivity of fly ash. Gadkar and Subramaniam [113] also explored the influence of the solution to binder ratio and Ms value on the rheological behaviour of alkali-activated fly ash pastes. They reported that the yield stress in suspension with a high solid content is controlled by the viscosity of the activator solution rather than the reaction of precursors at early ages. Some author also investigated the physical effects of fly ash on the rheological behaviour in the blended system. Aboulayt et al. [114] reported that with the increased replacement level of metakaolin by fly ash, the alkali-activated metakaolin-fly ash blended system showed a higher maximum packing volume fraction due to the dense packing model of spherical fly ash particles. Additionally, the fly ash with a lower specific surface in the blended system led to more surface wetting water being free. Thus, the viscosity (consistency) was reduced while the setting time and bleeding were increased. Other authors [110] studied the rheological properties of alkali-activated slag-fly ash-limestone mixtures. They pointed out that with the increasing content of fly ash in the ternary mixtures, the plastic viscosity decreased as expected by the particle packing effect and the increased water film thickness. In the meantime, the increasing amount of fly ash in the ternary mixtures led to a lower yield stress, this is because the fly ash particles can work as 'ball-bearing', which can reduce the internal friction between particles [115]–[117].

Another calcium free type of precursor is metakaolin, which is the anhydrous calcined form of the clay mineral kaolinite. Due to the high specific surface area of metakaolin [50], [118], [119], the alkali-activated metakaolin mixture needs suitable activators, dispersing agents and sufficient water to achieve good workability [107]. Producing a workable alkali-activated metakaolin paste (also known as geopolymer) at a low water-to-binder ratio is extremely difficult. Due to the high water requirement of metakaolin particles, it requires extremely strong shear during mixing. However, excessive water must be avoided for the sake of improved workability [116]; otherwise, the strength and durability of the concrete would be compromised. In comparison to Portland cement, where a portion of the mixing water is consumed during the hydration reaction and fills the pores, the water utilized in geopolymer mixtures is comparatively unbound. As a result, unreacted water in geopolymer mixtures may result in decreased mechanical and durability properties due to increased porosity [120]. Therefore, many authors tried to find different methods rather than simply increasing water amounts in the mixtures to improve the

workability metakaolin-based mixtures. Rovnanik et al. [118] reported that the plastic viscosity of metakaolin-based geopolymer can be reduced by the addition of waste red brick powder. Wang et al. [121] studied the effects of soluble aluminium species addition on the fresh properties of phosphate-activated geopolymer. The authors found that due to the addition of aluminium species to the phosphate activator solution, a quick sol/gel transition occurred in the early state (in six-coordination). As a result, the fresh prepared geopolymer paste demonstrated excellent workability. Aluminium species acted similarly to a plasticizer, reducing the yield stress of the fresh geopolymer paste while maintaining its viscosity unchanged. Benavent et al. [122] also discovered a similar plasticizing effect when utilizing an aluminosilicate activator instead of a silicate-based solution, which can improve the workability of fresh paste.

### 1.6.2 Activators

As well known, the reaction mechanisms and the microstructural properties of AAC are governed by the chemical composition of the solid reactant, the type and the concentration of the activating solution. Therefore, the rheological performance and setting behaviour is significantly influenced by the activator solution. The most widely available and economic alkaline solutions are sodium-based activators, such as NaOH,  $\text{Na}_2\text{O}\cdot n\text{SiO}_2$ ,  $\text{Na}_2\text{CO}_3$ ,  $\text{Na}_2\text{SO}_4$  and the combination of these activators. Next to that, some researchers also a proposed new type of alkaline solution produced by silica fume or rice husk ash to further decrease the price and carbon emission. These will be discussed further on.

#### 1.6.2.1 Sodium hydroxide activator

The rheological and setting behaviour can be significantly influenced by the concentration of sodium hydroxide activator. Riffaai et al. [48] reported that the yield stress, storage modulus and the rigidification rate of the geopolymer (alkali-activated fly ash pastes) increased with an increase of NaOH concentration from 2 to 7 mol/L, and the initial setting times of geopolymer activated by NaOH at 8 mol/L was around 3 h, however using higher concentrations (at 14 mol/L) resulted in an initial setting times up to 7 days. The authors pointed out that increasing NaOH concentrations up to 14 mol/L accelerated dissolving but had no effect on geopolymerization rates. Indeed, geopolymerization showed a slower rate than dissolution, leading to a lower storage modulus and rate of rigidification. This is most likely due to the formation of negatively charged monomers, which increases repulsive forces and hence prevents geopolymerization.

Besides, Vance et al. [123] also reported that the rheological properties of NaOH- and KOH- activated fly ash pastes were highly influenced by the viscosity change of the suspending fluid and surface charge of the fly ash particles. With an increase in the activator solution concentration from 4 to 8 mol/L, the yield stress and plastic

viscosity of suspensions increased. They believed that there are two factors that could account for the relative increase in yield stress with increasing molarity: the interaction potential and the viscosity of the activator solution. Previous studies [124], [125] have shown that the ion type, ion concentration and the pH of the suspending solution have a significantly influence on the zeta potential of fly ash particles. Fly ash has negative zeta potential in solutions of NaOH and KOH, with a greater negative potential in NaOH solutions. This behaviour is ascribed to the fact that  $K^+$  ions preferentially adsorb on the surfaces of fly ash particles over  $Na^+$  ions, thereby leading to a smaller negative surface charge as the  $K^+$  concentration increases. As the zeta potential lowers (i.e., becomes less negative), the yield stress increases as the repulsive force between fly ash particles reduces. The lower increase in yield stress with increasing molarity in NaOH solutions compared to KOH solutions can thus be attributed to the higher negative surface charge of the fly ash particles in NaOH, which results in stronger repulsive forces.

Puertas et al. [31] also investigated the effect of activator concentration on the shear stress of alkali-activated slag mixtures. They also pointed out that increasing the activator concentration (from 3% to 5%) induced the a higher shear stress in AAS mixtures. This is due to the increasing concentration of hydroxyl ions promoting slag dissolution, generating large quantities of stable reaction products [126].

#### 1.6.2.2 Sodium silicates activator

It is reported that sodium silicate-activated mixtures generally showed a lower yield stress as compared to mixtures prepared with other activators [47], [110], [127], [128] because sodium silicate caused a lower pH environment and increased the degree of polymerization of the silicates species leading to cyclic silicates, which delay the reaction of precursors [20], [47]. Additionally, these silicate species adsorb on the surface of precursors and increase the negative charges of the particles, resulting in a higher magnitude of interparticle double-layer repulsive forces, deflocculation of particles, and improved fluidity [102].

Generally, the  $M_s$  value ( $SiO_2/Na_2O$ ) and the  $Na_2O\%$  content of sodium silicate activator solution can significantly influence the rheological behaviour of AAC. It is reported that the yield stress of alkali-activated slag/fly ash pastes decreased when the  $M_s$  value of sodium silicate activator increased from 0.4 to 1.6 [47]. Similarly, other authors have also showed that increasing the  $M_s$  value from 1.1 to 1.5 resulted in a decrease in yield stress from 0.63 Pa to 0.12 Pa [49]. By contrast, the authors also indicated that the plastic viscosity increased with an increase in  $M_s$  value. This behaviour can be explained by the viscous effect arising from the high  $M_s$  value of the activator resulted in an increase in the shear forces between precursors particles [115]. As a result, increasing the amount of sodium silicate increased the overall viscosity of the alkaline solution, which resulted in an increase in the plastic viscosity of the pastes. The effects of the  $Na_2O\%$  content of sodium silicate on the rheological

behaviour of AAC is relative complex, Puertas et al. [31] found that with a lower Ms value ( $<0.8$ ), increasing the  $\text{Na}_2\text{O}$ % content increased the yield stress of pastes. On the other hand, the AAC pastes did not exhibit the same behaviour when the concentration of  $\text{Na}_2\text{O}$  was raised at a higher Ms value ( $>1.2$ ) of the sodium silicate solutions. The authors pointed out that the Ms value required for the formation and breakdown of primary C-(A)-S-H gel under dynamic shearing conditions decreased as  $\text{Na}_2\text{O}$  concentration increased.

In general, the mixture prepared by sodium silicate mixtures showed a lower yield stress as compared to the mixture activated by sodium hydroxide [47]. However, the silicate-based mixtures normally have quicker setting times and their workability decreased faster than for hydroxide-based mixtures [47]. Previous studies also pointed out that the silicate-based mixtures showed a much shorter initial setting time and for some mixtures even shorter than 30 min [129], which is not acceptable for the practical applications. Therefore, to extend the setting times of silicate-based mixtures, many authors have found different methods. It is reported that prolonging the mixing time can extend the initial setting times of alkali-activated slag mixtures [30]. Some authors pointed out that increasing the amount of low-calcium or free-calcium materials in the precursors also can delay setting process of AAC. Previous study [47] found that the initial setting times of alkali-activated slag mixtures can be prolonged by the addition of fly ash due to their difference in dissolution and activation kinetics. Li et al. [130] also reported that when 10% metakaolin is incorporated into alkali-activated slag mixtures, the initial and final setting times of AAC were increased by 21% and 39%, respectively. Increasing the amount of metakaolin from 10% to 20% even lead to a longer setting time. Some authors [131] also used a lower temperature of mixing water to extend the setting times of AAC prepared by sodium silicate solution. They found that lowering the temperature of mixing water can partially compensate for the effect of dissolution heat by delaying chemical reactions and prolonging the setting times. In comparison, warm mixing water can accelerate hydration, resulting in a quicker setting time. This indicates the potential of AAC activated by sodium silicate solution for winter engineering applications. Furthermore, changing the Ms value also can be used to extend the initial and final setting times as shown in Fig. 2-13. It seems that AAC mixtures prepared with sodium silicate activator solution with lower Ms value generally showed a longer setting times. This indicates that the setting times required for practical engineering can be extended or changed by a better mixture design. Additionally, chemical retarders also can be used to extend the setting times of AAC. This will be discussed in section 1.6.4 in detail.

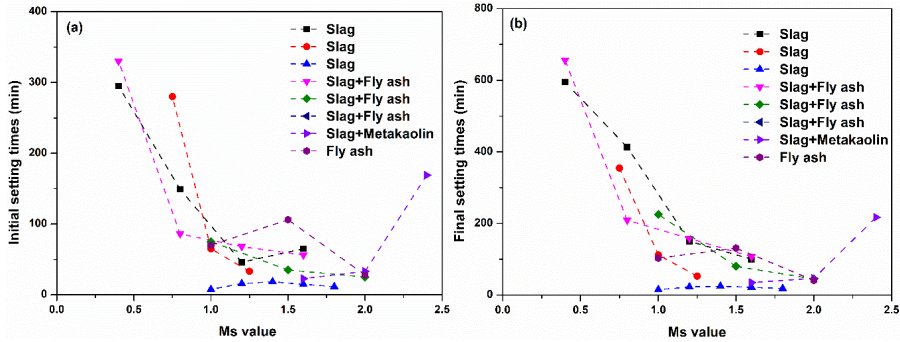


Fig. 2-13 Initial and final setting times of AAC mixtures prepared with sodium silicate solution with various Ms value ( $\text{SiO}_2/\text{Na}_2\text{O}$ ) [47], [111], [132]–[137].

### 1.6.2.3 Sodium carbonate activator

Sodium carbonate is seen as a more sustainable activator as compared to sodium hydroxide due to its low cost, commercial availability and also helps in reducing the pH of the alkaline solution [138]. Activation of slag with sodium carbonate activator has been reported for the production of activated slag products. It is reported [139] that at early ages  $\text{Ca}^{2+}$  dissolved from slag preferentially combines with  $\text{CO}_3^{2-}$  from the activator, generating calcium carbonates and gaylussite, whereas the aluminosilicate component of the slag reacts separately with the sodium from the alkaline solution, forming zeolite (NaA). These phases lack the high degree of cohesion necessary for development of high early mechanical strength, and the reaction proceeds slowly due to the slow dissolution of slag under the moderate pH conditions provided by the sodium carbonate activator. Once the  $\text{CO}_3^{2-}$  is depleted, the activation process proceeds similarly to that of a sodium hydroxide-activated slag binder, yielding the conventional binder phases calcium aluminum silicate hydrate and hydroxalite, as well as Ca-heulandite as an additional (Ca,Al)-rich product.

Regarding the effects of sodium carbonate activator on the setting behaviour of AAC, due to the mild pH environment provided by sodium carbonate, the AAC mixtures prepared with sodium carbonate normally showed a lower reaction process. It is reported that the sodium carbonated-activated slag mixtures with a  $\text{Na}_2\text{O}\%$  content of 3% showed an initial setting time higher than 3 days [140]. Similarly, Bernal et al. [139] also reported that the activation of slag by sodium carbonate (8% wt of slag) have to be demoulded after 4 days curing. Yuan et al. [141] used FTIR technique to observe that the gelation of C-(A)-S-H occurred 3 days of curing. This also can explain the low reaction speed of sodium carbonate-activated slag mixtures.

As mentioned before, the slag mixtures prepared with sodium silicate and sodium hydroxide normally result in fast setting times, while sodium carbonate-activated can retard the activation of slag. Therefore, many researchers pointed out that the careful

selection and combination of activators can be a potential way to manipulate the setting times of AAC. Li et al. [142] investigate the effect of combined ternary activator of  $\text{Na}_2\text{CO}_3$ - $\text{NaOH}$ - $\text{Na}_2\text{O}\cdot 2\text{SiO}_2$  on the setting times and compressive strength of AAC. They found that a better mixture design of this combined activator can not only achieve reasonable setting time, but also high compressive strength. As shown in Fig. 2-14, specifically, the authors found that increasing the dosage of  $\text{Na}_2\text{CO}_3$  as activator lengthened the setting time particularly when considering the final setting time and using a slag with a moderate content of  $\text{MgO}$ . While the addition of  $\text{NaOH}$  and  $\text{Na}_2\text{SiO}_3$  can dramatically shorten the initial setting times. Jimenez et al. [126] also summarized that the  $\text{OH}^-$  ion in solution is critical for early dissolution of slag, and the  $\text{CO}_3^{2-}$  ion retards the setting times of alkali-activated slag mixtures, whereas  $(\text{SiO}_4)^+$  can accelerate the setting times.

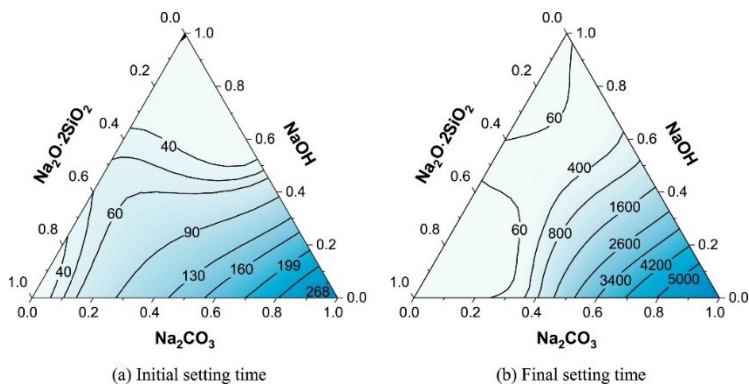


Fig. 2-14 Setting times (min) of alkali-activated slag with  $\text{Na}_2\text{CO}_3$ - $\text{NaOH}$ - $\text{Na}_2\text{SiO}_3$  activators: (a) initial setting times, (b) final setting times [142].

#### 1.6.2.4 Silica fume-derived and rice husk ash-derived activator

More recently, to further reduce the energy consumption and  $\text{CO}_2$  emission during the activator production, some authors also produced other types alkaline solution, such as silica fume-derived and rice husk ash-derived activators. The silica fume-derived activator is prepared with silica fume and an alkaline solution [143]. According to Rousekova et al. [144], silica fume activator is highly effective in activating the Portland cement and slag mixtures or the slag alone. The positive effect of silica fume activator is ascribed to its enhancement of calcium silicate hydrate formation and densification of the pore structure. The mechanical properties of slag and fly ash mixtures activated with silica fume activator are shown to be superior to those of sodium silicate-based mixtures [145]. Besides, Bernal et al. [146] also demonstrated that the silica fume activator could promote the formation of a highly densified structure. These findings demonstrate that silica fume is a superior and more cost-

effective option than the sodium silicate activator. Furthermore, some authors [111] also investigate the effects of silica fume activator (SFA) and sodium silicate activator (SSA) on the rheological behaviour and setting times of alkali-activated slag mixtures. They found that sodium silicate-activated slag mixtures showed a fast increase in shear stress, whereas the slag mixture prepared with silica fume activator exhibited a low and steady-state shear stress over time, indicating the lack of reaction products formation at early times and better workability retention. As shown in Fig. 2-15, the effects of sodium silicate and silica fume activator with different Ms value on the setting times of AAC were compared. It can be seen that the silica fume activator with a Ms value of 1.2 showed a significantly longer setting time as compared to other mixtures, which can be acceptable in practical engineering. Besides, the authors also found that SFA showed a lower cost and CO<sub>2</sub> emission, enabling this activator become a more economical and sustainable solution than SSA.

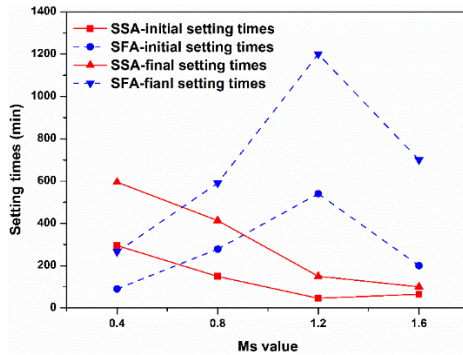


Fig. 2-15 Setting times comparison between the sodium silicate-activated and silica fume activator-based slag mixtures [111].

Another green alkaline activator that can be used is rice husk ash-derived activator. Rice husk ash (RHA), which is produced when rice husk is burned in biomass power plants, has the potential to be a promising supply of silica for AAC activators. Similar to silica fume activator, the rice husk ash-derived activator is produced from dissolving RHA in an alkaline solution at temperatures of up to 100 °C [147]–[149]. Alnahhal et al. [150] compared the effects of commercial sodium silicate activator and RHA-derived activator on the rheology and structural build-up behaviour of alkali-activated slag/fly ash pastes. They found that RHA-derived mixtures have a similar setting time as compared to the commercial sodium silicate-activated slag mixtures. The author reported that although RHA had a higher proportion of monomers and a lower concentration of condensed silicate species than commercial sodium silicate, the overall structural build-up of AAC paste activated with filtered RHA was quite similar to that activated with commercial sodium silicate. This indicates that similar

reaction products are formed and that the type of the silicate species in the activator has a minor influence.

### 1.6.3 Mineral additions

To further reduce the greenhouse gas emissions in the Portland cement production, supplementary materials, such as limestone, slag, silica fume and fly ash, can be used to replace the amount of clinker. In AAC production, because slag and fly ash are the main binders, the main mineral supplementary materials are limestone and silica fume. It is reported that the influence of limestone on Portland cements normally can be classified as, filler effect, nucleation effect, dilution effect and chemical effect [151]. The addition of limestone into AAC mixtures normally can improve rheological properties by working as filler to optimize the particle packing of the blended system, and increase water for lubrication. Some authors [110] reported that the dynamic yield stress of ternary slag-fly ash-limestone mixtures prepared with high Ms value sodium silicate decreased as the limestone powder replacement decreased from 50% to 0%. The mixtures with a higher amount of limestone powder can achieve a better particle packing, which lead to more free water to lubricate the particles [152]. The relationship between water thickness and plastic viscosity is also given in Fig. 2-16. The plastic viscosity of AAC mixtures prepared with high Ms value sodium silicate solution showed an inverse correlation to the calculated water film thickness, which also follows the same trend in the Portland cement system [117]. Similarly, Xiang et al. [153] also reported that the addition of 5%-20%wt limestone powder in slag-fly ash mixtures prepared by sodium silicate solution did not change the rheology (Bingham model), and further induces a reduction in yield stress and plastic viscosity.

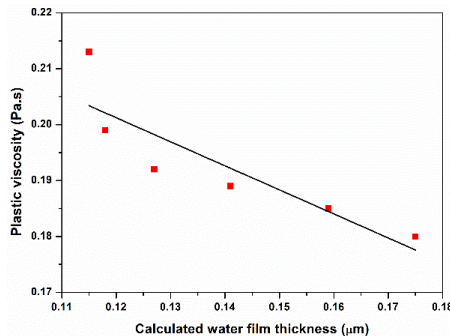


Fig. 2-16 The relationship between calculated water film thickness and plastic viscosity, data adopted from Ref. [110].

Silica fume is another common supplementary addition in the Portland cement production. Recently, some researchers also have attempted to replace the GGBFS or

fly ash in AAC with silica fume because silica fume normally presents a pozzolanic nature. Güllü et al. [154] has reported that at high amount of silica fume addition (>50%) in AAC mixtures, the yield stress and plastic viscosity increased significantly as the water to binder ratio decreased, while this enhancing effect was significantly reduced when the addition of silica fume was less than 20%. As summarized by Lu et al. [107], there exist a limit addition of silica fume, when the use of silica fume exceeds the critical point, the yield stress and plastic viscosity increased significantly due to the high specific surface of silica fume leading to insufficient water to wet and react. Meanwhile, the reactivity of silica fume in the high alkaline environment will also contribute to the reaction [155]–[157]. However, once the incorporation of silica fume is lower than the critical point, the silica fume can act as a ‘ball-bearing’ to reduce the yield stress and plastic viscosity due to its spherical particles [154].

Furthermore, nano clay also recently was used to increase the buildability in 3D-printing construction [158]. Previous studies [159] found that the thixotropy of alkali-activated slag-fly ash mixtures can be significantly increased by a lower amount of nano clay addition due to nano clay particles having a negative and positive charge on their opposite ends, which enabling them to form a “card-house” or scaffolding structure in aqueous suspensions when the material is at rest [160].

#### 1.6.4 Chemical admixtures

As well known, there are several types of water-reducing admixtures, such as naphthalene-based, aminosulfonate-based, melamine-based, lignosulfonate-based water reducing admixtures and polycarboxylate-based superplasticizers, which are commonly used in Portland cement production. It is reported that only the naphthalene-based water reducing admixtures considerably increased fluidity in NaOH-activated slag pastes [30]. This is due to the naphthalene admixtures being stable in alkaline solution and retaining its plasticizing capabilities [161]. In comparison, melamine, polycarboxylate, and vinyl copolymer admixtures degrade in a very high alkaline condition, hence losing their fluidizing properties. However, for the silicate-based mixtures, no existing superplasticizer was discovered to be very effective to increase fluidity in silicate media. This is due to a very weak percolated network formation in the silicate-based mixtures at early ages, indicating less flocculation [49], [101]. Therefore, the working mechanism for PC superplasticizers might not be applicable in silicate-based AAC mixtures.

However, to solve the problem of silicate-based mixtures showing rapid settings, adding retarder chemicals can be an option to slow down the activation process [162]–[165]. Table 2-4 summarizes and compares effects of various chemical retarders admixtures with different dosages on the rheological properties or setting behaviour of AAC. In general, these types of retarder admixtures have strong chemical intervention that results in changes in the setting process due to involvement of special anions or cations disturbing geopolymerisation potentially [166], [167]. As shown in

Table 2-4, phosphoric acid and phosphate normally can extend the setting process of AAC, but they also lead to the reduction of mechanical performance. While the addition of boric acid and borate normally can increase the setting time without negative effect on compressive strength. Up to date, the nano-ZnO and zinc salts have also been reported to effectively retard alkaline reaction [168], [169]. Garg and White [168] reported how nano-ZnO retards the setting process of AAC, by pair distribution function (PDF) analysis and isothermal calorimetry. They found the retarding mechanism of nano-ZnO in alkali-activated slag mixtures as shown in Fig. 2-17. Calcium ions will bind with tetrahydroxozincate ions ( $Zn(OH)_4^{2-}$ ), which can alter the nucleation/growth of the C-(A)-S-H type gel.

Table 2-4 The comparison of effects of various chemical retarders with different dosages on rheology and setting behaviour of AAC

Chemical retarders	Dosage / concentration	Precursors	Activators	Main performance	Ref.
Phosphoric acid ( $H_3PO_4$ )	0M; 0.78M; 0.81M; 0.84M; 0.87M	Slag (pastes)	Sodium silicate	When the $H_3PO_4$ concentration approached 0.84M, the setting time was significantly prolonged (also reduced early strength).	[162]
Phosphoric acid ( $H_3PO_4$ )	0.82M	Slag and gypsum (pastes)	Sodium silicate	The retarding effect of $H_3PO_4$ can be reduced by adding gypsum	[170]
Tartaric acid (TA)	0.01%; 0.02%; 0.03%; 0.04% (by mass of binder)	Slag (pastes)	Sodium hydroxide	The initial setting times were prolonged from 0.52 h (without TA) to 9.12 h (with 0.04% TA)	[171]
Citric acid (CA)	3% (by mass of binder)	Coal fly ash and lime kiln dust (pastes)	Sodium hydroxide	The incorporation of CA allowed for the retention of acceptable levels of yield stress and plastic viscosity up to 60 min.	[172]
$Na_3PO_4$	$Na_3PO_4$ were recalculated to wt % of $P_2O_5$ .  0.5%; 1.0%, 2.5%; 5.0% wt% of $P_2O_5$ (by mass of binder)	Slag (pastes)	Sodium silicate	The setting times were prolonged, while the workability were decreased.	[173]
Borax	2%; 4%; 6%; 8% (by mass of binder)	Slag and fly ash (pastes)	Sodium silicate	Both setting times and flowability were increased with an increase of Borax addition	[163]
Borax	10% (by mass of binder)	Slag and fly ash (pastes)	Sodium silicate	The initial setting times and 28-d compressive strength both	[174]

				increased by 78% and 18%, respectively.	
Borax	2.5%; 5%; 10%; 15%; 20% (by mass of binder)	Class F fly ash (pastes)	Sodium hydroxide	When Broax is 10% or 15% wt, the composite activator of NaOH and anhydrous borax may significantly prolong the setting time at 60 and 75 °C, respectively.	[175]
Sucrose	1.5%; 2.5% (by mass of binder)	Fly ash (mortars)	Sodium silicate	The addition of sucrose can slightly delay the initial setting times and moderately delay the final setting times	[176]
Chelators (HIDS; EDTA-4Na; GLDA-4Na)	4% (by mass of binder)	Slag and fly ash (pastes)	Potassium silicate	All chelators prolonged the setting times. HIDS is the most effective.	[177]
Mecury salt	0.1%, 0.5% and 2.0% $Hg^{2+}$ in $(NO_3)_26H_2O$	Slag (pastes)	Sodium silicate	The setting times slightly increased at 0.1% and 0.5%, further significantly increased at 2%.	[178]
Nano-ZnO	0.1%; 0.5%; 1.0% (by mass of binder)	Slag (pastes)	Sodium silicate	The heat release were significantly delay.	[168]
Styrene-butadiene (SB) latex	5% and 10% (by mass of binder)	Slag and fly ash (pastes)	Sodium silicate	The addition of SB increased setting times. Meanwhile the bond and flexural strength also increased with addition of SB.	[179]

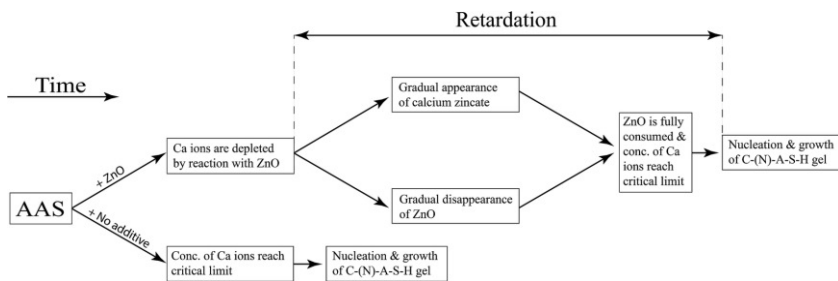


Fig. 2-17 The retardation mechanism of nano-ZnO in alkali-activated slag mixtures.

### 1.6.5 External factors

Apart from the aforementioned chemical effects, such as activator and retarder nature on the rheological properties and setting behaviour, some external factors, such as

mixing and temperature, also have a great influence on the rheology of AAC. Puertas et al. [180] investigated the effects of different mixing time on fresh behaviour of alkali-activated slag concrete. They pointed out that in Portland cement and hydroxide-based mixtures, longer mixing periods had a detrimental influence on dynamic and static yield stress and resulted in considerable and permanent coagulation of cement particles (decreased workability). In comparison, longer mixing time were beneficial in silicate-based mixtures, where they were necessary to break down the microstructure and improve rheological behaviour. These findings established that for sodium silicate-activated slag concrete preparation, a longer mixing time is necessary. This would have an impact on the future standardization of these environmentally friendly building materials. Furthermore, Alrefaei et al. [181] also investigated different mixing method on the rheological and mechanical performance on alkali-activated slag/fly ash pastes. They used three different mixing methods: 1) The water was added to the binder and solid activator to produce pastes; 2) The binder was mixed with an alkaline solution; 3) the alkaline solution was prepared with the solid activator and 60%-80% water, then mixed with the binder, lastly the remaining water was added to produce pastes. They pointed out that these mixing methods affected the flowability, compressive strength and porosity, but no influence on the chemical composition and mineralogy of AAC reaction products.

Temperature is another significantly important factor that affects the rheology of AAC mixtures. Mehdizadeh et al. [108] discovered that the viscosity of alkali-activated phosphorous slag increased when temperature increased from 10°C to 40°C. The apparent activation energy of these pastes was determined to be 39.2 to 44.5 kJ/mol for the chemical composition using rheology data based on the Arrhenius viscosity model and at varied temperatures (10, 25, and 40 °C). The correctness and dependence of the Arrhenius viscosity model were established in comparison to the calorimetric technique by estimating the activation energy of Portland cement as a blank sample and a known material, which was determined to be 36.7 kJ/mol. Palacios et al. [182] reported that when the temperature above was 65 °C, the yield stress and apparent viscosity were increased significantly, indicating the dissolution of fly ash and the precipitation of hydration products are enhanced. This also suggest that a high curing temperature can be used for the alkali-activated fly ash mixture to shorten its long setting time.



## **Part II**

---

### **Materials and methods**



### **Chapter 3 Materials and methods**

---

This chapter gives a summary of the materials and testing methods in this thesis.

## 1. Materials properties

The properties of precursors, mineral additions and activators used in this thesis are introduced.

### 1.1 Precursors and mineral additions properties

Ground granulated blast furnace slag (GGBFS, slag) and fly ash (FA) are the main precursors in this thesis. Silica fume (SF), limestone (LSP) and CEM I 52.5-N Portland cement (PC) are the mineral additions used in a part of this thesis. The specific gravities and BET surface areas of the GGBFS, SF, LSP and FA are 2.92, 2.25, 2.81 and 2.32, and 0.85, 22.5, 4.43 and 1.67 m<sup>2</sup>/g, respectively. The specific gravities and Blaine fineness of PC is 3.15 and 450 m<sup>2</sup>/kg, respectively. The chemical composition by X-ray fluorescence (XRF) and particle size distribution by laser diffraction of these precursors are given in Table 3-1 and Fig. 3-1. The GGBFS, SF, LSP, FA and PC had a median particle size ( $d_{50}$ ) of 11.6, 7.8, 3.9, 4.0 and 7.3  $\mu\text{m}$ , respectively.

Table 3-1 Chemical composition of precursors and mineral additions.

Oxide (wt.%)	CaO	SiO <sub>2</sub>	Al <sub>2</sub> O <sub>3</sub>	MgO	SO <sub>3</sub>	TiO <sub>2</sub>	K <sub>2</sub> O	Na <sub>2</sub> O	Fe <sub>2</sub> O <sub>3</sub>	MnO	BaO	LOI
GGBFS	40.80	33.30	12.30	7.84	2.30	1.29	0.67	0.44	0.39	0.36	0.31	0.01
SF	0.3	97.0	0.7	0.4	0.2	-	0.8	0.3	0.1	-	-	-
LSP	48.85	8.15	1.28	1.41	0.05	-	0.28	1.25	0.88	-	-	37.29
FA	4.33	56.7	23.5	1.43	1.16	1.23	2.65	0.91	5.92	-	0.21	0.03
PC	64.3	18.3	5.2	-	3.5	-	0.43	0.32	0.88	-	-	2.7

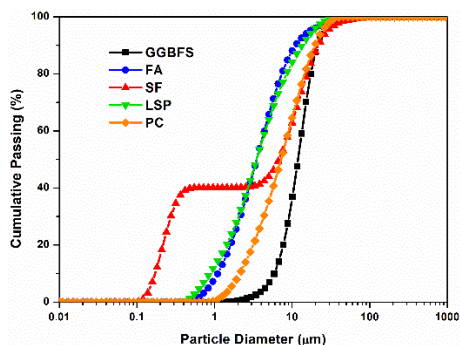


Fig. 3-1 Particle size distribution.

## 1.2 Activator properties

---

There are three chemicals used to prepare the alkaline solution (or activator) in this thesis. The first one is the caustic soda (NaOH) with purity of 97%, which is mixed with deionized water to prepare the sodium hydroxide solution. The second one is the liquid sodium silicate solution with a Ms value ( $\text{SiO}_2/\text{Na}_2\text{O}$ ) of 1.6, which is comprised 28.5%  $\text{SiO}_2$ , 17.95%  $\text{Na}_2\text{O}$ , and 53.55%  $\text{H}_2\text{O}$  by mass. The sodium silicate activator is mixed with a certain amount of NaOH and deionized water to achieve various Ms values. Lastly, sodium sulfate with purity of 98% is mixed with deionized water to prepare the sodium sulfate activator solution.

## 2. Testing methods

---

Fresh and mechanical properties of AAC mixtures are evaluated by various methods, and the change in microstructure of AAC mixtures is investigated by additional advanced techniques.

### 2.1 Fresh properties testing methods

---

#### 2.1.1 Mini slump tests

The flow spread of the pastes was determined by the mini-slump test according to the ASTM C1437-15 [183]. A truncated cone with dimensions of 46 mm top and 68 mm base diameters and height of 40 mm was used in the mini-slump test. Mini-slump spread diameter (%) values were calculated by Eq. (3-1).

$$\text{Spread diameter (\%)} = \left( \frac{\text{flow diameter}}{68} - 1 \right) \times 100 \quad (3-1)$$

#### 2.1.2 Setting times

Initial and final setting times were determined by an automatic Vicat needle apparatus, according to EN 196-3 [40]. The initial setting time was determined when the depth between the needle and the bottom plate was around  $6 \pm 3$  mm, and the final setting time was determined by the time at which the needle first penetrates only 0.5 mm.

#### 2.1.3 Flow curves

A rotational rheometer (Anton Paar, MCR102) was applied to measure the flow curves of AAC pastes in this thesis. Both a six-vane blade vane rotor and a custom building materials cell were used. The outer diameter and the depth of the cup were 27.6 mm and 75 mm, respectively. The six-blade vane diameter was 22 mm. It should be noted that AAC pastes are influenced by many factors, thereby exhibiting a very wide

variety of rheological behaviour. In this thesis, depending on the characteristics of pastes, different shear protocols are used. These protocols will be separately introduced in the different chapters.

#### 2.1.4 Small amplitude oscillation shear tests (SAOS)

The structural build-up of AAC mixtures was determined by a rotational and oscillatory rheometer (Anton Paar MCR 102). The rheological measurements were carried out under constant temperature conditions at  $20 \pm 0.5$  °C and each mixture was tested with three new samples to check the repeatability of the tests. The presented curves are representative curves, which are fitted to the average of three tests. A six-blade vane geometry in a cylindrical cup was used to avoid the influence of slippage between paste and the metal surface of either a plate or cylindrical geometry custom to other rotational and oscillatory geometries [184], [185]. To minimize the influence of evaporation, a plastic lid covered the cup without touching the rotary axis of the vane geometry.

In SAOS testing, the response of the material being subjected to a continuous sinusoidal excitation is measured to evaluate the structural build-up of the material over time. As the introduced excitation is very small and in the range of the linear viscoelastic domain (LVER) of the material, this method can promise the sample is not influenced and ruptured during structural evolution, and therefore it is assumed to be non-destructive. The measured responses (shear stress amplitude against a deformation excitation or vice versa) are converted to parameters called storage modulus ( $G'$ ) and loss modulus ( $G''$ ). Storage modulus relates the elastic behaviour of the material and it is proportional to the energy stored in each cycle of the excitation. On the other hand, the loss modulus relates to the viscous behaviour of the material and it is proportional to the lost or dissipated energy in each cycle. The loss factor is the ratio between  $G''$  and  $G'$ . The storage modulus and the loss factor are considered in this work to investigate the network structure development as a function of time.

Strain-sweep tests with strain amplitude from 0.0001% to 10% (or 20%) and constant frequency of 1 Hz were carried out to determine the LVER before the time-sweep tests, which is also commonly applied in other studies [186], [187]. The strain amplitude of 0.005% was selected in order to guarantee that all the mixtures are in the LVER, which was consistent with the order of  $10^{-5}$  used in Yuan et al. [27] and Mostafa et al. [188].

The fresh paste was loaded to the cup after mixing and was subjected to the first pre-shear at a rotational speed of  $100 \text{ s}^{-1}$  for 30 s to achieve a reference state. Afterwards, the samples rested for 30 s to dissipate residual stresses due to mixing, then the time-sweep test was immediately conducted.

### 2.1.5 Ultrasonic pulse velocity (UPV)

The ultrasonic pulse velocity measurements can be used to assess the microstructural changes and structural build-up, which are correlated to the isothermal heat evolution and Vicat setting times. Fig. 3-2 presents the UPV test configuration. In this study, P-waves were sent every 1 min through a 47.5 mm-wide paste sample, and the data were collected over 24 h. The received ultrasound signals and their frequency spectrum were calculated by the FreshCon software.

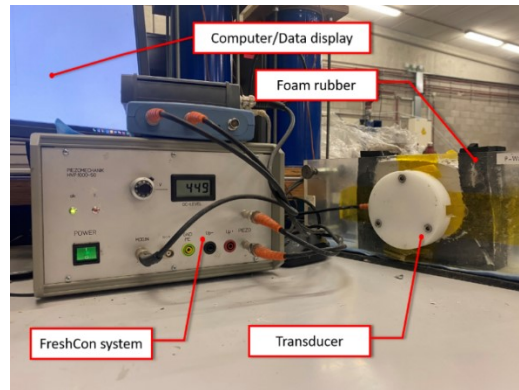


Fig. 3-2 Ultrasonic pulse velocity measurement configuration.

## 2.2 Mechanical properties and drying shrinkage testing methods

### 2.2.1 Mechanical performance

Mechanical properties of the mixtures were evaluated on mortar scale. All mixtures had the same aggregate to binder ratio of 3. Standard CEN sand was used as aggregate. The fresh mortars were poured into plastic molds of  $40 \times 40 \times 160 \text{ mm}^3$  and vibrated for 1 min, then covered with a plastic film for 24 h. After demolding, all mortar samples were cured under  $20 \text{ }^\circ\text{C}$  temperature and 95% relative humidity conditions until the testing day. Flexural and compressive strength of the samples were determined according to EN 196-1 [189] at the age of 2, 7 and 28 days.

### 2.2.2 Mercury intrusion porosimetry (MIP)

At the testing ages, the paste samples were crushed into small pieces with dimensions of around  $1 \text{ cm}^3$ , and then these small sample pieces were immersed in isopropanol for one week to stop the reaction of the slag and dried in a  $40 \text{ }^\circ\text{C}$  oven for 1h. The dried samples were stored in a low vacuum desiccator before the analyses. A Pascal 440 mercury porosimeter with a maximum load capacity of 420 MPa was used in the

MIP test. However, the maximum pressure was limited to 200 MPa in order to avoid cracks induced by the mercury pressure [79], [190]. The adopted mercury surface tension and contact angle between the mercury and the solid surface were 0.482 N/m and 142°, respectively.

### 2.2.3 Drying shrinkage

The drying shrinkage values of the mortar specimens were determined by DEMEC (DEmountable MEChanical) gauges method. For each mixture, three prismatic specimens were used. After two days of curing in a moisture room, all specimens were moved to a temperature and moisture-controlled room (20 °C and 65% RH). Two measuring points were glued (DEMEC point locations) to the central line of the three surfaces of the specimens. For each specimen, three surfaces were measured (except for the troweled surface). The distance between two points (gauge length) was 100 mm. The details of the test set-up can be found in the paper of Tenório Filho et al. [191]. The measurements were recorded up to 70 days.

## 2.3 Microstructure analysis

---

### 2.3.1 Pore solution chemistry

The pore solution chemistry of AAC mixtures at the early ages was analyzed by Inductively Coupled Plasma – Optical Emission Spectrometry (ICP-OES, 720 ES Varian/Agilent). The pore solutions of AAC mixtures were obtained by the centrifugation (3500 rpm for 5 min) of paste samples at different early ages. The obtained pore solutions were filtered by a syringe connected to a disposable 0.45 µm syringe filter. The pore solutions were diluted with pure water. The dilution ratios for determining low concentration elements (Al, Mg, Ca and Fe) and high concentration elements (Na, Si, B and P) were 1:20 and 1:4000, respectively. ICP – OES analyses were conducted on the pore solution samples as quickly as possible on the same day to prevent any salt precipitation. The ion concentrations of the activator solutions were shown at zero time in the ICP analysis results.

### 2.3.2 X-ray diffraction (XRD)

The samples were taken from the hardened paste samples at the testing ages. Following the RILEM TC-238 methodology [72], 3 g of the crushed pieces with a size between 125 µm and 1 mm were mixed with 100 ml isopropanol for 15 min. The suspension was filtered and rinsed with isopropanol and diethyl ether before drying at 40 °C for 8 min. Then the dried samples were stored in a low vacuum desiccator before the analysis. The XRD measurements were conducted on a Rigaku D/Max-2200/PC X-ray diffractometer with CuK $\alpha$  radiation ( $\lambda = 0.1542$  nm) at 40 kV and 36 mA,

scanning from  $5^\circ$  to  $70^\circ 2\theta$  with  $0.02^\circ$  step size.

### 2.3.3 Fourier transform infrared spectroscopy (FTIR)

FTIR spectra were used to investigate the main bands assigned to the Si-O-Si bonds of the activator solution. The measurements were carried out using a Bruker FTIR spectrometer by placing several drops of the solutions on a 3 mm diameter diamond/ZnSe crystal of attenuated total reflector (ATR) accessory. Before each test, the background was scanned to check the cleanness of the ATR. The spectra resolution was  $1\text{ cm}^{-1}$  and an average of two scans was taken into consideration for each sample.

The hardened AAC samples were tested at the testing ages. Following the RILEM TC-238 [72] methodology, after crushing the hardened pieces to a size of  $125\ \mu\text{m}$  to  $1\text{ mm}$ ,  $3\text{ g}$  of the powder was mixed with  $100\text{ ml}$  isopropanol for  $15\text{ min}$ . The suspension was filtered and rinsed with isopropanol and diethyl ether before drying at  $40^\circ\text{C}$  for  $8\text{ min}$ . Then the dried samples were stored in a low vacuum desiccator prior to analysis. KBr pellets were prepared by mixing  $1\text{ mg}$  of sample and  $100\text{ mg}$  of KBr. The FTIR tests were conducted on a Perkin Elmer spectrum BX FT-IR system, at the frequency range of  $400 - 4000\text{ cm}^{-1}$  with  $4\text{ cm}^{-1}$  resolution

### 2.3.4 Scanning electron microscopy (SEM) and Image analysis (IA)

The sample preparation is followed by RILEM TC-238 methodology [72]. For the fractured samples, they were coated with carbon before SEM secondary electron (SE) imaging. For polished samples, paste at the age of testing days were immersed into epoxy, and then sectioned, followed by polishing up to  $0.25\ \mu\text{m}$  surface fineness using diamond paste. Afterwards, the polished samples were observed by SEM with backscattering electron (BSE) mode at an acceleration voltage of  $15.0\text{ kV}$  under low vacuum mode. The magnification of each image was  $500\times$ . A representative BSE image and an analytical procedure for calculating the reaction degree from BSE images are illustrated in Fig. 3-3. The discrimination between hydrated/anhydrous regions using the original BSE image is not easy, since no distinctive peaks according to gray level are observable from the gray-level histogram. The bilateral filter available in ImageJ software (<https://imagej.nih.gov/ij/>) was used to make the BSE images smoother and keep the particle edges in BSE images. The gray-level histogram (Fig. 3-3b) was obtained from the cropped/filtered image. As can be seen from Fig. 3-3b, there were two distinct regions allowing the determination of the thresholds for quantifying the areas corresponding to unreacted GGBFS and hydrated phases, as well as cracks or pores. By applying an appropriate threshold value (Fig. 3-3b), the areas corresponding to the unreacted GGBFS were obtained as shown in Fig. 3-3b. As well known, the first principle of stereology (or the Delesse Principe [192]), a determination of the area fraction of a phase in random sections is an unbiased estimator of the volume fraction of this phase. As such, the degree of reaction of

GGBFS can be estimated as follows in Eq. (3-2):

$$\alpha(t) = \left(1 - \frac{V_t}{V_i}\right) \times 100\% \cong \left(1 - \frac{A_t}{A_i}\right) \times 100\% \quad (3-2)$$

where  $\alpha(t)$  is the degree of reaction of GGBFS at age  $t$ ,  $V_t$  and  $V_i$  are the volume fraction of unreacted slag relative to the total volume of mixture at given curing time and at the initial state, respectively, and  $A_t$  and  $A_i$  are the area fraction of unreacted slag relative to the total cross section of mixture at given curing time and at the initial state, respectively, as obtained by the BSE image analysis. It is reported that the image analysis based on 12 or more BSE images could enable a 95% degree of confidence [193]. Consequently, a total number of 20 images on randomly selected locations for each sample were submitted to image analysis.

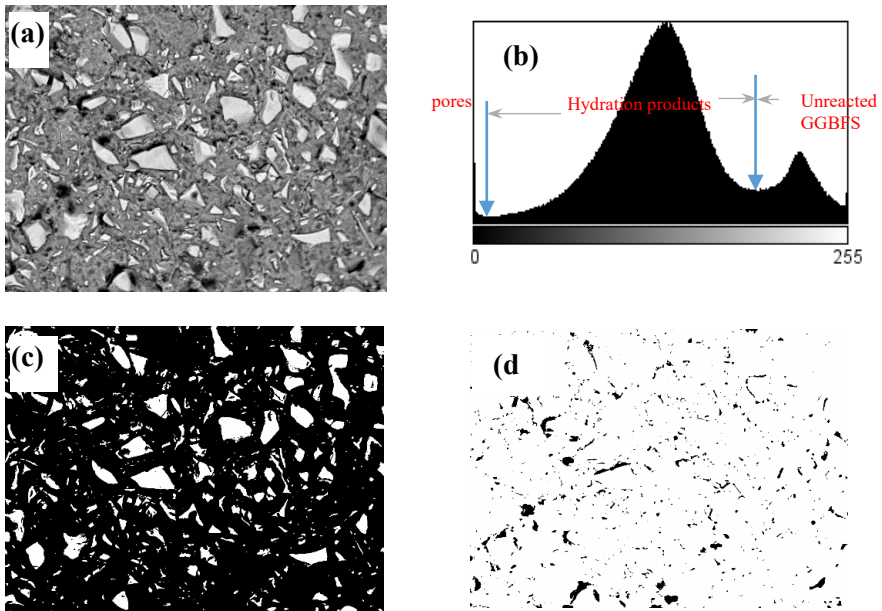


Fig. 3-3 A representative filtered backscattering electron (BSE) image by Bilateral filter (a) with its gray level histogram (b), unreacted GGBFS (c) and cracks or pores (d) obtained after applying thresholds on the filtered BSE image.

### 2.3.5 Isothermal calorimetry

Heat evolutions of paste samples were recorded for 7 days using an isothermal calorimeter (TAM Air, TA Instruments, USA) at 20 °C. After mixing, a glass ampoule bottle was used to weigh the 14 g paste sample, and then the sealed bottle was loaded into the isothermal calorimeter.

### 2.3.6 Nuclear magnetic resonance (NMR)

It is important to select the appropriate method to stop the hydration of cementitious materials prior to  $^{29}\text{Si}$  Magic angle spinning (MAS) NMR tests as aforementioned in Chapter 2. In this study, the method to arrest hydration of alkali-activated slag (AAS) pastes was the one followed by Chen et al. [73]. Firstly, the fresh pastes were mixed with deionized water and then subjected to centrifugation, after which the liquid can be removed. This water extraction can be repeated and be used to remove the soluble silicate species. Afterwards, a chemical extraction was carried out, the solid part was put on the 0.2  $\mu\text{m}$  nylon filter membrane, and then at least 400 ml solvent (50/50 volume of methanol/acetone) was added to wash the solid part and remove the water. The remaining particles were collected and placed into a moderate vacuum for 24 h prior to NMR analysis. Recently, Palacios et al. [20] has also pointed out that the initial washing of the AAS pastes with water and subsequent treatment with isopropanol can be the most appropriate method to achieve the stoppage hydration of AAS pastes.

Solid-state  $^1\text{H}$ - $^{29}\text{Si}$  Cross polarized MAS NMR spectra (Solid-state  $^{29}\text{Si}$  MAS NMR) were acquired on an Agilent VNMRs DirectDrive 400 MHz spectrometer (9.4 Tesla) equipped with a T3HX 3.2 mm probe. Magic angle spinning was performed at 8 kHz (6.5 kHz) using ceramic zirconia rotors. The signal of talc was used to calibrate the silicon chemical shift scale (-98 ppm). Acquisition parameters used were: a spectral width of 24 kHz, a  $90^\circ$  pulse length of 3.2  $\mu\text{s}$  (4.5  $\mu\text{s}$ ), an acquisition time of 15 ms, a recycle delay time of 3 s (20 s), a spin-lock field of 80 kHz, a contact time of 1 ms, and about 100000 (8000) accumulations. High power proton dipolar decoupling during the acquisition time was set to 80 kHz. (It should be noted that the parameters used for solid-state  $^{29}\text{Si}$  MAS NMR were listed in parentheses) Regarding the deconvolution of spectra, they were decomposed by the Gaussians peaks [194], [195].

## **Part III**

---

### **Influence of activator nature on the rheological and setting behaviour of AACs**



## **Chapter 4 Sodium hydroxide activator**

---

This chapter presents the effects of the concentration and solution to binder ratio of sodium hydroxide activator on the rheological and setting behaviour of alkali-activated slag mixtures (AAS).

## 1. Introduction

---

As well known, the most common used alkali hydroxide in AACs is sodium hydroxide (NaOH). In this chapter, the effects of concentration of sodium hydroxide activator on the rheological and setting behaviour of AACs is studied. Various techniques, such as UPV and ICP-OES were used to understand the reaction process of AACs. Next to that, the rheological tests were conducted to reveal its rheological behaviour.

A general model for the reaction process of alkali activation was suggested by Glukhovskiy [196]. Glukhovskiy [196] proposed that the alkali activation of aluminosilicate-based precursors contains four stages: dissolution, reconstruction, condensation and crystallization. As well known, the early age reaction process of AACs can influence the microstructure [197], strength development [80], [198], and durability-related properties, such as permeability [80], shrinkage [83] and efflorescence [199]. Therefore, it is crucial to fully understand the early reaction process of AACs. Although AACs represent a potential alternative to traditional cementitious materials, very limited information is available on their rheology and setting behaviour. As a typical non-destructive test method, the ultrasonic wave technique has been applied to continuously monitor the early age reaction process of cementitious materials due to its advantages, such as good orientation, strong penetrating ability, and easy detection [43]. Cao et al. [43] stated that this method is very suitable for the alkali-activated slag systems considering the quick setting and rapid hardening characteristics of AACs. The same authors investigated the effects of different types of activators (sodium hydroxide and sodium silicate) on reaction processes and microstructure evolution, and reported that the early age geopolymerization of sodium silicate-activated pastes was more complex as compared to sodium hydroxide-activated pastes. Uppalapati et al. [44] evaluated the setting process of alkali-activated slag/fly ash mixtures using ultrasonic P-wave velocity, and recognized the reaction process stages as dissolution, precipitation, rapid polycondensation and densification by forming more reaction products. Consequently, it is believed that the use of ultrasonic monitoring can achieve the in-situ monitoring of the rapid reaction processes at very early age of the AACs. Moreover, in this chapter, the effect of sodium hydroxide concentration on the rheology of AACs such as, yield stress, viscosity and shear-thinning/shear-thickening behaviour was explored and discussed.

## 2. Experimental program

---

### 2.1 Mixture design

---

Table 4-1 shows the mixture designs for the investigated AAS with NaOH concentrations varying between 0.5 and 8 mol/L and the PC paste of standard consistency with water to cement ratio of 0.30. The AAS mixtures with different NaOH concentrations were prepared by using a constant solution to binder ratio (S/B)

| Sodium hydroxide activator

of 0.5.

Table 4-1 Mixture design of AAS mixtures and Newtonian viscosity of the activator solutions.

Mixture	NaOH concentration	Solution to binder ratio (S/B)	Newtonian viscosity of the activator solutions (Pa·s)
8M	8 mol/L	0.50	0.038
6M	6 mol/L	0.50	0.029
4M	4 mol/L	0.50	0.025
2M	2 mol/L	0.50	0.022
0.5M	0.5 mol/L	0.50	0.018

## 2.2 Sample preparation

The required amount of water for standard consistency of PC was determined by a penetration test following EN196-3:2005 [40], resulting in a water to cement ratio of 0.30.

The fresh NaOH-activated GGBFS pastes were mixed using a rotational rheometer with a helix geometry. The mixing procedure was set as follows: the precursors were first manually mixed with NaOH activator solution in a container with a diameter of 28 mm and height of 70 mm. Afterwards, the helix geometry was inserted into the sample, and the shear rate was gradually increased from 0 to 3000  $\text{min}^{-1}$  within 30 s, and subsequently the mixture was mixed for 120 s at a rotational speed of 3000  $\text{min}^{-1}$ . The fresh paste samples obtained in the rheometer were used for the rheological tests and the isothermal calorimetric measurements. As for Vicat setting, ultrasonic pulse wave, and pore solution chemistry tests, the paste samples were prepared in a Hobart mixer by mixing all the ingredients at low ( $140 \pm 5$  rpm) and high ( $285 \pm 5$  rpm) speeds for 90 s each.

## 2.3 Protocol for flow curves

The paste was pre-sheared at a shear rate of 200  $\text{s}^{-1}$  for 30 s and was kept at rest for 30 s to release the residual stress. Then the paste was sheared with the following shear protocol: a linear shear rate ramp-up from 0 to 10  $\text{s}^{-1}$  in 60 s and 10 to 200  $\text{s}^{-1}$  in the next 60 s, followed by a ramp-down from 200 to 10  $\text{s}^{-1}$  in 60 s and 10 to 0  $\text{s}^{-1}$  in the next 60 s, as illustrated in Fig. 4-1. This cycle was repeated nine times with a pause of 6 min between the cycles. The yield stress was measured by fitting the Herschel-

Bulkley equation (Eq. (2-3)) to the downward curve of the flow curve and the apparent viscosity (the ratio between shear stress and shear rate) was calculated at a shear rate of  $125 \text{ s}^{-1}$ .

All measurements were performed at the temperature of  $20 \pm 0.5 \text{ }^\circ\text{C}$ . The viscosity of NaOH solutions given in Table 4-1 was also determined using the same shear protocol (Fig. 4-1).

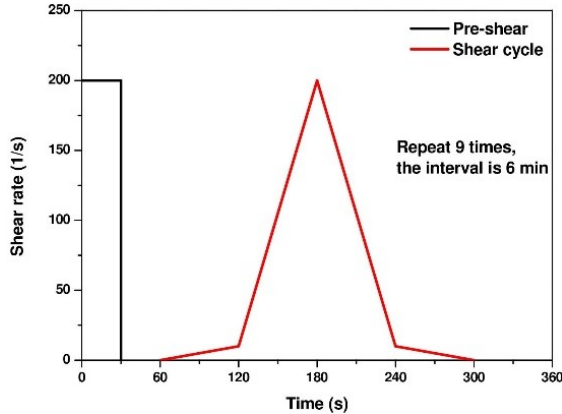


Fig. 4-1 Shear protocol.

## 2.4 Thermodynamic modeling

Thermodynamic modelling can be a useful tool to understand chemical reactions. Once the alkaline solution contacts with aluminosilicate precursors, the dissolution starts, and some solid reaction products are formed when the aqueous solution is saturated with the ions.

In this study, the pore solutions of 8M, 4M and 0.5M were considered for thermodynamic modelling. The saturation index (SI; Eq. (4-1)) was used to predict whether a solid reaction product can be formed or not.

$$SI = \text{Log} \frac{IAP}{K_{s0}} \quad (4-1)$$

where IAP and  $K_{s0}$  are the ion activity product and equilibrium solubility product of a solid, respectively. It is noted here that  $SI > 0$ ,  $SI < 0$  and  $SI = 0$  indicate oversaturation, undersaturation, and equilibrium between solution and solid, respectively. As the use of SI can be misleading when comparing phases that are dissociated into a different number of ions, an effective saturation index (ESI; Eq. (4-2)) is introduced to analyze thermodynamic modelling of the pore solution.

$$ESI = SI/N \quad (4-2)$$

where N is the number of ions participating in the reactions to form the solids. The Gibbs energy minimization software GEM-Selektor v.3 and the thermodynamic database developed by Myers et al. [87] and Lothenbach et al. [200], respectively were used for the thermodynamic modelling of alkali-activated slag paste. The elemental concentrations measured by ICP - OES were used as INPUT to calculate the activities of ions. Myers et al. [85] used a set of eight CNASH<sub>ss</sub> end members to elucidate the calcium aluminosilicate hydrates in AAS. Among the eight end-members for the calcium aluminosilicate hydrates, 5CA and INFCA are two C-A-S-H gel end members, 5CNA and INFCNA are two C-N-A-S-H gel end-members, INFCN is a C-N-S-H gel end-member, and T2C\*, T5C\* and TobH\* are three C-S-H gel end-members. Besides the calcium aluminosilicate hydrates, there are other crystalline reaction products found in AAS, such as hydrotoalcite, tetracalcium aluminate hydrate (C<sub>4</sub>AH<sub>13</sub>), katoite (C<sub>3</sub>AH<sub>6</sub>) and stratlingite (C<sub>2</sub>ASH<sub>8</sub>). The corresponding chemical reactions and equilibrium solubility products of these eight end-members and their corresponding chemical reactions and equilibrium solubility products can be found in ref. [201].

### 3. Results and discussions

#### 3.1 Comparison between UPV and Vicat setting results

Typical ultrasonic P-wave velocity curves and their first derivative curves of AAC pastes are illustrated in Fig. 4-2 and Fig. 4-3, respectively. As can be seen in Fig. 4-2, a higher concentration of NaOH activator generally resulted in a higher P-wave velocity in the first 24 hours. Zuo et al. [88] also confirmed that an increase in NaOH content could accelerate the reaction kinetics and increased the volume proportion of crystalline reaction products, leading to a more rigid microstructure.

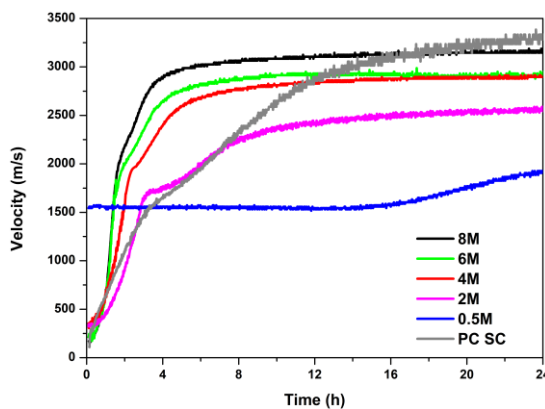


Fig. 4-2 Ultrasonic pulse velocity of AAC pastes and PC pastes.

Fig. 4-3 shows the comparison of initial setting times of the pastes determined by UPV

and Vicat needle tests. Previous studies reported that the initial setting can be determined by the UPV curve with different methods: 1) by the first inflection point of the P-wave [202], 2) by the time when the P-wave development starts to increase [203], [204], 3) by the time when the P-wave reaches the velocity valid for water between 1400 and 1500 m/s [44], [202], 4) or at the intersection of three straight lines tangent to the P-wave curve [205]. As shown in Fig. 4-3, the time at which the first inflection point appeared on the UPV curve was very close to the initial setting time determined by Vicat needle test for both sodium hydroxide-activated cements and Portland cements. In the meantime, the values of P-wave were also close to 1550 m/s when the initial setting occurred. It is well known that a higher concentration of NaOH results in a shorter initial setting time. These phenomena can also be observed in Table 4-2. The initial setting times of the pastes activated by 2M NaOH was 156 / 151 min by UPV / Vicat needle test. The initial setting times significantly decreased to 80 / 87 min by UPV / Vicat needle tests when the activator concentration was increased to 8M. Since the 0.5 M mixture contained a plateau period without any increase in velocity, it was difficult to determine its initial setting time by using UPV technique. The reasons for the occurrence of this plateau will be discussed in Section 3.2. Therefore, in this study, two strategies were found appropriate to analyze the setting behaviour of alkali-activated slag mixtures and to determine their initial setting time by using ultrasonic velocity measurement. One is based on the identification of the characteristic points or inflection points in the ultrasonic curves. Another approach is the time to reach a specific value or range of ultrasonic velocity.

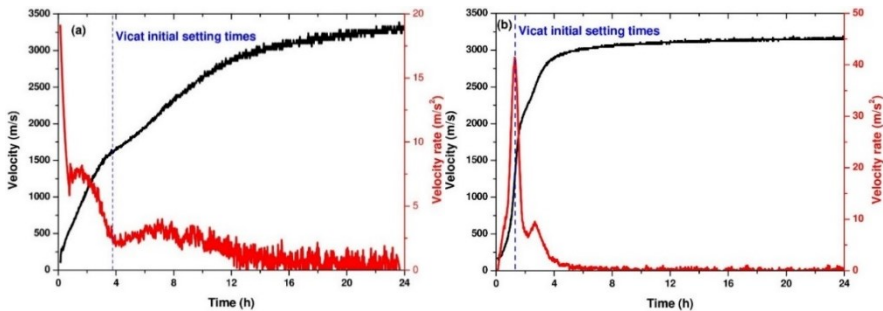


Fig. 4-3 Examples of the comparison between Vicat needle tests and UPV (a) PC SC, (b) 8M.

Table 4-2 Summary of the initial setting times determined by UPV and Vicat needle tests.

Mixtures	PC SC	8M	6M	4M	2M	0.5M
Vicat initial setting (min)	232	87	94	118	151	780
UPV (min)	248	80	88	119	156	/

### 3.2 Comparison between UPV and calorimetric results

Ultrasonic P-wave velocity (UPV) curves of AAC pastes and the comparison between UPV and calorimetric measurements are illustrated in Fig. 4-4. The UPV curve of PC-based pastes at the early age can be divided into four stages such as dissolution stage (stage I), induction stage (stage I<sub>a</sub>), acceleration stage (stage II), and the deceleration stage (stage III). In comparison, there were only three stages (dissolution stage I, condensation/acceleration stage II, and deceleration stage III) in the NaOH-activated slag mixtures since the induction period was too short.

Stage I: In the dissolution stage, the measured P-wave velocities in both fresh AAS and PC pastes are substantially lower than that of the alkaline solution (1450-1580 m/s). The main reasons for this can be associated with some factors as follows. The first reason is air bubbles entrapped into the mixture during the mixing, as pointed out by some previous studies [44] and [206]. The second reason can be related to the extended length of the wave-path length due to the suspended slag grains in the solution being similar to the observed case for Portland cement systems [202]. Meanwhile, the first peak of the heat flow curve, namely dissolution peak, occurred in the Stage I. A number of studies [51], [207] pointed out that this peak was related to wetting of particles, dissolution of the starting materials (the breakdown of Me-O and T-O bonds of GGBFS), and also partly owing to the formation of initially dissolved silicate units and their interactions with Ca and Na ions. The cumulative heat curve in this stage for the PC and AAS pastes exhibited very limited growth. At the end of the dissolution stage, initially formed oligomers and/or monomers in the solution mingle with slag particles forming a network structure that provides a better pathway for the propagation of ultrasonic waves, and the P-wave velocity starts to increase. As clearly shown in Fig. 4-4a, it was found that an induction period lasting approximately 2h (Stage I<sub>a</sub>) also could be found for the PC paste, which is consistent with the existing literature [208]. But, there was no apparent induction period during early reaction time for the AAS pastes.

Stage II: In the acceleration/condensation period, P-wave velocity starts to increase rapidly. This is due to the rapid development of the solid percolation path, leading to ultrasonic waves passing through the solid phase instead of the liquid phase. Thus, a sudden increase in the ultrasonic wave was observed in Stage II. In the meantime, the

heat flow curve also started to increase rapidly in this stage. The remarkable acceleration of heat flow and ultrasonic waves can be attributed to two phenomena. On the one hand, a large amount of the previously formed aluminosilicate oligomers and monomers starts to interconnect, and hence the larger aluminosilicate structural units are formed around the slag particles due to the massive condensation between different oligomer units. On the other hand, filling the pore space with the rapid formation of the reaction products formed by the combination of the anions with the dissolved  $\text{Ca}^{2+}$  from the slag contributes to the ultrasonic velocity increase in Stage II [44], [209], [210]. As a result, the system started to change from a suspension state to a solid network frame, and it is worth noting that in most cases, initial setting of the AAC pastes occurred in this period. Therefore, it can be summarized that the accelerated P-wave during the rapid increase in heat flow reflects that the reaction stage of AAS activated by NaOH can be separated into the dissolution followed by precipitation and rapid condensation between initially formed aluminosilicate oligomers and/or monomers. Besides, the mixture of 4M and 8M showed a very similar cumulative heat value around 150 J/g binder at the age of 24h, indicating that when the addition of NaOH reached a threshold, the heat release would not increase dramatically. This is also in agreement with the findings of Xie et al. [211]. Furthermore, the PC paste also exhibited the same calorimetric and ultrasonic trend with AAS pastes, concluding that both PC paste and AAS paste activated by NaOH might have a similar reaction mechanism.

Stage III: In the deceleration stage, a slight increase in the ultrasonic velocity is observed and it reaches a plateau. In the meantime, the heat flow also exhibits a rapidly decreasing trend in Stage III. Cao et al. [43] pointed out that the capillary pores in the compact matrix were almost fully filled with the further reaction products in this stage. Consequently, the P-wave curve did not change substantially.

Interestingly, it was difficult to separate the mentioned stages in the 0.5M mixture as it showed a plateau without any increase in ultrasonic velocity from the beginning. A previous study [212] reported that the presence of the plateau could be associated with the water to binder ratio and the particle fineness. However, the plateau can only be related to the water to binder ratio in this study since the slag fineness was the same for all mixtures. Obviously, the mixture of 0.5M contained the highest amount of water compared to other mixtures. Consequently, this can be due to the intensive retardation of the formation of the connected solid network caused by the availability of water to prevent the close contact of the hydrating particles [212]. The calorimetric results of 0.5M mixture showed no increase in the heat flow at this stage, which can validate the plateau in the ultrasonic velocity readings. Besides, since bleeding also occurred in the sample 0.5M, the monitored ultrasonic velocity can be the signal that travels through the liquid [213]. As presented before, the speed of the sound in the activator solution was around 1450-1580 m/s, the recorded sound velocity for sample 0.5M was in the range of the speed in its liquid phase and thus no microstructural evolution could be observed. Afterwards, it was observed that an increase in velocity

occurred for sample 0.5M after approx. 14h. This increase of the ultrasound velocity in the induction period can also be explained by some physical phenomena: air bubble migration to the surface due to the bleeding, workability loss due to intake of solution by initial chemical reactions and the densification of the internal structure by settling of the particles due to gravity, resulting in a mechanical bounding between particles [44]. In the meantime, there was no noticeable increase in heat release for sample 0.5M in the first 24h.

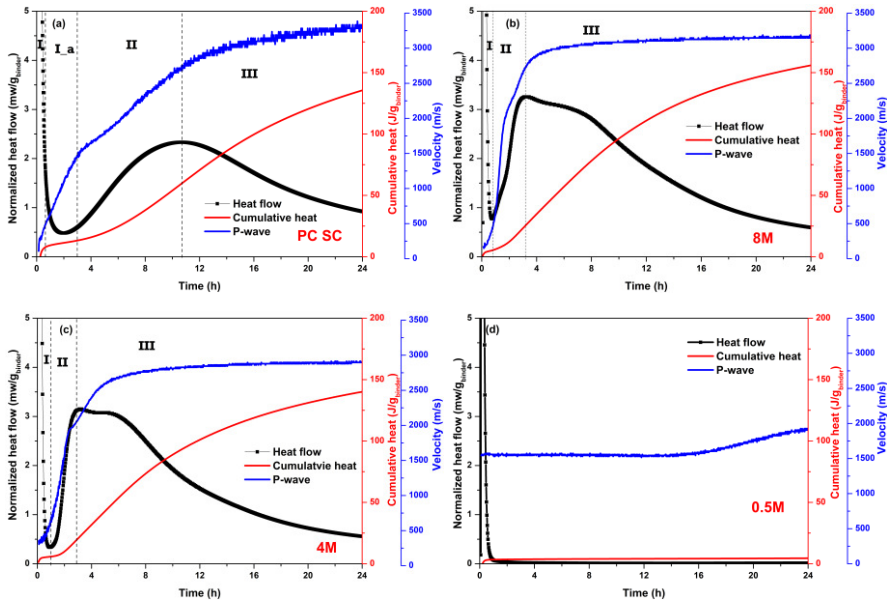


Fig. 4-4 Comparison between the evolution of UPV and calorimetric curves (a) PC SC, (b) 8M, (c) 4M, (d) 0.5M.

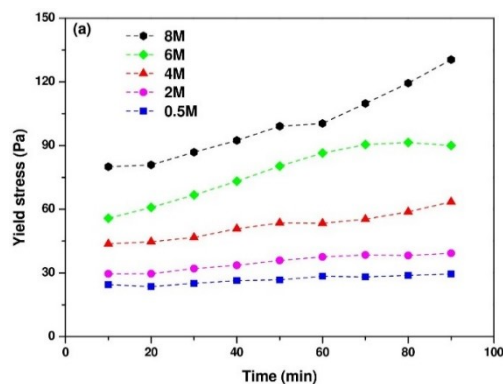
### 3.3 Rheological test results

Fig. 4-5a shows the yield stress evolution of AAC pastes with time. It can be seen from Fig. 4-5a that an increase in molarity of NaOH solution resulted in a higher yield stress. In particular, the yield stress of the 8M mixture evolved quickly with an increasing rate, while the yield stress of the mixture of 4M, 2M, 0.5M retained a constant value lower than 50 Pa, indicating better workability compared to the 8M mixture. The evolution of the apparent viscosity of AAC pastes is presented in Fig. 4-5b. The general trend was similar to yield stress evolution: a higher concentration of the activator solution led to higher apparent viscosity. The paste activated by 8M NaOH exhibited a pretty high apparent viscosity compared to other mixtures having apparent viscosities ranging from 0.70 to 3.53 Pa·s. Puertas et al. [31] also pointed out that raising the activator concentration (from 3% to 5% Na<sub>2</sub>O) in the AAS pastes

induced an increase in both plastic viscosity and yield stress values, similar to the findings in this study. This was directly owing to the rise in the concentration of OH ions, which favored more intense slag dissolution and consequently the formation of more reaction products like calcium aluminum silicate hydrate (C-A-S-H) gel [31].

Besides, previous studies [33] [49] showed that the rheological behaviour is strongly influenced by the alkaline solution composition and its viscosity. In this study, the Newtonian viscosity of the NaOH activator solution was measured using the same shear protocol, and the results are given in Table 4-1. The correlations between the Newtonian viscosity of the activator solution and apparent viscosity of the pastes (cycle 1 at the age of 10 min) are shown in Fig. 4-6. It should be noted that the Newtonian viscosity of the activator solution is strongly dependent on the applied shear protocol, rheometer and the geometry of the system [48], [49]. Obviously, the viscosity of the activator solution increased with an increase in NaOH concentration. The results revealed that the viscosity of the pastes increased with an increase in the viscosity of the activator solution. This is also consistent with the previous studies [48]. The linear correlation between the Newtonian viscosity of the alkaline solution and the viscosity of pastes can be observed for mixture 0.5M, 2M, 4M and 6M. However, the mixture of 8M did not follow the trend, showing much higher values than given by the linear trend line. This means that the apparent viscosity of 8M mixture is not only controlled by the Newtonian viscosity of the activator solution. In this mixture, the more rapid formation of the reaction products probably increased the apparent viscosity of the paste.

As such, a significant impact of the activator is expected on the rheological behaviour due to the viscous dissipation, which is distinctly different from the rheological behaviour of Portland cement pastes. However, when the NaOH concentration reaches 8M, the chemical process is more important to determine the apparent viscosity than the viscosity of the activator solution.



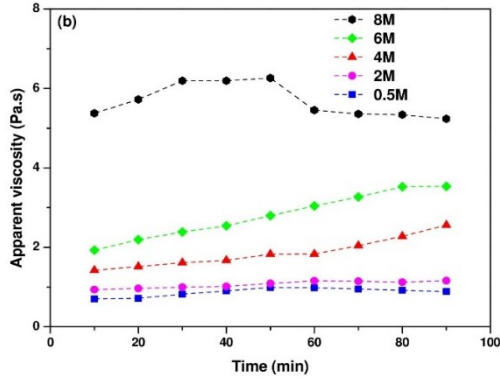


Fig. 4-5 The evolution of yield stress and apparent viscosity of AAS pastes.

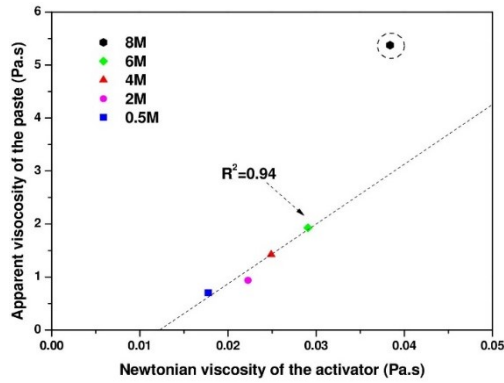


Fig. 4-6 Correlation between the viscosity of the activator and the apparent viscosity of AAS pastes (cycle 1 at the age of 10 min).

Fig. 4-7 presents the rheological behaviour of the AAS pastes associated with the shear thickening/shear-thinning behaviour (the  $n$  value in Eq. (2-3)). Feys et al. [214] have pointed out that the shear thickening behaviour plays a significant role in the cementitious materials production, especially during the mixing and pumping process. As shown in Fig. 4-7, it could be noted that the mixture of 8M always showed shear thickening behaviour, while other mixtures presented shear thinning behaviour during most of the measurement time. Theoretically, the shear thickening behaviour is caused by the formation of the clusters and the influencing factors such as particle size, volume fraction of solids [214], bi- or polydispersion, particle shape, polymer coatings and flocculated particles. In this study, the shear thickening behaviour of AAS pastes is dominated by the volume fraction of solids and the formation of flocculated structures. As the NaOH concentration of the activator solution increases, the amount of water decreases and the volumetric fraction of the solids increases in the mixtures. Previous studies [214] revealed that the intensity of shear thickening

increases with increasing volume fraction of suspended particles. Consequently, only the mixture of 8M showed shear thickening behaviour due to its higher volume fraction, while other mixtures did not present shear thickening behaviour due to their relatively lower volume fraction. Furthermore, another more important factor is the formation of clusters, as the mixture of 8M had higher OH<sup>-</sup> ion concentration leading to faster massive reaction product formation. Although other mixtures exhibit shear-thinning behaviour in the beginning stage, the formation of clusters in the suspension started to accumulate with time elapsing; thus the  $n$  index of mixtures 6M, 4M and 2M also increased. Eventually, for the mixture of 6M, it transferred from shear-thinning to shear-thickening behaviour at the end of the measurement.

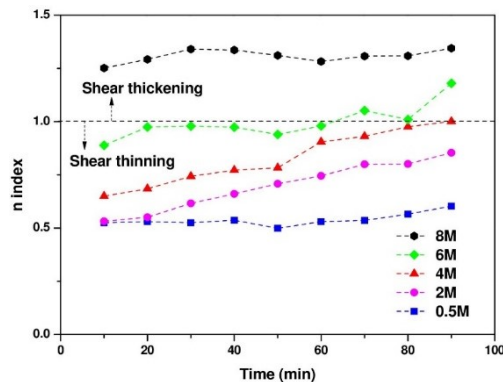


Fig. 4-7 The rheological behaviour of AAS pastes.

Fig. 4-8 shows the first and last hysteresis cycles of the AAS pastes during the measurement time, and Table 4-3 summarizes the rheological parameters of AAS pastes measured by the dynamic shear test. The area of the hysteresis loop is considered as the level of thixotropy [215]. Generally, thixotropy is known as a phenomenon of a physico-chemical reaction. However, as the flocculation and hydration occur simultaneously, attributing the structural build-up or break down solely to one of these phenomena is not straightforward [216]. From the data presented in Table 4-3, it was apparent that the thixotropic behaviour of AAS pastes did not increase significantly with an increase in NaOH concentration in the early time (cycle 1) except for the mixture of 8M showing approximately three times higher thixotropic area as compared to the mixture of 0.5M. While with time elapsing, the increase in NaOH concentration of activator solution can substantially increase the thixotropic area of the AAS pastes (cycle 9).

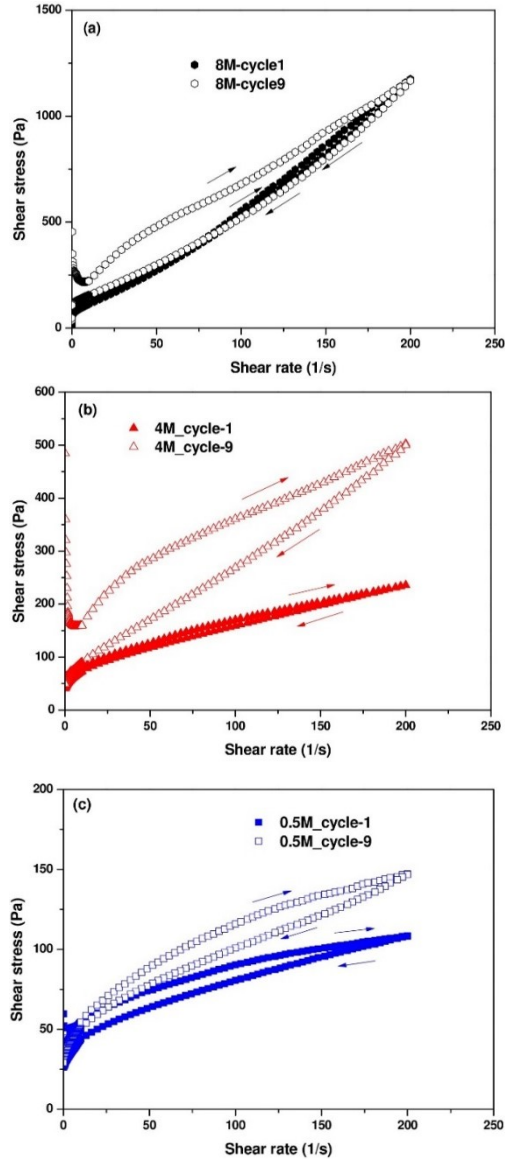


Fig. 4-8 Examples of the AAS pastes hysteresis cycles (a) 8M, (b) 4M, (c) 0.5M.

Table 4-3 Thixotropic area of the AAS pastes hysteresis loops.

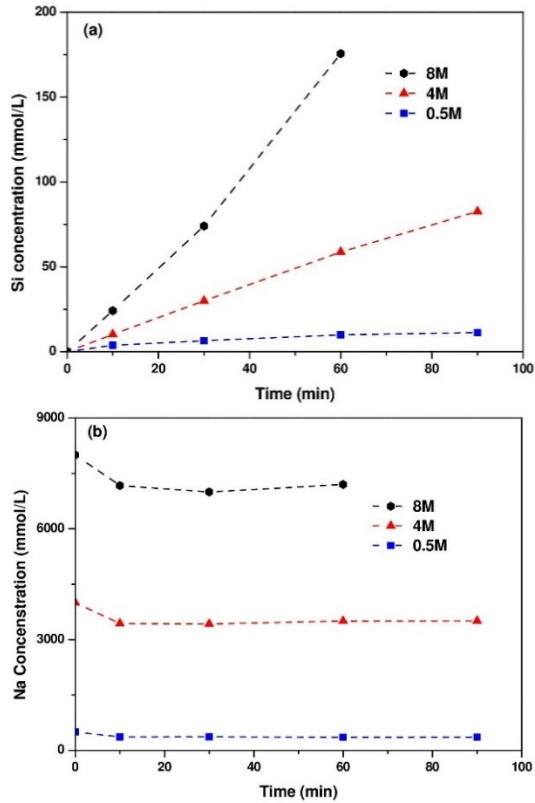
Mixture	Cycle 1-Thixotropic area (Pa/s)		Cycle 9-Thixotropic area (Pa/s)	
	Measured value	Nominal value	Measured value	Nominal value
8M	4908.48	3.07	31000.23	14.61
6M	1954.24	1.22	29977.57	14.13
4M	1556.40	0.97	15443.49	7.28
2M	1430.77	0.90	6471.49	3.05
0.5M	1597.44	1.00	2121.29	1.00

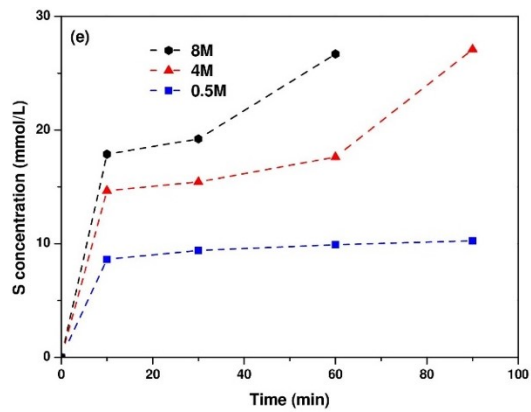
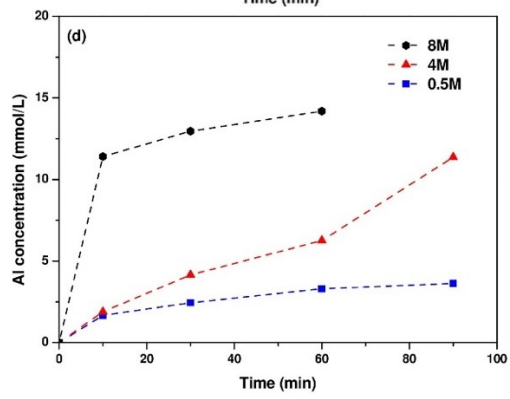
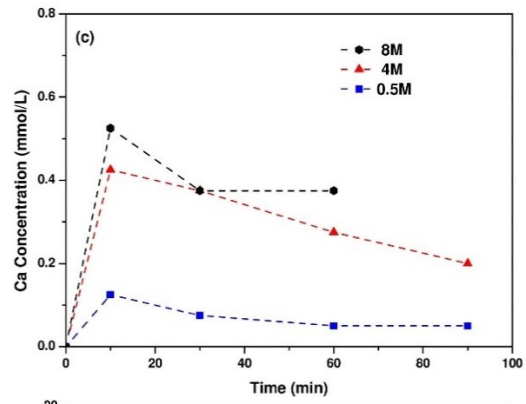
### 3.4 Pore solution chemistry

Three mixtures activated by the different alkaline activators (8M, 4M and 0.5M with S/B=0.5) were chosen to observe the effects of activator concentration on the evolution of the pore solution composition with respect to ionic concentrations starting from 10 min to 90 min. The evolution of the ionic concentrations in the pore solution is given in Fig. 4-9. It should be noted that the evolution of these ionic concentrations reflects the remaining ion amounts in the pore solution after the consumption of the released elements from the precursor for the formation of the reaction products. It can be seen from Fig. 4-9 that the pore solution composition was dominated by OH<sup>-</sup> and Na<sup>+</sup> ions, while other elemental concentrations, such as Ca, Al, S and Si, were relatively much lower. All elemental concentrations increased with an increase in NaOH dosage from 0.5M to 8M. The Si was rapidly released from the GGBFS grains, especially for the mixture of 8M. Al and S were relatively lower than Si, possibly because the GGBFS contains higher SiO<sub>2</sub>% than Al<sub>2</sub>O<sub>3</sub>% and SO<sub>3</sub>%. A previous study [88] also reported the same trend with this observation. Besides, it was observed that Ca remained at a very low level in the pore solution, probably due to its high consumption during the reaction product formations by its combinations with Si, Na and OH<sup>-</sup> [47], [88]. Therefore, it should be noted that Ca experienced a rapid increase in the first 10 min because of the initial dissolution of GGBFS, then decreased for all mixtures due to the participation of Ca into the reaction products.

Na and OH<sup>-</sup> both decreased after the first contact of GGBFS and activator solution, then kept almost constant during the measurement time. It could be seen that the OH<sup>-</sup> presented a very similar value or even slightly lower as compared to Na. This observation is also in agreement with the previous findings by Zuo et al. [88]. There could be two possible reasons leading to this difference. The first explanation could be related to the measurement technique. The concentration of Na was measured by an accurate technique – ICP-OES, while the OH<sup>-</sup> concentration was determined by titration against hydrochloride acid. It should be noted that during the titration test,

when the color turned from red to colorless, the pH of the pore solution was only titrated below 8.2. In other words, the solution was basic and contained some  $\text{OH}^-$  ions that were not completely titrated. Consequently, by this method, the  $\text{OH}^-$  concentration could be relatively underestimated. Another possible explanation is that many other anions, such as  $\text{SiO}_3^{2-}$ ,  $\text{AlO}_2^-$ ,  $\text{S}^{2-}$  and  $\text{HS}^-$ , were also shown in the pore solution, while the pore solution should be electrically neutral, as such the presence of other anions would result in smaller  $\text{OH}^-$  than Na. Furthermore, in this study, Mg and Fe were also measured, but the results showed no Mg and Fe in the pore solution for all mixtures. For Mg, it is possibly due to the rapid formation of hydrotalcite, leading to the consumption of Mg. However, the confirmation of the hydrotalcite formation in the early time needs further microstructural investigations. For Fe, the low amount of  $\text{Fe}_2\text{O}_3$  in GGBFS (0.39 %) could be the reason for the lack of Fe detection in the pore solution.





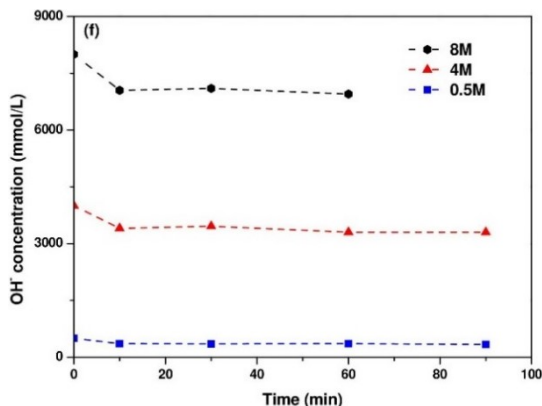


Fig. 4-9 Evolution of ion concentration in pore solution (a) Silicon, (b) Sodium, (c) Calcium, (d) Aluminum, (e) Sulfur, (f) OH<sup>-</sup>

### 3.5 Pore solution thermodynamic modelling

In GEM-Selektor, the activity coefficients of the aqueous species were calculated using the extended Debye-Huckel equation [217], which is applicable up to approx. 1 to 2 molal ionic strength. Fig. 4-10 shows the ionic strengths in the pore solution of AAS paste. The ionic strength in the pore solution of 4M and 0.5M were within 1-2 molal, while the pore solution of 8M was beyond the valid range (~1-2 molal). However, using an improved aqueous phases model, such as the Pitzer model, is limited in the current version of GEM-Selektor. This is because the description of aqueous silicate species in the database of GEM-Selektor does not extend beyond dimeric silicate and aluminosilicate units [85]. On the other hand, GEM-Selektor has been commonly used in the thermodynamic modelling of alkali-activated slag, and the modelling results agreed well with the experimental data [85], [87], [200]. As such, a slight excess of ionic strengths (>2 molal) would not impose a serious impact on the modelling results.

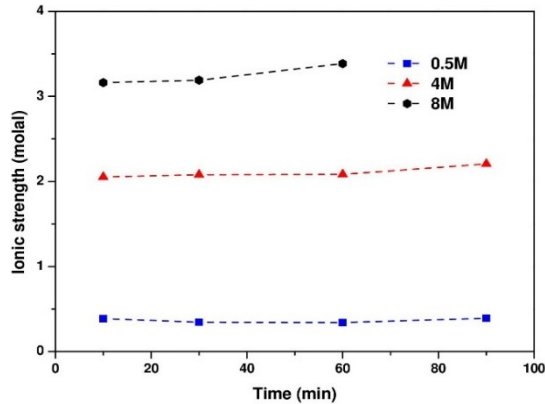
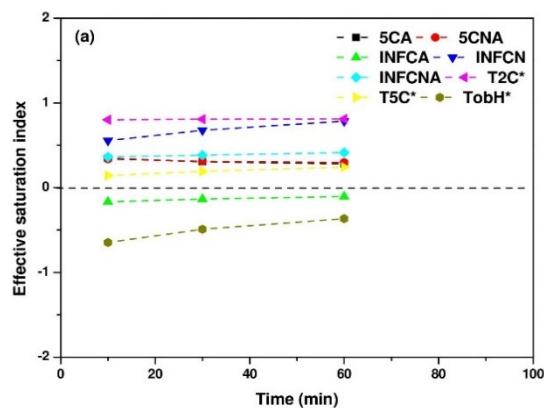
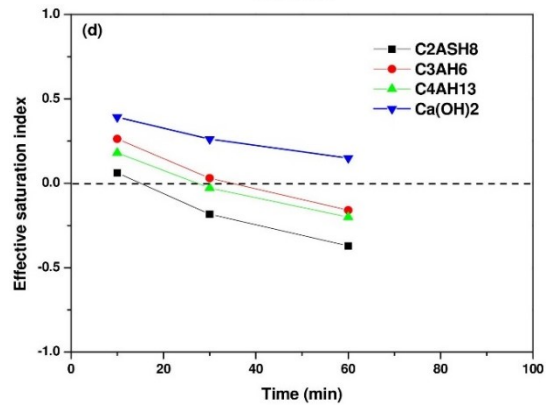
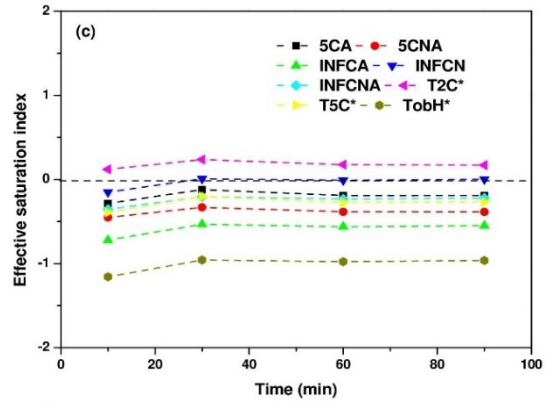
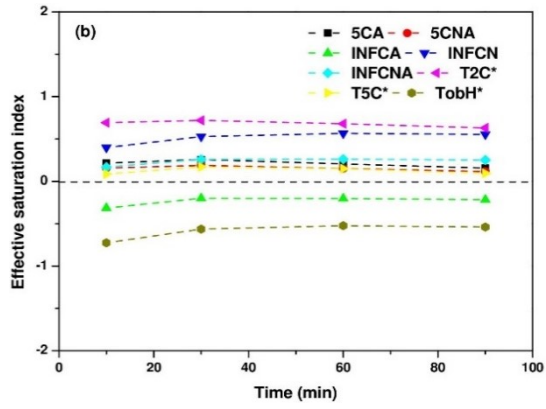


Fig. 4-10 The ionic strengths in the pore solutions of alkali-activated slag pastes, calculated by GEM-Selektor.

Fig. 4-11 presents the effective saturation indices with regards to the eight end-members and crystalline reaction products. As can be seen from Fig. 4-11, for the mixtures of 8M and 4M, C-S-H (T2C\* and T5C\*), C-N-S-H (INFCN), C-N-A-S-H (5CNA and INFCNA) and C-A-S-H (5CA) could be formed in the early reaction time. While only C-S-H (T2C\*) was predicted to form in the mixture of 0.5M, which was in agreement with the pore solution composition of 0.5M, showing the lowest Ca, Si and Al as compared to the other two mixtures. In the meantime, the effective saturation indices of 8M show a slightly higher value than that of the mixture 4M, which was consistent with the initial setting results as presented in Section 3.1. As for the crystalline reaction products, there was no possibility of the formation of crystalline reaction products for the mixture of 0.5M, while for the mixture of 4M and 8M,  $\text{Ca}(\text{OH})_2$  was more dominated during the measurement time.





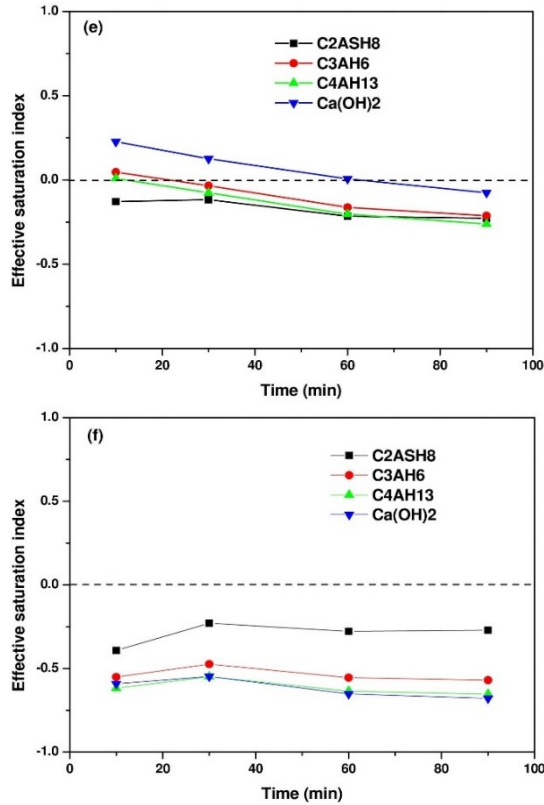


Fig. 4-11 Calculated effective saturation indices as a function of reaction time. (a) and (d) 8M, (b) and (e) 4M, (c) and (f) 0.5M.

### 3.6 Compressive strength of AAC mixtures

Table 4-4 shows the compressive strength of NaOH-activated slag mixtures at the age of 2, 7 and 28 days. It was clear that the higher concentrations led to a higher compressive strength due to the increase in the formation of reaction products (C-S-H, C-N-S-H, C-N-A-S-H and C-A-S-H) by the increase in alkalinity, as reported by ref [81]. However, it should be noted that when the NaOH concentration exceeded 4M, the compressive strength did not increase significantly. For example, at the age of 28 days, the samples with 4M, 6M and 8M NaOH showed the compressive strength values of 41.8, 44.5 and 45.0 MPa, respectively. In other words, the excessive addition of NaOH upon 4M cannot improve the mechanical performance of AAS mixtures. On the other hand, using a very low NaOH concentration such as 0.5M may cause not to develop the compressive strength at the early ages, as also observed in the calorimetric results presented in Section 3.2.

Table 4-4 Compressive strength (MPa) of AAS mixtures.

Mixtures	Compressive strength (MPa)		
	2 days	7 days	28 days
8M	23.5 ± 0.5*	31.9 ± 1.6	45.0 ± 0.3
6M	23.3 ± 0.3	31.1 ± 0.4	44.5 ± 1.2
4M	21.9 ± 0.1	29.3 ± 0.9	41.8 ± 1.5
2M	15.9 ± 0.6	23.3 ± 0.5	30.4 ± 1.3
0.5M	0	9.4 ± 0.1	14.6 ± 0.4

\* Standard error.

#### 4. Conclusion

---

This chapter aims to study the early reaction process and rheological behaviour of sodium hydroxide – activated slag mixtures by using ultrasonic pulse velocity, rheometer and ICP-OES. The following conclusions are drawn:

1. The UPV technique showed similar results with Vicat needle tests. The initial setting time of the sodium hydroxide-activated slag mixtures could be determined by identifying the characteristic points or inflection points in the ultrasonic curves or the time to reach a specific value or range of ultrasonic velocity.
2. The early reaction process of sodium hydroxide-activated slag pastes could be distinguished by three stages: (I) dissolution, (II) acceleration/condensation period and (III) deceleration stage. Furthermore, PC pastes had a significantly more extended induction period as compared to AAS pastes.
3. AAS pastes showed a shorter initial setting time, higher yield stress and apparent viscosity with an increase in NaOH concentration. The viscosity of the AAS pastes was found to be dependent on the viscosity of the activator solution. Additional chemical contributions were found for a NaOH concentration as high as 8M which caused even a shear-thickening behaviour.
4. The pore solution of the sodium hydroxide-activated slag mixtures was dominated by Na and OH<sup>-</sup> ions. The concentrations of Si, Al and Ca increased with an increase in NaOH concentration.
5. Based on the thermodynamic modelling study, the formation of C-S-H gel was found possible in the mixture of 0.5M, while for the mixtures of 4M and 8M the formation of C-S-H, C-N-S-H, C-N-A-S-H and C-A-S-H were predicted.
6. Compressive strength of AAC mixtures increased with an increase in NaOH concentration. However, the mechanical performance would not improve significantly when the NaOH concentration exceeded 4M.
7. Using an activator solution with 4M NaOH was found more favorable for activating the slag used in this study with respect to rheology, setting and mechanical properties.

## **Chapter 5 Sodium silicate activator**

---

In this chapter, the effects of silicate modulus and concentration of sodium silicate activator on the structural build-up of alkali-activated slag/fly ash pastes are investigated. The relationship between structural build-up and pore solution chemistry of alkali-activated slag/fly ash is also studied.

## 1. Introduction

---

The successful application of AAC depends on understanding its rheological behaviour because it can be used to guide mix design concerning flowability, stability, pumpability, pouring and casting processes of fresh concrete. The rheological properties of AAC depend on the physical and chemical properties of the used precursors, type and content of the activators, mixing protocol as well as the ambient conditions. Palacios et al. [30] reported that flow curves of sodium silicate-activated GGBFS pastes fit better to the Herschel-Bulkley model whereas NaOH-activated ones fit Bingham model. Rifaai et al. [48] studied the flow and viscoelastic properties of NaOH-activated fly ash (FA) based geopolymers and reported the NaOH concentration dependence of the yield stress, the storage modulus, and the rigidification rate of the geopolymers. These rheological properties increase with an increase in NaOH concentrations up to 7 mol/L however, the higher concentrations of NaOH up to 14 mol/L cause a decrease in these parameters. Puertas et al. [180] reported that the mixing protocol affects the AAC concrete rheology more than its strength. Mehdizadeh et al. [218] reported that the phosphorus slag mixtures activated with sodium carbonate and calcium hydroxide present shear-thinning and thixotropic behaviour. Another study by Ishwarya et al. [138] pointed out that the shear-thinning behaviour of alkali-activated slag-fly ash pastes becomes more pronounced with an increase of water-binder ratio. In addition, some shear-thickening behaviours are also reported by other researchers [30], [219]. It was evidenced in many studies that the AAC pastes can be classified as thixotropic and non-Newtonian material presenting workability loss in time due to chemical reactions. The formation of primary C-S-H gel in alkali-activated GGBFS-FA mixtures and its effect on paste rheology were confirmed.

From the rheological point of view, small amplitude oscillatory shear (SAOS) can be employed to monitor the structural evolution during geopolymerization from the end of the mixing to setting [52], [63]. During the SAOS test, a sample is subjected to a sinusoidal strain or a given shear stress. The response of the material to the deformation is used to evaluate the structural build-up of the material. The structural build-up of cementitious materials at early age is an important property that affects the formwork pressure generated by fresh concrete, stability of concrete after casting, 3D printability of concrete, and the formation of lift line in multi-layer casting. The higher structural build-up rates are preferred in many concrete applications, such as reduction of formwork pressure, slip form paving, fresh state stability, and 3D printing concrete, while lower structural build-up rates are generally desired in some cases, such as multi-layer casting applications to increase the bond strength between the layers. Poulesquen et al. [50] investigated the storage modulus and loss modulus of metakaolin pastes activated by different activation solutions. It was reported that the metakaolin activated with NaOH had the faster reaction kinetics as compared to KOH, although the structure formed with KOH was more rigid, forming larger oligomers or favoring the connectivity of the tetrahedral network. Steins et al. [63] indicated that

the maximum loss factor of geopolymers corresponds to the appearance of a rigid percolating network as the transition of the precursors to the vitreous state [50]. As can be seen from the literature, there are several studies concerning the basic rheological properties and structuration of AAC mixtures however, the studies on the structural build-up of AACs produced with the single and hybrid usage of GGBFS-FA activated by NaOH and liquid sodium silicate are limited.

As well known, due to the rapid initial set of GGBFS-based mixtures made with sodium silicate solution, the hybrid use of GGBFS and FA in AAC production has recently attracted considerable attention to eliminate the deficiencies of AACs produced with single use of these precursors. However, there are limited studies on the rheological properties and structure build-up of hybrid GGBFS-FA based AAC. Therefore, the activator solution related ( $M_s$  value and liquid sodium silicate dosage) AAC design parameters were studied comparatively with respect to the setting time, the rheological parameters and the mechanical properties. Besides, the effects of GGBFS/FA ratio on rheological behaviour were also explored in this study. In addition, the evolution of storage modulus of some selected alkali-activated GGBFS-FA pastes was related with pore solution chemistry studies by inductively coupled plasma-optical emission spectroscopy (ICP-OES) analysis technique.

## **2. Experimental program**

---

### **2.1 Mixture design**

---

The mixture properties are given in Table 5-1. This experimental study consists of three different groups of AAC mixtures designed for investigating the influences of binary mixture of GGBFS and FA,  $M_s$  value of activator solution and the sodium silicate dosage on AAC rheological properties. In the first group, five different AAC mixtures (Mix 1 to 5) were prepared with different GGBFS/FA ratios with an activator solution having  $M_s$  value of 1.2 at a constant 5%  $\text{Na}_2\text{O}$  content. GGBFS was replaced with 30, 50, 70 and 100% FA in these mixtures. It was observed that the water requirement of the mixtures decreased significantly by the increase of FA content of the mixtures, possibly due to the spherical particle shape of FA. For this reason, the spread diameter value of  $175 \pm 5$  mm (determined by using a truncated cone with the dimensions of 46 mm top, 68 mm base and height of 40 mm) was kept constant in these series. Otherwise, excessive bleeding or insufficient workability occurred for the high-volume FA mixtures and GGBFS mixtures, respectively. Therefore, as shown in Table 5-1, the W/B ratios were gradually decreased from 0.45 to 0.31 with the increase of FA amount for keeping the spread diameter constant.

In the second group of the mixtures (Mix 3 and Mix 6 to 9), the effects of  $M_s$  value on the rheological properties of AAC were investigated on the 50% of GGBFS and 50% of FA hybrid mixture.  $M_s$  value of the activator solution was varied between 0 and 1.6 by the combination of sodium silicate and sodium hydroxide. The boundaries

of Ms value (0 and 1.6) were obtained by using a single activator, NaOH and sodium silicate, respectively.

In the third group (Mix 9 to 12), the effects of sodium silicate dosage were investigated by using solely sodium silicate solution with different Na<sub>2</sub>O and SiO<sub>2</sub> contents varying between 3% to 6% and 4.8% to 9.6%, respectively. The mixture notation shows the alkali activator dosage as sum of the Na<sub>2</sub>O% and SiO<sub>2</sub>%. The mixture notations S, F and SS indicate the weight percentages of GGBFS, FA and dry part in water glass (as per precursor), respectively.

Table 5-1 Mixture design of alkali-activated AAC mixtures

Mix	Mixture notation	GGBFS	Fly ash	Ms value	W/B*	Na <sub>2</sub> O	SiO <sub>2</sub>	pH of activator solution
		content (%)	content (%)					
1	S0F100 / N5 Ms1.2	0	100	1.2	0.31	5	6	13.72
2	S30F70 / N5 Ms1.2	30	70	1.2	0.33	5	6	13.68
3	S50F50 / N5 Ms1.2	50	50	1.2	0.37	5	6	13.65
4	S70F30 / N5 Ms1.2	70	30	1.2	0.41	5	6	13.60
5	S100F0 / N5 Ms1.2	100	0	1.2	0.45	5	6	13.56
6	S50F50 / N5 Ms0	50	50	0	0.37	5	0	13.90
7	S50F50 / N5 Ms0.4	50	50	0.4	0.37	5	2	13.78
8	S50F50 N5 Ms0.8	50	50	0.8	0.37	5	4	13.73
9	N5Ms1.6 / SS13	50	50	1.6	0.37	5	8	13.45
10	N3Ms1.6 / SS7.8	50	50	1.6	0.37	3	4.8	13.36
11	N4Ms1.6 / SS10.4	50	50	1.6	0.37	4	6.4	13.40
12	N6Ms1.6 / SS15.6	50	50	1.6	0.37	6	9.6	13.50

\* W-water, B-solid binder (binder+ solid in activator solution), S-GGBFS, F-Fly ash, N-Na<sub>2</sub>O%, SS-dry part in sodium silicate

\*\* by mass of precursors

## 2.2 Sample preparation

Activator solutions were prepared by mixing the liquid sodium silicate and sodium hydroxide solution one day before paste and mortar preparation. The pH values of the activators were measured by a pH meter. It should be noted here that the pH measurements of the activator solutions by a pH meter may lead to some errors, to some extent, due to very high alkali ion concentrations and the availability of silica in the activator solution [105]. For the preparation of the paste samples, the activator solution was poured into the Hobart mixer bowl first, then the dry-blended binders (GGBFS & FA) were added and mixed at low ( $140 \pm 5$  rpm) and high ( $285 \pm 5$  rpm) speeds for 90s for each, respectively. Just after finishing the mixing stage, the

consistencies of the fresh pastes were assessed by the slump-flow test according to ASTM C1437 [183].

### 2.3 Protocol for flow curves

The experimental protocol consisted of pre-shearing at  $200 \text{ s}^{-1}$  for 30 s, followed by a resting period of 30 s. The flow curve was then determined by increasing the shear rate in eight consecutive steps from  $25 \text{ s}^{-1}$  to  $200 \text{ s}^{-1}$ . The total time for flow curve measurement was approximately 15 min as shown in Fig. 5-1, each shear rate was maintained for 1 min in order to ensure that the paste reached a steady-state condition under the given shear rate. The data was recorded every second, and the last 30 data points, providing an equilibrium shear stress at a given shear rate, were averaged to represent the average shear stress at that shear rate. Dynamic yield stress and plastic viscosity were determined from the down ramp curves that satisfactorily fit the Herschel-Bulkley model (Eq. (2-3)).

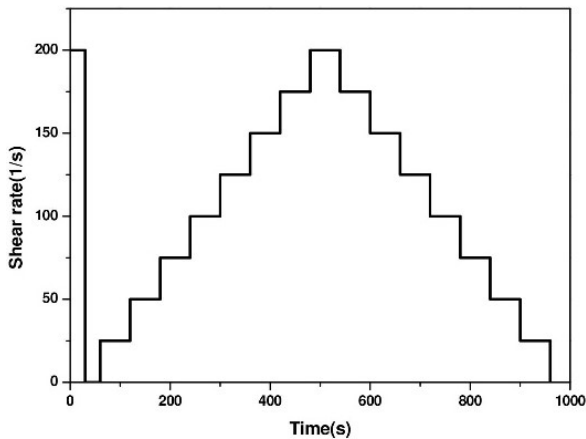


Fig. 5-1 Shear protocol used for sodium silicate-based mixtures.

## 3. Results and discussions

### 3.1 Setting times

Initial and final setting times of the mixtures are presented Table 5-2. Setting times with different GGBFS-FA ratios varied over a wide range. Initial and final setting times of AAC pastes decreased with the increasing content of GGBFS despite the increase in W/B ratio. Due to very slow reaction rate of FA at room temperature conditions [220], the mixture containing only FA (S0F100) had a very long setting time of 18 hours even in very low W/B ratio case. This very long setting time

shortened to 101, 68, 59 and 44 minutes for the GGBFS incorporation ratios of 30%, 50%, 70% and 100%, respectively. The rapid solidification of GGBFS incorporated mixtures can be attributed to the difference in dissolution and activation kinetics of the FA and GGBFS. As reported before [221], [222], the main reason for the accelerated solidification rate by the GGBFS incorporation into FA systems could be associated to the rapid formation of some reaction products through the interaction of  $\text{Ca}^{2+}$  released from the GGBFS with silicates and aluminates.

Table 5-2 Initial and final setting times of the AAC pastes made with sodium silicate activator.

Parameters	Mix	Mixture Notation	Initial setting time (min)	Final setting time (min)
GGBFS/FA ratio	1	S0F100	1101	/
	2	S30F70	101	188
	3	S50F50	68	158
	4	S70F30	59	149
	5	S100F0	44	119
Ms value	6	N5Ms0	132	236
	7	N5Ms0.4	330	656
	8	N5Ms0.8	86	209
	3	N5Ms1.2	68	158
	9	N5Ms1.6	56	107
Liquid sodium silicate dosage	10	SS7.8	45	147
	11	SS10.4	45	129
	9	SS13	56	107
	12	SS15.6	69	110

For AAC mixture produced with the usage of equal amounts of GGBFS and FA precursors, the Ms value of the activator solution also significantly influences the setting behaviour of the paste as explained below. The initial and final setting times of the GGBFS-FA mixture activated by NaOH (Ms=0) were 132 and 236 min, respectively as presented in Table 3. Incorporation of a low amount of sodium silicate to activator solution (i.e. Ms=0.4) extended the initial and final setting times to 330 and 656 minutes, respectively. However, a further increase of sodium silicate amount

to reach an Ms value of 0.8 caused a significant decrease in setting times. But, a further increase in Ms value upon 0.8 decreased the setting times in a lower rate. The increase of sodium silicate content in the activator solution lowered the pH of the solution (Table 5-1) and provided more soluble silica available in the medium. The shorter setting times with the presence of soluble silicates are associated to the acceleration of the  $\text{Ca}^{2+}$  release from GGBFS, and the reactions of silicates with  $\text{Ca}^{2+}$  [223]. It seems there is a threshold value for sodium silicate with respect to reaction kinetics. Activation with only NaOH promoted the dissolution and product formation simultaneously due to the high  $\text{OH}^-$  concentration, causing a reaction ring formed around the surface of GGBFS grains [81]. This reaction ring may have prevented a further ion release to be used for the formation of the reaction products and hence led to a decrease of reaction rate leading to a prolonged setting time. On the other hand, an excessive higher Ms value (i.e. Ms=1.6 WG-activated) provided additional silica causing a less alkaline medium. This probably allowed a higher dissolution degree of precursors, and many nucleation sites were offered for the precipitation of reaction products. Therefore, the solidification process was accelerated by the faster polycondensation to form the primary C-S-H. Aydin and Baradan [80] reported that the effect of Ms on setting time of alkali-activated slag pastes depends on the  $\text{Na}_2\text{O}$  content of activator solution. They showed that setting time of the mixtures decreased slightly with an increase of Ms for 4%  $\text{Na}_2\text{O}$  content, while significantly shorter setting times were reported for intermediate Ms values of 0.4 and 0.8. On the other hand, Humad et al. [224] reported longer setting times for the intermediate Ms value in GGBFS-FA mixtures. It seems that the setting behaviour of AAC is not only driven by the Ms value of the activator solution, but also by the  $\text{Na}_2\text{O}$  content of the solution, GGBFS properties and the presence of FA in the system.

The increase of sodium silicate activator dosage led to a contradictory influence on the initial and final setting times. The increase of sodium silicate dosage slightly extended the initial setting time but shortened the final setting time. A general evaluation concludes that the setting times of alkali-activated GGBFS-FA mixtures are found to be more dependent on the GGBFS-FA ratio and the Ms value of the activator solution.

### 3.2 Critical strain of AAC mixtures

---

Fig. 5-2 presents the strain-sweep responses of AAC pastes with different GGBFS/FA ratios, Ms values and sodium silicate activator dosages. As can be seen from Fig. 5-2, two main regions, an initial plateau and a subsequent decrease corresponding to the shear-induced breakdown, are observed in storage modulus curve. The strain level corresponding to a decrease in storage modulus is defined as critical strain determining the limit of the linear viscoelastic domain (LVER) of the material. To determine the LVER, strain-sweep tests with strain amplitude from 0.0001% to 10% and a constant frequency of 1 Hz were conducted. For all mixtures given in Table 5-1,

all of the critical strain values were found to be within 0.01% to 0.1% interval. In order to remain in LVER in time sweep tests, the strain amplitude of 0.005% was selected for all mixtures.

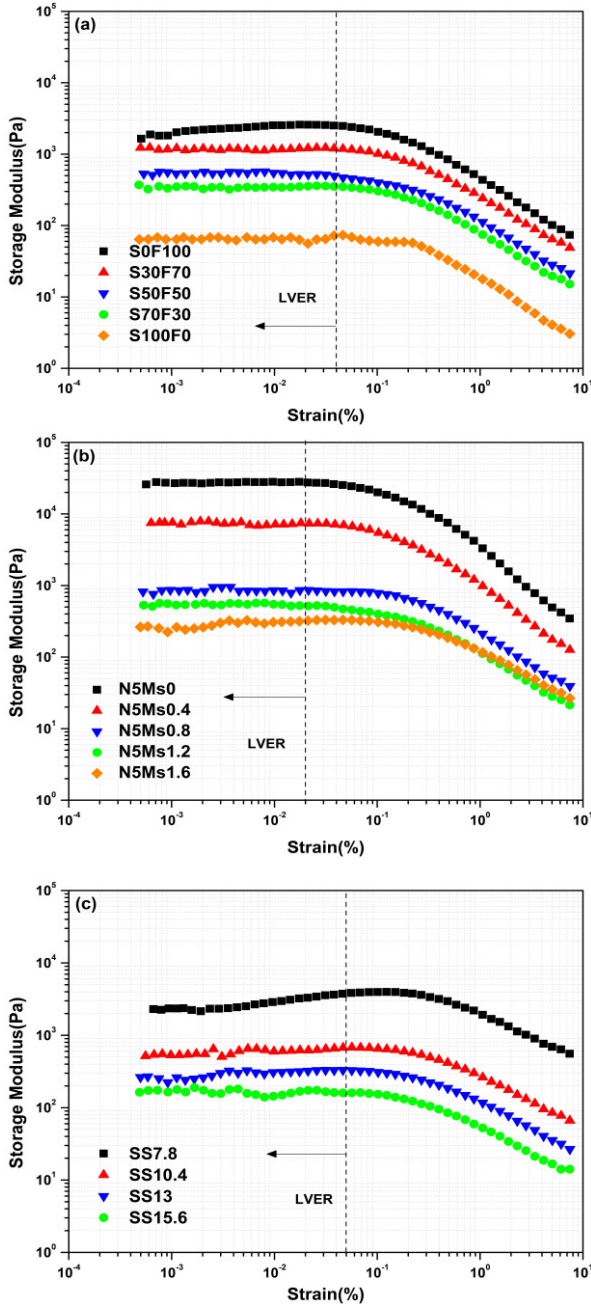


Fig. 5-2 Linear viscoelastic range of GGBFS-FA pastes with different parameters by

the strain-sweep tests at frequency 1 Hz and 20 °C (a) GGBFS-FA ratio (b) Ms value (c) Liquid sodium silicate dosage.

### 3.3 Structural build-up of AAC mixtures

The effect of GGBFS content on the structural formation in the early stage was presented in Fig. 5-3. The zero time in all graphs presented in this study shows the first contact time of the activator solutions and the precursors. Fig. 5-3b shows the storage modulus of the mixtures having different GGBFS contents on a logarithmic scale to observe very early stage storage modulus development in more detail.

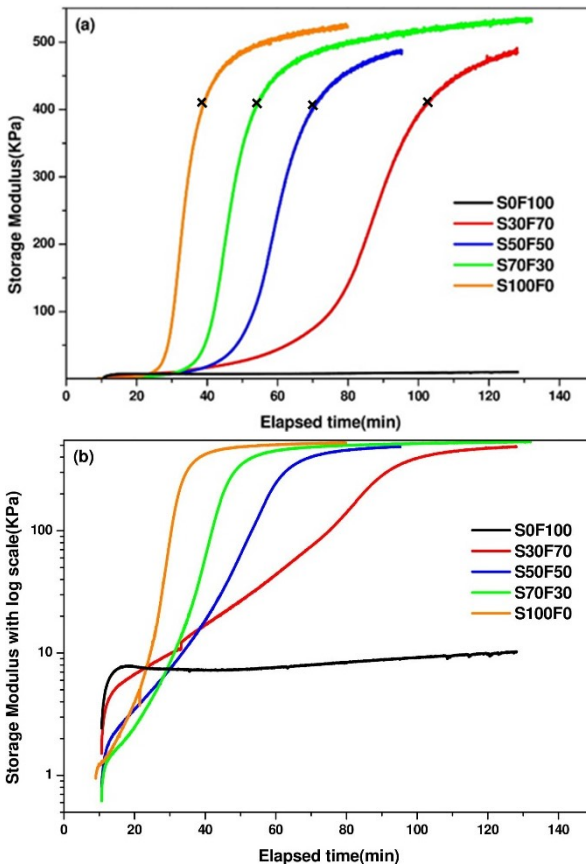


Fig. 5-3 Evolution of storage modulus in the alkali-activated GGBFS-FA pastes with different GGBFS-FA ratios ( $M_s=1.2$ ) using SAOS test at strain of 0.005% , frequency of 1 Hz and 20 °C (a) Normal scale (b) Log scale.

The evolution of storage modulus and loss modulus can show different physico-chemical stages of the geopolymers such as initial reorganization, dissolution/oligomerization, incubation, percolation/hardening and consolidation [52]. Generally, there are many types of non-contact interactions occurring within a cementitious suspension [225], such as Brownian forces, inter-particle interaction forces (such as electrostatic or steric repulsion and the van der Waals forces), hydrodynamic force, gravitational and the inertial forces [26], [95]. Different particles interact via attractive van der Waals forces due to the short distance [93] which leads to the formation of their flocculated microstructure [226]. Electrostatic forces originating from the presence of the adsorbed ions on the surface of the particles are normally insufficient alone to prevent agglomeration due to the van der Waals forces [94]. The Brownian motion and inertial forces can be neglected when compared to the aforementioned strong inter-particle interaction forces. For example, in the very early stage, it was observed that the mixtures with higher FA contents and lower W/B ratios showed higher initial storage modulus (Fig. 5-3). This indicates a more rigid structural formation probably caused by the inter-particle interaction forces induced by the finer particles of FA and lower W/B ratio of FA incorporated mixtures. As well known, cementitious suspensions can withstand the flow with a small amount of internal stress generated by the nucleation of early hydration products and a percolated network of inter-particle colloidal interactions. The smaller particle size of FA and lower W/B ratio may dominate the attractive colloidal interactions (as the flocculation time is inversely proportional to the number of particles per unit volume as shown in [33]) making the flocculated particles strong enough to increase the stored energy, i.e. fast development of  $G'$  in the very early stage of the hydration. In addition, a continuous increase of the storage modulus in the induction period has also been attributed to the C-S-H bridge formations between cement particles [33] and the dissolution of ions causing a quick structure development [227]. Similar to these findings, at rest, the observed rapid evolution and higher structural build-up rate of higher GGBFS content can be ascribed to the rapid formation of very early reaction products. It should also be noted that the increasing rate of storage modulus was enhanced by the addition of GGBFS. This can be confirmed by the specimen S0F100 such that there was no obvious increase in the storage modulus for a 100% FA system upon a very early time. Sun and Vollpracht [67] also pointed out that GGBFS had a significantly higher dissolution rate as compared to FA based AAC. Another interesting observation that could be noticed from Fig. 5-3 is the existence of an inflection point presenting a gradual decrease in the increasing rate of storage modulus (marked with the crosses presented in Fig. 5-3a). In all mixtures, except for S0F100, the increasing rate of storage modulus evaluation started to show a gradual decrease with some fluctuations in storage modulus values.

Fig. 5-4 shows the evolution of the loss factor of alkali-activated pastes produced with different combinations of GGBFS and FA. With time elapsing, the loss factors experienced several stages with different decreasing rates, followed by stabilizing to 0, except for specimen S0F100. The time when the loss factor starts to stabilize to 0

can be defined as percolation time, which is the required time to build a percolated elastic network [188], also reflecting the transition from viscous behaviour to elastic behaviour. Two different behaviours can be identified during the measurement time. The loss factor of S0F100 gradually decreased but did not reach 0, showing a more viscous behaviour. By contrast, the loss factor of all other mixtures decreased to 0, reflecting a more elastic behaviour. It is worth noting that the percolation times of S100F0, S70F30, S50F50 and S30F70 are around 51, 76, 88 and 127 minutes, which is in agreement with the trend of their initial setting times. With the addition of GGBFS into the mixtures, the loss factor decreased faster and earlier showing a more rigid structure.

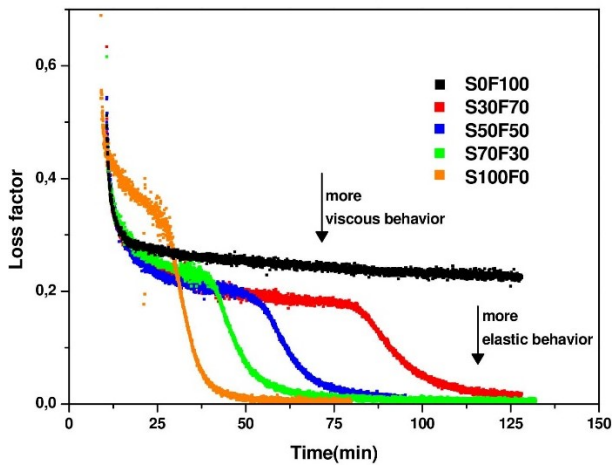


Fig. 5-4 Evolution of loss factor of alkali-activated pastes with different GGBFS-FA ratio (using SAOS test at strain of 0.005% , frequency of 1 Hz and 20 °C).

GGBFS and FA may play different roles during the reaction process. Gao et al. [207] confirmed that hybrid GGBFS-FA samples with higher GGBFS content resulted in a higher dissolution heat flow, which indicated that dissolving of GGBFS is easier than FA, resulting in the rapid formation of reaction products to establish a rigid network. Samples with a higher amount of FA have a longer induction period due to the low reactivity of FA. On the other hand, fly ash particles may act as nucleation sites for the further deposition of the reaction products as reported in [3], [51], [207]. This needs further microstructural studies.

Fig. 5-5 shows the evolution of the structural build-up of alkali-activated pastes with different  $M_s$  values. More detailed information on structuration in the early stage can be observed from Fig. 5-5b. As can be seen in Fig. 5-5, two different behaviours for evaluation of storage modulus were observed depending on the  $M_s$  value. For low  $M_s$

values (0 and 0.4), a continuous increase of structural formation was observed. On the other hand, for  $M_s$  values higher than 0.4, a sudden increase of structural build-up was obtained after an induction period as shown in Fig. 5-5a. Gao et al. [207] also reported the same phenomena by isothermal calorimetry tests. Since the  $\text{Na}_2\text{O}$  contents of all activators are the same, the activators with low  $M_s$  values have higher pH value. Thus the dissolution rate of silica and alumina and the reaction degree of slag enhanced in low  $M_s$  cases [69], [228]. This might be the reason why N5Ms0 had the highest storage modulus as compared to others in the earlier stages.

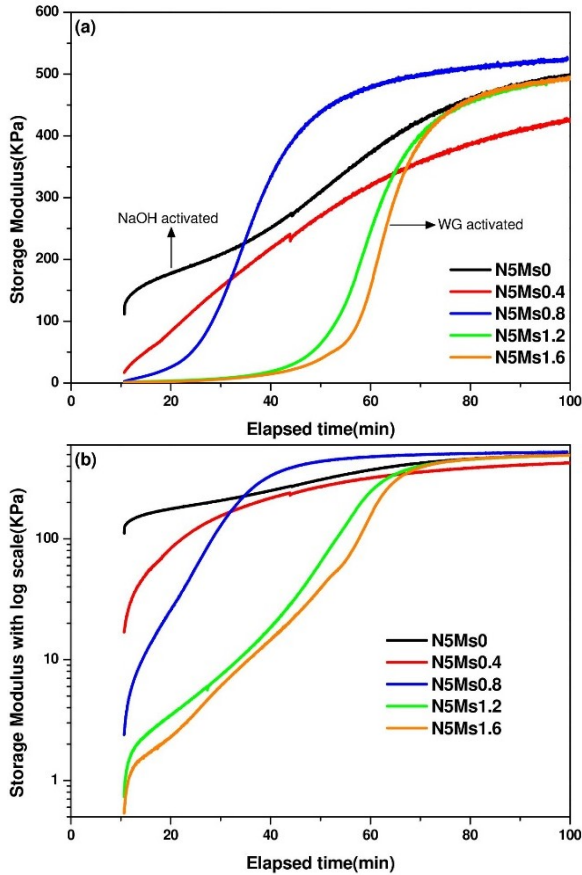


Fig. 5-5 Evolution of storage modulus of alkali-activated GGBFS-FA pastes with different  $M_s$  values using SAOS test at strain of 0.005%, frequency of 1 Hz and 20 °C (a) Normal scale (b) Log scale.

Furthermore, two different activators should be discussed as they showed two absolutely different behaviours: (i) For NaOH activated mixture (N5Ms0), an early increasing storage modulus can be observed due to rapid product formation around

individual GGBFS particles as well as in the matrix of the system after mixing the precursors and the activator. GGBFS made the main contribution to the structural build-up as presented before. Gebregziabihier et al. [81] reported that the formation of a reaction ring corresponding to the activated gel products around the GGBFS grains was identified at an early age, which hinders the degree of dissolution of the GGBFS grain. That is the reason why the structural formation is very high at the earliest time, while the further increasing rate of structural build-up is significantly low since it is limited by the diffusion rate of the activator solution into the GGBFS grain. With the time elapsed, the diffusion rate of ions played a more significant role in the microstructural development at the early time due to the availability of the ions in the pore solution and their ability to penetrate the inner product shell have a direct influence on the formation of reaction products [198], [229]. The microstructural evolution of NaOH activated mixture was from grain surface to inside unreacted GGBFS, which is similar to the shrinking core model generally used for PC hydration [229], [230]. (ii) For water glass (SS) activated mixture (N5Ms1.6), SS activators promote the dissolution of GGBFS for a considerable amount of time [231], which led to a longer time for microstructural development in the early ages. Thus, there is no significant increase in storage modulus at an early age indicating slow structural formation. Indeed, during this time duration, the dissolution of the source materials and also partly the formation of initial dissolved silicate units and their reactions with Ca and Na lead to the formation of a large number of oligomers [3], [207]. As the reactions progress, the SS activated mixture showed a dense matrix developed in the matrix [81] with a significantly increased rate of structural build-up. This might be attributed to the condensation between different oligomers, leading to a larger and rigid percolation network.

The effect of SS dosage on the structural formation of alkali-activated pastes is shown in Fig. 5-6. The increase of the structural build-up delayed by the increase of activator dosages ( $\text{Na}_2\text{O}$  and  $\text{SiO}_2$  content of activator) exhibited a sudden increase of structuration rate in the later stage. This storage modulus evolution is in agreement with setting time measurements (Table 5-2) showing the extended initial setting time but shortened final setting time with the increase of SS dosages.

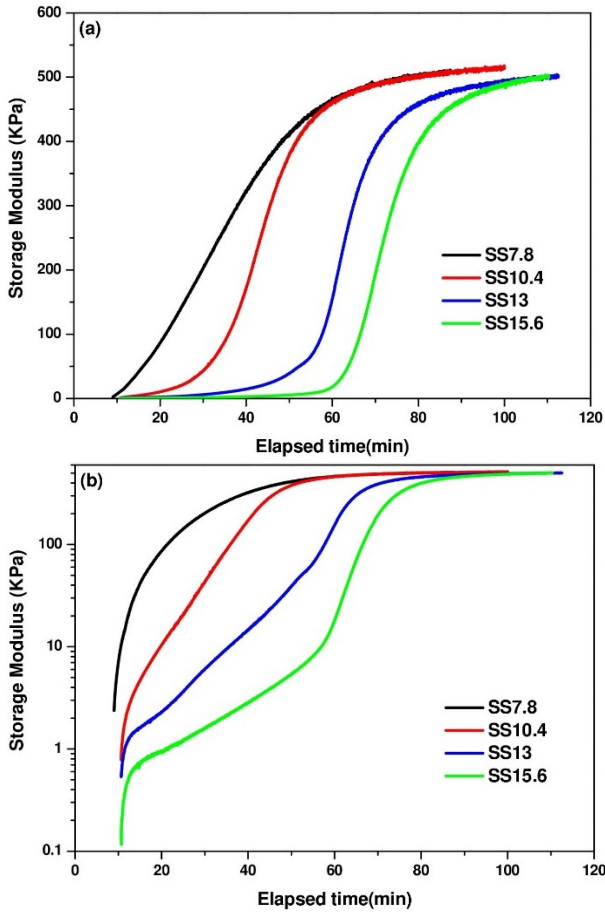


Fig. 5-6 Evolution of storage modulus of Alkali-activated GGBFS-FA pastes with different Liquid sodium silicate dosage using SAOS test at strain of 0.005%, frequency of 1 Hz and 20 °C (a) Normal scale (b) Log scale.

There is a competition between dissolution and the condensation process to form inorganic polymers during the sol-gel process as elucidated by Kline et al. [232]. The condensation process depends on the pH value and the electrostatic forces etc. An increase in activator dosage led to a slight increase in pH value (see in Table 5-1), thereby promoting the dissolution stage [233]. However, as pointed out by Rifaai et al. [48] a high amount of  $\text{OH}^-$  concentration does not always support the condensation and polymerization process. Because the presence of excessive negatively charged monomers increase the repulsive forces and delays the condensation process. Therefore, until attractive forces overcome the repulsive ones between monomers, the delayed condensation would be promoted by the monomers remaining in the pore solution. With elapsing time, mixtures with high activator dosage showed a faster

increasing rate of structural formation, this might be owing to the considerable extent of condensation process occurred, establishing a more rigid network [48].

Fig. 5-7 shows the evolution of the loss factor of mixtures with different  $\text{Na}_2\text{O}$  contents. As can be seen from Fig. 5-7, the percolation times extended by the increase of SS dosages. This is in agreement with the trend of the initial setting times of the mixtures (Table 5-2). Interestingly, a peak or hump could be observed for high dosages of SS where the black arrow is shown. These peaks are actually linked to the more rapid increase in the lost deformation energy (i.e.  $G''$ ) over the stored deformation energy (i.e.  $G'$ ) for a given time. The peaks, observed during the rapid increasing structural build-up stage, might also be related to the condensation stage. Because, in the condensation stage, a large amount of water is released by the condensation of  $\text{Si}(\text{OH})_4$  elements [234], [235]. Therefore, this extra water probably increased the loss factor and also revealed more liquid-like behaviour of the pastes in this stage. As the intensity of the peak could reflect a high degree of condensation, its presence points out more dense microstructural development resulting in high compressive strength in the hardened state. Some researchers also related these peaks to the gelation [63]. After the peak, the gradual decrease in loss factor may be attributed to the more lubricated contact of particles leading to less loss of dissipated energy as compared to more direct contact [236].

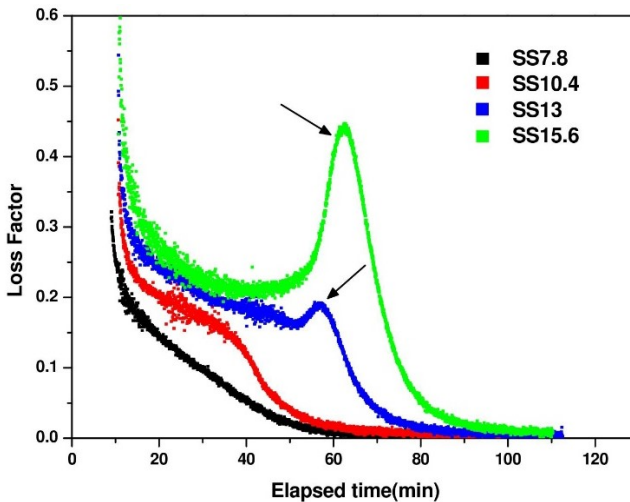
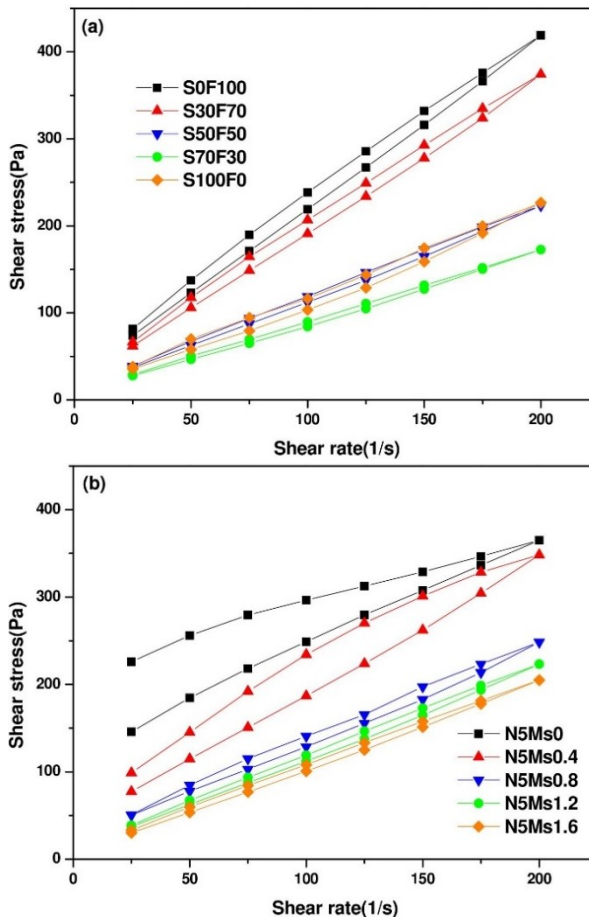


Fig. 5-7 Evolution of loss factor of alkali-activated pastes with different liquid sodium silicate dosage using SAOS test at strain of 0.005%, frequency of 1 Hz and 20 °C.

### 3.4 Rheological parameters (flow curve)

The flow curves of the mixtures are given in Fig. 5-8. As shown in Fig. 5-8, the shear stress of the ascending curve was higher than the descending curve for all pastes during the whole shear process, reflecting there is no permanent structural formation [138]. The area of the hysteresis loop is known as the level of thixotropy [215]. Generally, thixotropy is considered as a phenomenon of a physico-chemical reaction. However, as the flocculation and hydration occur simultaneously, attributing the build-up or breakdown solely to one of these phenomena is not straightforward [216]. In this study, the downward curves of all mixtures were employed to determine the dynamic yield stress. Herschel-Bulkley model was applied to determine the dynamic yield stress and power index ( $n$ ) of the mixtures in this study. This non-linear equation was expressed by the exponent ( $n$ ) in the Eq. (2-3) and indicates shear-thickening if  $n > 1$ , shear-thinning if  $n < 1$  and Bingham model if  $n = 1$  [185]. Mehdizadeh et al. [218] confirmed that SS activated slag pastes fit the Herschel-Bulkley model.



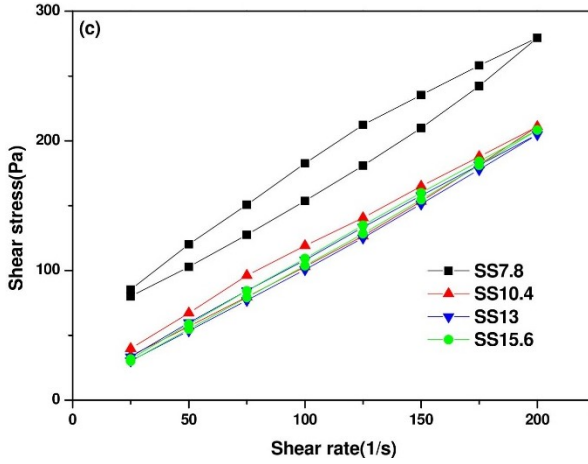


Fig. 5-8 Flow curves of GGBFS- FA pastes (a) GGBFS-FA ratio (b) Ms value (c) Liquid sodium silicate dosage.

The rheological parameters of the mixtures are summarized in Table 5-3. It should be noted that the Herschel-Bulkley model overestimates the yield stress as reported by [237].

Table 5-3 Rheological parameters of the mixtures.

Parameters	Mixture	Herschel-Bulkley model			R <sup>2</sup>	Area of thixotropy (Pa/s)
		Dynamic yield stress (Pa)	Consistency index (k)	Power index (n)		
	S0F100	30.31	1.58	1.00	0.99987	2501
	S30F70	26.65	1.16	1.00	0.99959	2171
GGBFS/FA	S50F50	18.73	0.52	1.13	0.99962	1018
	S70F30	14.98	0.30	1.18	0.99983	659
	S100F0	26.34	0.14	1.38	0.99920	1981
	N5Ms0	96.86	3.66	0.81	0.99989	7113
	N5Ms0.4	50.51	0.77	1.12	0.99948	5975
Ms value	N5Ms0.8	33.67	0.48	1.17	0.99876	1639

	N5Ms1.2	18.73	0.52	1.13	0.99962	1018
	N5Ms1.6	12.06	0.51	1.12	0.99989	1012
	SS7.8	67.34	0.21	1.30	0.99930	3624
Liquid sodium silicate dosages	SS10.4	19.64	0.33	1.20	0.99953	1943
	SS13	12.06	0.51	1.11	0.99989	1012
	SS15.6	9.43	0.66	1.00	0.99989	762

When considering the effects of the GGBFS-FA ratio on the rheological properties, it was observed that the fly ash paste (S0F100) showed a Bingham behaviour ( $n=1$ ) as reported by other previous studies [123], [238]. A simultaneous increase of GGBFS amount and W/B ratio increased the shear-thickening character of the pastes. For example, S70F30 and S100F0 mixtures showed more shear-thickening behaviour with the  $n$  values of 1.18 and 1.38, respectively. Shear-thickening behaviour for GGBFS mixtures was also reported by Palacios et al. [30]. The thixotropy degree of the mixtures can be observed from Fig. 5-8, and the calculated thixotropy area of the mixtures are given in Table 5-3. As can be seen from Table 5-3, the thixotropy degree of S70F30 mixture was the lowest and an increase of the FA content resulted in a more thixotropic behaviour. This is probably because of a more flocculated structure induced by the attractive inter-particle forces due to the lower W/B ratio of the high-volume FA mixtures. This is also in agreement with the initial  $G'$  results presented in section 3.3. This flocculated structure of very fine FA particles might be destroyed by the introduced shear energy during the rheology test. The mixture with single use of GGBFS (S100F0) having the highest W/B ratio among the mixtures had somehow a higher area of thixotropy as compared to S50F50 and S70F30 mixtures. This could be related to the higher reaction rate of GGBFS, resulting in the early formation of primary C-S-H gel [30]. It should be noted here that the dynamic yield stress results also followed the same trend as the area of thixotropy.

Fig. 5-8b shows the effects of  $M_s$  value on the rheological behaviour of hybrid mixtures. NaOH-activated AAC ( $M_s=0$ ) showed a shear-thinning response and behaved like a pseudo-plastic fluid. Thus, decreasing the shear rate leads to an increase in the apparent viscosity. However, once SS was added into the activator solution, it apparently showed a shear-thickening response. In addition, the dynamic yield stress and the degree of thixotropy decrease as the  $M_s$  value increases. For example,  $M_{s0.4}$  and  $M_{s1.2}$  mixtures showed the dynamic yield stress of 50.51 Pa and 18.73 Pa, and the thixotropy area of 5975 Pa/s and 1018 Pa/s, respectively. This finding is also in agreement with the initial storage modulus as presented in section

3.3.

Fig. 5-8c shows the effects of sodium silicate dosage on the rheological behaviour of hybrid mixtures. A higher shear-thickening response was observed for the mixture having the lowest SS dosage (7.8%). However, as the SS content increases the shear-thickening response decreases and may completely disappear for high SS content of 15.6%. This mixture behaved like a Newtonian fluid with an  $n$  index of 1 (Eq. (2-3)). The dynamic yield stress and the area of thixotropy decreased with an increase of SS dosage. These results followed the same trend with initial storage modulus as presented in section 3.3, reflecting a very good correlation in results between different tests.

### 3.5 Chemistry of pore solution

The pore solution chemistry of N5Ms0.4 and N5Ms1.2 mixtures (50% GGBFS + 50% FA), whose structural formation behaviours are significantly different from each other, were investigated by ICP-OES tests. Fig. 5-9 and Fig. 5-10 present the relationship between structural formation (storage modulus up to the rheometer measurement capacity of 500 kPa) and ion concentrations of Si, Na, Al, Ca, Mg and Fe in the pore solution as a function of time up to at around initial setting time. Table 5-4 and Table 5-5 show the values of elemental concentrations with time. The ion concentrations at zero time indicate the composition of the activator solution itself. The pore solution composition was dominated by Na and Si whereas much lower Al, Ca, Mg and Fe were identified.

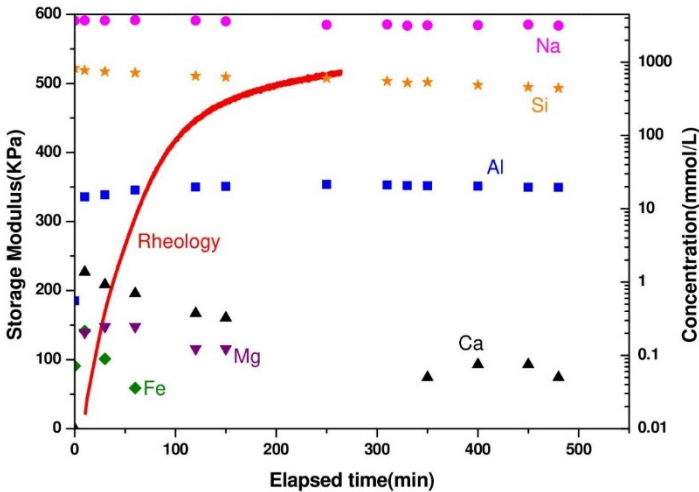


Fig. 5-9 Pore solution chemistry of N5Ms0.4 mixture.

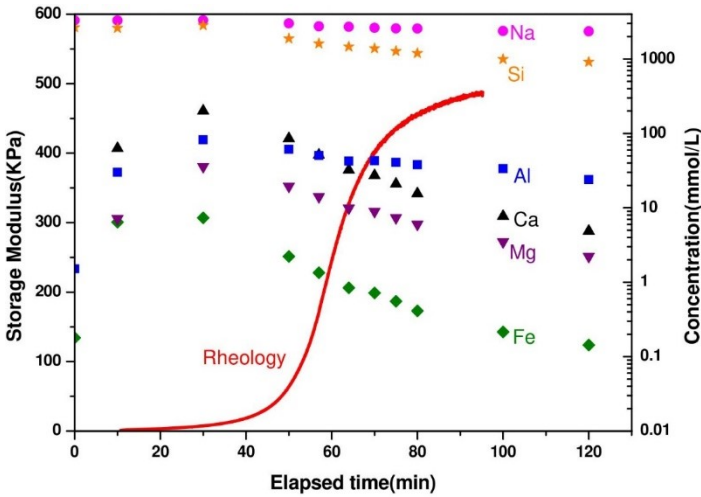


Fig. 5-10 Pore solution chemistry of N5Ms1.2 mixture.

Table 5-4 Elemental concentrations of N5Ms0.4 mixture.

Time (min)	Na (mmol/L)	Si (mmol/L)	Al (mmol/L)	Ca (mmol/L)	Mg (mmol/L)	Fe (mmol/L)
0	3695.65	832.09	0.56	0.00	0.00	0.07
10	3727.19	775.58	14.53	1.37	0.21	0.21
30	3707.61	748.38	15.53	0.92	0.25	0.09
60	3750.02	719.36	17.94	0.70	0.25	0.04
120	3704.09	649.90	19.90	0.37	0.12	0.00
150	3609.44	628.21	20.16	0.32	0.12	0.00
250	3240.89	604.50	21.46	0.00	0.00	0.00
310	3275.86	551.84	21.16	0.00	0.00	0.00
330	3157.20	524.67	20.72	0.00	0.00	0.00
350	3193.82	533.58	20.57	0.05	0.00	0.00
400	3198.17	487.68	20.31	0.07	0.00	0.00
450	3260.16	458.73	19.75	0.07	0.00	0.00
480	3156.94	443.14	19.68	0.05	0.00	0.00

Table 5-5 Elemental concentrations of N5Ms1.2 mixture.

Time (min)	Na (mmol/L)	Si (mmol/L)	Al (mmol/L)	Ca (mmol/L)	Mg (mmol/L)	Fe (mmol/L)
0	3315.70	2652.03	1.52	0.00	0.00	0.18
10	3300.61	2610.94	30.17	63.13	7.16	6.41
30	3330.80	2834.05	82.09	201.23	35.80	7.34
50	3010.66	1883.71	61.23	85.56	19.50	2.22
57	2752.46	1609.91	50.52	51.35	14.11	1.34
64	2710.83	1466.18	42.47	32.31	9.92	0.84
70	2628.19	1391.30	42.92	27.17	8.97	0.72
75	2584.86	1271.74	40.77	20.91	7.36	0.56
80	2575.95	1195.79	37.95	15.52	6.01	0.41
100	2379.82	996.33	33.58	7.71	3.50	0.21
120	2358.98	911.84	24.02	4.87	2.22	0.14

The measured ion concentrations of the pore solution indicate the remaining part of the dissolved ions from the precursor or existing ions after their consumptions to produce reaction products. Si in the activator solution of N5Ms1.2 was much higher than that of N5Ms0.4 due to its higher Ms value. Al and Ca concentrations started from zero as they sourced from the dissolution of the precursors. Then their concentration increased to a peak value due to the ongoing dissolution and finally decreased in different rates. It is observed that all ion concentrations, especially Al and Ca, increased up to 30 min for N5Ms1.2, and then started to decrease, showing the consumption rate of the ions exceeding the dissolution rate. This peak point also corresponds approximately to the beginning of the massive structuration. The concentration of Ca is greater than Al before the age of 55 min. This is because CaO content in the precursors is higher than Al<sub>2</sub>O<sub>3</sub> content and also the bond dissociation energy of Ca-O is weaker than Al-O [16]. After that time, Al concentration is higher than Ca, indicating a higher consumption rate of Ca. The pore solution of N5Ms1.2 paste has significantly higher Al and Ca concentrations than that of AAC paste activated with low Ms value activator (N5Ms0.4). The higher Ca content for the pore solution of N5Ms1.2 paste is related to the increased solubility of Ca ions with decreasing pH value of the activator solution [69]. The enhanced dissolution of FA by the silicates may lead to an increase of Al in the pore solution. Previous studies [239], [240] showed that there is a siliceous layer on the FA grains formed due to the initial preferential dissolution of Al from the FA in the NaOH activated FA paste. The

adsorption of initially dissolved alumina species on the siliceous layers prevents the approach of hydroxide ions to FA particles, thereby slowing down the dissolution of FA [241]. With an increase of soluble silicate in the activator solution, Al released from FA could quickly be captured by silicates, thereby prevents the passivation of FA surface and provides more rapid dissolution of FA [242].

As shown in Fig. 5-10, the consumption rate of Ca was significantly higher than Al after 30 min and it became dramatic after 50 min. On the other hand, the Al concentration is nearly constant upon 50 min which corresponds to the initial setting time of N5Ms1.2. For Ms=0.4 mixture, the dissolution rates of Na and Al ions are slightly higher than the consumption rates until 120 and 310 min, respectively. On the other hand, the dissolution rates of Ca and Si ions are lower than their consumption rates from 10 to 480 min. It means that Ca ions from slag were dissolved just after contact with an activator solution similar to Al ions, and Ca and Si may be used to produce reaction products. It supports the findings of Hajimohammadi et al. [14] that the gel nucleation increases with the increase of dissolved silicate in the activator solution [243]. For low Ms value case (e.g. N5Ms0.4), the gel nucleation may occur the places closer to the precursor particles. This is owing to the formation of a reaction product ring, taking place around precursor particles, which is formed by the initially dissolved calcium, alumina and available silicate as discussed in aforementioned section 3.3. The early reaction product formation around the slag particles may prevent the further dissolution of the ions from the slag for Ms=0.4 case. The further reactions is possibly controlled by the diffusion of OH<sup>-</sup> ions, so the reactions slow down and the setting time extends to 5 hours for N5Ms0.4. For both mixtures, Na is mainly sourced from the alkaline activator solution and decreases slightly with time. Favier et al. [78] have investigated the concentration of alumina and sodium in the liquid phase of metakaolin with static NMR measurement in order to understand the hardening behaviour of geopolymers. Their findings support the evolution of alumina and sodium in the pore solution presented in this study. They point out that after some time, alumina and sodium evolution in the liquid phase are concomitant. This indicates that Al is taken up in the tetrahedral position of the aluminosilicate phase and Na compensates the charge. It should be noted that N5Ms0.4 has a higher pH value, i.e. higher OH<sup>-</sup> concentration, than that of N5Ms1.2 as shown in Table 5-1. Therefore, the higher OH<sup>-</sup> concentration induces a fierce reaction process of precursors, but the reaction is immediately controlled by the diffusion rate of hydroxide ions due to the formation of the reaction product ring. From the rheological point of view, this may explain why N5Ms0.4 paste has higher initial storage modulus followed by a lower and continuous increasing rate and longer initial setting time. On the other hand, from the pore solution chemistry point of view, a low amount of Al and Ca caused by the prevention of the ion release by the reaction product ring around the precursor, leads to a low reaction rate as compared to N5Ms1.2. Besides, the decrease of Al is more gradual as compared to Ca. This might be attributed to initial utilization of calcium in the formation of C-S-H gel, and the later incorporation of Al to C-S-H gel. Conversely, in the N5Ms1.2 paste, the gel nucleation takes place far away from the precursors,

resulting in a rapid and higher release of calcium and alumina into the pore solution to react with Si from the activator solution. From the rheological point of view, there is nearly no structural formation before the age of 30 min since the dissolution of precursors is dominating the process. Once sufficient alumina and calcium are accumulated in the pore solution, the possibility to encounter silicate ions increases dramatically. It is inevitable that the condensation between different oligomers occurs rapidly, thus the structural formation increases quickly. Simultaneously, the concentrations of alumina, calcium and sodium in the pore solution start to decrease. It shows that Na was taken up during the reaction product formation [244], [245]. Although both activator solutions have the same amount of Na, its concentration in the pore solution of  $M_s=1.2$  was lower than  $M_s=0.4$ . Si was sourced from both the activator solution and dissolution of the precursors. The time corresponding to the maximum concentrations for Na and Si indicates that the release rate of Si from precursors is equal to its consumption rate.

Structural formation before the initial setting time may also be related to the silicate species and their amounts in the activator solution. The amount of sodium hydroxide used for the preparation of  $M_s=1.2$  activator solution is significantly lower than that of  $M_s=0.4$ . Liquid state  $^{29}\text{Si}$  NMR tests on activator solutions showed that the silicate connectivity, i.e. highly polymeric silicates with large rings is increased with an increase of  $M_s$ , showing depolymerization of the silicate species with an increase of NaOH added [105], [129]. In other words, the attack of dissolved OH ions (coming from added NaOH to adjust  $M_s$  of solution) to siloxo (Si-O-Si) bonds results in the depolymerization and the formation of various low molecule species. Since the activation energy barrier for highly polymeric silicates is higher than the small species, the reaction product formation is retarded for the activators with high  $M_s$  values. On the other hand, the availability of silica contributes to C-A-S-H nucleation and gel growth [129]. These may be the reasons for the negligible initial structural formation until 30 min and the development of a faster structuration for later ages in high  $M_s$  value mixtures. With regard to the early time reaction products for GGBFS-FA based AAC, the C-S-H or C-A-S-H gel formations could be expected rather than N-A-S-H because of the high OH concentrations in the presence of Ca ions. This can explain the decrease of Ca, Al and Si in the pore solution with time. Meanwhile, the decrease in Na concentration over time may show the incorporation of Na ions into C-S-H and particularly into C-A-S-H structures due to its higher binding capacity as compared to C-S-H [13], [244].

Mg and Fe ion concentrations over time for both two mixtures were not shown in Fig. 5-9, as their concentrations were lower than 0.01 mmol/L (Table 5-4). The Fe and Mg of both two mixture first increased at an early age, followed by a rapid decrease. With regard to the decrease of Mg, it might be incorporated into the early reaction products such as C-S-H rather than hydrotalcite [246] formation as the hydrotalcite is normally expected to be formed in GGBFS based AAC mixtures in the later ages [69].

### 3.6 Microstructure analysis of AAC

---

Fig. 5-11 presents the SEM (BSE) images of S50+F50 mixtures with activator solutions of N5Ms0.4 and N5Ms1.2 at 1-day. SEM analyses were performed on 1-day samples to see the microstructure as early as possible, because the matrix phase in earlier times, such as around the final setting, could easily be damaged during grinding for SEM observation. In Fig. 5-11, the irregularly shaped light grey areas indicate unreacted slag grains, the spherical particles show unreacted fly ash, the grey regions between the particles indicate the reaction products and the black regions show the pores. SEM images showed that the N5Ms1.2 mixture had a better-packed structure as compared to N5Ms0.4 and this was in accordance with the mechanical strength test results at 2-day. As shown from the SEM images, the small-size slag particles were completely or partially reacted, while the larger ones showed a limited reaction. In addition, Fig. 5-11 shows that FA particles remain unreacted at 1 day for both Ms values. A reaction ring (marked with red arrows in Fig. 5-11a), which may slow down the hydration of GGBFS [81], was observed around some unreacted slag grains in the case of N5Ms0.4. This observation was tried to be confirmed by EDX analyses which were performed on 16 different points of the reaction products. EDX analyses on the N5Ms0.4 showed that the atomic Ca/Si, Al/Si and Na/Si ratios were between 0.40 - 0.95, 0.30 - 0.52, and 0.08 - 0.27, respectively. These ratios for the reaction products of N5Ms1.2 were between 0.25 - 1.06, 0.25 - 0.43 and 0.02 - 0.15, respectively. Based on these findings, the main reaction products of both mixtures could be categorized as Al and Na substituted calcium silicate hydrate gel (C-N-A-S-H) as shown by Lee et al. [247] and Ismail et al. [248] on alkali-activated slag/fly ash mixtures. Ismail et al. [248] also reported the formation of a hybrid binding phase of N-C-A-S-H and C-A-S-H for the precursor system having fly ash higher than 50%. For both mixtures, the Ca/Si ratio was found high around the unreacted slag grain and it decreased as being moved away from slag grains. The average atomic Ca amount in the reaction products of N5Ms1.2 and N5Ms0.4 were found as 11.4% and 9.4%, respectively. This shows higher amounts of Ca dissolution from the slag in case of higher Si containing activator solution (Ms=1.2), possibly because of low solubility of calcium in high pH medium [69], [103].

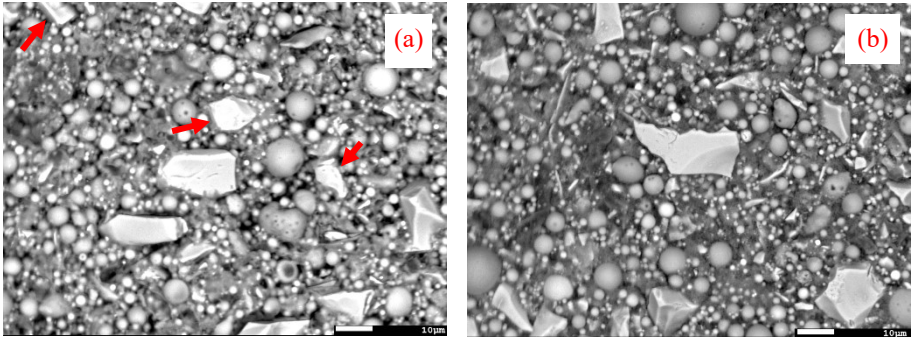


Fig. 5-11 SEM (BSE) images of 50% FA+50% GGBFS AAC mixtures at one day  
(a) N5Ms0.4, (b) N5Ms1.2

### 3.7 Mechanical properties

Compressive strength values of AAC mortars are given in Table 5-6. As can be seen from Table 5-6, compressive strength values of the mortar mixtures, except S0F100 and SS7.8 mixtures, comply with the strength class of cement standards. Compressive strength values of hybrid AAC mixtures increased with the increasing GGBFS/FA ratios, however, a 100% GGBFS mixture (S100F0) showed a relatively lower compressive strength due to its higher W/B ratio. On the other hand, compressive strength values of a 100% FA mixture (S0F100) at early and later ages were significantly lower as compared to the AAC mixtures that incorporated GGBFS. These findings are attributed to the low  $\text{Na}_2\text{O}$  content of activator solution which is probably not sufficient for the activation of FA [249].

As the Ms value increased in the mixtures, the compressive strength increased significantly in the later stage (e.g. 28 days) especially for Ms values higher than 0.4, possibly due to more homogenous microstructure formation with high Ms value [80]. However, at the age of 2 days, the compressive strength values of the mixtures were similar to each other except for Ms 0.8 case.

The mortar having low sodium silicate dosages of 7.8% (corresponding to 3%  $\text{Na}_2\text{O}$ ) did not gain any compressive strength at 2 days. On the other hand, as the sodium silicate content increases in the mixtures, mortars gained better mechanical performance. Previous studies [198] also reported that 4% Na content by mass of GGBFS binder was considered as the lowest level to induce the sufficient activation of GGBFS. Fernandez-Jimenez et al. [250] recommended the minimum concentration of activator as 3%  $\text{Na}_2\text{O}$  by GGBFS weight.

Table 5-6 Compressive strength of AAC mixtures.

Parameters	Mixtures	2-day (MPa)	7-day (MPa)	28-day (MPa)
GGBFS/FA ratio	S0F100	2.2	7.9	12.8
	S30F70	10.9	47.3	78.0
	S50F50	26.4	61.8	88.7
	S70F30	24.6	66.2	87.5
	S100F0	20.9	61.3	73.5
Ms value	N5Ms0	21.3	33.4	48.3
	N5Ms0.4	23.4	52.8	74.1
	N5Ms0.8	12.1	57.8	87.4
	N5Ms1.2	26.4	61.8	88.7
	N5Ms1.6	22.1	56.8	85.2
Liquid sodium silicate dosage	SS7.8	0	3.5	15.2
	SS10.4	4.8	46.7	70.7
	SS13	22.1	56.8	83.9
	SS15.6	22.3	58.8	82.7

#### 4. Conclusion

---

This chapter focused on the fresh state properties including the structural build-up and the rheology of AAC with respect to the GGBFS/FA ratio and the activator solution properties. The following conclusions can be drawn for the precursors and activators used in this study:

1. Setting times of AAC are mainly influenced by GGBFS/FA, Ms value and the dosage of sodium silicate activator. Setting times of AAC extended with the increase of FA content and sodium silicate activator dosage. It was revealed that the effect of the Ms value on the setting times is more prominent than the other two factors. An increase in Ms value from 0 to 0.4 resulted in a significant increase in setting times, while a further increase of Ms beyond 0.4 led to a sharp decrease in setting times of AAC.
2. The structural build-up increased earlier and faster with the simultaneous increase of GGBFS/FA and W/B ratio of the mixture, due to the higher dissolution of the glassy structure of GGBFS as compared to FA.
3. The increase of the sodium silicate dosage and Ms value resulted in a delayed structural build-up followed by a rapid increase. The effect of Ms value on the structural build-up of AAC led to two different rheological behaviours. AAC with a low Ms value showed a higher initial storage modulus, followed by a slow and continuous increasing rate of structural build-up. Conversely, a steep structural build-up for higher Ms values of AAC was observed after a long induction period with limited structural formation. This is attributed to the formation of a reaction product ring around the precursor particles preventing the further reactions in the low Ms value case. In the pore solution of AAC pastes, the lower Ms value resulted in a decrease in the concentration of Al and Ca. A higher Ms value led to a higher concentration of these elements in the pore solution.
4. A relationship was found between the ion concentrations of the pore solution and the structural build-up and setting time of the mixtures.
5. The flow curves of AAC pastes fit well with the Herschel-Bulkley model with a strong shear thickening behaviour with an increase of GGBFS amount and Ms value of the activator, and with a decrease in sodium silicate dosage.
6. The higher GGBFS/FA ratio in the precursor and higher Ms value and sodium silicate dosages in the activator solution were found to be more beneficial for a better strength development of AAC pastes.

**Chapter 6 Possibilities of using silica fume activator**

---

In this chapter, a more sustainable activator, silica fume activator (SFA), was introduced and compared with commercial sodium silicate activator (SSA). The effects of SFA and SSA on the rheology, setting behaviour and microstructure of alkali-activated slag cements were studied.

## 1. Introduction

---

The common activators in AAS production include sodium hydroxide, sodium silicate, and sodium sulfate, etc. In general, the required concentrations of sodium hydroxide activator needed for activation of AAS are usually high, and the high concentrations can cause significant occupational health and safety problems in large production facilities. Therefore, sodium hydroxide is classified as a corrosive solution under existing workplace legislation in almost every country in the world [76]. In addition to its corrosive nature, efflorescence is another significant problem in the sodium hydroxide-based binders due to the reaction of unreacted sodium ions and calcium hydroxide with atmospheric carbon dioxide [251]. Sodium sulfate and sodium silicate are the other two common activators for AAS activation. Sodium sulfate activators exhibit a slower reaction process and lower mechanical performance than sodium silicate solutions of comparable concentration [79], [252]. Sodium silicate activator (SSA) generally provides the best mechanical and durability performance among the common types. On the other hand, despite its many technical advantages, sodium silicate solution is the highest contributor to the CO<sub>2</sub> emissions of AAC [253]–[255]. In addition to its environmental drawbacks, sodium silicate-activated AAS have some technical drawbacks such as high drying shrinkage and significantly shorter setting time. Therefore, further studies on the development of alternative activator solutions providing comparable mechanical properties with SSA without its mentioned drawbacks are needed.

Recently, many researchers also started to investigate the mechanical properties and microstructure of AAS produced with silica fume activator (SFA) [143], [146], [256], [257]. It has been found that the SFA, which is prepared by the mixture of silica fume and an alkaline solution, is more active than sodium hydroxide and water glass [143]. Rousekova et al. [144] reported that SFA was highly effective in activating the PC, SF and GGBFS mixtures or the slag alone. The beneficial effect of SFA is attributed to the intensification of the production of calcium silicate hydrates and the densification of the pore structure. The mechanical performance of SFA-activated GGBFS and FA mixtures has been found better than that of the mixtures based on SSA. These findings make the SFA a better and more economical alternative to the SSA [145]. The microstructural investigations by Bernal et al. [146] also revealed that the SFA could promote the formation of a highly densified structure. Although there are many studies on the beneficial influences of SFA on the mechanical and microstructural properties of AAS, there is no study evaluating the rheology of GGBFS mixtures activated by SFA. In this study, setting times, rheological properties and the structural build-up of AAS mixtures activated by SFA and SSA were investigated comparatively. In addition, drying shrinkage and mechanical properties were determined on some selected mixtures. The effects of SFA on the microstructural properties were assessed by scanning electron microscope (SEM) images and Mercury intrusion porosimeter (MIP) tests.

## 2. Experimental program

### 2.1 Mixture design

Two different types of activator solutions were prepared by mixing NaOH solution with liquid sodium silicate or silica fume to achieve the Ms values of 0.4, 0.8, 1.2 and 1.6. These activator solutions were called ‘sodium silicate-based activator solution’ (SSA) and ‘silica fume-based activator solution’ (SFA), respectively. The mixture design and formulations of AAS mixtures is given in Table 6-1. The Ms value of the activator solution is following the abbreviation of the activator type in the mixture names. The Na<sub>2</sub>O content of all the activator solutions had 5% of the GGBFS weight, and the W/B ratios of the paste and mortar samples were kept constant as 0.45.

Table 6-1 Mixture designs of AAS made with SSA and SFA.

Mixtures	GGBFS (g/L*)	Liquid sodium silicate (g/L)	NaOH (g/L)	Silica fume (g/L)	Deionized water (g/L)	W/B**	Ms value (SiO <sub>2</sub> /Na <sub>2</sub> O)	Na <sub>2</sub> O content (%)	SiO <sub>2</sub> content (%)	pH of activator solution
SSA0.4	1294	91	64	-	470	0.45	0.4	5	2	13.61
SSA0.8	1287	181	42	-	426	0.45	0.8	5	4	13.55
SSA1.2	1279	269	21	-	383	0.45	1.2	5	6	13.49
SSA1.6	1272	354	0	-	342	0.45	1.6	5	8	13.37
SFA0.4	1146	-	76	24	561	0.45	0.4	5	2	13.51
SFA0.8	1123	-	75	47	559	0.45	0.8	5	4	13.45
SFA1.2	1100	-	73	69	558	0.45	1.2	5	6	13.36
SFA1.6	1079	-	72	90	556	0.45	1.6	5	8	13.29

\*g/L: gram per liter of paste

\*\*W-water, B-solid binder (GGBFS + solids in the activator solution).

### 2.2 Dissolution ratio of silica fume

Activator solutions were prepared one day before the casting of the mixtures. The pH of the activator solutions given in Table 6-1 was measured with a pH meter. In the preparation of the activator solution, the NaOH granules were mixed with deionized water first to obtain a NaOH solution. SFA was then prepared by mixing the silica fume powder with the NaOH solution. SSA was prepared by mixing the liquid sodium silicate solution with the NaOH solution.

To determine the amount of dissolved silica fume, the SFA was diluted by adding deionized water (by 5 times the volume of SFA) and then the diluted SFA was centrifuged at 3500 rpm for 5 min. After pouring out the centrifuged liquid, the solid part was mixed with methanol and then was centrifuged at 3500 rpm for 5 min. This

process was repeated two times to remove the soluble silicates and water in the suspension. The details of the applied method can be found in the literature [73]. After the centrifugation processes, the solid particles were collected and washed by methanol again by using a 0.2  $\mu\text{m}$  nylon filter paper. The undissolved silica fume amount was determined from the dried residuals over the filter paper at 100 °C for 24 hours. The dissolution ratios of SFA activators are presented in Table 6-2.

Table 6-2 Dissolution ratio of SFA.

Mixtures	SFA0.4	SFA0.8	SFA1.2	SFA1.6
Dissolution ratio (%)	91.75	52.11	35.71	28.02

### 2.3 Sample preparation

The paste samples were prepared using a Hobart mixer with the following mixture procedure: First the activator solution was poured into the mixer bowl, then the solid raw materials. The mixtures were mixed at a low speed ( $140 \pm 5$  rpm) for 90s, followed by scraping solids from the bottom of the mixing bowl and paddle, then the pastes were mixed at high speed ( $285 \pm 5$  rpm) for an additional 90s.

### 2.4 Protocol for flow curves and constant shear rate

As well known, the concreting consists of mixing, transporting, pumping, consolidating and surface finishing stages. Shear stress is always applied to the fresh concrete during the concreting stages mentioned above. In particular, high shear rates (stresses) during transport can hinder the formation of flocculating structure, and improve the flowability and workability during the casting process [258]. In order to predict the response of the concrete during transporting, alkali-activated GGBFS pastes were tested at a high constant shear rate ( $200 \text{ s}^{-1}$ ) for 60 min to observe the evolution of the shear stress under a high shear rate. Yield stress values of the mixtures were determined by using the shear cycle protocol given in Fig. 6-1. The time in Fig. 6-1 shows the total elapsed time from the first contact of the activators with the precursors. Just after the completion of the Hobart mixing, a fresh sample was placed on the rheometer cup and the paste was first subjected to a pre-shearing at  $200 \text{ s}^{-1}$  for 2 min to obtain a reference state. Subsequently, a shear cycle consisting of shear rate ramps from 0 to  $10 \text{ s}^{-1}$  in 1 min, 10 to  $200 \text{ s}^{-1}$  in 1 min and a ramp-down from 200 to  $0 \text{ s}^{-1}$  in 2 min was applied. This cycle was repeated eight times. A similar shear protocol was also used in the other studies [30], [31].

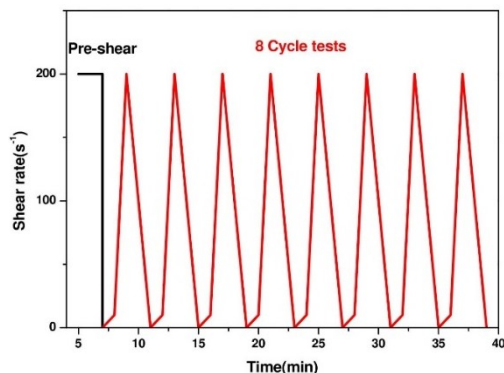


Fig. 6-1 Protocol of shear cycle tests.

### 3. Results and discussions

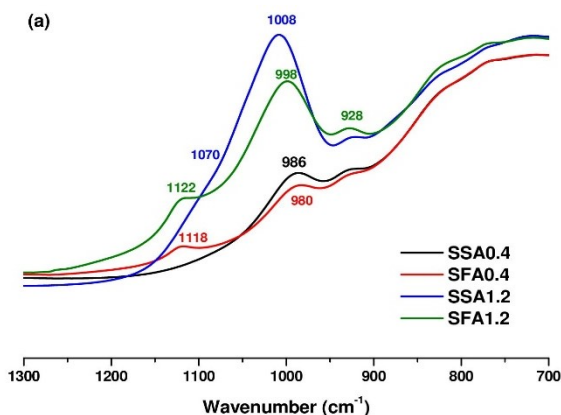
#### 3.1 Activator solution characterization from FTIR spectroscopy

ATR-FTIR spectra measurements were performed on the SSA and SFA based alkaline activators (Fig. 6-2) to investigate the differences in silicate bond types or molecular structures. The ATR-FTIR spectra show the relative proportion of transmission at a specific wavenumber in the silicate bonding region. Only the infrared absorption bands between  $1300\text{ cm}^{-1}$  and  $700\text{ cm}^{-1}$  were shown in Fig. 6-2a as fingerprint of silicate groups [259] since the other peaks in the out of this range belong to stretching (centered around  $3410\text{ cm}^{-1}$ ) and bending (around  $1650\text{ cm}^{-1}$ ) of OH groups. The fraction of tetrahedron silicon sites having non-bridging oxygen is linked to the transmission intensity in the silicate bonding region between  $1200\text{ cm}^{-1}$  and  $850\text{ cm}^{-1}$  [260], [261]. These peaks are the overlapped Si-O-Si bands of different  $Q^n$  species in the activator solution. The structural  $Q^n$  units are connected to the quantity of bridging oxygen per silicon site. The parameter  $n$ , ranging between 0 and 4, shows the degree of crosslinks in the silicate network [262].

As shown in Fig. 6-2a, the transmission bands showed a main peak for each activator solution at the wavenumbers between  $970\text{--}1010\text{ cm}^{-1}$ , which is related to the linear  $Q^1$  [263]. Generally lower intensities at these regions were obtained for low  $M_s$  cases (SSA0.4 and SFA0.4) as compared to high  $M_s$  solutions. A decrease in the  $M_s$  ratio led to a shift of the Si-O-Si stretching band to lower wavenumbers due to a depolymerization phenomenon. Lucas et al. [264] presented that an increase in pH value (i.e., a decrease in the  $M_s$  ratio) favors depolymerization by breaking the Si-O-Si bonds to create Si-O $^-$  groups. As can be seen from Fig. 6-2a, the activator solutions with high  $M_s$  ratio ( $M_s=1.2$ ) presented a broader peak of transmission bands with higher intensity shifting the wavenumbers to higher values due to the contribution of different high  $Q$  species as compared to the solutions with low  $M_s$  ratio ( $M_s=0.4$ ). Thus, it can be concluded that the activator solutions with a lower  $M_s$  ratio,

irrespective of being SSA or SFA based, seems to be more depolymerized. Considering the same Ms case, generally, the SFA-based solutions had lower wavenumbers, showing the SFA-based solutions are more depolymerized as compared to SSA.

A slight trace of a shoulder was observed at around  $1070\text{ cm}^{-1}$  for SSA1.2 solution, indicating the presence of  $Q^3$  with 3 rings,  $Q^2$  with 4 rings and/or linear  $Q^2$  species in this solution [263]. On the other hand, SFA mixtures presented intensity peaks in the wavenumber region between  $1050 - 1170\text{ cm}^{-1}$ . The peaks between these wavenumbers are shown as the fingerprint of  $Q^3$  with 4 rings structure [263]. Based on the recorded intensity around  $1120\text{ cm}^{-1}$  it can be said that SFA1.2 has more  $Q^3$  with 4 rings structure as compared to SFA0.4. To understand the main reason for the existence of these peaks and its relation with possible undissolved silica fume in SFA solution, an FTIR scan was also carried out on the filtered solution (Fig. 6-2b). As can be seen from the enlarged Fig. 6-2b, the reason of this peak was the undissolved silica fume as the filtered solution SFA1.2\_F showed no peaks around  $1120\text{ cm}^{-1}$ . The impact of the undissolved amount of silica fume in SFA solution on the initial structuration and setting time is explained in detail in the further section based on this finding.



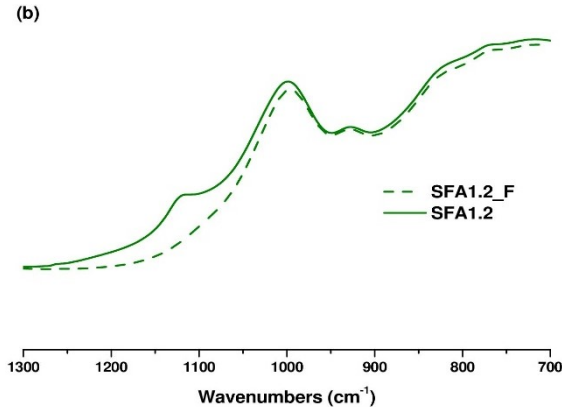


Fig. 6-2 FTIR spectra of (a) unfiltered SFA and SSA solution, (b) the comparison between unfiltered (SFA1.2) and filtered solution (SFA1.2\_F).

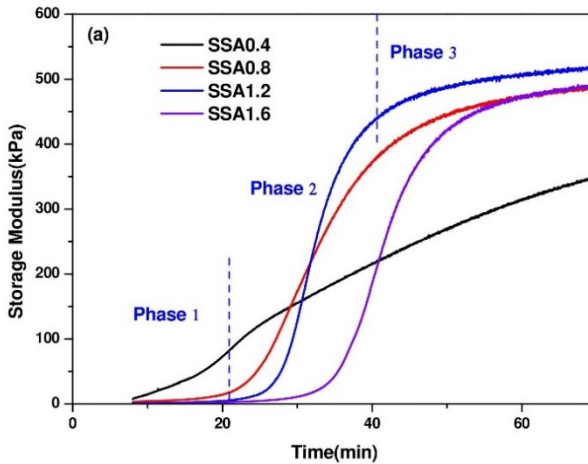
## 3.2 Rheology of AAS made with SFA and SSA

### 3.2.1 Structural build-up

A small amplitude oscillatory shear (SAOS) test was used to investigate the structural build-up process of AAS pastes at fresh state. In the SAOS test, as the applied excitation is sufficiently low and the samples are still within the LVER, the fresh samples can still be considered to be in non-destructive state [27]. Fig. 6-3 presents the structural evolution of AAS pastes activated by SSA and SFA activator solutions. In all diagrams, zero time indicates the first contact between GGBFS and the activator solution.

As shown in Fig. 6-3a, the structuration of the pastes activated by SSA0.4 increased more rapidly as compared to other SSA mixtures in the first 25 min, then the storage modulus of SSA0.4 mixture kept a constant growth rate. In contrast to SSA0.4, the evolution of storage modulus of other mixtures (SSA0.8, SSA1.2 and SSA1.6) consisted of the following three phases (the mentioned phases are shown for SSA1.2 in Fig. 6-3a as an example). In the first phase, the structural build-up was very low and constant and this was followed by a second phase where the storage modulus was rapidly increasing. After that, a decrease in the structural build-up was observed (Phase 3) due to reaching the torque capacity of the used rheometer. The high initial storage modulus of SSA0.4 mixture can probably be attributed to the fast initial dissolution of GGBFS and the formation of solid reaction products taking place simultaneously [47], [81] due to the higher alkaline environment provided by SSA0.4 activator and the more depolymerized structure as approved by FTIR results. The more depolymerized structure for the low- $M_s$  ratio case has already been reported by [105], [129] based on the liquid state  $^{29}\text{Si}$  NMR tests. The early reaction products formation, i.e. the higher initial storage modulus observed in the mixtures with low-

Ms value, can be explained by the presence of more depolymerized structures having lower activation energy as compared to highly polymeric structures. The monotonic increase in the storage modulus for SSA0.4 mixture (Fig. 6-3a) could be associated with the hindrance of further ion release to the environment due to the formation of initial reaction products covering the surfaces of the GGBFS grains. On the other hand, as shown in Fig. 6-3a, the AAS pastes activated by SSA having Ms value higher than 0.4 showed faster structuration after 30 min (Stage 2). The low structuration rate in the first 30 min can be associated with low Ca ion solubility from GGBFS due to the low-pH of high-Ms value activator environment [47]. Once enough ion types (mainly Ca and Al) reached a sufficient concentration in the solution over time, the possibility of encountering silicate ions that are already available in the solution increases [47]. Therefore, the structuration starts to accelerate due to the silica availability from the activator contributing to the C-A-S-H nucleation and gel growth [129]. This stage could be linked to the gradual gelation in the microstructure of the AAC as reported in the literature [265].



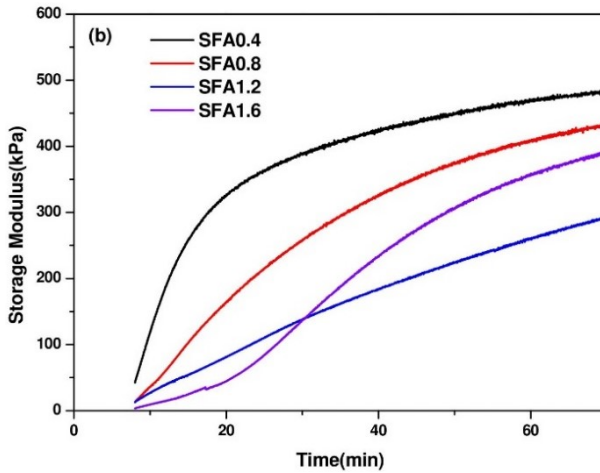
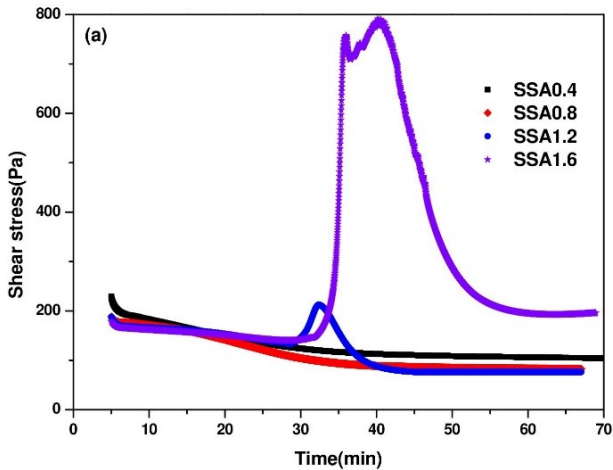


Fig. 6-3 Evolution of structural build-up of AAS mixtures (a) SSA-activated, (b) SFA-activated.

As seen in Fig. 6-3b, SFA mixtures exhibited significantly higher storage modulus as compared to corresponding SSA mixtures in the first 20 min. In particular, the structural evolution of the SFA0.4 mixture developed fiercely as compared to other SFA mixtures. As mentioned in Section 3.1, the SFA0.4 contains more depolymerized structures (Fig. 6-2a) available to take part in the reaction products formation quickly. For other SFA mixtures (SFA0.8, SFA1.2 and SFA1.6), due to the high amount of undissolved very fine silica fume particles, the colloidal attractive forces (i.e., van der Waals forces) between silica fume and GGBFS particles were more pronounced. As shown in Table 6-2, SFA contains a high amount of undissolved silica fume particles. Therefore, in addition to the effect of more depolymerized silicates on structuration, the flocculation of these undissolved particles, caused by the attractive colloidal forces, may play an important role in the higher structural build-up of SFA mixtures as compared to SSA. However, the increasing rate of structural build-up for SFA mixtures was also lower than that of SSA mixtures. This is probably because the further reactions of GGBFS were prevented by undissolved silica fume particles covering the surface of GGBFS grains. Another possible explanation as reported by Vance et al. [123], is that silica fume was more easily dissolved at the beginning of mixing and silica-based complexes were formed. These silica-based complexes might adsorb to the surface of the grains and serve as a superplasticizer due to a sort of steric repulsion. From the macroscopic point of view, it was obvious that the SFA-activated pastes tended to be more flowable. Particularly, it was observed that SFA1.2 could maintain its low structural build-up in the later stages, indicating its better workability retention.

### 3.2.2 Behaviour under high constant shear rate

The SSA and SFA mixtures were subjected to a high constant shear rate ( $200 \text{ s}^{-1}$ ) for 60 min to observe the evolution of shear stress as shown in Fig. 6-4. The shear stress started from a high initial value, and subsequently decreased to an equilibrium state. Some mixtures (SSA1.2 and SSA1.6) experienced an obvious shear stress peak related to the formation and break down of primary C-A-S-H gel. The shear stress curves of SSA1.2 and SSA1.6 exhibited a peak at around 33 and 40 min, respectively. These peaks could be related to the interaction between a higher concentration of Si in the pore solution and the calcium released from GGBFS [30], [31], [81]. Then the subsequent decreasing shear stress could be the indicator of the breakdown of the primary gel, which is attributed to the applying continuous shear energy. The primary gel formation plays an important role in setting times and workability of AAS [126]. Palacios et al. [30] also reported that prolonging the mixing times could delay the setting times of sodium silicate-activated AAS. It was found that SSA1.6 had a higher intensity shear stress peak than SSA1.2, indicating that more initial reaction products were formed. Also, the final shear stress at 70 min was higher than its initial shear stress, showing that some permanent structures were remained after structural breakdown due to the applied shear during the measurement time.



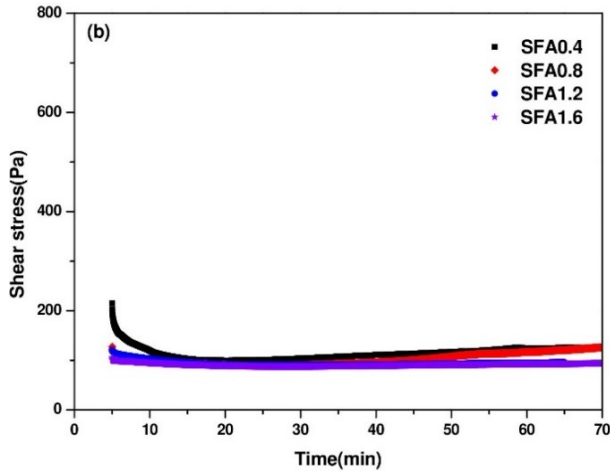


Fig. 6-4 Evolution of shear stress of AAS mixtures at high constant shear rate (200 s<sup>-1</sup>) (a) SSA-activated, (b) SFA-activated.

As can be seen from Fig. 6-4b, SFA mixtures reached to a stable flow and were kept at equilibrium state after the initial shear stress decay. There were no peaks in the shear stress history of the mixtures, indicating that there was no sufficient amount of reaction products to resist the applied shear during the measurement. Furthermore, SFA mixtures with varying  $M_s$  values had excellent workability retention under a high shear rate due to the ball-bearing effect of silica fume particles [266]. The better workability of SFA-based AAS mixtures explains their easy placing and compaction in practice.

### 3.2.3 Behaviour under shear cycles (Yield stress)

Fig. 6-5 presents the yield stress of AAS under eight successive shearing cycles. The yield stress values in Fig. 6-5 were determined by the down ramp of the flow curves fitting the Bingham model. The trend of SSA-activated mixtures was very similar to that subjected to the high constant shear rate previously presented. In SSA-activated mixtures, pastes with lower  $M_s$  value ( $M_s0.4$ ) exhibited higher yield stress without any increase with time. This is parallel with the results of storage modulus. However, the other three mixtures showed a peak of yield stress with different intensities with the time elapsing, probably owing to the formation of primary C-A-S-H gel [31]. From Fig. 6-5a, it was found that the increase of yield stress of SSA1.6 was delayed as compared to SSA1.2 and SSA0.8. This might be attributed to the higher  $M_s$  value prolonging the dissolution stage due to its relatively mild alkaline environment.

Concerning the SFA mixture, the phenomenon was different. Basically, all the SFA mixtures remained at a relatively low yield stress level (below 50 Pa), explaining their

good workability during the shearing cycle. This is also in agreement with the previous results of a constant high shear rate.

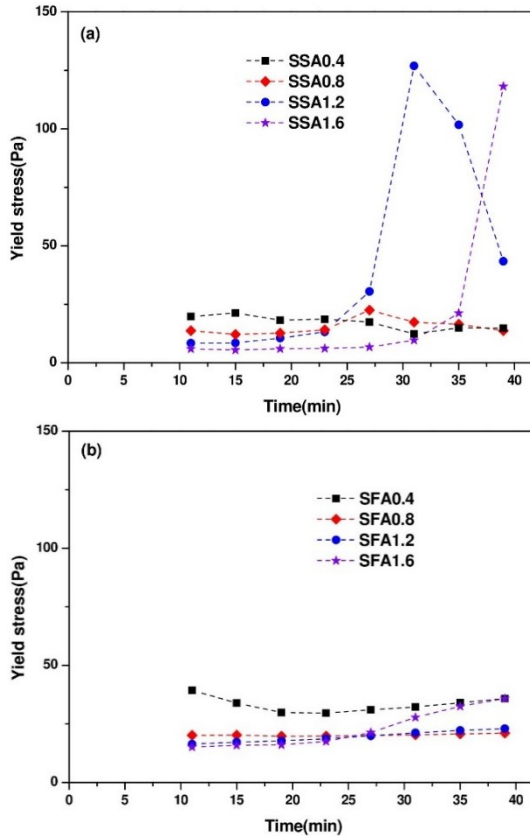


Fig. 6-5 Evolution of yield stress of AAS mixtures during the shear cycle (a) SSA-activated, (b) SFA-activated.

### 3.3 Setting times of AAS

The Vicat setting times of SSA and SFA mixtures are given in Fig. 6-6. With an increase of Ms value, SSA mixtures tend to set more quickly, supported by SAOS test results of the increasing rate of structural build-up beyond 20 min. The presented results in Fig. 6-6 for SSA-activated mixtures were in agreement with the results of Chang [162], stating that the setting times decreased as the alkali activator dosage (as the sum of the  $\text{SiO}_2$  and  $\text{Na}_2\text{O}$  concentrations in the solution) increases. Previous studies [162], [267] have also concluded that the increasing sodium silicate dosage led to a higher concentration of  $[\text{SiO}_4]^{4-}$ , which induced a higher reaction rate.

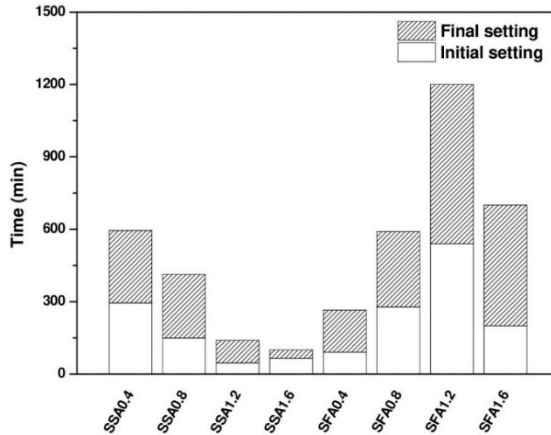


Fig. 6-6 Initial and final setting times of SSA and SFA mixtures.

However, the setting time trend in SFA mixtures was the opposite such that SFA mixtures with high Ms value generally had a longer setting time for a Ms value increase. Particularly, SFA1.2 exhibited extremely extended setting times (the initial and final setting times reached 540 min and 1200 min, respectively) as compared to the other mixtures. Therefore, it can be concluded that it is possible to produce AAS having more reasonable, or very long if it is specifically desired, setting times by using SFA instead of SSA. With an increase of Ms value, more undissolved silica fume particles may be adsorbed on the GGBFS surfaces through electrostatic interaction [123]. To confirm this adsorption and its effect on setting time, the setting times of the mixture prepared by the filtered SFA activator (SFA1.2\_F) were determined. The initial and final setting times of GGBFS and SFA1.2\_F activator were 126 min and 656 min, respectively, which were significantly shorter than SFA1.2 mixture prepared by unfiltered SFA activator. Therefore, it was confirmed that the extended setting time of SFA1.2 mixture was related to the undissolved silica fume particles.

As can be seen from Table 6-2, most of the silicates are dissolved by  $\text{OH}^-$  from NaOH solution in case of SFA activator with low Ms value. These silicates may have reacted with the dissolved  $\text{Ca}^{2+}$  from GGBFS to form C-A-S-H in the earliest time of the reaction, resulting in a shorter setting time. In Fig. 6-2a, the transmission band of SFA0.4 also showed lower wavenumbers of the peak than that of SSA0.4, indicating that SFA0.4 had more depolymerized silicates. These depolymerized silicates are more reactive due to their lower activation energies [264], leading to the shorter setting times of SFA0.4.

### 3.4 Mechanical properties, reaction kinetics and drying shrinkage

The mechanical properties, reaction kinetics and drying shrinkage of AAS were

investigated on SFA1.2 and SSA1.2 mixtures. As shown before, SFA1.2 mixture presented a satisfying setting time and rheological results, with better structural build-up evolution, flowability and workability retention properties under different rheological states. For comparison purpose, the results of this mixture were compared with the results of SSA1.2. In addition, the lower amount of sodium silicates in activator solutions having Ms value lower than 1.5 are more beneficial for the production of low carbon footprint AAC concrete. Additionally, the highest mechanical and durability performances have been reported in the literature with solutions having an Ms value between 1.0-1.5 [268].

### 3.4.1 Mechanical properties

The flexural and compressive strength of SSA1.2 and SFA1.2 mortar samples are presented in Table 6-3. As can be seen from Table 6-3, the early and later age mechanical performances of SFA1.2 were higher than SSA1.2. Compressive and flexural strength of SFA1.2 at 2 days were found approximately 20% and 17% higher than that of SSA1.2, respectively. For 28 days, these ratios were 6% and 17%, respectively. A previous study [257] reported that using silica fume activators in AAS could promote the formation of a highly dense structure (mainly C-A-S-H gel), enhancing the compressive strength of the mixture. Zivica [143] also reported that AAS activated by SFA had higher compressive strength and good resistance to the permeability of water due to its densified microstructure. As known, since the flexural strength of cementitious materials is generally more sensitive to micro-cracks than the compressive strength, the better flexural strength of SFA1.2 mixtures may be associated to reduced micro-cracking of SFA1.2 as compared to SSA1.2 as to be discussed in section 3.5.

Table 6-3 Flexural strength and compressive strength of SSA1.2 and SFA1.2 mixtures.

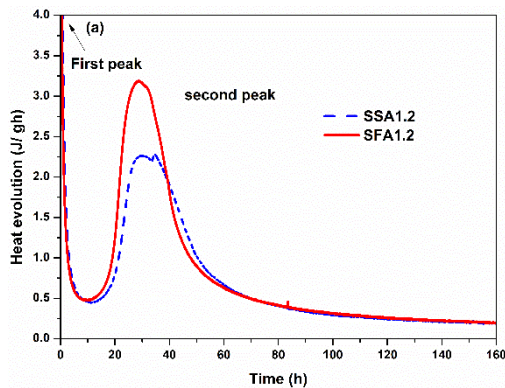
Mixture	Flexural strength (MPa)			Compressive strength (MPa)		
	2 days	7 days	28 days	2 days	7 days	28 days
SSA1.2	4.1 (0.26)*	8.1 (0.37)	8.6 (0.51)	33.3 (1.16)	65.1 (0.88)	76.2 (1.70)
SFA1.2	4.8 (0.94)	8.9 (0.13)	10.1 (0.67)	40.0 (0.58)	67.7 (2.08)	80.5 (1.28)

\*The values given in parenthesis show the standard deviation.

### 3.4.2 Reaction kinetics

Fig. 6-7 shows the heat evolution and the cumulative heat release of SSA1.2 and SFA1.2 mixtures. The known five distinctive stages are observed in the heat of

hydration evolution of ordinary Portland cement (PC): dissolution, induction, acceleration, deceleration and steady-state [269]–[271]. Similar to PC, the first initial peaks shown in Fig. 6-7a were related to wetting of the particles, dissolution of GGBFS (the breakdown of Me-O and T-O bonds of GGBFS) and also partly to the formation of the initial reaction products from the dissolved units such as Si, Ca and Na in the solution [81], [207], [272]. The second peaks were shown at around 30 h for both mixtures and the existence of this second peak can be associated with the massive reaction products formation [134], [271]. In the first 20 hours, a similar trend was recorded in the heat evolution for both mixtures, but the cumulative heat release of SSA1.2 was slightly higher than SFA1.2. This could be related to the earlier formation of the reaction product for SSA1.2 as observed in storage modulus measurements. However, it was obvious that the maximum heat evolution around 30 h (the second peaks in the Fig. 6-7a) was significantly higher for SFA1.2 mixture as compared to SSA1.2. In addition, the acceleration stage of SFA1.2 was slightly earlier than SSA1.2. Meanwhile, the cumulative heat of SFA1.2 exceeded SSA1.2 beyond 24 h, meaning that more reaction products formed in SFA1.2. Thus, the SFA usage may have resulted in a dense and rigid microstructure as reported by [257]. This is also consistent with the higher flexural and compressive strength of SFA1.2.



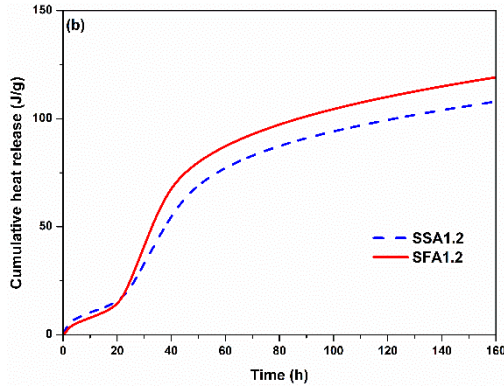


Fig. 6-7 Reaction kinetics of SSA1.2 and SFA1.2 (a) Heat evolution, (b) Cumulative heat release.

### 3.4.3 Drying shrinkage of AAC mixtures

The drying shrinkage of SSA1.2 and SFA1.2 is presented in Fig. 6-8. The drying shrinkage of SFA1.2 was lower than that of SSA1.2 during the whole measuring time up to 70 days. No visible cracks were observed on the surface of the samples during the measurement time. More than half of the drying shrinkage occurred in the first 20 days, and only slight drying shrinkage could be observed for both mixtures after 28 days. The drying shrinkage of SSA1.2 at 70 days was approximately 25% higher than that of SFA1.2. This is probably due to the pore-refining effect of undissolved silica fume particles in SFA1.2 activator. Indeed, the MIP results (to be discussed in Section 3.5) also confirmed that SFA1.2 has less mesopores as compared to SSA1.2.

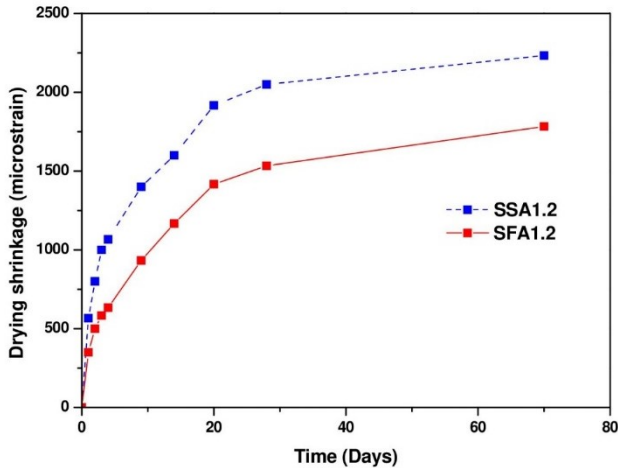


Fig. 6-8 Drying shrinkage of SSA1.2 and SFA1.2.

### 3.5 Microstructure of AAS

---

Fig. 6-9 shows SEM secondary electron (SE) and backscattered electron (BSE) images of SSA0.4, SSA1.2 and SFA1.2 pastes at the age of 28 days. The highlight white regions in SEM (BSE) images presented in Fig. 6-9 represent the unhydrated slag grains, the grey regions between the particles indicate reaction products and the black regions show the pores and micro-cracks. It is obvious that the SSA0.4 has a very distinct microstructure when compared to the other two mixtures. In Fig. 6-9b (SSA0.4-BSE), a porous and rough microstructure with larger unhydrated GGBFS grains could be identified. However, SSA1.2 and SFA1.2 showed a well-packed microstructure with very massive reaction products, indicating that the reaction degree of SSA1.2 and SFA1.2 are higher than SSA0.4. More micro-cracks could be observed in SSA1.2 and SFA1.2 as compared to SSA0.4. These micro-cracks can be attributed to the tensile stresses generated by autogenous or chemical shrinkage as the specimens were cured under moisture conditions. This is in agreement with Puertas et al. [71] and Aydin et al. [198], who reported that the crack intensity in the matrix phase increases with the increase of  $M_s$  values. However, more and wider crack formations were observed in SSA1.2 as compared to SFA1.2. This may explain the slightly better mechanical properties of SFA1.2 as compared to SSA1.2 (Table 6-3).

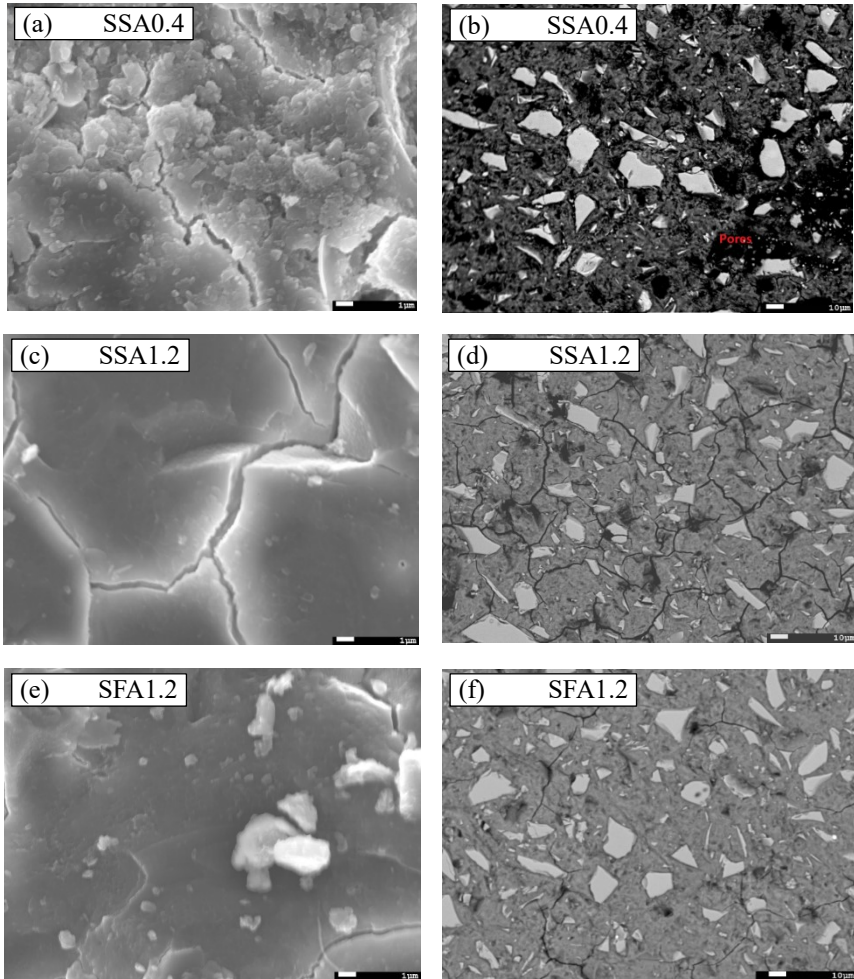


Fig. 6-9 SEM images of AAS pastes (left side SE, right BSE images).

Table 6-4 presents the average EDX results of 10 points obtained from different regions of the matrix. EDX analysis showed that the main reaction product in all mixtures is Na-incorporated C-A-S-H. The Ca/Si ratio of SSA0.4 (1.95) was significantly higher than SSA1.2 (1.21) and SFA1.2 (0.86). In other words, Ca/Si ratio decreased by an increase in Ms value. This is in agreement with the findings provided by Aydın et al. [198] and Puertas et al. [210]. Previous studies concluded that the binding property of C-S-H structure and the mean chain length of C-S-H increased with a decrease in the Ca/Si ratio [198], [210], [273]. SFA1.2 exhibited relatively lower Ca/Si ratio as compared to SSA1.2, meaning that SFA1.2 has a more dense and compact microstructure with a higher degree of hydrated parts of GGBFS grains as also observed in SEM pictures (Fig. 6-9c-d vs. Fig. 6-9e-f). These findings and observations confirm better mechanical properties of SFA1.2 as compared to SSA1.2.

This is due to positive effect of SFA on the intensification of C-A-S-H formation and the densification of the pore structure of the activated binder [267].

Table 6-4 Reaction degrees of GGBFS and average atomic ratios obtained by SEM-BSE.

Mixture	Reaction degree (%)	Ca/Si	Al/Si	Na/Si	Mg/Si	Al/Ca	Na/Al
SSA0.4	72.0 ± 0.2	1.95	0.35	0.68	0.29	0.22	1.63
SSA1.2	79.2 ± 0.1	1.21	0.31	0.47	0.21	0.28	1.84
SFA1.2	82.3 ± 0.4	0.86	0.36	0.52	0.30	0.42	1.50

The Al/Si ratio of SSA0.4 mixture was higher than that of SSA1.2 as parallel to the findings of Puertas et al. [71]. SFA1.2 also exhibited a higher Al/Si ratio, meaning that more Al were incorporated into C-A-S-H structure. In this study, the EDX analyses revealed that C-A-S-H structure consists of 4.42%, 4.51% and 5.17% Al elements by mass in SSA0.4, SSA1.2 and SFA1.2 mixtures, respectively. The substitution of Si by Al in tetrahedral positions in the silicate chain has already been reported by [274] and [210], [275]. As for sodium, EDX analyses revealed that C-A-S-H structure consists of 4.9%, 5.7% and 6.2% Na element by mass in SSA0.4, SSA1.2 and SFA1.2 mixtures, respectively. The uptake of sodium is to compensate the charge imbalance created by the substitution of Al<sup>3+</sup> for Si<sup>4+</sup> [210]. Magnesium was found 2.8%, 2.6% and 3.8% by mass in SSA0.4, SSA1.2 and SFA1.2 mixtures, respectively. The magnesium might participate in the formation of the hydrotalcite type sub-micrometer phase as reported previously by Wang and Scrivener [276]. Song and Jennings [69] also concluded that the hydrotalcite would form at a later stage when a high degree of GGBFS hydration was reached.

The reaction degree of GGBFS was evaluated by image analysis on BSE images and was shown in Table 6-4. As shown in Table 6-4, the reaction degree of SSA mixtures increased from 72% to 79.2% by the increase of Ms value from 0.4 to 1.2. At the Ms value of 1.2, a higher reaction degree was found for SFA mixtures as compared to the SSA. These findings support the better mechanical performance of SFA1.2 as compared to SSA1.2 (Table 6-3). Furthermore, the SSA0.4 showed the lowest reaction degree as compared to the other two mixtures, this is probably due to relatively lower amount of silicates provided by the activator solution in this mixture, leading to less reaction products [80].

Fig. 6-10 shows the pore size distribution of some selective AAS mixtures. The pore size classification according to the International Union of Pure and Applied Chemistry

(IUPAC) system [277] are also shown in Fig. 6-10. In the case of SSA activator, the envelope of SSA1.2 exhibited less macropores than SSA0.4, but more mesopores and higher capillary porosity [80], [278]. The capillary pores consists of mesopores, macropores, and the water-filled space existing between original cement grains [278]. SFA1.2 showed a lower porosity as compared to SSA1.2, and the amount of mesopores was also lower than SSA1.2. Shrinkage under various conditions depends on the loss of water from mesopores and the size of the macropores, influencing the easiness of evaporation of water from the mesopores [278]. Therefore, the lower total volume of mesopores in SFA1.2 may explain the lower drying shrinkage of SFA1.2 compared to SSA1.2.

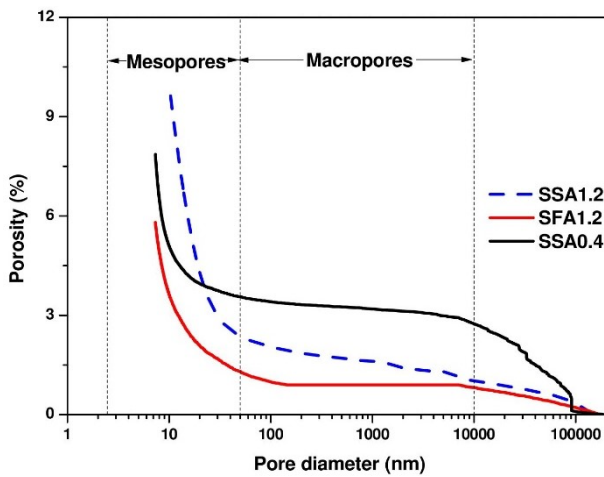


Fig. 6-10 Pore size distribution of AAS.

### 3.6 Comparison of carbon dioxide emission and cost of activator solutions

One significant advantage of AAS is its lower carbon footprint as compared to PC. The main contributor to carbon dioxide ( $\text{CO}_2$ ) emission and also the cost of AAS is the activator solution. Since the AAS produced with SFA1.2 and SSA1.2 have comparable early and later age mechanical properties, a comparison in terms of  $\text{CO}_2$  emission and price have been performed. The precursor and fine aggregate amounts of AAS produced with SFA1.2 and SSA1.2 are equal to each other, so these comparisons were performed only for the activator solutions. The unit price of the activator solution ingredients provided from BRENNTAG company (Belgium) and Elkem (The Netherlands) and the  $\text{CO}_2$  emissions associated with their manufacturing process [5], [279], [280] are given in Table 6-5. The amounts of liquid sodium silicate, silica fume and NaOH to produce  $1 \text{ m}^3$  of AAS mortar with SSA1.2 and SFA1.2 are given in Table 6-5 with the calculated  $\text{CO}_2$  emissions and price. As shown in Table 6-5, total  $\text{CO}_2$  emissions associated with SFA1.2 activator were significantly lower

than that of SSA1.2, and the cost of SFA1.2 solution is also lower than SSA1.2.

Table 6-5 Comparison of CO<sub>2</sub> emissions and cost of activator solutions

Ingredients	Price (Euro/ton)	CO <sub>2</sub> Emissions (ton/ton)	For 1 m <sup>3</sup> AAS mortar production					
			Material amounts (kg)		Cost (Euro)		CO <sub>2</sub> Emissions (ton)	
			SSA1.2	SFA1.2	SSA1.2	SFA1.2	SSA1.2	SFA1.2
Liquid sodium silicate	840	1.514	94.4	---	79.3	---	0.143	---
Silica fume	700	7×10 <sup>-9</sup>	---	28	---	19.6	---	0.000
NaOH	1100	1.915	7.3	29.5	8.0	32.5	0.014	0.056
Total	---	---	---	---	87.3	52.1	0.157	0.056

#### 4. Conclusion

---

This Chapter investigates the effects of sodium silicate-based activator (SSA) and silica fume based activator (SFA) with different  $M_s$  values on the rheological and microstructural properties of alkali-activated GGBFS mixtures. Based on the findings, the following conclusions can be drawn:

1. SFA contains more depolymerized structures as compared to SSA at the same  $M_s$  value according to the FTIR results. Both activators were found to be more depolymerized by the decrease in  $M_s$  value.
2. The structuration rate of SFA mixtures was generally lower than for SSA mixtures. Under the high constant shear rate of  $200 \text{ s}^{-1}$ , SFA mixtures exhibited a low and steady-state shear stress with time, indicating the lack of reaction product formation during the measurement. However, a sudden increase followed by a gradual decrease in shear stress was observed in SSA1.2 and SSA1.6 mixtures, indicating the C-A-S-H formations. SFA and SSA mixtures subjected to shear cycles had a similar rheological response with the mixtures exposed to high constant shear rate.
3. The setting times of SSA mixtures decreased with the increase of  $M_s$  value. Conversely, a higher  $M_s$  value prolonged the setting times of SFA mixtures; in particular, the setting times of the SFA1.2 mixture were extended significantly. The SSA-activated mixtures with higher  $M_s$  values had a very short setting time that could be problematic in concrete practice. On the other hand, it was shown that the initial and final setting times of AAS could be extended up to 5 hours by the use of SFA without any detrimental effects on the early and later age strength.
4. The SFA1.2 mixture exhibited better workability and mechanical performance with lower drying shrinkage as compared to the SSA1.2 mixture. Regarding the microstructure analysis, SFA1.2 and SSA1.2 showed a well-packed microstructure with a higher reaction degree of GGBFS as compared to SSA0.4. In addition, SFA1.2 exhibited fewer micro-cracks than SSA1.2. The EDX analysis showed that SFA1.2 had a lower Ca/Si ratio compared to SSA1.2 and SSA0.4.
5. SFA seems to be more beneficial and possibly a better solution for practical applications as compared to SSA having faster setting and higher drying shrinkage. In addition, the lower cost and  $\text{CO}_2$  emission of SFA make this activator a more economical and sustainable solution than SSA.

## **Part IV**

---

### **Influence of mineral additions on the rheological and setting behaviour of AACs**



**Chapter 7 Effects of mineral addition on rheology in a binary system**

---

In this chapter, the effects of supplementary materials on the rheology, structural build-up, early age reaction and microstructure of AAS are studied.

## 1. Introduction

---

To meet different engineering requirements, the rheology and structural build-up behaviour of AAC concrete are of great importance. Structural build-up behaviour of AAC, an important indicator to characterize the early age reaction of cementitious materials, is generally a result of the combination of physical and chemical processes [47], [111]. The early structural build-up of cementitious materials is critical because it impacts the formwork pressure created by fresh concrete, the stability of the concrete after casting, the 3D printability of concrete, and the formation of lift lines in multilayer casting. Higher structural build-up rates are preferred in a variety of concrete applications, including pressure reduction of formwork, fresh state stability, slip form paving and 3D printing concrete; however, lower structural build-up rates are generally desired in other instances, such as multilayer casting applications to increase the bond strength between the layers [27], [28]. Previous studies have elucidated that the addition of supplementary material can significantly change the structural build-up behaviour of cementitious materials. Kawashima et al. [160] pointed out that the early structural build-up of Portland cement can be increased by adding purified attapulgite clays. Dai et al. [159] also found that using purified attapulgite clays can also increase the structural build-up of alkali-activated slag/fly ash pastes at an early age. Rahman et al. [281] found that the thixotropy of cement can be enhanced by the addition of silica fume, limestone powder and fly ash due to their strong nucleation properties. Besides, the activator type can also influence the structural build-up behaviour of AAC. Dai et al. [47] reported that the sodium hydroxide-activated slag/fly ash pastes showed a very higher initial storage modulus as compared to sodium silicate-activated pastes, while the latter one showed a rapid increase in structural build-up following the long induction period.

In this Chapter, the effects of supplementary materials addition and activator type on the rheology, structural build-up, early reaction kinetics and microstructure have been studied. The non-destructive ultrasonic pulse velocity was used to measure the solidification process of AAC, and combined with the calorimetric measurements to clarify the reaction stages. The rheology and structural build-up of AAC pastes have also been evaluated by rotational and oscillatory rheometry. Finally, the microstructure and gel composition of AAC pastes has been analyzed by the scanning electron microscope/energy-dispersive X-ray spectroscopy.

## 2. Experimental program

---

### 2.1 Mixture design

---

The mixture designs of AAC are given in Table 7-1. The activator solutions were prepared with five Ms values of 0, 0.4, 0.8, 1.2 and 1.6 with a constant Na<sub>2</sub>O content of 5% and water to solid binder ratio of 0.37. It should be noted that the activator solution with Ms0 is the pure sodium hydroxide activator, the alkaline solution with

Ms1.6 is the pure sodium silicate activator, other activator solutions are the mix of sodium hydroxide and sodium silicate in required amounts. These activator solutions were prepared one day before to ensure the complete dissolution of the sodium hydroxide prior to mixing. The pH values of the activators were measured by a pH meter; however, it should be noted here that using a pH meter to measure the pH of the activator solutions with extreme alkali ion concentration may result in some errors due to the extremely high alkali ion concentrations and the presence of aqueous silicates in the alkaline solutions [105]. Previous literature has been reporting that the sodium silicate activator solution contains silicate monomers, dimers, trimmers and other high-order units [259], and that the decrease in Ms value is more favorable to the presence of more depolymerized silicate units [105]. To investigate the effects of the various supplementary materials on the rheological performance and microstructural evolution of AAC, the GGBFS was replaced with 30% silica fume (SF), limestone powder (LSP), fly ash (FA) and cements (PC), respectively.

Table 7-1 Mixture designs of AAC.

Mixture	GGBFS (% by mass)	SF (% by mass)	LSP (% by mass)	FA (% by mass)	PC (% by mass)	W/sb*	Ms	SiO <sub>2</sub> %	Na <sub>2</sub> O %	pH value of activator solution
Ms0_30SF70Slag	70	30				0.37	0	0	5	13.90
Ms0_30LSP70Slag	70		30			0.37	0	0	5	13.90
Ms0_30FA70Slag	70			30		0.37	0	0	5	13.90
Ms0_30PC70Slag	70				30	0.37	0	0	5	13.90
Ms0.4_30SF70Slag	70	30				0.37	0.4	2	5	13.78
Ms0.4_30LSP70Slag	70		30			0.37	0.4	2	5	13.78
Ms0.4_30FA70Slag	70			30		0.37	0.4	2	5	13.78
Ms0.4_30PC70Slag	70				30	0.37	0.4	2	5	13.78
Ms0.8_30SF70Slag	70	30				0.37	0.8	4	5	13.73
Ms0.8_30LSP70Slag	70		30			0.37	0.8	4	5	13.73
Ms0.8_30FA70Slag	70			30		0.37	0.8	4	5	13.73
Ms0.8_30PC70Slag	70				30	0.37	0.8	4	5	13.73
Ms1.2_30SF70Slag	70	30				0.37	1.2	6	5	13.72
Ms1.2_30LSP70Slag	70		30			0.37	1.2	6	5	13.72
Ms1.2_30FA70Slag	70			30		0.37	1.2	6	5	13.72
Ms1.2_30PC70Slag	70				30	0.37	1.2	6	5	13.72
Ms1.6_30SF70Slag	70	30				0.37	1.6	8	5	13.45
Ms1.6_30LSP70Slag	70		30			0.37	1.6	8	5	13.45
Ms1.6_30FA70Slag	70			30		0.37	1.6	8	5	13.45
Ms1.6_30PC70Slag	70				30	0.37	1.6	8	5	13.45

\*The sum of GGBFS, SF, LSP, FA, PC and the dry part of the activator solution are

considered as the binder.

## 2.2 Sample preparation

---

The following procedure was used in the paste sample preparation: First, the activator solution was poured into the Hobart mixer bowl, then the dry blended binders were added and mixed at low speed ( $140 \pm 5$  rpm) and high ( $285 \pm 5$  rpm) for 90s each.

## 2.3 Protocol for flow curves

---

Fig. 7-1 presents the shear protocol. After the pre-shear of the mixture at 600 rpm for 60 s and a rest of 30 s, the shearing speed of the rotor was 3/6/10/20/30/60/100/200/300/600 rpm for the step-wise increasing part of the shear protocol, followed by the same values of the rotor to provide the step-wise decreasing part, each step continued for 20 s. The dynamic yield stress and plastic viscosity were determined by the equilibrium part of the descending steps of the flow curve. Bingham model (Eq. (7-1)) was used to fit the downward curves of AAC pastes.

$$T = G + HN \quad (7-1)$$

where  $T$  is the torque in  $\text{mN}\cdot\text{m}$ ,  $G$  is a variable linked to yield stress in  $\text{mN}\cdot\text{m}$ ,  $H$  is a variable associated with plastic viscosity in  $\text{mNm}\cdot\text{s}$ ,  $N$  is the speed of rotation in rpm. The Reiner-Riwlin equations were applied to transform the torque and rotational velocity data into fundamental rheological parameters (Eq. (7-2) for dynamic yield stress and Eq. (7-3) for plastic viscosity) for the Bingham model.

$$\tau_0 = \frac{\left(\frac{1}{R_1^2} - \frac{1}{R_2^2}\right)}{4\pi h \ln\left(\frac{R_2}{R_1}\right)} G \quad (7-2)$$

$$\mu = \frac{\left(\frac{1}{R_1^2} - \frac{1}{R_2^2}\right)}{8\pi^2 h} H \quad (7-3)$$

where  $\tau_0$  is the dynamic yield stress (Pa),  $\mu$  is the plastic viscosity ( $\text{Pa}\cdot\text{s}$ ),  $R_1$  is the vane radius (mm),  $R_2$  is the inner cup radius (mm),  $h$  is the vane height (mm),  $G$  is the intercept of the curve with the T-axis ( $\text{mN}\cdot\text{m}$ ),  $H$  is the inclination of the straight line in the T-N graph.

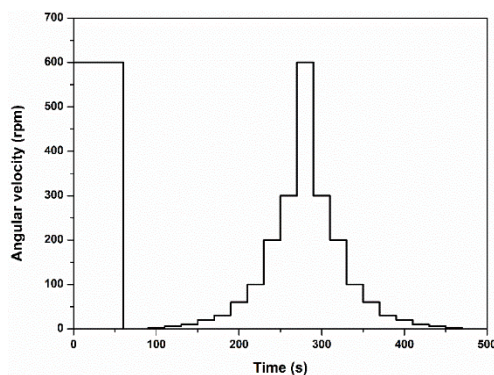


Fig. 7-1 Shear protocol used for flow curve.

### 3. Results and discussions

#### 3.1 Isothermal Calorimetric results of AAC pastes

Fig. 7-2 illustrates the isothermal calorimetric curves of AAC pastes with different supplementary materials. As well known, five distinctive stages are observed for AAC: dissolution, induction, acceleration, deceleration and steady-state stages, respectively [271], [276]. In this study, the AAC pastes generally showed the same trend, exhibiting at least two peaks during the measurement time. The first peak is the dissolution peak which is linked to the wetting of particles, the dissolution of precursors, and partly due to the formation of some initial reaction products [16], [110], [207]. The second one is the main exothermal peak, which was associated with the main reaction products formation and microstructural development [16], [51], [110], [152]. With a decrease of the Ms value of the activator solutions, the main exothermal peak occurred earlier with higher intensity, and the induction period was shortened. Fig. 7-2a and b present the heat flow and cumulative heat release of AAC pastes with different supplementary materials activated by Ms0 (sodium hydroxide activator solution), respectively. Generally, the occurrence of the second peak for the mixture with the addition of SF, LSP and FA were very similar, and the mixture with SF addition exhibited the highest second peak intensity, which was followed by LSP and FA. However, in the case of PC addition (Ms0\_30PC70Slag), a small additional exothermal peak was observed 2h after the dissolution peak, while the main exothermal peak was seen at 10 h. As shown in Fig. 7-2b, the mixture Ms0\_30SF70Slag exhibited the highest cumulative heat release during most of the measurement time, reaching 146 J/g at the age of 7d. The cumulative heat release of Ms0\_30PC70Slag reached a similar value (145 J/g) with Ms0\_30SF70Slag at the age of 7d. The mixtures with the addition of LSP and FA presented almost the same cumulative heat release curves during the measurement time, showing 135 J/g, at the end of the measurement time.

Fig. 7-2c and d present the heat flow and cumulative heat release curves of AAC pastes activated by Ms0.4 (sodium silicate and sodium hydroxide activator solution), respectively. All mixtures showed an additional peak between the dissolution peak and the main acceleration peak. Previous studies have also reported that the appearance of an additional peak before the induction period depends on the activator dosage, slag activity and hydration temperature [271]. However, this additional peak and dissolution peak appeared very close and maybe merged into one peak for the mixture with the addition of PC activated by Ms0.8, Ms1.2 and Ms1.6 due to higher silicate concentration and high reactivity of PC. The additional peak of the mixture Ms0.4\_30PC70Slag showed much higher intensity than that of Ms0\_30PC70Slag. This is possibly because the calcium ions dissolved from Portland cement may quickly interact with silicates originating from the activator solution to form initial reaction products [282] and, maybe up to some extent, the alkali substituted C<sub>3</sub>A conversion to the ettringite [283] and an instant formation of nano-size ettringite crystals on the surface of cement grains [284]. As a result, the heat release for the mixture Ms0.4\_30PC70Slag was enhanced at an early age. As for the other three mixtures activated by Ms0.4, the trend was similar to the case of Ms0: the occurrence of the main exothermal peak with a higher intensity was earlier for the mixture Ms0.4\_30SF70Slag, followed by Ms0.4\_30LSP70Slag and Ms0.4\_30FA70Slag. Regarding the cumulative heat release, the mixture Ms0.4\_30PC70Slag presented the highest cumulative heat release during the whole measurement time, showing 157 J/g at the age of 7 d. The other three mixtures with the addition of SF, LSP and FA showed a cumulative heat release at the age of 7d of 142, 131, 135 J/g, respectively.

The heat flow and cumulative heat release curves are given in Fig. 7-2e and f, respectively, for the mixtures with an Ms value of 0.8 (sodium silicate and sodium hydroxide activator solution). The main exothermal peak of the mixture Ms0.8\_30PC70Slag appeared earlier as compared to the case in Ms0 and Ms0.4. In other words, the induction period was shortened for the mixture Ms0.8\_30PC70Slag. By contrast, the induction period of the other three mixtures was prolonged as compared to that of Ms0 and Ms.0.4. Similar to the Ms0 and Ms0.4 cases, the mixture Ms0.8\_30PC70Slag showed the main exothermal peak earlier than the LSP and FA incorporated mixtures. Regarding the cumulative heat release, the mixture Ms0.8\_30PC70Slag always presented the highest cumulative heat as compared to the other three mixtures, releasing 147 J/g at the end of the measurement. The other three mixtures showed the same cumulative heat release of 135 J/g at the age of 7d. But it should be noted that the heat release rate of Ms0.8\_30PC70Slag was high in the first 12 hours but low at the later ages.

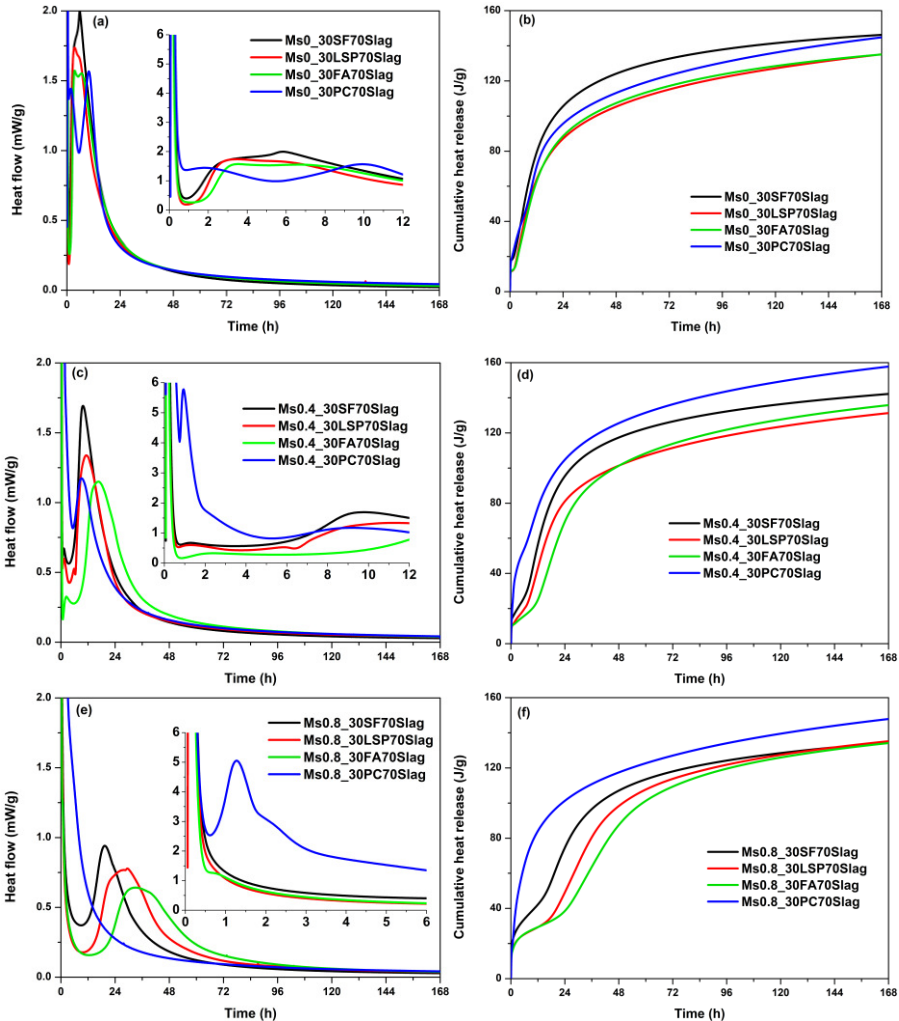
Fig. 7-2g and h illustrate the heat flow and cumulative heat release curves of AAC pastes activated by the activating solution with Ms1.2 (sodium silicate and sodium hydroxide activator solution, respectively). It should be noted that the mixture with the addition of PC still showed the highest intensity of the main exothermal peak and

cumulative heat release (137 J/g at the age of 7d) as compared to other mixtures. However, the mixture with the addition of SF showed the longest induction period as compared to the other three mixtures, which was different from the cases of Ms0, Ms0.4 and Ms0.8. The cumulative heat release for the mixture with the addition of SF, LSP and FA was almost the same at the age of 7d, which was around 123 J/g.

Fig. 7-2i and j exhibit the heat flow and cumulative heat release of AAC pastes activated by Ms1.6 (sodium silicate activator solution), respectively. In general, the trend of the heat flow evolution for these four mixtures activated by Ms1.6 was very similar to the case of Ms1.2. However, the additional peak for SF, LSP and FA incorporated mixtures activated by Ms1.6 was much more obvious than the case of Ms1.2, where the additional peaks were merged with the dissolution peaks. As for the cumulative heat release, the mixture with the addition of SF, LSP, FA and PC showed 111, 108, 108 and 144 J/g, respectively.

In this study, LSP incorporated pastes always showed an earlier main exothermal peak with a higher intensity as compared to the pastes containing FA regardless of the type of activator solution. This is possibly because the finer LSP with a BET surface area of 4.43 m<sup>2</sup>/g can provide more nucleation sites to promote more precipitation and growth of the reaction products as compared to FA (BET surface area 1.67 m<sup>2</sup>/g), thereby shortening the induction period and increasing the intensity of the main exothermal peak. It should be mentioned that according to Fig. 3-1 the particle size distribution of LSP and FA seems similar to each other, but the finer proportion of LSP ( $d_{10} = 0.21 \mu\text{m}$ ) is significantly higher than FA ( $d_{10} = 1.26 \mu\text{m}$ ). Previous studies also observed the same phenomena [110], [152]. SF incorporated mixtures even showed a shorter induction period and a higher intensity of the main exothermal peak as compared to the mixture with LSP and FA addition when the activator solution had a Ms value of 0, 0.4 and 0.8. Previous studies [285] reported that the addition of SF can increase the reactivity of slag, causing the reaction of the Al in the slag with the SF. Besides, SF, normally consisting mostly of amorphous phases, has significantly higher reactivity than FA which consists of amorphous and crystalline phases [285]. As a result, the alkaline activator reacted more favorably with SF rather than with FA. Moreover, due to the super high specific surface of SF as compared to LSP and FA, the nucleation effect of SF is more dominant [286]. However, this phenomenon was reversed when a higher silicate concentration was used as activator solution (Ms1.2 and Ms1.6). The intensity of the main exothermic peak and induction period of mixture with addition of SF was decreased and prolonged, respectively, as compared to the mixture with LSP and FA. The reaction mechanism behind this observation is very complicated, and the most plausible explanation could be the following: In the presence of the activator solution with lower Ms and higher pH, the SF is dissolved strongly in the beginning and silica-based complexes are formed stronger than in case of using the activator with higher Ms and lower pH [111], [256]. Due to the strong dissolution of SF, an oversaturation is reached very quickly and intense precipitation and the formation of reaction products occurred earlier. Besides, the fastest reaction

process was observed for the mixture with PC addition in the case of Ms values exceeding 0.8. This is probably due to both the PC and slag showing strong reactivity during the measurement time [282], [287], [288]. In this study, the highest cumulative heat release was observed in the mixture with PC addition regardless of the Ms value of the activator solution. Furthermore, this effect is more pronounced for the mixture with high Ms value. Previous studies [289] have shown that the presence of alkalis could significantly accelerate the hydration of cement.



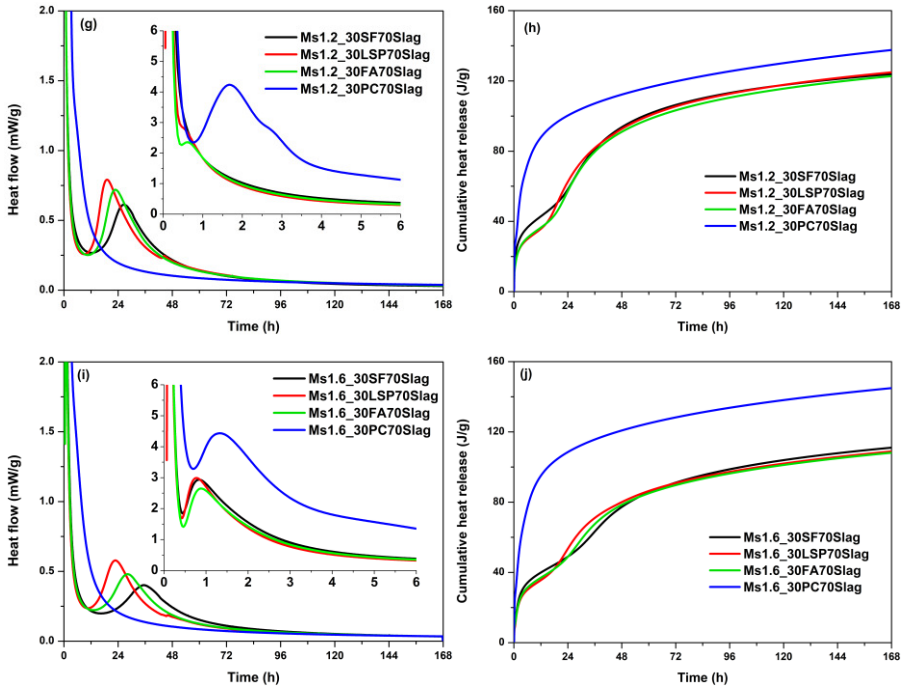


Fig. 7-2 The evolution of heat flow and cumulative heat release with supplementary materials. (a) and (b) Ms 0, (c) and (d) Ms 0.4, (e) and (f) Ms 0.8, (g) and (h) Ms 1.2, (i) and (j) Ms 1.6.

For the effects of the Ms value on the heat evolution of AAC pastes, the heat flow curves and cumulative heat release of alkali-activated fly ash/slag pastes activated by various activator solutions are given in Fig. 7-3 as an example. The time of appearance of the acceleration peak has been reported by previous studies to be influenced by the Ms value of the activator solution [290]–[293]. The end of the induction period is the time required for dissolved species to reach a critical concentration [294] and start forming reaction products, as indicated by the acceleration peaks immediately following the induction period. In this study, the induction period was prolonged with an increase in Ms value except the paste activated by Ms0.8, which showed the longest induction period. With a constant  $\text{Na}_2\text{O}$  content of 5%, the activator solution contains a higher concentration of  $\text{OH}^-$  with a decrease in Ms value of the alkaline solution. The high availability of  $\text{OH}^-$  ions from the activator with a low Ms value led to the interaction between the dissolved Ca, Mg and Al ions from slag grains and Si from the activator solution, resulting in a higher heat flow intensity [291]. However, it seems there is a balance between the dissolution rate of slag and the consumption of silicates in the activator solution. Once the Ms value was higher than 0.8, the activator solution with more silicates can shorten the induction period, probably due to the more  $\text{SiO}_4^{4-}$  ions participating in the reaction [43]. A more detailed discussion will be

presented in the next section.

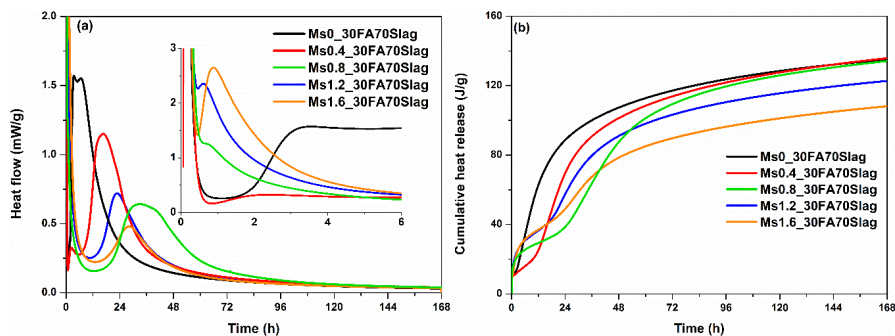


Fig. 7-3 The evolution of (a) heat flow and (b) cumulative heat release of the alkali-activated fly ash-slag pastes.

## 3.2 Ultrasonic pulse velocity of AAC pastes and its correlation with heat evolution and Vicat setting times

### 3.2.1 Comparison between ultrasonic pulse velocity and heat evolution

To better understand the early age reaction of AAC paste, the changes in ultrasonic pulse velocity of AAC pastes with different supplementary materials in the first 24 h are given in Fig. 7-4. The UPV curves of the pastes with Ms0 and Ms1.2 activators were given in Fig. 7-4a and b, respectively. As shown in Fig. 7-4a and b, the paste with the addition of PC always showed a higher UPV as compared to other pastes regardless of the activator type. All AAC pastes activated by Ms0 showed a similar trend and magnitude of the velocity over time. This indicates that the sodium hydroxide activator did not significantly change the reaction mechanism of AAC pastes with various mineral addition. However, when the sodium silicate activator solution (Ms1.2) was used, the evolution of UPV and the magnitude of the velocity varied by the supplementary material used. The mixture Ms1.2\_30PC70Slag exhibited a rapid increase of UPV in a very short period, and the velocity increased to around 3000 m/s in the first 3 h. The UPV evolution of the other three mixtures with the addition of SF, LSP and FA showed an induction period without any increase in velocity. And the time to the end of the induction period was also similar to the time for the end of the dormant period observed in the isothermal calorimetric curves. After this induction period, the UPV started to increase again.

To investigate the effects of Ms value on the early age reaction of AAC pastes, the alkali-activated fly ash-slag pastes activated by Ms0, Ms0.4, Ms0.8, Ms1.2 and Ms1.6 also are given in Fig. 7-4c. The Vicat setting times, isothermal calorimetric results and the UPV curves are plotted in Fig. 7-5.  $T_i$  and  $T_f$  indicate the initial and final setting times in this figure, respectively.

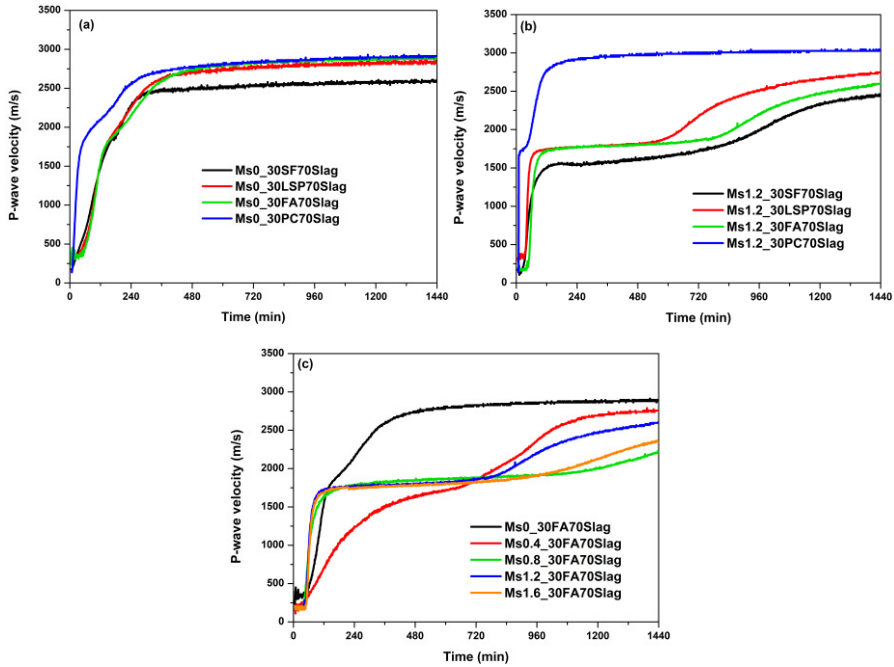
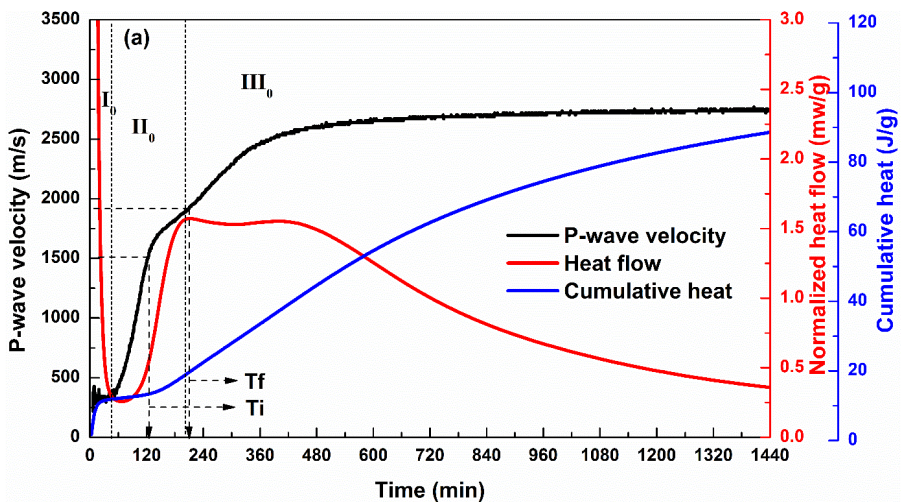
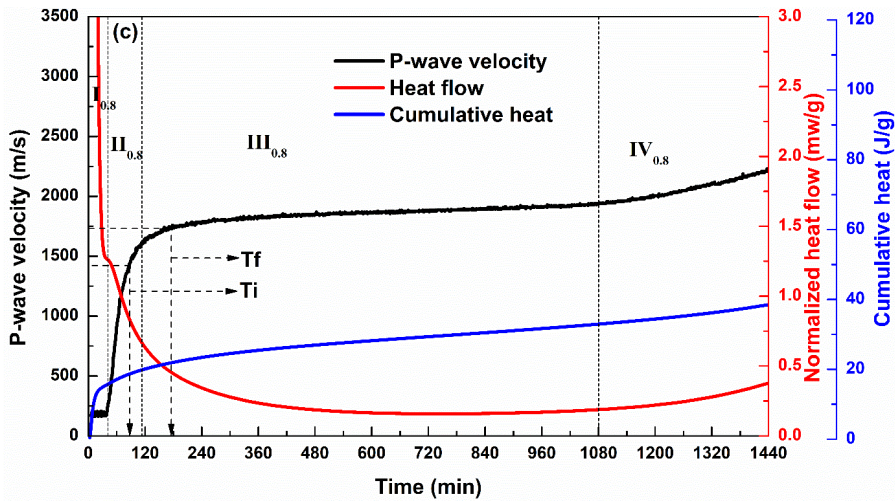
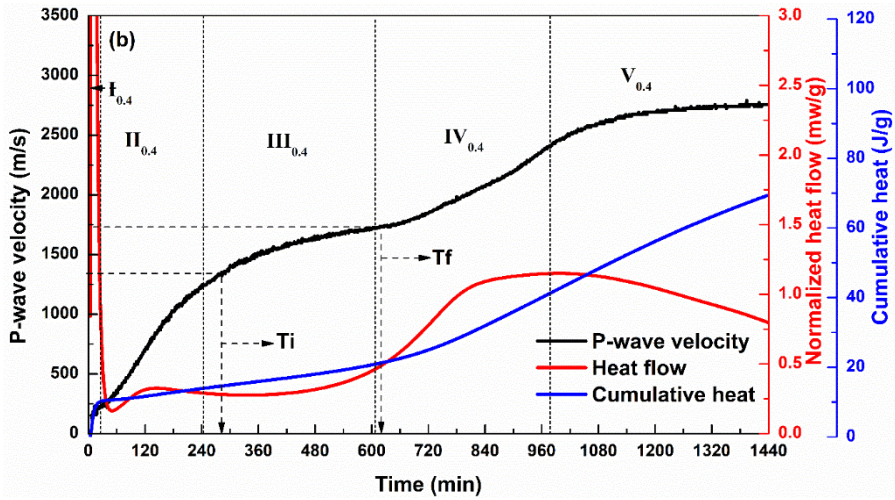


Fig. 7-4 The evolution of UPV (a) Ms 0 with different supplementary materials, (b) Ms 1.2 with different supplementary materials, (c) effects of different Ms ratios for 30FA70slag mixture.

Generally, the evolution of calorimetric results well agreed with the evolution of UPV. For all the pastes, the initial and final setting times occurred when the UPV ranged from 1350 to 1550 m/s, and between 1650 and 1950 m/s, respectively.





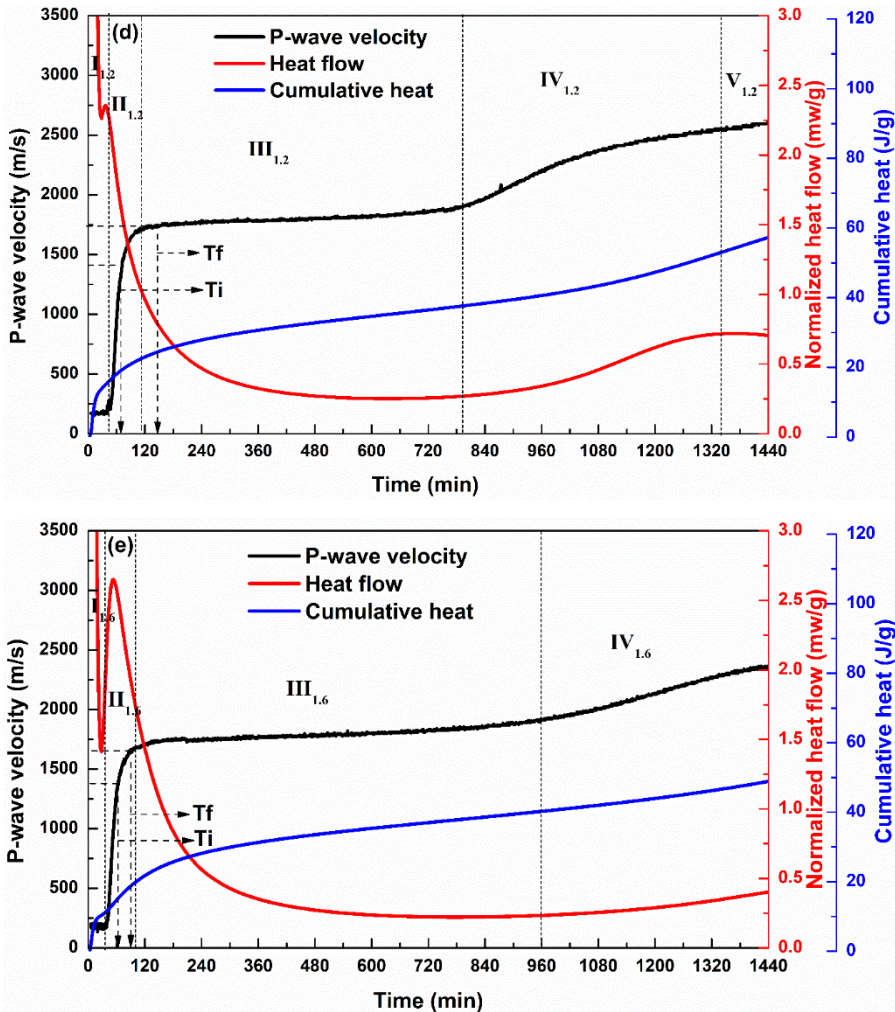


Fig. 7-5 The correlation between UPV, heat flow, cumulative heat and Vicat setting times results of 30FA70Slag (a) Ms0 (b) Ms0.4, (c) Ms0.8 (d) Ms1.2 (e) Ms1.6.

As shown in Fig. 7-5a, the UPV evolution of mixture Ms0\_30FA70Slag (sodium hydroxide activator) presents three stages: (I<sub>0</sub>) dormant period, (II<sub>0</sub>) acceleration period, (III<sub>0</sub>) deceleration period. In stage I<sub>0</sub>, the UPV kept around 350 m/s, which was also consistent with the value reported for Portland cement in the literature [295]. This P-wave value in this stage was significantly less than that in pure water (1510 m/s at 30 °C), owing to energy attenuation of the ultrasonic wave signals induced by interface scattering, reflection and absorption and air bubbles in the suspension. A previous study [150] also considered the AAC paste in this stage to show the liquid-like behaviour. In this stage, the dissolution and initial reaction products formations

occurred simultaneously, which was also evidenced by the dissolution peak of the heat flow. The interaction between the Ca and Si dissolved from precursors resulted in initial reaction product formation [43], [44]. As a result of this initial network, a better passageway for the propagation of ultrasonic waves in stage II<sub>0</sub> was formed. In stage II<sub>0</sub>, a rapid increase of ultrasonic waves was observed, meanwhile, the heat flow also reached the acceleration peak point at the end of this stage. This is probably due to a large number of reaction products having been formed and the connection between different solid phases has been strengthened, leading to the propagation path of P-wave from the liquid-like to the solid-like behaviour. It was previously reported that very high alkaline conditions (sodium hydroxide) could accelerate the activation process as the presence of OH<sup>-</sup> promotes slag dissolution and increases the solubility of silica and aluminum [70], [296]. This indicates that the sodium hydroxide activator (Ms0) contributed to the further dissolution of slag, resulting quicker reaction. In stage III<sub>0</sub>, the P-wave increased slowly and the heat flow also started to decrease. This is probably due to the formation of reaction products starting to fully fill the capillary network of the matrix and hence the increasing rate of UPV began to decrease.

As shown in Fig. 7-5b, c, d and e, sodium silicate activated mixtures generally showed five stages in the first 24 h: (I) dormant period, (II) first acceleration period, (III) first deceleration period, (IV) second acceleration period and (V) second deceleration period. In stage I, all the pastes also exhibited a very low velocity, which was also similar to the sodium hydroxide-activated paste (Ms0\_30FA70Slag). The initial reaction products are formed by the interaction between the silicon ions originating from the sodium silicate solutions and the Ca, Al, Mg and Fe dissolved from the precursor particles surface as reported in many studies [71], [267], [296]. In stage II, the velocity started to increase, and the Ca ions continuously dissolving from the precursors - interacted with the silicates in the sodium silicate solution, forming a large amount of reaction products. Therefore, an additional exothermal peak was observed for the sodium silicate-activated pastes in stage II and the intensity of the peak decreased with a decrease in the Ms value of the activator solution. Due to the presence of higher amounts of silicates in the activator solution of Ms0.8, Ms1.2 and Ms1.6, the reaction rates for these pastes in stage II were accelerated, and the initial setting for these pastes occurred in this stage. The reason for the quick setting times and faster UPV of sodium silicate-activated pastes in this stage as compared to sodium hydroxide-activated pastes under the same Na<sub>2</sub>O % could be explained by the time difference required to reach a critical concentration of ionic species in the suspension to form reaction products. This time is longer for the sodium hydroxide-activated pastes due to the lack of aqueous silicates in the activator solution [43], [70].

However, it is interesting to note that the pastes with Ms0.4 showed the lowest increasing rate of velocity in this stage as compared to all other pastes (as shown in Fig. 7-4c). As elucidated in previous literature, the sodium silicate activator solution with low Ms value contained more silicate monomers, which readily reacted with calcium or aluminum ions, while more cyclic trimers reacting relatively slow with the

calcium or aluminum ions were detected in the sodium silicate activator with high Ms value, [105], [259], [297]. Yet, because of the initial high reaction rate in the low Ms value case (Ms0.4), the initial reaction products could cover the precursors' surface, which in turn delays the further reaction in the following stage [47], [81]. The high-Ms activator with lower pH can allow a longer time for the dissolution of precursors. Once the calcium and aluminum ions reach the critical concentration in the matrix, the subsequent reaction takes place rapidly, forming a large amount of reaction products [47], [49], [150]. Therefore, the high Ms value paste showed shorter setting times than those with low Ms value.

In stage III, sodium silicate-activated pastes showed different induction period times. The UPV showed an increasing rate while the heat flow rate had a decreasing trend in this stage. This can be due to the substantial consumption of silicates originating from the activator solution causing the reaction between silicates and calcium ions to reach an equilibrium state at the end of the previous stage. Many authors [43], [44] have introduced this stage as the dissolution-controlled stage since the dissolution of precursors controls the reaction rate. They pointed out that the previous reaction products like C-A-S-H or C-S-H would form near the surface of precursors acting as a barrier and temporarily suppress further dissolution to form new reaction products. It is interesting to note that once the Ms value exceeded 0.8 the induction period at this stage was relatively shortened, possibly due to more residue silicates from the activator solution after the consumption in the previous stage becomes available to reach a new critical concentration to form new reaction products.

In stage IV, the UPV started to increase again, and the heat flow also reached the peak value of the acceleration stage. Puertas et al. [71] reported that within 3h and 24h, the OH<sup>-</sup> content in the sodium silicate paste increases dramatically, increasing the solution pH and promoting the dissolution of slag. As a result, the interaction between silicates and calcium dissolved from slag took place to form further reaction products, which could also be linked to the solid phases in this stage. Therefore, the total solid volume fraction is further increased and results in a gradual increase in UPV during this stage. Cao et al. [43] also investigated the early-age reaction process of sodium silicate-activated pastes using the FTIR technique and reported that the shift in the Si-O-Si(Al) from 978 cm<sup>-1</sup> at 250 min to 970 cm<sup>-1</sup> at 1200 min, indicating the change of gel composition with a higher polymerization degree, providing a highly polymerized unit gel.

In stage V, a slight increase in the UPV was recorded and it started to reach a plateau. During this time, the heat flow reached the deceleration stage. This indicates the dissolution of precursors and chemical reaction process reached a new equilibrium state, therefore the reaction rate declined gradually and the UPV increased at a slower rate.

The early age reaction process of sodium hydroxide-activated pastes was more straightforward with only three stages compared to those with sodium silicate

activator. The main difference between sodium hydroxide-activated and sodium silicate-activated pastes seems to be the silicates from the activator solution, which can significantly change the reaction mechanism [43].

### 3.2.2 Comparison between Vicat setting times and cumulative heat release

Normally, the setting takes place when a specific reaction degree or a certain degree of microstructure formation occurs [298]. As a result, it is meaningful to compare the reaction degree, cumulative heat release and UPV with setting times. The reaction degree is generally defined as the ratio of the cumulative heat released during the reaction process at time “t” to the total heat released at infinite time  $Q_{\infty}$  (Eq. (7-4)) [44], [58], [242]. Uppalapati et al. [44] reported that using the cumulative heat release to determine the reaction degree is a possible way of assessing the setting times. However, as the determination of the ultimate heat release  $Q_{\infty}$  at an infinite time is not possible. In this study, an exponential model suggested by many authors [55], [242] was used to determine the  $Q_{\infty}$  (Eq. (7-5)).

$$\alpha(t) = \frac{Q(t)}{Q_{\infty}} \quad (7-4)$$

$$Q(t) = Q_{\infty} \exp\left(\left[\frac{-\tau}{t}\right]^{\beta}\right) \quad (7-5)$$

where  $\alpha(t)$  is the degree of reaction at a certain age t,  $Q(t)$  is the cumulative heat release at time t,  $Q_{\infty}$  is the ultimate heat release at infinite time,  $\tau$  and  $\beta$  are the time and shape parameters, respectively.

After fitting Eq. (7-5) to the cumulative heat release curves of alkali-activated fly ash-slag pastes, the  $Q_{\infty}$  of the mixture Ms0\_30FA70Slag, Ms0.4\_30FA70Slag, Ms0.8\_30FA70Slag, Ms1.2\_30FA70Slag and Ms1.6\_30FA70Slag were found as 145, 150, 161, 139 and 116 J/g, respectively. Therefore, the reaction degree of AAC pastes at initial and final setting times can be calculated using Eq. (7-4). Table 7-2 presents the reaction degree, cumulative heat release and UPV at setting times of AAC pastes. The reaction degree of around 9.24 – 13.70 % and 13.51 – 17.58 % indicated the formation of critical volume fraction of reaction products, leading to initial and final setting times in AAC with different Ms values. Uppalapati et al. [44] pointed out that the difference in the reaction degree between the AAC pastes in terms of Vicat setting times was ascribed to the degree of polycondensation between initially formed reaction products. In general, it could be seen that the mixtures with a higher amount of silicates in the activator solution showed a higher reaction degree when they reached their initial and final setting times.

Table 7-2 Comparing Vicat setting times with reaction degree, cumulative heat release and UPV.

Mixtures	Initial set				Final set			
	Initial setting times (min)	UPV (m/s)	Cumulative heat release (J/g)	Reaction degree (%)	Final setting times (min)	UPV (m/s)	Cumulative heat release (J/g)	Reaction degree (%)
Ms0_30FA70Slag	125	1540	13.40	9.24	210	1920	19.60	13.51
Ms0.4_30FA70Slag	282	1350	14.61	9.74	620	1730	21.27	14.18
Ms0.8_30FA70Slag	87	1435	18.65	11.58	175	1739	21.89	13.60
Ms1.2_30FA70Slag	69	1326	19.04	13.70	146	1746	24.43	17.58
Ms1.6_30FA70Slag	63	1372	15.22	13.12	90	1649	18.82	16.22

### 3.3 Flow curves and very early structural build-up of AAC pastes

Fig. 7-6 presents the downward flow curves of AAC pastes with different mineral additions. For reasons of clarity, only the pastes activated by Ms0 and Ms1.2 will be reported. The dynamic yield stress and plastic viscosity of the AAC mixtures were calculated by Eq. (7-2) and (7-3), respectively, and were summarized in Table 7-3. For the pastes activated by Ms0, SF incorporated mixture showed the highest dynamic yield stress due to the ultra-high fineness of SF. Collins and Sanjayan [299] also pointed out that the replacement of 10% condensed SF with slag can lead to a significant loss in workability with a very low initial slump value. LSP and FA incorporated mixtures showed much lower dynamic yield stress as compared to SF and PC incorporated pastes. Therein, Ms0\_30FA70Slag has a lower dynamic yield stress than Ms0\_30LSP70Slag due to the “ball-bearing” effect of spherical FA particles [110], [300]. PC incorporated mixture also exhibited a higher dynamic yield stress with the highest plastic viscosity due to the higher amount of initial reaction products formed at an early age.

Regarding the mixture activated by sodium silicate solution (Ms1.2), due to the presence of aqueous silicates in the activator, the reaction in Ms1.2\_30PC70Slag was accelerated. Due to the rapid stiffening, it was difficult to obtain a homogeneous and flowable mixture. Therefore, the flow curves for only SF, LSP and FA incorporated mixtures with Ms1.2 are presented in Fig. 7-6b. As can be seen from the figure, the general trend in the flow curves of Ms1.2 was similar to the pastes activated by Ms0. As seen from Table 7-3, the mixture with the addition of SF showed significantly higher dynamic yield stress than Ms1.2\_30LSP70Slag and Ms1.2\_30FA70Slag. However, it should be noted that the mixtures activated by Ms1.2 generally had lower yield stress than those activated by Ms0, probably due to the plasticizing and deflocculating effects of the repulsive double-layer electric forces originated from the adsorption of the aqueous silicates on the particle surfaces [102].

Table 7-3 The rheological parameters of AAC pastes.

Mixture	Dynamic yield stress (Pa)	Plastic viscosity (Pa·s)
Ms0_30SF70Slag	516.31	0.74
Ms0_30LSP70Slag	64.67	0.87
Ms0_30FA70Slag	38.36	0.91
Ms0_30PC70Slag	236.55	1.22
Ms1.2_30SF70Slag	111.56	0.64
Ms1.2_30LSP70Slag	3.51	1.33
Ms1.2_30FA70Slag	4.44	0.96

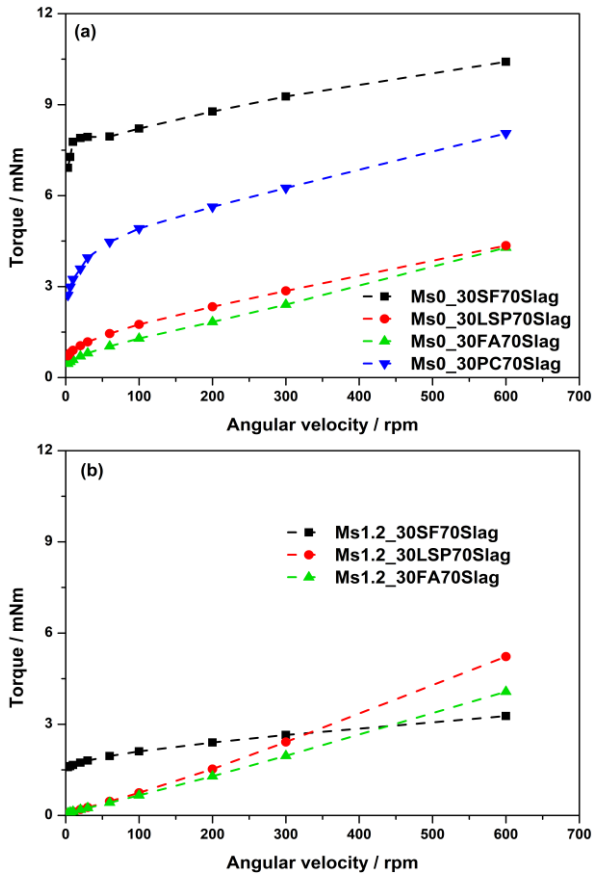


Fig. 7-6 Flow curves of AAC pastes with different mineral addition, (a) sodium

hydroxide pastes activation (Ms0), (b) sodium silicate (Ms1.2) activation.

To better understand the very early structural build-up of AAC pastes with different supplementary materials, the SAOS measurements were conducted and presented in Fig. 7-7. As shown in Fig. 7-7a, the incorporation of PC into AAC mixture activated by Ms0 led to a rapid increase in storage modulus with the highest increasing rate. In addition, SF incorporated mixtures exhibited a higher storage modulus than LSP and FA, possibly due to the increased interparticle interaction of ultra-fine SF particles and their role in providing more nucleation sites leading to a relatively faster reaction rate and particle packing of SF.

Regarding the pastes activated by Ms1.2, the pastes with PC addition still showed the rapid increase in storage modulus since both PC and the slag were reacted to form a large amount of reaction products owing to the aqueous silicates in the activator solution. It should be noted that the mixture activated by Ms1.2 generally showed a lower storage modulus as compared to that activated by Ms0. This can be explained by two mechanisms, on the one hand, the solution with Ms0 has a higher pH, resulting in a faster reaction at the initial time [47]; on the other hand, the solution with Ms1.2 provides more silicates providing a lubricating effect through the adsorption on the particle surface [102]. Afterwards, sufficiently high but lower alkalinity of the solution with Ms1.2 compared to one with Ms0 may allow a continuous dissolution of precursors in a certain period. Therefore, once the calcium, aluminum and silicates reach the critical concentration, the reaction products would form rapidly during a short time period. This phenomenon is more obvious for the case of the addition of LSP and FA, which showed a rapid increase in storage modulus in a short time (beyond 40 min.).

As a result, it can be concluded that the pastes incorporating PC or SF have a potential to be used in the practical engineering requiring a high structural build-up rate, such as the reduction of formwork pressure, slip form paving, stability and 3D printing concrete. While the early lower structural build-up rate for the mixture with the addition of FA and LSP activated by Ms1.2 are preferred for the application of multi-layers casting.

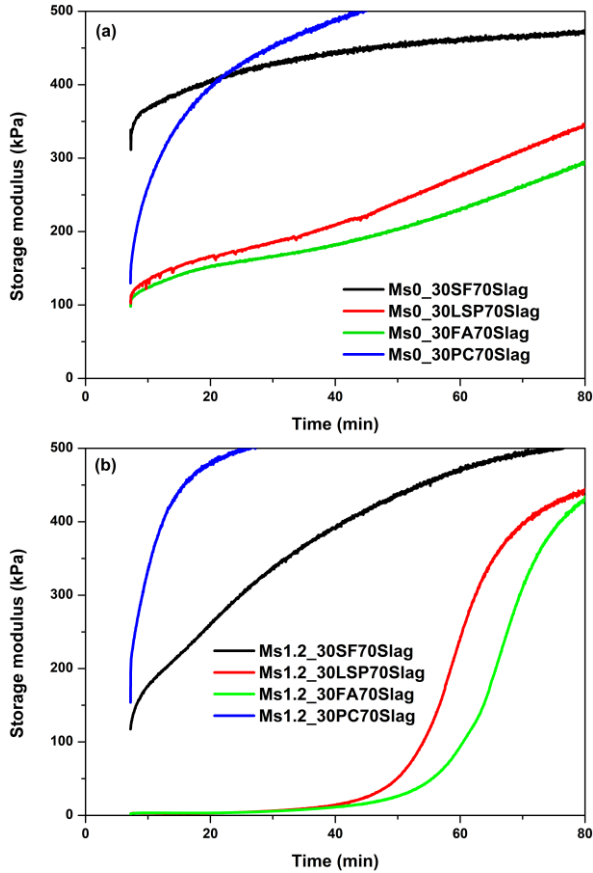


Fig. 7-7 The evolution of storage modulus of AAC pastes with different mineral addition, (a) sodium hydroxide pastes activation (Ms0), (b) sodium silicate (Ms1.2) activation.

### 3.4 Microstructure and chemical composition of reaction products of AAC pastes

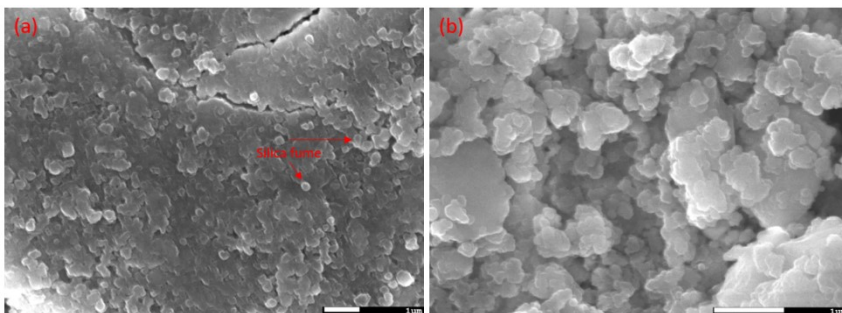
To investigate the early-age microstructure of AAC pastes, SEM analyses were conducted on the fractured surface of the samples at the age of 1d. The morphology of the reaction products and microstructure of AAC pastes with different supplementary materials are given in Fig. 7-8 and Fig. 7-9.

Unreacted very fine spherical SF particles, unreacted spherical FA particles and the irregular-shaped LSP and unreacted slag particles with high angularity can be observed in Fig. 7-8 and Fig. 7-9. The formations filling the spaces between unreacted particles are the reaction products. For the mixture with CE incorporation, the needle-like formations are ettringite. A lot of reaction products were covered on SF, LSP and FA particles surface, indicating their nucleation sites effects during reaction [110],

[111].

Furthermore, to understand the chemical composition of reaction products, EDX analyses for multiple points were conducted on the fractured surface. Calcium, aluminum and silicon contents of the reaction products at the age of 1d were determined and renormalized to 100% on an oxide for plotting on the ternary diagrams in Fig. 7-10. These plots clearly showed the high variation in the gel composition depending on the supplementary materials and Ms value of the activator solution. As shown in Fig. 7-10a and b, the main reaction product of SF incorporated mixtures was C-(N)-A-S-H with high Ca content regardless of Ms value of activator solution. The pastes with the addition of LSP contained a mixture of reaction products C-(A)-S-H and C-S-H regardless of activator type in this study. The pastes with the addition of FA activated by Ms0 mainly had the C-(A)-S-H and C-(N)-A-S-H with high Ca content, while when increasing Ms to 1.2, only C-(N)-A-S-H with high Ca content could be detected. It should be noted that the reaction products of the pastes with addition of PC activated by Ms0 were mainly C-S-H with a high content of Ca, which was rarely documented in literature. This is possibly due to some ettringite formations being also included. At the same time, the gel C-(A)-S-H and C-S-H has also been found in the mixture Ms1.2\_30PC70Slag.

It should be noted that, although the N-A-S-H gel phase was not detected somehow in any mixtures in this study, the previous studies pointed out that the existence of N-A-S-H type gel could not be plausibly excluded [301]. Regarding C-(N)-A-S-H/C-S-H/C-(A)-S-H as the primary reaction products, the interaction volume was approximately 1.0 to 2.0  $\mu\text{m}$  into the sample surface at a 15 kV acceleration voltage [302]. Therefore, the possibility of C-(N)-A-S-H and N-A-S-H/(N,C)-A-S-H gel intermixing may still exist, however the differentiation of intermixed gels is quite difficult due to the resolution limit of EDX technique [248]. However, the amount of N-A-S-H/(N,C)-A-S-H is typically regarded to be negligible as compared to C-(N)-A-S-H or C-(A)-S-H [303]. Similarly, the formation of hydrotalcite phase rich in Al and Mg is also possible due to the high amount of Mg in slag, which has been well documented in the previous literature [31], [48]. To validate the existence of N-A-S-H gel, a further microstructural technique (i.e.  $^{29}\text{Si}$  Nuclear magnetic resonance) is needed.



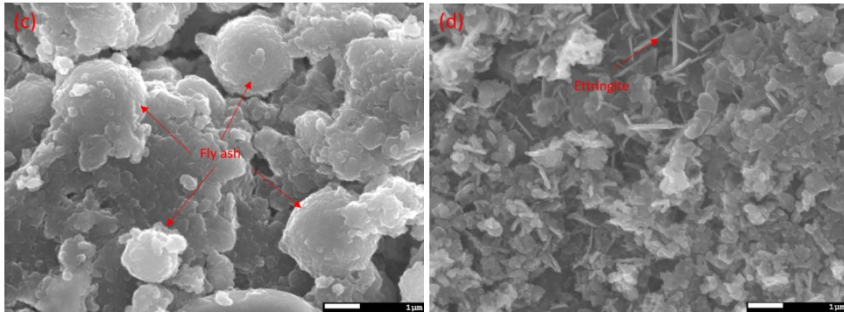


Fig. 7-8 SEM images of AAC pastes activated by sodium hydroxide activator (Ms0), (a) Ms0\_30SF70Slag, (b) Ms0\_30LSP70Slag, (c) Ms0\_30FA70Slag, (d) Ms0\_30PC70Slag.

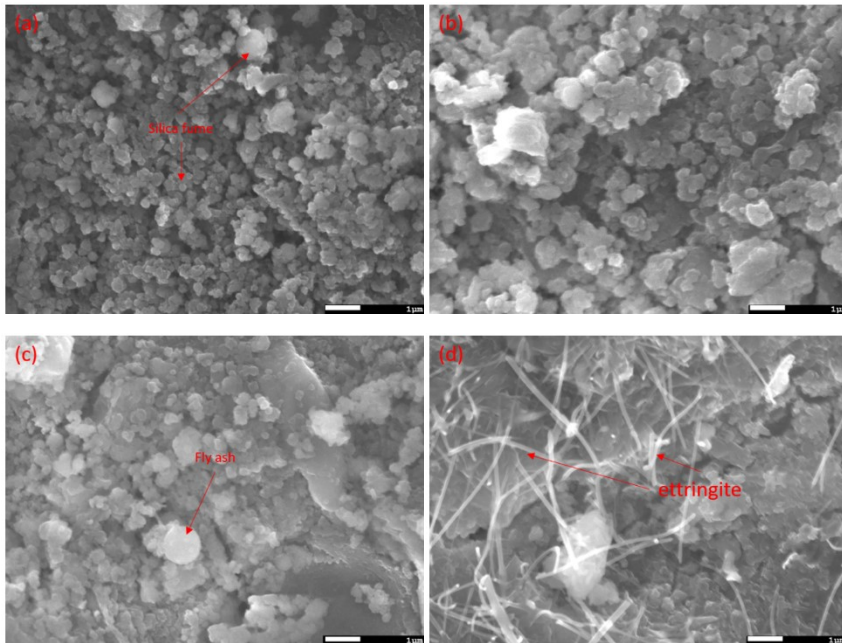


Fig. 7-9 SEM images of AAC pastes activated by sodium silicate activator (Ms1.2), (a) Ms1.2\_30SF70Slag, (b) Ms1.2\_30LSP70Slag, (c) Ms1.2\_30FA70Slag, (d) Ms1.2\_30PC70Slag.

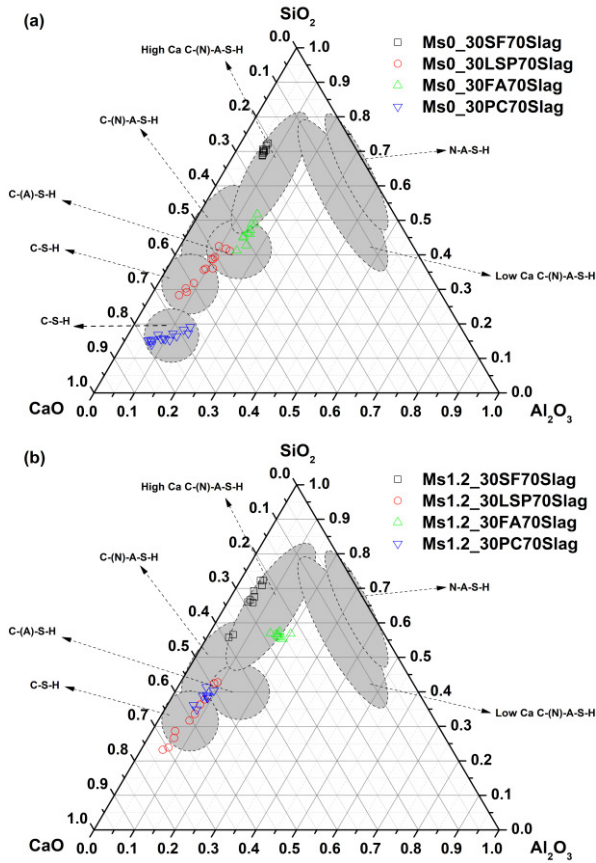


Fig. 7-10 Ternary representations of EDX data for AAC pastes with different mineral additions at the age of 1d, (a) the pastes activated by Ms0, (b) the pastes activated by Ms1.2, showing literature for C-S-H [304]–[306], C-(A)-S-H [248], [303], [307], C-(N)-A-S-H [70], [308], C-(N)-A-S-H with high Ca [89], [248], [305] and low Ca content [248], [309], and N-A-S-H [248], [307].

#### 4. Conclusion

---

This chapter focuses on the effects of supplementary materials on the rheology, structural build-up and early age reaction of alkali activated slag cement pastes. The following conclusions can be drawn in this study:

1. The addition of Portland cement significantly shortened the induction period and accelerated the acceleration/deceleration stages of AAC pastes. However, an increase in Ms value in the activator solution resulted in the extension of the induction period with a decrease in the intensity of the acceleration peak in the heat curve of AAC.
2. Based on the isothermal calorimetric and ultrasonic measurements, the early reaction process of sodium hydroxide-activated slag/fly ash pastes consists of three stages: induction, acceleration and deceleration stage, while five stages are observed in the sodium silicate-activated slag/fly ash pastes: induction, acceleration, deceleration, second acceleration and second deceleration period. The main difference between the sodium hydroxide and sodium silicate-activated pastes is the aqueous silicates originating from the activator solution, which can increase the reaction rate at an early age, leading to quick setting times.
3. A specific value of the cumulative heat release or ultrasonic pulse velocity range can be used to estimate the setting times of pastes.
4. The studied AAC pastes produced by different supplementary materials fit the Bingham model. The AAC pastes with PC or SF incorporation have a significantly higher storage modulus regardless of the activator type.
5. The FA or LSP added AAC pastes activated by sodium silicate solution show an induction period without a significant increase in storage modulus, followed by a rapid increase in storage modulus.
6. The main reaction products of AAC pastes determined by SEM/EDX technique seem to be the C-(N)-A-S-H/C-(A)-S-H and C-S-H at the early age. However, the existence of N-A-S-H reaction products could not be readily ignored due to the limitation of SEM/EDX. A further microstructure analysis (i.e. Nuclear magnetic resonance) may need to validate the presence of N-A-S-H.

## **Part V**

---

### **Influence of chemical admixtures on the rheological and setting behaviour of AACs**



## **Chapter 8 Influence of retarders on the rheological and setting behaviour of AACs**

---

As well known, the AAC made with sodium silicate solution shows a very quick setting time. In this chapter, the effects of several chemical retarders on rheological and setting behaviour of AACs are investigated.

## 1. Introduction

---

As well known, the setting time of cementitious materials is of high importance for a successful casting process. The sodium silicate-based activators (sodium silicate and sodium hydroxide) were found to show the best performance in terms of strength development; however, the main shortcoming of the sodium silicate-activated slag cements (AAS) is the rapid set [162]. Despite the superior mechanical performance of the AAS activated by sodium silicate-based activators, their quick and uncontrolled setting significantly hinders their common usage in real practice. Therefore, it is vital to find an appropriate chemical admixture to retard the rapid setting of these types of AAS. Chang [162] found that phosphoric acid ( $\text{H}_3\text{PO}_4$ ) can work as a retarder in sodium silicate-activated GGBFS systems. The author pointed out that incorporating 0.87 M phosphoric acid ( $\text{H}_3\text{PO}_4$ ) into the AAS mixture could retard the setting time; however, it reduced the early age compressive strength and increased the drying shrinkage. Some studies also investigated the role of phosphates in the setting of AAC. Kalina et al. [173] reported that the phosphate anion from the trisodium phosphate ( $\text{Na}_3\text{PO}_4$ ) used as a retarder would bond to the  $\text{Ca}^{2+}$  ions released from the GGBFS in a highly alkaline environment, thereby forming calcium dihydrogen, later hydrogen phosphate structures. Therefore, it is theorized that the lack of calcium ions in the solution reduces the nucleation and development of the C-S-H phase and hence the initial setting time delays. Gong and Yang [165] also observed the same phenomenon that relatively high sodium phosphate concentration had a strong retarding effect on the setting of the alkali silicate-activated GGBFS-red mud blended system. However, Shi and Li [310] reported no notable retardation effect when  $\text{Na}_3\text{PO}_4$  was added to the alkali-activated phosphorus slag systems. Furthermore, the use of borates as retarders for PC is well known [311]. Yousefi et al. [163] found that borax can improve the fresh state properties of alkali-activated slag/fly ash systems in terms of workability and setting time without negatively affecting the mechanical properties. They also reported that a dosage of 6% borax was optimal in improving the fresh state properties while keeping the mechanical performance. Revathi et al. [312] also pointed out that both initial and final setting times were prolonged, and the yield stress of AACs decreased in the presence of borax. The same authors revealed that the presence of borate ions significantly influenced the early dissolution of alumina and silicate species due to the reaction of  $\text{BO}_4$  tetrahedron with  $[\text{SiO}_4]$ , causing the retardation of  $[\text{AlO}_4]$  in the network resulting in increased setting time. Furthermore, some researchers also tried to use organic acids as retarder in AAC [171], [313]. Sun et al. [171] investigated the effect of tartaric acid on the early hydration of sodium hydroxide-activated slag pastes. They pointed out that tartaric acid can prolong the initial setting time due to the complexation reaction of Al rather than Ca.

To improve the understanding of the roles of different retarders on the rheology, structural build-up, setting time, strength development and the microstructure of AAS, sodium-silicate activated GGBFS mixtures with citric acid, sodium tetraborate decahydrate, and sodium triphosphate pentabasic were produced and tested in this

study. The structural build-up of the AAS pastes with different types of retarders in different dosages was assessed by small-amplitude oscillation shear tests (SAOS). The initial workability and the workability loss of AAS with different retarders were evaluated by a mini-slump test. X-ray diffraction (XRD) analysis and pore solution chemistry by inductively coupled plasma – optical emission spectrometry (ICP-OES) were applied to find out the mechanism behind the setting characteristics. The porosity and the pore size distribution of the hardened samples were assessed by mercury intrusion porosimetry (MIP). The compressive and flexural strength of the mixtures were also determined to see the effect of retarding chemicals on the mechanical properties. Scanning electron microscopy (SEM) was also employed to observe the morphology of hydrates.

## 2. Experimental program

---

### 2.1 Mixture design

---

It was reported that the sodium silicate activators with an Ms value of around 1.0 - 1.5 could result in the highest mechanical and durability performance for alkali-activated slag cement [268]. For this reason, the sodium silicate activator with a Ms value of 1.2 was used in this study. The Na<sub>2</sub>O content and water to solid binder (w/b) ratio were kept constant as 5% and 0.45 for all mixtures, respectively. Three types of chemicals, citric acid (CA, C<sub>6</sub>H<sub>8</sub>O<sub>7</sub>) with purity of 99.0%, sodium tetraborate decahydrate – Borax (SB, Na<sub>2</sub>B<sub>4</sub>O<sub>7</sub>·10H<sub>2</sub>O) with purity higher than 99.5% and sodium triphosphate pentabasic (SP, Na<sub>5</sub>O<sub>10</sub>P<sub>3</sub>) with purity higher than 98.0% provided by Sigma-Aldrich, were used as retarding chemicals in this study. These three chemicals were added to the activator solution in different amounts (3%, 4% and 5% by weight of the total precursors) one day before, prior to mixing with precursors. The detailed mix proportions are shown in Table 8-1.

Table 8-1 Mixture proportions of the paste samples.

Mixture notation	Na <sub>2</sub> O%	Ms	W/SB*	GGBFS (%)	CA** (%)	SB** (%)	SP** (%)
REF_Ms1.2	5	1.2	0.45	100	0	0	0
CA3	5	1.2	0.45	97	3	0	0
CA4	5	1.2	0.45	96	4	0	0
CA5	5	1.2	0.45	95	5	0	0
SB3	5	1.2	0.45	97	0	3	0
SB4	5	1.2	0.45	96	0	4	0
SB5	5	1.2	0.45	95	0	5	0
SP3	5	1.2	0.45	97	0	0	3
SP4	5	1.2	0.45	96	0	0	4
SP5	5	1.2	0.45	95	0	0	5

\* The sum of GGBFS, chemicals and dry part of activator solution is considered as the solid binder.

\*\* CA, SB and SP indicate the chemical admixture citric acid, sodium tetraborate decahydrate and sodium triphosphate pentabasic.

## 2.2 Sample preparation

The AAS pastes for the rheological measurements were mixed by using a rotational rheometer with a helix geometry [159]. The mixing protocol consisted of two stages: firstly, the shear rate was gradually increased from 0 to 3000 min<sup>-1</sup> within 30 s, and then the mixing speed was kept constant at 3000 min<sup>-1</sup> for 120 s. For the other tests, the paste samples were prepared in a Hobart mixer. GGBFS was added to the activator solution in the Hobart mixing bowl and mixed at low (140 ± 5 rpm) and high (285 ± 5 rpm) speeds for 90 s each.

## 3. Results and discussions

### 3.1 Workability loss, setting times and mechanical performance

The influence of different retarders on the spread diameter (%) of AAS pastes is given in Fig. 8-1. As shown in Fig. 8-1, the AAS mixture without any retarding chemicals (REF\_Ms1.2) presented a rapid workability loss within 20 min and lost all workability at the age of 27 min. The sodium triphosphate pentabasic (SP) addition provided a

higher initial spread diameter as compared to the reference mixture, but SP addition could not provide enough workability retention at all used dosages. Increasing the SP dosage from 3% to 5%, the time to complete loss of workability just prolonged from 33 min to 39 min. These findings are also consistent with the previous studies [163], showing that the SP can only slightly increase the time to retain the flowability of the pastes.

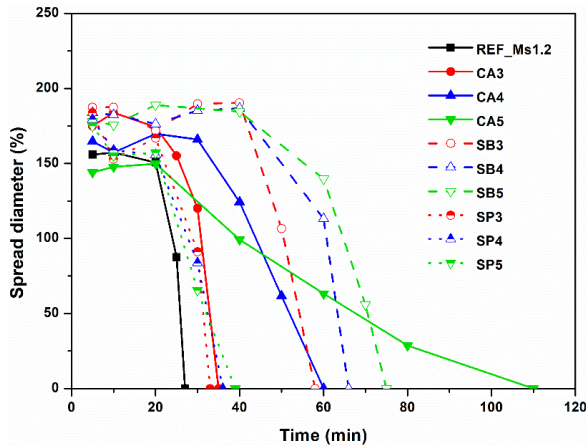


Fig. 8-1 Mini-slump retention of AAS pastes at 20 °C.

The organic citric acid (CA) addition improved the initial workability and provided longer workability retention as compared to the control mixture and the SP. The highest initial workability among CA mixtures was obtained at 3% dosage (CA3). However, CA3 presented a sudden workability loss after around 25 min. At 4% CA dosage, the initial workability was slightly lower than that of CA3, but the mixture kept its initial workability longer than CA3. In addition, the workability loss observed in CA4 was more gradual as compared to CA3. Increasing the CA dosage to 5% (CA5) caused a slightly lower initial workability compared to REF\_Ms1.2; however, the workability loss was more gradual, and the complete loss of workability in the CA5 mixture lasted the longest among all tested mixtures (around 115 min). On the other hand, it should be noted here that the flow diameter of CA5 was significantly lower than CA4 in the first hour.

Sodium tetraborate decahydrate (SB) led to a relatively appropriate initial flow diameter and workability retention as compared to SP and CA. The initial spread diameter and the workability retention within the first 40 min of SB3, SB4 and SB5 were significantly higher than REF\_Ms1.2 AAS mixture. SB3 showed a sudden workability loss after 40 min and lost its all flowability at 58 min. SB4 and SB5 also showed significant workability loss upon 40 min as well but their workability loss rate were slower than SB3. The time for the complete loss of workability was prolonged from 58 min to 75 min when the dosage of SB increased from 3% to 5%. Yousefi et

al. [163] also found that the mixtures with SB had a better workability retention as compared to the mixtures with SP addition, which was also consistent with the results of storage modulus (as presented in Section 3.3) in this study.

Table 8-2 presents the initial and final setting times of the tested AAS mixtures. As can be seen from the Table 8-2, REF\_Ms1.2 showed rapid initial and final setting times of 46 min and 150 min, respectively. Although there is no well-defined or suggested minimum initial setting time for AAS yet, it is for sure that an AAS paste with a setting time shorter than 60 min would not be appropriate for general use. Furthermore, even much longer setting times would be more suitable for the common use of the AAS for general purposes. In this respect, revealing the performance of different types of retarding chemicals in extending the short setting times of sodium silicate-activated AAS without a detrimental effect on strength development is important. Table 8-2 clearly shows that all of the tested three different types of chemicals retards the setting times of sodium silicate (Ms 1.2) activated AAS to different extents. It is observed that their influence on final setting time was more pronounced than the initial setting time.

Table 8-2 Setting times of AAS pastes.

Mixture notation	Initial setting times (min)	Final setting times (min)
REF_Ms1.2	46	150
CA3	69	393
CA4	126	425
CA5	>4d	/
SB3	86	392
SB4	106	460
SB5	120	676
SP3	70	270
SP4	73	275
SP5	76	277

As can be seen in Table 8-2, similar to the results of mini-slump, the incorporation of SP at 3% dosage could prolong the initial setting time from 46 min to 70 min, and the further increase up to 5% did not significantly prolong the initial setting time, ranging from approximately 70 min to 76 min. The same tendency was also observed in the final setting times, which fell between 270 min and 277 min. The CA and SB were

found to be more dosage-sensitive in increasing setting times. The CA with 3% dosage prolonged the initial and final setting times 23 min and 243 min, respectively, compared to REF\_Ms1.2. These extensions in initial and final setting was 80 min and 275 min, respectively, at 4% CA dosage. The further increase of the CA dosage to 5% caused extremely long setting times (exceeding four days for the initial setting time). The addition of SB at 3% extended the initial and final setting times 40 min and 242 min compared to the reference. The further dosage increase to 5% resulted in the extension of the initial and final setting time with 74 min and 526 min compared to the reference. An overall evaluation of the setting time results presented in Table 8-2 reveals that the borax-based retarder presents more reasonable setting times at different usage dosages. It also allows the dosage-based arrangement to reach the desired setting properties in AAS design. In previous literature, Yousefi et al. [163] also indicated that the setting time increased almost linearly as the borax content was increased from 2% to 8% of the weight of precursors.

The flexural and compressive strengths of AAS mixtures are presented in Table 8-3. It was obvious that the flexural and compressive strength for all mixtures increased with age. It could be seen that the CA incorporated mixtures did not gain any measurable strength at 2 days. These mixtures could gain flexural and compressive strength at the ages of 7 and 28 days, but the obtained strength levels were much lower than the REF\_Ms1.2. The low mechanical performance of CA incorporated mixtures was more pronounced in high dosage cases, probably due to the decrease in pH value of the activator solution by the dosage increase. Therefore, it can be concluded that the mixtures with CA addition were far inferior to REF\_Ms1.2 in terms of mechanical performance.

Interestingly, among all mixtures, the best mechanical performances were obtained from SP incorporated samples. The compressive strength of SP mixtures was higher than 40 MPa at the age of 2 days in all used dosages. The flexural and compressive strength values even slightly increased with a higher dosage of SP. The mixtures with the addition of SB showed a lower flexural and compressive strength than that of REF\_Ms1.2 at 2 and 7 days. However, SB3, SB4 and SB5 showed higher mechanical properties than REF\_Ms1.2 at 28 days. These results are also parallel with the results of isothermal calorimetric tests (Section 3.2).

Table 8-3 Mechanical performance of AAS pastes.

Mixture notation	Flexural strength (MPa)			Compressive strength (MPa)		
	2-day	7-day	28-day	2-day	7-day	28-day
REF_Ms1.2	4.1 ± 0.3*	8.1 ± 0.4	8.6 ± 0.5	33.3 ± 1.2	65.1 ± 0.9	76.2 ± 1.7
CA3	0	3.8 ± 0.2	7.0 ± 0.3	0	29.5 ± 0.8	44.8 ± 1.2
CA4	0	2.4 ± 0.4	3.5 ± 0.1	0	16.3 ± 1.1	23.3 ± 0.5
CA5	0	0	1.6 ± 0.9	0	0	8.9 ± 0.2
SB3	3.5 ± 0.1	6.7 ± 0.7	8.7 ± 0.5	23.2 ± 0.3	62.6 ± 1.2	85.1 ± 1.4
SB4	3.5 ± 0.4	6.9 ± 0.2	8.5 ± 0.2	23.2 ± 0.2	60.4 ± 0.9	82.4 ± 1.3
SB5	3.7 ± 0.2	6.1 ± 0.4	8.1 ± 0.8	19.6 ± 0.5	59.1 ± 0.5	80.2 ± 0.5
SP3	5.3 ± 0.4	7.9 ± 0.2	8.6 ± 0.6	43.2 ± 0.6	65.8 ± 0.7	86.9 ± 0.9
SP4	5.5 ± 0.5	8.1 ± 0.5	8.6 ± 0.7	43.3 ± 0.6	66.1 ± 1.2	87.7 ± 1.0
SP5	5.8 ± 0.3	8.3 ± 0.3	9.0 ± 1.2	44.6 ± 0.1	67.7 ± 0.6	88.6 ± 0.8

\* Standard errors.

### 3.2 Reaction kinetics of AAS pastes

Calorimetric curves for AAS pastes with different retarders are presented in Fig. 8-2. It has been reported that the calorimetric curve for sodium silicate-based GGBFS mixtures has five distinctive stages: dissolution, induction, acceleration, deceleration and steady-state [51], [81], [152].

In general, during the first 20 min a sharp local peak is observed for all sodium silicate-based GGBFS mixtures. The heat flow evolved rapidly upon contact between the activator and the GGBFS was mainly attributed to wetting and dissolution of GGBFS particles and partly the interaction of silicate units and sodium with calcium dissolved from GGBFS [207], [272]. After the dissolution stage, the heat flow for the AAS pastes starts to show an induction period. The main calorimetric peaks after the induction period for the AAS pastes are usually associated to the strength and microstructural development [271].

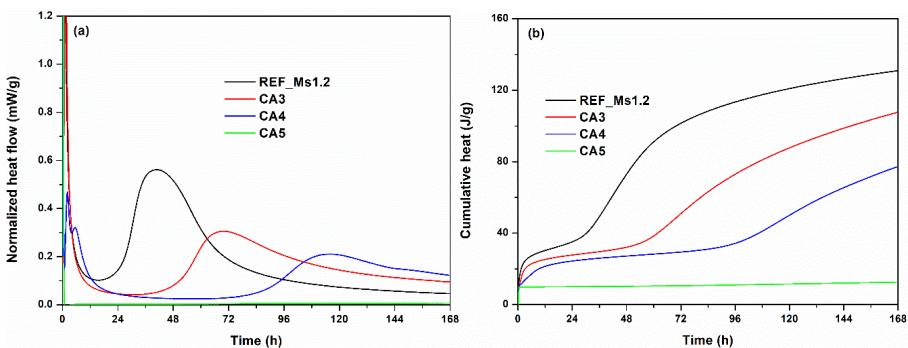
It could be seen that CA was the most effective retarder to prolong the induction period of AAS mixtures. As compared to REF\_Ms1.2, the onset of the acceleration stage was delayed from 14.9 h to 30.5 h and 56.5 h for 3% and 4% CA, respectively. However, such a pronounced retarding effect of CA costs the loss of strength development (Table 8-3). Following the compressive strength development trend of CA incorporated mixtures, the induction period and time to reach the end of acceleration period were longer than the REF\_Ms1.2 and the intensity of the main calorimetric peak was much lower as compared to that of REF\_Ms1.2. It should be noted that when the dosage of CA reached to 5%, no second calorimetric peak was observed during the measurement

time. Therefore, the heat evolution of the mixtures was very sensitive to the CA dosages, which was also consistent with the mechanical performance of the mixtures incorporated with CA.

SP showed a converse trend as compared to CA in terms of heat flow. As shown in Fig. 8-2, in the SP incorporated mixtures, the onset of the acceleration period occurred much earlier than that of REF\_Ms1.2 and this was followed by a very sharp increase in the intensity of the main calorimetric peaks. These observations agree well with the better mechanical performance of SP incorporated mixtures as compared to REF\_Ms1.2.

No very significant heat flow differences as compared to REF\_Ms1.2 were observed in SB incorporated mixtures in the first 24 hours. The time of the end of the acceleration period was achieved earlier than that of REF\_Ms1.2; however, the intensity of the main peaks of SB incorporated mixtures were slightly lower as compared to the mixture REF\_Ms1.2. These were also consistent with the compressive strength results at early ages.

Regarding the cumulative heat release, the cumulative heat release of REF\_Ms1.2 reached to 131 J/g at 7 days (Fig. 8-2b) and the cumulative heat release of the mixtures with CA was significantly lower than the reference mixture without CA. As can be seen from Fig. 8-2b, increasing the CA dosage from 3% to 5% resulted in the decrease of cumulative heat release at 7 days from 107 J/g to 13 J/g. This shows that the CA addition is very effective in slowing down the GGBFS reactions and its dosage should be limited in a certain range, otherwise the activator solution would not activate the reaction of GGBFS. The inclusion of SB from 3% to 5% can only slightly decrease the cumulative heat at the age of 7 days from 121 J/g to 114 J/g. The trend in the case of SP was inverted. The cumulative heat at the age of 7 days increased from 141 J/g to 149 J/g, supporting its better mechanical properties as compared to REF\_Ms1.2.



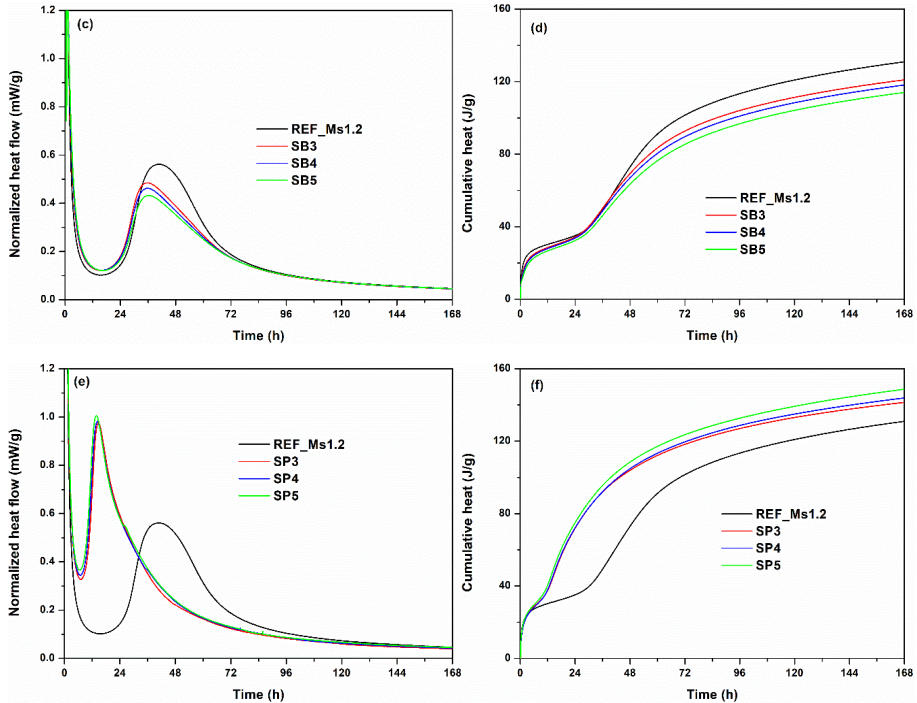


Fig. 8-2 The evolution of heat flow and cumulative heat release of AAS pastes (a), (c) and (e) are the heat evolution for CA, SB and SP addition, respectively. (b), (d) and (f) are the cumulative heat release for CA, SB and SP addition.

To better correlate the initial setting time with the reaction kinetics of AAS pastes with different types of chemical retarders, the first three hours of heat flow and cumulative heat curves of four mixtures (REF\_Ms1.2, CA4, SB4 and SP4) were measured and plotted in Fig. 8-3. As shown in Fig. 8-3a, after the dissolution peak, an additional exothermic peak was observed for each AAS mixture, as also reported by Gebregziabihier et al. [81] and Shi et al. [271]. It was observed that these additional exothermic peaks occurred essentially before the initial setting times of AAS pastes. The arrows in Fig. 8-3b show the cumulative heat values of AAS pastes with different types of chemical retarders when they reached initial setting times. As could be seen from Fig. 8-3b, REF\_Ms1.2, SB4 and SP4 exhibited their cumulative heat around 17 J/g at the initial setting time. However, the trend was slightly different for CA4 as its cumulative heat showed only 12 J/g at the initial setting time possibly due to the low reaction rate of the mixture leading to the physical effects, such as water loss by evaporation, more dominant in setting time test.

Overall, it is therefore likely that these additional exothermic peaks made an important contribution to the initial setting of AAS mixtures.

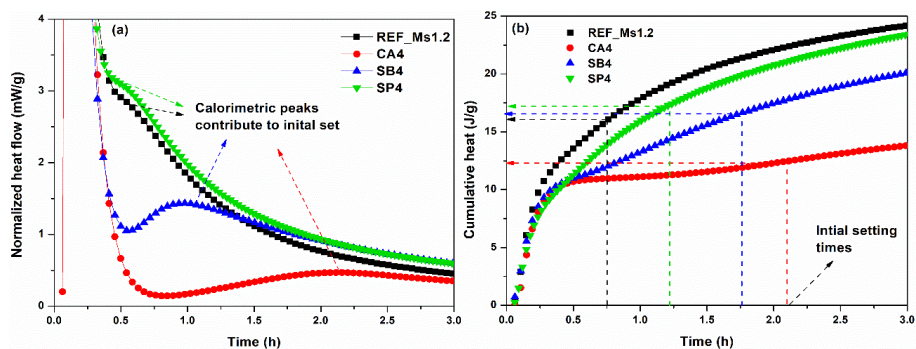


Fig. 8-3 The evolution of heat flow (a) and cumulative heat release (b) of AAS pastes in the first three hours.

### 3.3 FTIR-ATR and pH value analysis of activator solutions

The FTIR-ATR and pH value measurements were conducted on four selected activator solutions (REF\_Ms1.2, CA4, SB4 and SP4), and their results are presented in Fig. 8-4 and Table 8-4, respectively. As shown in Fig. 8-4, all activator solutions showed a main band with a peak at around  $1010\text{ cm}^{-1}$ , which was related to the overlapped Si-O-Si bands of different  $Q^n$  species in the activator solution. The peak position for REF\_Ms1.2 is located at  $1006\text{ cm}^{-1}$ , while the peak shifted to  $1016\text{ cm}^{-1}$ ,  $1008\text{ cm}^{-1}$  and  $1008\text{ cm}^{-1}$  for CA4, SB4 and SP4 activator, respectively. The spectra shift towards higher wavelengths compared to the REF\_Ms1.2 spectra shows the increase in Si-O-Si bond strength for the activators with chemical retarders [314]. New peaks were formed for the solutions CA4 and SP4 while some broad humps were appeared in the spectra of SB4 solution, showing the formation of new bonds. In Fig. 8-4a, the additional peak located at  $1590\text{ cm}^{-1}$  could possibly linked to C=C aromatic stretching vibrations as reported in ref [315], [316]. Another peak at  $1392\text{ cm}^{-1}$  could be attributed to Si-OH bonding [316]. Besides, the observed peak at  $1280\text{ cm}^{-1}$  was normally related to the Si-C bonding [317], indicating the citric acid was modified by silicate species in the alkaline solution. It should be noted that there is a significant decrease in the intensity of the band region between around  $900\text{ cm}^{-1}$  and  $950\text{ cm}^{-1}$ . This is possibly due to the  $\text{H}^+$  released from CA consumes small silicate anions in the sodium silicate solution [314].

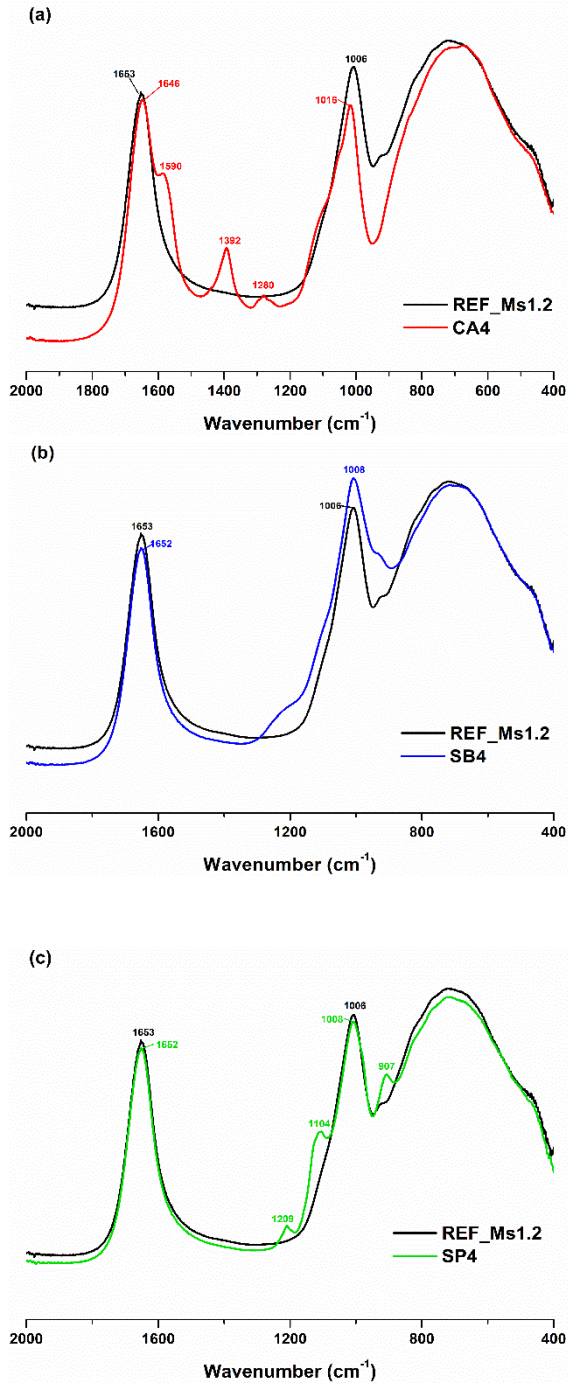


Fig. 8-4 The comparison between FTIR spectra for different activator solutions with addition of chemical retarders and REF\_Ms1.2, (a) CA4, (b) SB4, (c) SP4.

As shown in Fig. 8-4b, SB4 showed traces of shoulders at around  $950\text{ cm}^{-1}$ ,  $1100\text{ cm}^{-1}$  and  $1200\text{ cm}^{-1}$ . The wide absorption band at around  $1100\text{ cm}^{-1}$  can be attributed to tri-, tetra-, pentaborate, and diborate groups belonging to the  $\text{BO}_3$  and  $\text{BO}_4$  groups, as well as asymmetric stretching from Si-O-Si [318]. The band at around  $950\text{ cm}^{-1}$  should be associated with the B-O vibration of  $\text{BO}_4$  units and was also related to the stretching frequency of Si-O-B [319]. While the region centered at  $1200\text{ cm}^{-1}$  was possibly assigned to the stretching vibration of B-O of the  $\text{BO}_3$  units from the boroxol rings. As for the SP4 activator shown in Fig. 8-4c, three additional peaks at  $907\text{ cm}^{-1}$ ,  $1104\text{ cm}^{-1}$  and  $1209\text{ cm}^{-1}$  were also shown for the SP4 activator. The band at  $1104\text{ cm}^{-1}$  can be related to the bridging stretching Si-O-P and Si-O-Si vibrations [320]. While the band at  $907\text{ cm}^{-1}$  was possibly assigned to symmetric P-O vibrations [321]. Furthermore, presence of the band at  $1209\text{ cm}^{-1}$  can be assigned to the P=O structure [321]. These evidences showed that the addition of chemical retarders changed the various types of bridging bonds in the activator solution.

Table 8-4 presents the pH value of these four mixtures. CA4 activator had the lowest pH value as compared to other mixtures, indicating that CA4 led to less dissolution of GGBFS, which was also consistent with the setting times results. While REF\_Ms1.2 showed the highest pH value, which was consistent with its quick setting times.

Table 8-4 The pH values of selected activator solutions

Mixutre notation	REF_Ms1.2	CA4	SB4	SP4
pH values	13.56	12.84	13.22	13.35

### 3.4 Structural build-up of AAS pastes

It has been reported that SAOS measurement can successfully evaluate the structuration process of cementitious materials [46], [159]. Thus, the mixtures used in this study were tested by the SAOS method to monitor the structuration process of AAS mixtures through the storage modulus measurements.

Fig. 8-5 shows the storage modulus evolution of CA, SB and SP incorporated mixtures comparatively with REF\_Ms1.2. As can be seen from Fig. 8-5, the storage modulus evolution of AAS pastes has two phases: Phase one defines a gradual development of storage modulus evolution until the onset of another regime in storage modulus evolution which is characterized by a sharp and continuous increase of storage modulus (phase two). For the mixture REF\_Ms1.2, the first phase occurred before 20 min, where there was negligible growth in storage modulus. In this phase, the colloidal interaction forces between particles were dissipated owing to the viscous nature of the activator solution [49]. In the meantime, due to the high silicate concentration in the Ms1.2 solution, the silicate anions would adsorb on the particle surface, increasing the

magnitude of repulsive double-layer electric forces [102]. Thus, the storage modulus was negligible at an early age due to the plasticizing and deflocculating effects. Phase two was between 20 min and 45 min. A sharp increase in the storage modulus was observed during such a short period of time. This is probably due to the continuous dissolution of GGBFS in phase one, letting the ions in the suspension gradually saturate so that the interactions between different ions in phase two occurred rapidly and started to form a rigid network. The measurement was stopped when the storage modulus reached the limits of the measurement system of 400 kPa [20], [50].

As can be seen from Fig. 8-5, the addition of CA, SB and SP made a significant change on the onset of the sharp increase in storage modulus due to their retarding effect. As can be seen from Fig. 8-5a, the period of phase one slightly increased and the rigidification rate of storage modulus in phase two significantly decreased by the increasing dosage of CA. Previous studies reported that  $H^+$  provided by CA reduced the alkalinity of activator solution [313], slowing down the heat evolution. Similar to this, the CA addition can also delay the increase in storage modulus and setting times in this study.

The incorporation of SB significantly increased the period of phase one and delayed the main increase in storage modulus in phase two as compared to that of CA addition (Fig. 8-5b). On the other hand, unlike the CA addition, the incorporation of SB did not influence the structuration rate significantly, indicating that SB would only cause a delay on the onset of structuration but not change the microstructure of AAS pastes during the structuration phase. Yousefi et al. [163] also found that a higher amount of SB (i.e., 8% weight of precursors) can also improve the workability and setting times without any deterioration on compressive strength. This also indicates that SB has great potential to retard the hardening rate of AAS even at a high dosage.

In the presence of SP, AAS pastes also exhibited a more extended period of phase one. However, the retarding effect of SP on AAS pastes was not as strong as SB. The mixtures with 4% and 5% SP showed an almost similar trend of structural build-up, indicating that the excessive amount of SP cannot effectively retard the structuration process of AAS.

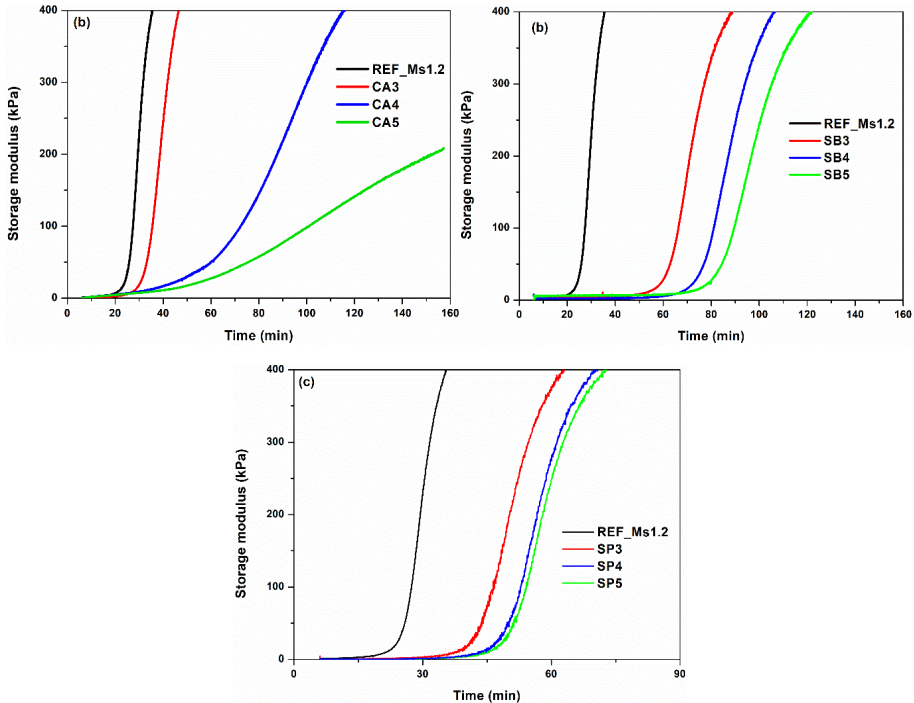


Fig. 8-5 The evolution of structural build-up of AAC pastes (a) CA addition, (b) SB addition and (c) SP addition.

### 3.5 Pore solution chemistry and its relation to the structural build-up of AAS pastes

Four mixtures (REF\_Ms1.2, CA4, B4 and SP4) were selected to investigate the reaction process of AAS at an early age. The relationship between the ion concentrations of Si, Na, Al, Ca, Mg, B, P and Fe in the pore solution and structural build-up of AAS as a function of time are presented in Fig. 8-6. The ion concentrations at zero time show the ion concentrations in the activator solution itself. As well known, on the one hand, the measured ion concentrations of the pore solution show the remaining part of the dissolved ions from the GGBFS or the existing ions in the pore solution after their consumptions to produce the reaction products [47]. On the other hand, it should be noted that the early structural build-up of AAS paste is a physico-chemical process with a combined result of colloidal interactions and chemical reaction processes, which is similar to PC system [33], [101]. Nevertheless, the correlation between pore solution chemistry and early structural build-up is very helpful to understand the dissolution kinetics and setting process of AAS.

According to Fig. 8-6, the pore solution chemistry of all AAS pastes was dominated by Na and Si, whereas much lower P, B, Al, Ca, Mg and Fe were identified. As

explained in Section 3.3, the evolution of storage modulus can be divided into two phases. In phase one, there was a negligible increase in storage modulus as the GGBFS particles were well dispersed in the activator solution. This dispersion effect leads to more interaction of the alkaline solution and GGBFS grains, thereby promoting the dissolution. Consequently, the concentration of Al, Ca, Mg and Fe increased to a peak value at the end of phase one due to the ongoing dissolution of GGBFS. While the main elements in pore solution, Na and Si, did not change significantly in phase one. Once the dissolved ions gradually reached the oversaturated state, the solid reaction products started to form, leading to the onset of the second phase. In this phase, a significant increase in storage modulus and the concomitant dramatic decrease in the concentration of Ca and Si was observed, probably due to the fast precipitation of C-S-H consuming Si and Ca in the pore solution [70]. Palacios et al. [20] also determined the saturation indices from the elemental concentration determined by ICP-OES to predict the solid reaction products that would form. Their thermodynamic calculations showed that M-S-H, C-N-A-S-H, hydrotalcite, siliceous hydrogarnet ( $\text{Ca}_3\text{Fe}_2(\text{SiO}_4)_{0.84}(\text{OH})_{8.64}$ ) and several Na-containing zeolites: hydroxy-sodalite ( $\text{Na}_8\text{Al}_6\text{Si}_6\text{O}_{24}(\text{OH})_2 \cdot 2\text{H}_2\text{O}$ ), natrolite ( $\text{Na}_2\text{Al}_2\text{Si}_3\text{O}_{10} \cdot 2\text{H}_2\text{O}$ ), Na-chabazite ( $\text{Na}_2\text{Al}_2\text{Si}_4\text{O}_{12} \cdot 6\text{H}_2\text{O}$ ) and faujasite X ( $\text{Na}_2\text{Al}_2\text{Si}_{2.5}\text{O}_9 \cdot 6.2\text{H}_2\text{O}$ ) were at all-time oversaturated, reflecting that these solids could potentially form. These solid reaction products could also possibly form in this study as the composition of their AAC mixtures was quite similar to REF\_Ms1.2. Correspondingly, it could be seen that the concentration of Na, Fe, Al and Mg also decreased in phase two as some potential solids started to form in this stage. Favier et al. [78] also showed that after some time, the decreasing trends of Al and Na in the liquid phase were concomitant, indicating the Al was taken up in the tetrahedral position of aluminosilicate phase and Na compensated for the charge balance. Their findings support the results of this study.

In general, the mixtures with the addition of CA did not significantly prolong phase one, and the concentration of Ca and Al were lower than that of REF\_Ms1.2. Also, the mixtures with CA addition spent more time in phase two than that of REF\_Ms1.2, indicating that CA4 had a lower structural build-up rate. Correspondingly, it could be seen that the concentrations of Ca and Si kept constant or slightly decreased in this stage, denoting less reaction products would form. This indicates that CA addition reduced the pH value of the activator solution, and thus the dissolution rate of GGBFS decreased. Eventually, the reaction process of CA4 was delayed.

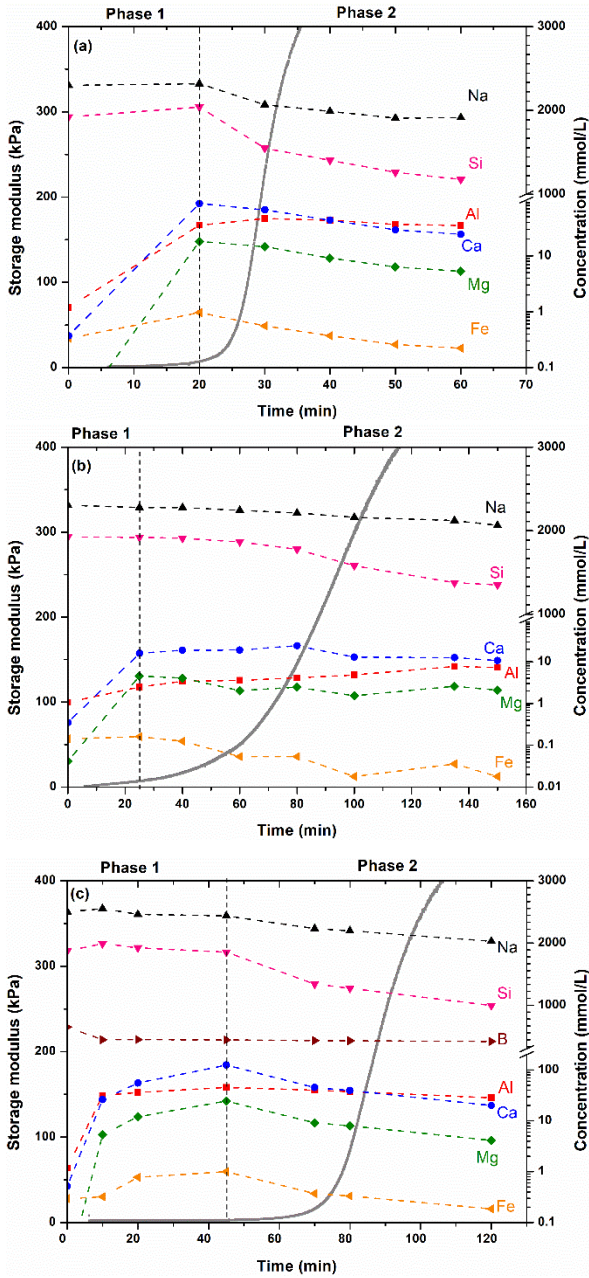
When the pore solution chemistry of REF\_Ms1.2 and SB4 mixtures were compared (Fig. 8-6a and c), it could be seen that the occurrence of the peak concentrations of Ca, Al, Mg and Fe was delayed in SB4 mixture, and their concentrations first quickly increased continuously in phase one. Herein, although the peak of Al was not easily visible in the log scale, its concentration actually increased to the maximum value (45 mmol/l) at the age of 45 min, and then decreased to 28 mmol/l at the age of 120 min. While the concentration of B rapidly decreased initially and continuously declined through the measurement time, more specifically, the B concentration rapidly

decreased from 649 mmol/l (at zero time) to 444 mmol/l (at the age of 10 min), and then slightly decreased to 417 mmol/l (at the age of 120 min). In previous literature, it was reported that the reason for the retardation effect of SB in Portland cement systems had been shown as the slowing down of hydration due to the calcium ion consumption by borax to form a calcium-based borate layer, which prevents the formation of reaction products [322]. Revathi et al. [312] reported that the higher early dissolution of alumina and silicate species was significantly disturbed by the presence of borate ions in the AACs pastes due to the reaction of  $\text{BO}_4$  tetrahedron with  $[\text{SiO}_4]$ , so that the retardation of  $[\text{AlO}_4]$  in the network was effected and thus setting time of the mixtures prolonged. For this reason, the borate in the pore solution would also possibly interact with Ca and Si ions, thereby delaying the structural build-up and setting of AACs.

The mixture SP4 presented a similar retarding mechanism with mixture SB4, characterized by a delayed reaction product formation due to the consumption of Ca ions from precursors by the SP. The consumption rate of Ca decreased for SP4 as compared to REF\_Ms1.2 as shown in Fig. 8-6. This finding also supports the retarding effect of SP. As shown in Fig. 8-6d, the concentration of P slightly decreased first and then almost kept constant through the measurement time. This could be because the Ca ions dissolved from the GGBFS would bond with the phosphate anion from the SP. Previous studies [323] stated that the phosphate anions have strong affinities to Ca cations. Shi and Day [271] furthermore indicated that the formation of  $\text{Ca}_3(\text{PO}_4)_2$  retarded the activation of GGBFS as usually observed during the hydration of PC. Besides, Kalina et al. [173] used Raman spectroscopy and X-ray photoelectron spectroscopy to investigate the effects of  $\text{Na}_3\text{PO}_4$  on the reaction process of alkali-activated GGBFS system and showed that the calcium hydrogen phosphate phases, which prolong the initial setting time by delaying the growth of C-S-H due to Ca ion consumption, was first formed in the system. However, it was reported that these phases were not stable and they dissolved by time and the formation of less soluble phases such as secondary C-S-H gel and calcium hydroxyapatite took place.

Moreover, Dupuy et al. [324] recently used magic angle spinning nuclear magnetic resonance (MAS NMR) to study the structural evolutions of geopolymers. The authors tried to correlate the setting time evolutions with the NMR spectral deconvolution results. They analyzed  $^{31}\text{P}$  results and found that the presence of phosphate groups ( $\text{PO}_4^{3-}$ ) and  $\text{P}^{\text{Q}^1}$  (bonds to Al and/or Si) were supposed to be at the terminal of the aluminosilicate chains, leading to partial geopolymerization. Therefore, this can induce the formation of a secondary network, resulting in an extended setting time. Although the situation in the boron-based system was more complicated as the boron atoms in a tetrahedral environment ( $\text{B}^{\text{IV}}$ ) were connected to silicon tetrahedrons, the increasing setting time was attributed to discrepancies between the geopolymer network and the secondary network, which were related to the  $\text{B}^{\text{IV}}$  quantity. Furthermore, the presence of asymmetric  $\text{B}^{\text{III}}$  with one non bridging oxygen among the residual  $\text{B}^{\text{III}}$  is recognized in relation to the declined pH value, which also

contributed to the increase in setting time.



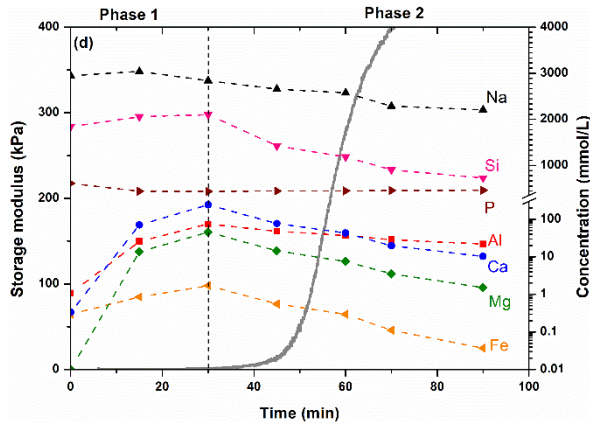


Fig. 8-6 The relationship between the evolution of structural build-up and pore solution chemistry of AAC pastes (a) REF\_Ms1.2, (b) CA4, (c) SB4 and (d) SP4.

### 3.6 X-ray diffraction of AAS pastes

The XRD patterns of AAS pastes at the age of initial set and 7 days are shown in Fig. 8-7. The main diffraction peak corresponding to C-A-S-H type gel for the AAS pastes are difficult to observe at the age of the initial setting time. Previous studies [44] also reported the same observation that the C-A-S-H gel was difficult to be identified at an early age. No new phase formations around the setting time of the mixtures REF\_Ms1.2 and CA4 could be identified by the XRD. However, some crystalline traces were observed for sample SB4, indicating the formation of a type of calcium-based borate mineral, colemanite ( $\text{Ca}_2\text{B}_6\text{O}_{11} \cdot 5\text{H}_2\text{O}$ ). This is also consistent with the results of pore solution chemistry that the concentration of B (boron) decreased in the first 10 min (Fig. 8-6c). Similarly, whitlockite ( $\text{Ca}_3(\text{PO}_4)_2$ ) traces were also observed for the mixture SP4, which was also in agreement with the decrease in P as shown in Fig. 8-6d. In previous studies, the researchers also pointed out that the formation of  $\text{Ca}_3(\text{PO}_4)_2$  has a retarding effect on the reaction of AACs [165].

As can be observed from Fig. 8-7b, the peaks around  $29.5^\circ$  in  $2\theta$  were visible for all the pastes [152], [163], [300], indicating the formation of poorly-crystalline C-A-S-H at the age of 7 days. It could be seen that CA4 showed a poorly crystalline structure for C-A-S-H as compared to the other mixtures. This was also consistent with the finding that CA4 could develop much lower strength at the age of 7 days (Table 8-3).

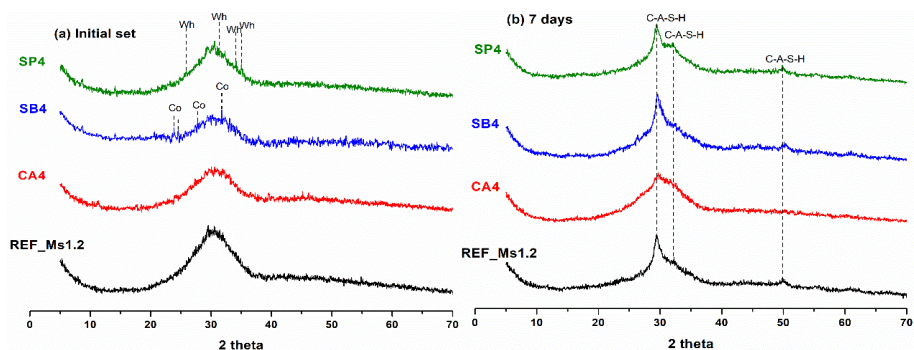


Fig. 8-7 X-ray diffractograms of AAC pastes at the age of (a) initial set and (b) 7 days. Peaks marked are Whitlockite (Wh, PDF# 09-0169), Colemanite (Co, PDF# 33-0267) and C-A-S-H (PDF# 89-6458).

### 3.7 Porosity of AAS pastes

Fig. 8-8 shows the pore size distribution of AAS pastes determined by MIP at the age of 28 days. In general, AAS paste had a very fine pore structure except for mixture CA5 and CA4. It could be seen that with the increasing addition of CA, the cumulative pore volume of AAS pastes increased. In particular, when the dosage of CA reached 5%, the microstructure of AAS pastes became very porous as compared to other mixtures. This is also consistent with the results of mechanical performance as presented in Table 8-3. As can be seen in Fig. 8-8b, the mixtures with the addition of SB showed much smaller cumulative pore volume than that of mixtures with CA addition. In addition, these mixtures incorporating SB exhibited very similar or slightly smaller cumulative pore volume as compared to that of REF\_Ms1.2, indicating there was no degradation of the microstructure of the AAS with the addition of SB. However, as can be seen in Fig. 8-8b, borate incorporated mixtures have a somewhat coarser pore size distribution as compared to REF\_Ms1.2.

Furthermore, SP showed a significant positive effect on the reduction of porosity, enhancing the microstructure of the AAS pastes. Unlike the other two chemical retarders, with increasing dosage of SP, the cumulative pore volume of AAS mixtures even decreased, which was also in agreement with the compressive strength. A denser microstructure of AAS pastes could be formed due to the addition of SP.

As shown in Fig. 8-8 and Table 8-3, the addition of SP or SB can increase the mechanical performance and reduce the porosity of AAS pastes. This is possibly because these chemical admixtures would also participate in the alkali-activation system [163]. Antoni et al. [164] have pointed out that the flash set of class-C fly-ash-based geopolymers could be prevented by adding anhydrous borax with a significant increase in the compressive strength of the geopolymer. A few researchers also confirmed that when borax was used as a part of alkaline activator for geopolymer

pastes, the flexural strength increased due to the formation of B-O bonds in the reaction products [325], [326]. Furthermore, Revathi and Jeyalakshmi [312] reported that using an appropriate dosage of borax into the GGBFS-Fly ash system could slightly increase the compressive strength, implying that competition between  $[\text{BO}_4]$  and  $[\text{AlO}_4]$  in the network of the silicate ended up with a lower degree of Al incorporation. Additionally, the very high reaction rate of Ref\_Ms1.2 may have retarded the subsequent reactions and produced a non-uniform distribution of reaction products as compared to those mixtures with chemical retarders (SB and SP).

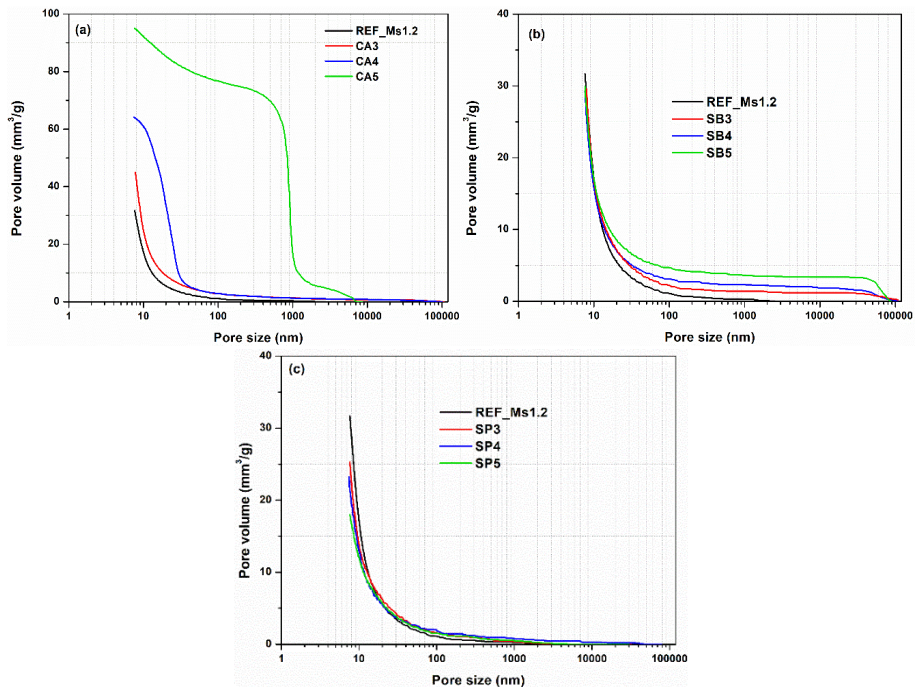


Fig. 8-8 Pore size distributions determined by MIP at the age of 28 days (a) CA, (b) SB and (c) SP.

### 3.8 SEM/EDX of AAS pastes

SEM/EDX analyses were carried out on the samples REF\_Ms1.2, CA4, SB4 and SP4. Backscattered electron imaging (BSE) and secondary electron imaging (SE) of AAS pastes at the age of 28 days are shown in Fig. 8-9. It should be noted that the highlighted white regions in SEM (BSE) images indicate the unhydrated GGBFS particles, the grey regions between the particles denote reaction products and the black regions represent the pores and micro-cracks. In general, from the morphology point of view, it seems that the binding paste in REF\_Ms1.2, SB4 and SP4 are denser and

present a more homogeneous morphology, while the CA4 sample shows heterogeneously distributed cavities, indicating a more porous microstructure. Besides, the amount of unhydrated GGBFS particles of SP4 seemed to be lower than in other mixtures. These are also in agreement with the MIP results as presented in Section 3.6. Similarly, as shown in SE images, SP4 showed a better packing and a denser microstructure, and this was followed by SB4, REF\_Ms1.2 and CA4.

The EDX results obtained for at least 15 points selected from within the binder region (BSE image) of AAS pastes are shown in Fig. 8-10 and Table 8-5. In literature [327], [328], researchers have demonstrated that a reduction of the Ca/Si ratio has a markedly beneficial impact on the mechanical properties of cementitious materials. It is believed that the higher molar quantities of C-S-H gel per volume were obtained when the Ca/Si ratio is low [327]. Indeed, the SP4 mixture had the lowest Ca/Si ratio of 0.91 and presented the best mechanical performance among all mixtures.

The Al/Si ratio of SB4 mixture was the lowest as compared to other mixtures, meaning that less Al was incorporated into the C-A-S-H structure. This may be related to the incorporation of 4-coordinated boron into the C-A-S-H structure. These interactions have been characterized by NMR studies by Du et al. [329], [330], who identified the chemical shift related to the B-O-Si bonds according to the number of silicon atoms associated with each boron. In the case of SP4, some researchers [331] also reported that  $Al^{3+}$  ions induce a modification of P-O-P bonds that are partly replaced by Al-O-P bonds. Other authors [332], [333] also pointed out that phosphorous atoms could be bonded to a different number of aluminum atoms which could also be linked to the silica network. This might be the reason why SP enhanced the mechanical performance of AAS. Indeed, the SP4 also showed the highest Na/Si ratio of all mixtures as the phosphate groups required a large amount of alkali for charge compensation [332].

As for magnesium, it is generally known that they would participate in the formation of hydrotalcite type sub-micrometer phase as reported previously by Wang and Scrivener [276]. However, the hydrotalcite reaction products were not detected by XRD carried out at the age of 7 days, as presented in Section 3.5. It could be possibly due to the fact that the hydrotalcite would start to form at a later age when a high degree of GGBFS reaction was reached, as reported by Song and Jennings [334].

Calcium, aluminum and silicon contents of samples with 28 days of curing are also renormalized to 100% on an oxide basis for plotting on the ternary graph (i.e., neglecting the other elements present). These plots clearly show the variation in the gel composition in terms of the effects of different chemical retarders. It could be seen that the major reaction product for these four mixtures was a chained-structure C-A-S-H, which was commonly recognized in the alkali-activated GGBFS system [248].

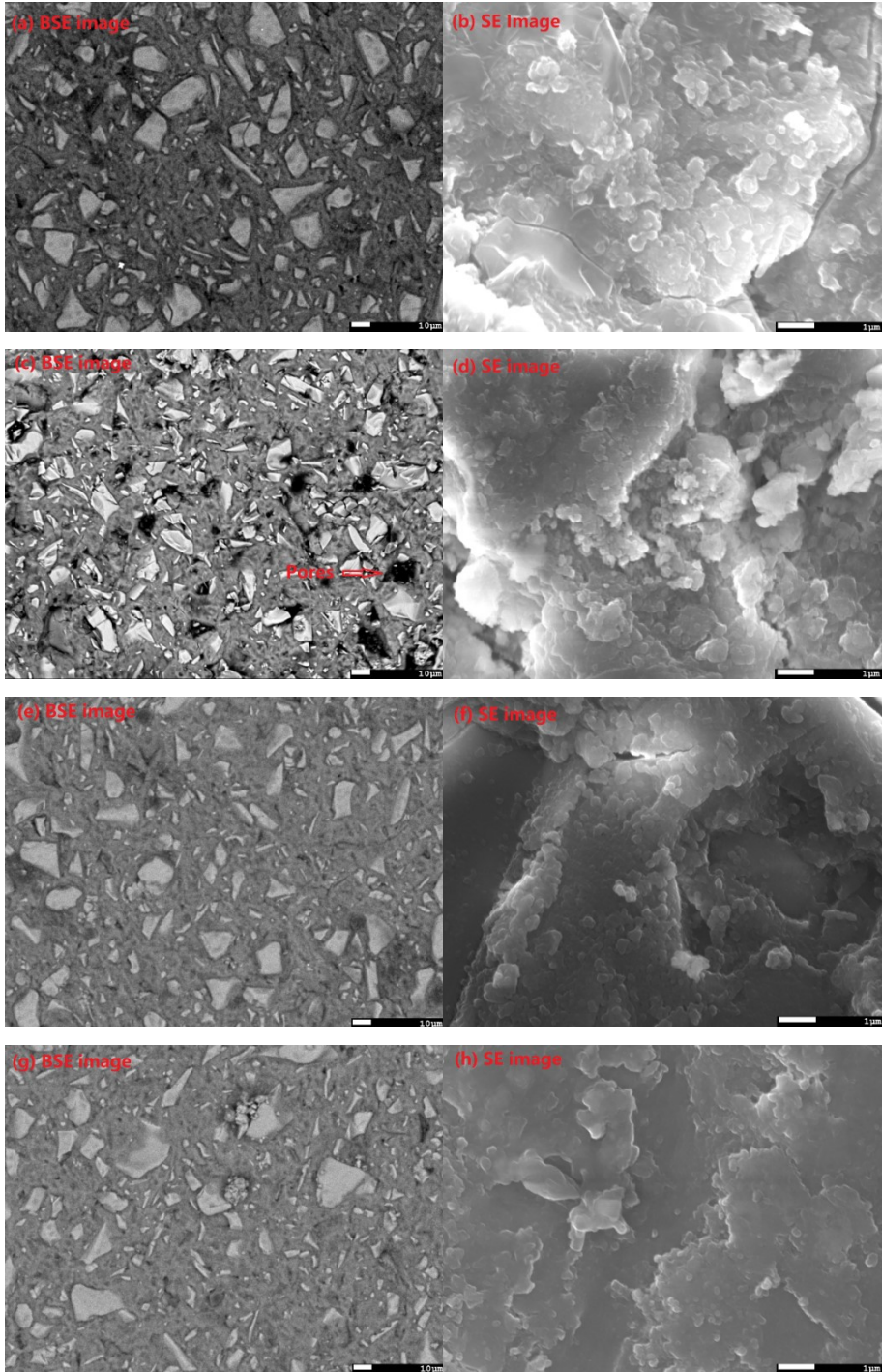


Fig. 8-9 SEM and BSE images of AAS pastes at the age of 28 days (a), (b)

REF\_Ms1.2, (c), (d) CA4, (e), (f) SB4 and (g), (h) SP4.

Table 8-5 Average atomic ratios determined by EDX analyses.

Mixture	Ca/Si	Al/Si	Na/Si	Mg/Si
REF_Ms1.2	1.06 ± 0.11	0.31 ± 0.03	0.32 ± 0.12	0.21 ± 0.11
CA4	1.19 ± 0.20	0.33 ± 0.02	0.27 ± 0.04	0.24 ± 0.31
SB4	0.94 ± 0.05	0.25 ± 0.04	0.39 ± 0.07	0.13 ± 0.05
SP4	0.91 ± 0.04	0.31 ± 0.05	0.42 ± 0.16	0.21 ± 0.06

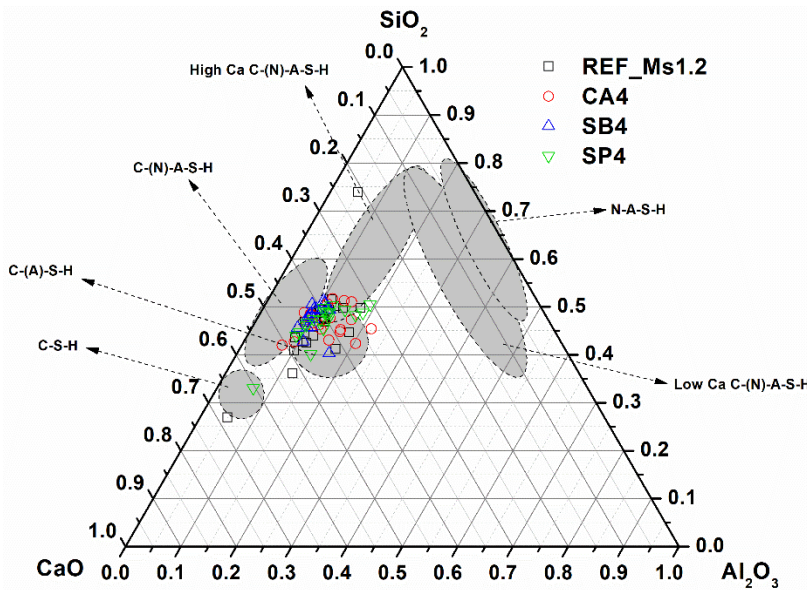


Fig. 8-10 Compositional Ternary Diagram Al<sub>2</sub>O<sub>3</sub>-SiO<sub>2</sub>-CaO (as normalized to 100%) of AAS at 28 days showing the literature for C-S-H [304], [305], C-(A)-S-H [248], [303], [307], C-(N)-A-S-H [70], [308], C-(N)-A-S-H with high Ca [89], [248], [305] and low Ca content [248], [309], and N-A-S-H [248], [307].

#### 4. Conclusion

---

This chapter compares the effects of different chemical retarders on the early structural build-up, setting behaviour, reaction kinetics, microstructure and mechanical properties of sodium silicate-activated GGBFS mixtures. The following conclusions can be drawn from this study:

1. The retarding effect of citric acid (CA) was found the most predominant, and it is followed by sodium tetraborate decahydrate (SB), then sodium triphosphate pentabasic (SP) in terms of flowability and setting times. However, the addition of CA had a negative effect on the mechanical performance, porosity and microstructure. The inclusion of SP could promote more heat release and significantly enhance the compressive strength at an early age. By considering fresh and hardened state properties together, SB has been found as the most appropriate chemical retarder as compared to CA and SP for sodium-silicate activated AAS mixtures tested under the experimental conditions used in this study.
2. The induction period of AAS paste could be significantly extended by the incorporation of CA and shortened by the addition of SP. The use of SB showed a very similar heat flow curve as compared to the reference sample but exhibited a lower cumulative heat at the age of 7 days.
3. Some meaningful relationships between early structural build-up and pore solution chemistry have been observed. The main increase in the structural build-up is delayed by the addition of chemical retarders. During the period of the main increase in the structural build-up, Ca, Al and Si decrease rapidly and interact together to form reaction products.
4. The MIP results and BSE images showed that the addition of SP could lead to a denser microstructure with lower porosity, while a porous microstructure was formed by the incorporation of CA. The XRD and EDX results confirmed that the main reaction product of AAS with the addition of chemical retarders was C-A-S-H.

## **Part VI**

---

### **Setting mechanism and nanostructure of sodium hydroxide- and sodium silicate-activated slag mixtures**



## **Chapter 9 Setting mechanism of AAS mixtures from rheological point of view**

---

In this chapter, the setting mechanism of AAS mixtures made with sodium hydroxide or sodium silicate is investigated from a rheological point of view.

## 1. Introduction

---

Revealing the fundamentals behind the structural build-up of cementitious materials is very important to industrial formulations due to the contradicting needs for rheology of fresh mixtures. For instance, fresh concrete should have low yield stress and a reasonable plastic viscosity for a good workability, however, after the concrete casting into the formwork, the rapid development of structural build-up is advantageous for decreasing formwork pressure and speeding up the casting process [35]. Additionally, in terms of 3D-printing of cement-based materials, it is critical to optimize the degree of structural build-up to ensure the sufficient buildability [159], [335], [336]. Indeed, rapid structural build-up can influence the bond between cast layers within the printed structures. Meanwhile, an acceptable structural build-up rate is necessary to achieve a strength level capable of supporting the weight of successive extruded layers [39]. Although there are many studies in the literature on the initial rheology and structuration over time for conventional casting processes or novel ones like 3D printing for Portland cement mixtures, few studies are available focusing on the kinetics of structuration of AAS pastes. Understanding of the effects of activator nature on the rheology and structural build-up of AAS is of importance. This chapter aims to distinguish the fundamental differences in the initial rheological properties and time-dependent behaviour between sodium hydroxide- and sodium silicate-activated pastes. The initial rheological properties were evaluated by yield stress and viscosity, and the effects of activator type on the yield stress and viscosity were investigated. The time-dependent behaviour was also evaluated by various tests, such as calorimetric measurement and small amplitude oscillation sweep test. The supplied data can be used to further the fundamental understanding of the kinetics of structural build-up in AAS suspension. This can enhance the knowledge and control of structural build-up of AAS pastes at fresh state.

## 2. Experimental program

---

### 2.1 Materials and mixture design

---

Ground granulated blast furnace slag (GGBFS) was used as a sole precursor in this chapter. In comparison with the rheological behaviour of AAS, CEM I 52.5-N type Portland cement (PC) and inert quartz powder were also used. Specifically, the quartz powder was subjected to a series of milling procedures and its particle size distribution to ensure that quartz powder and GGBFS have the identical particle size distribution as far as possible. Fig. 9-1 presents the particle size distributions of binding materials. The  $d_{10}$ ,  $d_{50}$  and  $d_{90}$  of the GGBFS / quartz powder is around 1.5 / 1.3  $\mu\text{m}$ , 11.6 / 13.2  $\mu\text{m}$  and 22.8 / 26.1  $\mu\text{m}$ , respectively. The specific gravity of PC, GGBFS and quartz are 3.15, 2.92 and 2.65, respectively.

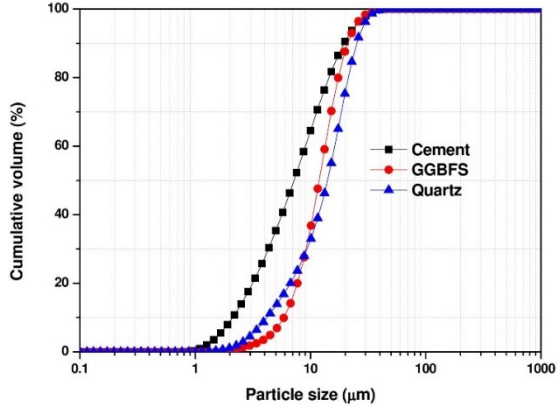


Fig. 9-1 Particle size distribution of binding materials.

The mixture properties are given in Table 9-1. As well known, in the manufacturing of AAS concrete, sodium silicates with a  $M_s$  value ( $\text{SiO}_2/\text{Na}_2\text{O}$ ) of less than 1.5 are commonly used for lower carbon emission solutions. Also, it was reported that the AAS concretes with a  $M_s$  ratio between 1.0 and 1.5 could provide better mechanical and durability performance [268]. For these reasons, the alkaline activator with a  $M_s$  value of 1.2 was investigated in this study. As shown in Table 9-1, PC is a Portland cement paste with water to cement ratio of 0.34. AAS0 is a sodium hydroxide-activated GGBFS mixture with a  $M_s$  value of 0, AAS1.2 is a sodium silicate-activated GGBFS mixture with a  $M_s$  value of 1.2. The AAS mixtures had a constant  $\text{Na}_2\text{O}\%$  concentration of 5% by weight of precursors. To eliminate the influence of the chemical interaction between slag and activator solution and investigate the physical effect of the particles on the rheological properties of AAS mixtures, the quartz powder mixtures were also prepared by using sodium hydroxide and sodium silicate solutions (AAQ0 and AAQ1.2). Solid volume fractions were similar for all the mixtures. Although quartz powder can show some very low amount of dissolution by time in high alkaline environment, quartz powder was still assumed as an inert material in this study since the measurements were carried out in a short time period.

Table 9-1 Mixture proportions of AAS and PC pastes.

Mixture notation	W/SB* /	Ms ratio (SiO <sub>2</sub> /Na <sub>2</sub> O)	Na <sub>2</sub> O% content	Liquid sodium silicate solution (g)	Sodium hydroxide (g)	Additional water (g)	GGBFS (g)	quartz (g)	PC (g)	Initial solid volume fraction (%)
	W/C									
PC	0.34	-	-	0	0	37	0	0	110	48.55
AAS0	0.37	0	5	0	6.24	37	93.76	0	0	48.64
AAQ0	0.41	0	5	0	6.24	37	0	85.10	0	48.64
AAS1.2	0.37	1.2	5	18.90	1.46	26.88	89.76	0	0	48.58
AAQ1.2	0.40	1.2	5	18.90	1.46	26.88	0	81.46	0	48.58

\* W-water, B-solid binder (GGBFS + solids in activator solution). 100 g solid binder was used in all the mixtures.

## 2.2 Sample preparation

A rotational rheometer with a helix geometry was used to prepare the AAS samples for the rheological and calorimetric tests. The mixing protocol consisted of two stages: First, the shear rate was gradually increased from 0 to 3,000 min<sup>-1</sup> within 30 s, and then the mixing speed was kept constant at 3,000 min<sup>-1</sup> for 120 s. The samples for setting times and ultrasonic wave tests were prepared by a Hobart mixer. The precursors particles were added to the activator solution in the Hobart mixing bowl, and mixed at low (140 ± 5 rpm) and high (285 ± 5 rpm) speeds for 90 s each.

## 2.3 Protocol for flow curves and SAOS tests

The flow tests were carried out by continuous shear rate ramping up and down to evaluate the rheological properties (yield stress and viscosity) of AAS and PC pastes under shear. After mixing and pouring the sample into the small rheometer cup, a pre-shearing with a shear rate of 100 s<sup>-1</sup> was first applied for 30 s, and then a rest period of 30 s was applied for avoiding residual stresses [49]. Afterwards, the shear rate was logarithmically increased from 0.1 s<sup>-1</sup> to 100 s<sup>-1</sup> within 300 s, and then it was decreased from 100 s<sup>-1</sup> to 0.1 s<sup>-1</sup> within the following 300 s. The shear stress and shear rate data were recorded every second. The downward flow curves obtained from each AAS paste fit well the Bingham model or modified Bingham model [49], [51], [159] (Eq. (2-1) and Eq. (2-2), respectively). The viscosities of the alkaline solutions (sodium hydroxide and sodium silicate) used in this study were also measured using the flow tests.

Small amplitude oscillatory shear (SAOS) tests were conducted to monitor the viscoelastic properties of AAS pastes in their non-destructive regimes. Therefore, the critical strains limiting the linear viscoelastic regions (LVER) of the pastes were determined by strain sweep tests. The strain amplitude was increased from 0.001% to

50% at a constant frequency of 1 Hz. As shown in Fig. 9-2, a strain amplitude of 0.005%, which is lower than the determined critical strain limiting the LVER, was used to guarantee the strain amplitude test was carried out within the LVER of the material. The temperature was controlled at  $20 \pm 0.5$  °C throughout the measurements.

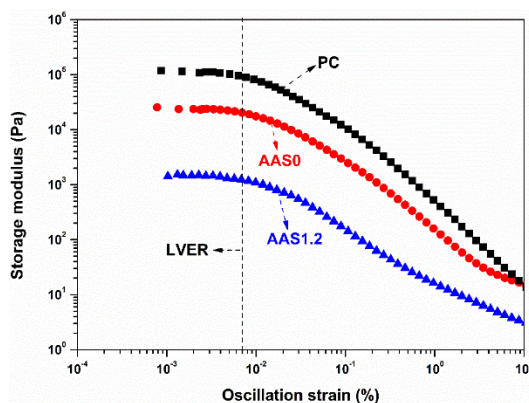


Fig. 9-2 Oscillation strain sweep for PC and AAS paste, a frequency of 1 Hz was used.

Continuous SAOS measurements were performed with the following steps: (i) After mixing, the fresh paste was loaded into the rheometer cup and was subjected to the pre-shear at a rotational speed of  $100 \text{ s}^{-1}$  for 30 s to reach the reference state. (ii) Afterwards, the paste samples rested for 30 s to dissipate residual stresses due to mixing and pre-shearing. (iii) Then, the time-sweep tests were conducted at around 8 min. In intermittent SAOS measurements, steps (i) and (ii) were the same as the continuous SAOS measurements. The time-sweep tests were carried out for 10 min, then the pastes were subjected to a high shear at  $600 \text{ s}^{-1}$  for 2 min. (iv) The procedure (iii) was repeated six times.

### 3. Results and discussions

#### 3.1 Rheological properties of AAS and PC pastes

##### 3.1.1 Yield stress and plastic viscosity

Fig. 9-3 presents the downward portion of the shear stress versus the shear rate of the pastes. The plastic viscosity and dynamic yield stress values determined from the flow curves in Fig. 9-3 are shown in Table 9-2. It could be seen that the dynamic yield stresses of AAS pastes were much lower than that of PC pastes, agreeing with the results by Alnahhal et al. [49] and Favier et al. [101]. Furthermore, the sodium silicate-

activated GGBFS mixture (AAS1.2) even showed significantly lower yield stress than sodium hydroxide-activated GGBFS mixtures (AAS0). Regarding the plastic viscosity, the AAS1.2 mixture exhibited the highest value as compared to AAS0 and PC pastes.

To investigate the effect of GGBFS on the early rheological properties of AAS pastes, the inert quartz powder having similar particle size distribution were used to prepare the AAQ pastes. It should be noted that the AAQ0 and AAQ1.2 pastes have the same solid volume fraction with AAS0 and AAS1.2 pastes, respectively.

Concerning the mixtures AAS0 and AAQ0, it could be found that AAS0 displayed a higher yield stress than that of AAQ0 at the same solid volume fraction. This observation supports the formation of initial reaction products in the mixtures AAS0; as a result, the solid volume fraction of AAS0 increased after mixing, leading to a higher yield stress. However, when comparing the yield stress of AAS1.2 and AAQ1.2, there was no significant difference between their yield stress. This indicates that almost no new reaction products are formed at very early age for the sodium silicate-activated system.

Besides, the plastic viscosity values of AAQ pastes are lower as compared to AAS pastes. This probably can be explained by the water film thickness theory. Previous studies [117], [337] pointed out that plastic viscosity generally showed inverse correlations to the water film thickness. As well known, quartz powder exhibits superior natural hydrophilic properties, leading to a higher water film thickness. As a result, the plastic viscosity of AAQ pastes decreased.

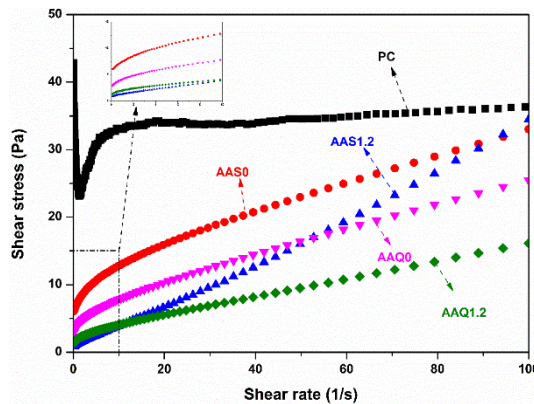


Fig. 9-3 Flow curves of AAS and PC pastes.

Table 9-2 Rheological parameters of the cementitious pastes and activator solution.

Mixture notation	Dynamic yield stress (Pa)	Plastic viscosity (Pa·s)	Interstitial fluid	Estimated yield stress of interstitial fluid (Pa)	Newtonian viscosity of interstitial fluid (Pa·s)
PC	27.88	0.94	Water	N/A	0.001
AAS0	8.00	2.13	Sodium hydroxide solution	~0.01	0.010
AAQ0	4.27	1.91			
AAS1.2	0.78	3.18	Sodium silicate solution	~0.009	0.015
AAQ1.2	1.00	1.49			

### 3.1.2 Shear thickening and shear thinning behaviour

As well known, fresh cement pastes can be considered as suspensions of particles with different sizes in a continuous fluid phase. Therefore, some interaction forces, such as surface forces (or colloidal interactions), Brownian forces, hydrodynamic forces and various contact forces between particles may exist [26]. Under the external shearing, these forces eventually determine whether the pastes exhibit shear thickening or shear thinning behaviour. In order to better observe the shear thickening and shear thinning behaviour of the cementitious materials at a wide range of shear rates, the shear rate was logarithmically increased from  $0.1 \text{ s}^{-1}$  to  $1000 \text{ s}^{-1}$ . The viscosity curves of PC paste in the log-log scale, as presented in Fig. 9-4, can be divided into two stages: (i) apparent viscosity decreased linearly when the shear rate was increased from  $0.1 \text{ s}^{-1}$  to  $100 \text{ s}^{-1}$ , due to the Van der Waals colloidal forces dominating the hydrodynamic forces (including both viscous and inertial) within the low strain rate regime [101]. In the meantime, this effect also gives rise to a shear-thinning macroscopic behaviour as shown in Fig. 9-3 and Fig. 9-4. (ii) with an increasing shear rate from  $100 \text{ s}^{-1}$  to  $1000 \text{ s}^{-1}$ , the apparent viscosity showed almost a constant value, showing that the viscous contribution was predominated above the contributions of colloidal interactions and particle inertia over a large range of shear rates. The apparent viscosity trend of sodium hydroxide-activated GGBFS mixture (AAS0) also presented almost the same trend with PC paste. In addition, the viscosity of AAS0 was lower than that of PC pastes at low shear rates but higher at high shear rates.

However, sodium silicate-activated GGBFS pastes (AAS1.2) showed a completely different rheological behaviour. The apparent viscosity of AAS1.2 was considerably lower than PC and AAS0 paste at the low shear rates ranging from  $0.1 \text{ s}^{-1}$  to  $10 \text{ s}^{-1}$ , indicating less colloidal interaction contributions to the viscosity of AAS1.2 pastes. With an increasing shear rate from  $10 \text{ s}^{-1}$  to  $50 \text{ s}^{-1}$ , the curves of apparent viscosity started to keep a constant value, showing that the viscous hydrodynamic forces were predominating during this shear regime. Furthermore, the apparent viscosity of AAS1.2 increased with an increase in shear rates from  $50 \text{ s}^{-1}$  to  $1000 \text{ s}^{-1}$ . This is

probably because particle inertia dominated the response at the high strain rates and may lead to shear thickening behaviour [26].

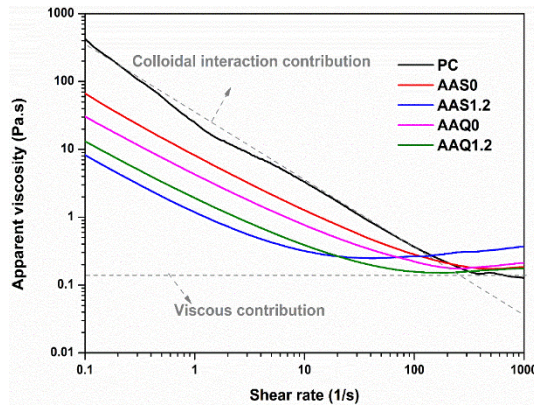


Fig. 9-4 Apparent viscosity as a function of shear rate from 0.1 s<sup>-1</sup> to 1000 s<sup>-1</sup> for AAS and PC paste.

### 3.1.3 The effect of activator on the yield stress of AAS pastes.

The source of the yield stress is due to the network of attractive particle-particle interactions that permit the suspension to withstand a finite amount of stress without flowing [26]. Therefore, it could be seen that PC pastes can exhibit higher yield stress due to the formation of an internal network of particles with attractive interactions either via direct contacts or via colloidal forces, and the contributions of the C-S-H formations bridging particles at the very early age [26], [49].

It is very interesting to observe that AAS1.2 mixture presented significantly lower yield stress as compared to that of PC and AAS0 mixtures although they all have a similar solid volume fraction (Table 9-1). The reason for the lower yield stress of AAS1.2 was probably because the colloidal interactions were no longer predominated in the case of sodium silicate-activated GGBFS mixture. In the existing literature [33], [47]–[49], [110], [338], the activator solution composition and its viscosity were considered to have a strong influence on the rheological and viscoelastic behaviour of alkali-activated pastes. Therefore, the estimated yield stress and Newtonian viscosity of the activator solution were determined by using the shear protocol in Section 2.2.1, and were shown in Table 9-2. One explanation of lower yield stress of sodium-silicate activated GGBFS (AAS1.2) might be the high viscosity of the activator solution, which is 15 times higher than that of water as shown in Table 9-2, dissipating the colloidal interactions between precursor particles [30], [31], [49], [110]. Some other researchers recently reported that the silicates in the AAS1.2 activator could be available to be adsorbed on the surface of GGBFS. As a result, the formation of the

strong double-layer repulsive forces between GGBFS particles led to the higher dispersion of the particles, also contributing to reducing the yield stress [102].

However, the mixture AAS0 exhibited higher yield stress as compared to AAS1.2. A possible explanation could be related to the higher pH of AAS0 compared to AAS1.2 at a constant content of  $\text{Na}_2\text{O}$  %, and the lack of aqueous silicates in the activator solution. Because, when the GGBFS was mixed with sodium hydroxide activator solution, a large number of GGBFS particles would accumulate in the absence of the lubricating effect of aqueous silicates, and the formation of early reaction products took place simultaneously due to the enhanced dissolution of GGBFS in highly alkaline environment [81], [110]. Besides, AAS0 activator showed a lower viscosity as compared to AAS1.2.

In order to demonstrate the presence of reaction products formation and colloidal interaction for the mixtures AAS0 and AAS1.2, the oscillation strain-sweep tests were carried out. Fig. 9-5 presents the evolution of oscillation stress for the mixtures AAS0 and AAS1.2 as a function of oscillation strain. As shown in Fig. 9-5, the evolution of oscillation stress of the mixture AAS0 showed two characteristic peaks, which is similar to what is commonly observed in a PC system [49], [101]. The first peak observed around a strain value of around 0.1 % has been associated with the breaking of calcium silicate hydrates (C-S-H) percolating between GGBFS particles [33], and this also was defined as the critical strain. The second peak at around 9% strain value indicates the network rupture of flocculated GGBFS particles. The formation of the flocculated structure was correlated to the colloidal interactions, which were also associated to the origins of yield stress [33]. For these reasons, the mixture AAS0 showed somewhat higher yield stress as shown in Table 9-2.

In contrast to AAS0, a distinctively different behaviour was observed in the mixture AAS1.2. There were no such noticeable peaks in the mixture AAS1.2, and the stress development as a function of oscillation strain was significantly lower than that of mixture AAS0. As discussed before, the particles are not flocculated due to the viscous effects of aqueous silicates preventing the formation of a network of interacting particles. Therefore, it could be concluded that the mixture activated by sodium hydroxide in general showed a similar rheological behaviour with PC pastes, whereas the initial rheological performance of sodium silicate-activated mixture was distinctively different and was mainly controlled by the viscosity of suspending activator solution.

As shown in Table 9-2, the yield stress of the activator solution is very low as compared to pastes mixtures, therefore they have no significant influence on paste rheology.

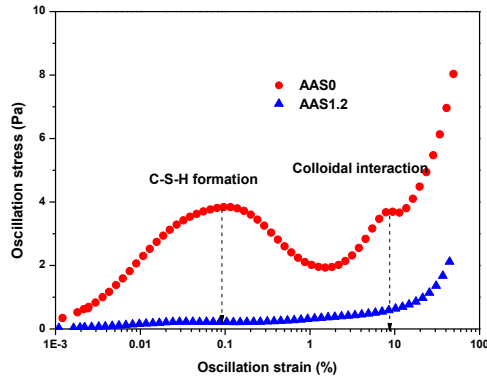


Fig. 9-5 Evolution of oscillation stress as a function of strain for sodium hydroxide-activated pastes (AAS0) and sodium silicate-activated pastes (AAS1.2).

### 3.1.4 The effect of activator on the viscosity of AAS pastes

The viscosity of AAS pastes is generally controlled by two parameters, the activator properties and the packing properties of the precursors since AAS pastes generally can be considered as suspensions of precursors in an activating solution with Newtonian behaviour [26], [33], [101].

As could be seen in Table 9-2, the estimated yield stress of activator solution is very small (almost zero), therefore the activator solution can be considered as a Newtonian fluid. The Newtonian viscosity of the activator AAS0 and AAS1.2 used in this study was 0.010 Pa·s and 0.015 Pa·s, which was 10 to 15 times higher than that of deionized water, respectively. As a result, as shown in Fig. 9-3 and Table 9-2, the plastic viscosity of AAS0 and AAS1.2 pastes was over 2 to 3 times higher than that of PC paste. Similarly, Alnahhal et al. [49] also reported that alkali-activated slag-fly ash pastes in general have a greater plastic viscosity than PC paste because of the high viscosity of the alkali activating solution.

Apart from the effect of viscous nature of activator solution, the solid volume fraction also plays an important role in the viscosity of cementitious pastes. To distinguish the contributions of the solid fraction to the viscosity, the relative viscosity is considered in this study, which is the ratio between the relative viscosity of AAS pastes and the viscosity of the activator solution (AAS0 and AAS1.2). Eight pastes of AAS0 and AAS1.2 were prepared with different solid volume fraction, respectively, and the relative viscosity of AAS pastes are shown in Fig. 9-6. As shown in Fig. 9-6, the relative viscosity of AAS0 and AAS1.2 converge when the solid volume fraction approaches to the value corresponding to the maximum packing fraction. Also, the evolution of the relative viscosity of these two mixtures showed a similar trend. Therefore, it is suggested that these two mixtures have a similar maximum packing

fraction, which is in the range of 0.5-0.55. In general the deflocculated cement paste in presence of superplasticizer always showed a maximum packing fraction in the range of 0.6-0.7 [101]. As a result, the grain contribution to the viscosity tends to be much higher for alkali-activated cements than for PC pastes at a same solid volume fraction. It should be noted that when the solid volume fraction was between 0.30-0.47, the relative viscosity of AAS0 was larger than that of AAS1.2. This is due to the sodium hydroxide results in more reaction products as compared to AAS1.2 in these range of solid volume fraction.

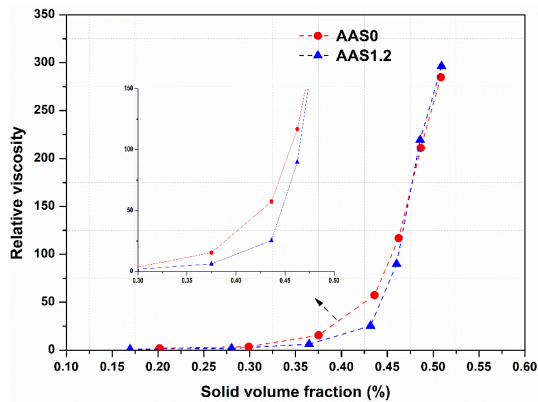


Fig. 9-6 The evolution of relative viscosity as a function of the solid volume fraction.

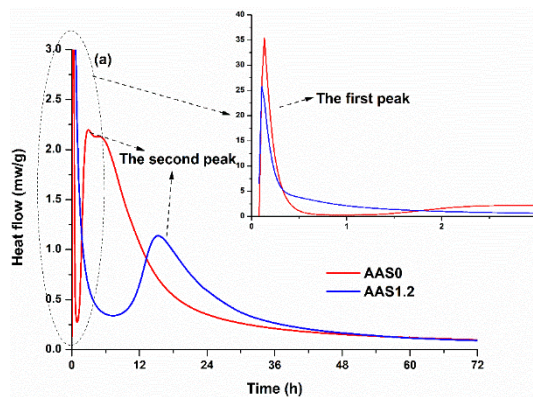
## 3.2 Time-dependent properties of AAS pastes

### 3.2.1 Vicat setting times and reaction kinetics of AAS pastes

The initial setting time of AAS1.2 mixture was around 51 min, which was significantly shorter than that of AAS0 (126 min). The final setting times also showed the same trend that sodium silicate-activated mixtures (120 min) reached to the final set earlier than the sodium hydroxide-activated mixtures (180 min). These results were in agreement with a previous study [162], reporting the shortened initial and final setting times by the alkali activator dosage (weight sum of  $\text{SiO}_2\%$  and  $\text{Na}_2\text{O}\%$ ) increase. It is also reported that the quick setting times of AAS mixture activated by sodium silicate solution is due to the dissolved  $\text{Ca}^{2+}$  and aluminate species interact with  $\text{Na}^+$  and silicate ions originated from activator solution, leading to the massive formation of reaction products [20]. The same authors also used thermodynamic calculations to indicate that the precipitation of reaction products can take several hours for sodium hydroxide-activated slag mixtures, this is due to no initial silicate species are present in solution and the concentration of silicate and aluminum species as well as Ca ions gradually increases as the slag dissolves.

As well known, the setting time determined by a Vicat needle penetration depth can provide some information on the setting evolution after the initial setting time, but it is not sensitive to the structuration changes before the initial setting time. Therefore, the more details about the structuration process of AAS mixtures before initial setting time by using SAOS measurements will be discussed in the following sections.

The heat evolution and cumulative heat release of AAS mixtures are given in Fig. 9-7. In general, the calorimetric curve for sodium hydroxide- and sodium silicate-based GGBFS mixtures can be divided into five distinctive stages: dissolution, induction, acceleration, deceleration and steady-state [51], [81], [207], [271]. Two recognizable peaks were observed for these two mixtures: the first one taking place before the first 30 min is assumed to be related to the wetting and dissolution of GGBFS particles and partly the interaction of silicate units and calcium dissolved from GGBFS [207], [272]; the second one after the induction period is normally associated with the strength and microstructural development [271]. It could be seen that the intensity of these two peaks for AAS0 were much higher than AAS1.2. The occurrence of the second peak for AAS0 was much earlier as compared to AAS1.2, indicating a quicker early-reaction process. Regarding the cumulative heat, the AAS0 and AAS1.2 mixtures exhibited approximately 125 J/g and 105 J/g heat at 72h, respectively. To investigate the relationship between the heat release rate and the initial setting times of AAS mixtures, the heat evolution of AAS mixtures in the first 3h is also given in Fig. 9-7. After the first exothermic peak, the heat flow of AAS1.2 decreased slowly in the first hour, and the released heat indicated more formation of reaction products, contributing to the quick initial setting of AAS1.2. Afterwards, the heat flow of AAS1.2 entered the induction period, and it started to increase until approximately the age of 8h. However, the heat flow of the AAS0 mixture rapidly decreased in the first 1.5h as compared to AAS1.2, and moved into the acceleration period from approximately the age of 1.5h. Meanwhile, in the acceleration period, the AAS0 reached to its initial and final setting times.



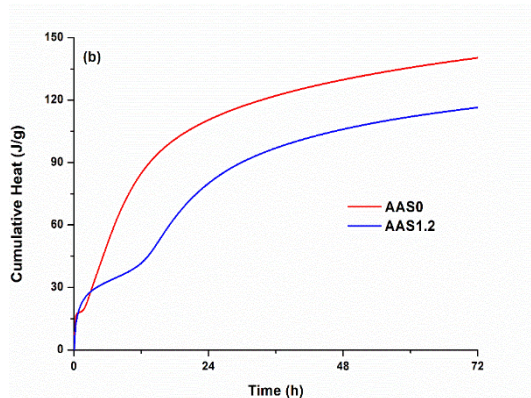


Fig. 9-7 The heat evolution (a) and cumulative heat release (b) of AAS mixtures.

### 3.2.2 Structural build-up of AAS and PC pastes.

The evolution of storage modulus of PC and AAS pastes by continuous and intermittent SAOS tests are illustrated in Fig. 9-8. The storage modulus evolution is assumed to be an important indicator for the structuration of cementitious materials at an early age [47], [49], [111], [159].

In the continuous SAOS measurements, regarding the PC pastes, the storage modulus started from a very high value and increased rapidly in the first 15 min. Afterwards, the storage modulus continued to increase with a significantly lower rate. The same trend was also observed in AAS0 paste, showing a rapid increase in storage modulus for the first 15 min and a significantly lower increasing rate beyond 15 min. The possible reason for the PC system has been explained by [33] as follows. The dispersed cement particles after mixing phase start to be flocculated and form a percolated network due to the colloidal interactions at rest. Afterwards, the nucleation of C-S-H starts immediately to transform locally the soft colloidal interactions between cement particles into far more rigid interactions. The percolated rigid network, which is formed by the linkage of C-S-H bridges between cement particles, is associated with the steady increase of the storage modulus of the PC mixtures [33]. It seems that AAS0 mixture also experiences the same aforementioned phases in PC system, resulting in an increase in storage modulus. Overall, for PC and AAS0, the percolation effect plays a very important role in the increase of structural build-up [110].

However, as shown in Fig. 9-8, AAS1.2 mixture exhibited a significantly different structuration trend, presenting very slow increase in the storage modulus for the first 20 min, and an accelerated increase for the next 30 min. As mentioned in Section 3.1, the flocculation of well dispersed GGBFS particles after mixing is prevented by the viscous effects of the activator solution and thus a colloidal network of interacting particles cannot be formed at rest in AAS1.2 mixture [49]. Kashani et al. [102] also

reported that the addition of sodium silicate would decrease the structural build-up due to the plasticizing and deflocculating effects of the silicate anions adsorbed on the particle surfaces caused by the increase of the magnitude of the repulsive double layer electric forces. For these reasons, the sodium silicate activator solution leads to more interaction of the alkaline solution and GGBFS grains, thereby promoting the continuous dissolution [110], [111]. Indeed, it is reported that the concentration of Al, Ca, Mg and Fe increased to a peak value with negligible increase in structural build-up due to the ongoing dissolution of GGBFS [47], while the main elements, Na and Si, did not change significantly in this stage. Once the dissolved ions gradually reached the oversaturated state, the solid reaction products would start to form. Afterwards, a significant increase in storage modulus and the concomitant dramatic decrease in the concentration of Ca and Si was observed, probably due to the fast precipitation of C-S-H consuming Si and Ca in the pore solution [20]. Therefore, it could be concluded that the higher number of nucleation sites in bulk region [243] in the AAS1.2 mixture cause a faster setting as compared to the AAS0 mixture in which the nucleation sites only occur around the GGBFS particles.

Recently, Zhang et al. [339] also investigated the effect of different activator solutions (sodium hydroxide, sodium silicate and water) on the dispersion properties of slag-fly ash powders. The size distribution, elongation and circularity of the pastes were measured by the Morphologi G3 particle characterization tool. Test results showed that the NaOH-activated pastes also exhibited highest size diameter of agglomerate structures as compared to that of sodium silicate-activated pastes. This is also consistent with this study that the initial storage modulus for sodium hydroxide-activated pastes is higher than the pastes activated by sodium silicate.

To prove the above statements, the storage modulus in the intermittent SAOS measurements are also presented in Fig. 9-8. In the intermittent SAOS measurements, a high shear rate reaching to  $600 \text{ s}^{-1}$  was introduced after each SAOS measurement to ensure that the temporary structures during the SAOS measurements were fully destroyed. As shown in Fig. 9-8, in the first interval, the storage modulus just increased as in the case of the continuous measurements; however, after high shearing, the storage modulus rapidly decreased to a low value for AAS0 and PC pastes, indicating the percolation network was destroyed. For the PC system, if the external shear energy is introduced periodically to break the percolation network, the increase of the storage modulus is considerably delayed. Unlike PC, under periodic external shear damage, the storage modulus of AAS0 increased at a progressively faster rate.

On the other hand, the trend in AAS1.2 was quite different from the case in AAS0 and PC. After introducing an external shear energy, the storage modulus of AAS1.2 did not change much and remained at a very low value, indicating the lack of the strong formation of the flocculation or percolation network. Only in the third cycle, the storage modulus of AAS1.2 increased to 200 kPa, which is still lower than the value of PC at the end of the first cycle. However, at this moment, applying the external shearing to the AAS1.2 pastes was not possible due to the already formed permanent

structures at this time. This shows the significant differences of structuration behaviour between sodium hydroxide-activated and sodium silicate-activated pastes.

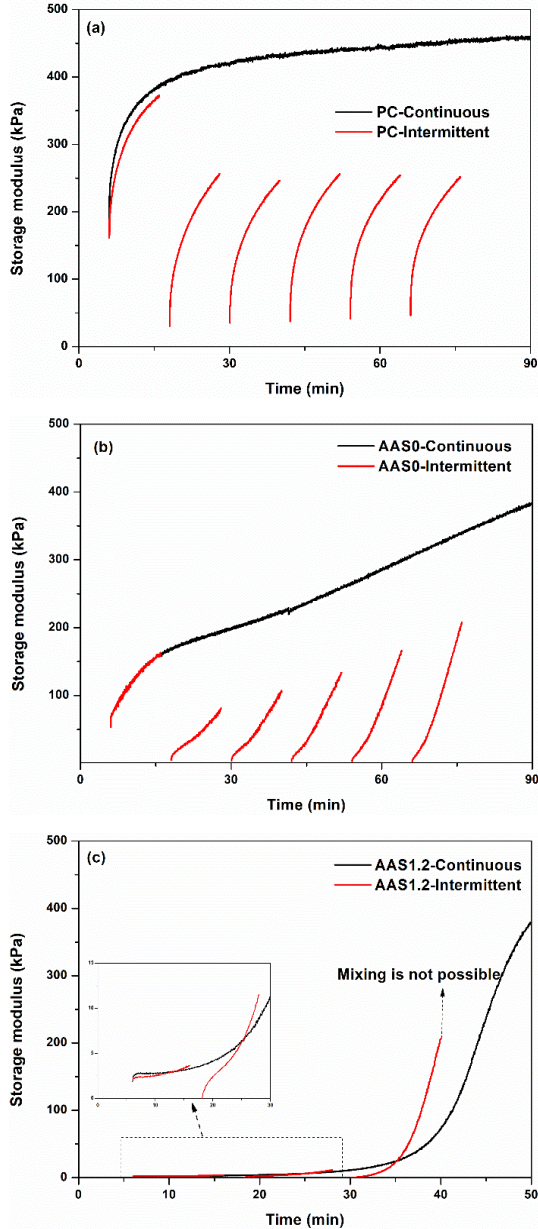
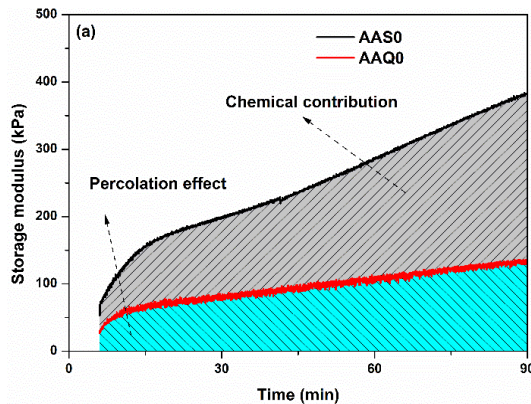


Fig. 9-8 The evolution of storage modulus of AAS mixtures by continuous and intermittent SAOS measurements (a) PC pastes, (b) AAS0 pastes and (c) AAS1.2 pastes.

To investigate the effect of activator solution on the formation of flocculation structures without the effects of strong chemical interaction between the activating solution and the particles, the continuous SAOS measurements were also carried out on the quartz pastes (consisting of the inert quartz and alkaline solution). As well known, no significant chemical interaction is expected between the quartz powder and the alkaline solution in a short time as the dissolution of quartz is hard at room temperature conditions [340]. As seen from Fig. 9-9, the AAQ0 mixture showed a significantly higher initial storage modulus and further increase rate than that of AAQ1.2, indicating a less flocculated structure in the AAQ1.2 case. The results obtained from the inert filler case reveals the less flocculated structure when aqueous silicates are present in the solution due to the lubricating effect [102]. As shown in Fig. 9-9a, the AAS0 always showed a higher storage modulus as compared to AAQ0 during the measurement time. The increase in storage modulus of AAQ0 originated from the physical percolation effects due to the colloidal interaction between particles, as there was almost no reaction between quartz powder and alkaline solution. Therefore, the area between the curves of AAS0 and AAQ0 can be roughly considered as the chemical contribution from the reaction of GGBFS. However, as there was no percolation effect in the case of sodium silicate solution, the total increase in the storage modulus AAS1.2 can be roughly associated to the reaction products. The reason why AAQ1.2 showed a higher storage modulus than AAS1.2 in the early time was because the GGBFS was dissolved in the sodium silicate solutions.

Overall, the increase in the structuration of sodium hydroxide-activated mixtures was achieved by the formation of the well-percolated network, while the structuration of sodium silicate-activated mixtures increased due to a result of accumulation of reaction products.



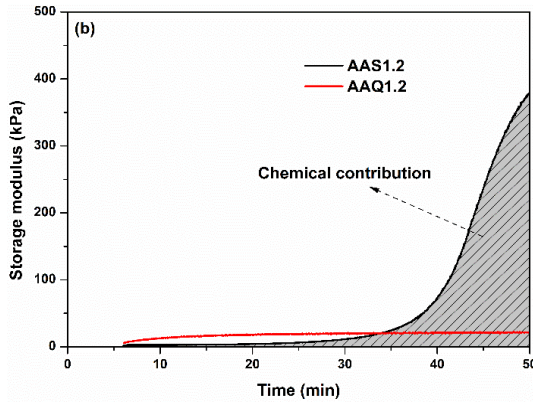


Fig. 9-9 The comparison of the evolution of storage modulus of quartz and GGBFS pastes by continuous SAOS measurements.

#### 4. Conclusion

---

This chapter presents the rheological properties and structural build-up process of sodium hydroxide- and sodium silicate- activated GGBFS mixtures. The following conclusions can be drawn:

1. Sodium silicate-activated GGBFS mixtures showed lower yield stress and higher plastic viscosity as compared to sodium hydroxide-activated GGBFS mixtures at a constant  $\text{Na}_2\text{O}\%$  concentration and solid volume fraction. At high shear rates, the sodium silicate-activated GGBFS mixtures tended to show shear-thickening behaviour, while a shear-thinning behaviour was observed for the sodium hydroxide-activated GGBFS mixtures.
2. Sodium hydroxide-activated GGBFS mixtures showed a longer setting time and lower heat release rate as compared to sodium silicate-activated GGBFS mixtures at very early ages; however, the heat release rate of sodium hydroxide-activated GGBFS mixtures was accelerated at later ages.
3. The increase in early structural build-up of sodium hydroxide-activated GGBFS mixtures was due to the formation of a well-percolated network; however, the massive formation of reaction products led to the increase in early structural build-up of sodium silicate-activated GGBFS mixtures.

This chapter exhibited fundamental differences between the sodium hydroxide-activated and sodium silicate-activated slag pastes in terms of rheological and structural build-up behaviour, could be guiding the industry in selecting the most appropriate activator for the production of GGBFS-based alkali-activated mixtures to be used for different needs. The structural build-up results can be utilized to develop the tool for predicting the setting evolution of AAS pastes activated by different activators.

## **Chapter 10 Nanostructure of AAS at initial setting times**

---

This chapter investigates the nanostructure of AAS at initial setting times, and tries to correlate the early reaction products with structural formation of AAS.

## 1. Introduction

---

The understanding of the change in nanostructure of AAS from mixing to initial sets is also very important. Palacios et al. [20] reported that the rapid loss of fluidity and fast setting of sodium silicate-activated mixtures is due to the initial precipitation of ill-defined N-A-S-H and C-N-A-S-H products. Li et al. [142] used various combined activators to understand the setting and hardening control of AAS. The authors elucidated that Ca (and hence also Mg) acts as a network modifier in slag, resulting in a faster dissolution of these precursors, but fly ash does not exhibit the same degree of reactivity. Furthermore, determining the nanostructure of AAS will also enable the industry to develop new strategies to design AAS mixtures and promote its application. There are a lot of ways of doing this, Chen et al. [341] used fourier-transform infrared spectroscopy (FTIR) to observe the  $Q^2$  band shifting to a higher wavenumber and becoming broader with an increase of silicate modulus in the activator solution. Puertas et al. [71] used various techniques, such as, X-ray diffraction (XRD) and FTIR and nuclear magnetic resonance (NMR) to determine the structure and composition of the main reaction products. Ismail et al. [248] used environmental scanning electron microscopy with energy dispersive X-ray (EDX) to determine the gel composition and reported that the silicate-activated slag showed a nanostructure dominated by a C-A-S-H type gel, while silicate-activated fly ash is dominated by N-A-S-H 'geopolymer' gel. However, all of these studies, mentioned above, focus on the later ages of the AAC. Due to the difficulties to determine the initial gel composition of AAS, there are few studies taking the early nanostructure of AAS into consideration, especially at the initial setting time.

Therefore, this chapter aims to determine the early gel composition at initial setting time of AAS, and investigate the relationship between the early structural build-up and nanostructure of AAS. The structural build-up of AAS evaluated by the small amplitude oscillation sweep tests. The nanostructure of AAS was determined by the combined use of  $^1\text{H}$ - $^{29}\text{Si}$  cross polarization magic-angle spinning NMR (CP MAS NMR) and  $^{29}\text{Si}$  MAS NMR. The rheological behaviour and gel composition at initial setting times was compared between sodium hydroxide-activated (NH-AAS) and sodium silicate-activated slag mixtures (SS-AAS). The new scientific findings provided by this study will enrich the understanding of the setting process of AAS.

## 2. Experimental program

---

### 2.1 Mixture design

---

The mixture designs are given in Table 10-1. Two AAS mixtures selected from chapter 6 were explored in this study, NH-AAS was activated by pure NaOH, while mixture SS-AAS was activated by the combination of NaOH and liquid sodium silicate with a Ms value of 1.2. The water to solid binder ratio (w/sb) and sodium content ( $\text{Na}_2\text{O}$  %) of mixture NH-AAS and SS-AAS are 0.45 and 5%, respectively. The pH value of

activator solutions were determined by a pH meter at 20 °C. It should be noted that using a pH meter to measure the pH of the activator solutions may result in some errors owing to the extremely high alkali ion concentrations and the presence of silica in the activator solution [105].

Table 10-1 Mixture design of AAS.

Mixture notation	Mixture nature	W/SB	Ms	Na <sub>2</sub> O%	SiO <sub>2</sub> %	pH
NH-AAS	Sodium hydroxide	0.45	0	5	0	13.82
SS-AAS	Sodium hydroxide and sodium silicate	0.45	1.2	5	6	13.50

## 2.2 Sample preparation

The activator solutions were prepared one day before to ensure the full dissolution of NaOH prior to mixing. For the preparation of the paste samples for rheological behaviour and microstructural analysis, the GGBFS was mixed with alkaline solution in a plastic container for 30 s at 200 rpm with a mechanical stirrer, then the pastes were mixed for 3 min at 1800 rpm.

## 3. Results and discussions

### 3.1 Structural build-up behaviour, initial setting times and heat evolution of AAS pastes

Fig. 10-1 presents the evolution of early structural build-up of AAS pastes activated by sodium hydroxide and sodium silicate, respectively. It can be seen that these two mixtures exhibited completely different structural build-up behaviour. The pastes activated by sodium hydroxide solution showed a higher initial storage modulus, followed by a continuous increasing rate of structural build-up with time. The trend of the structural build-up behaviour is quite similar to that of the Portland cement. Previous studies have reported that the sharp increase in the storage modulus of the Portland cement in the first 30 min is due to the formation of the percolated network [33], [49], [342], afterwards the storage modulus increases with a relatively lower rate, indicating the progressive formation of hydration products at the contact points between cement particles [33]. Due to the high alkaline environment for the mixture NH-AAS, the rapid reaction rate of GGBFS could also enhance the formation of reaction products, further inducing the occurrence of the percolated network [110]. In the meantime, the rapid formation of reaction products could cover on the surface of GGBFS, preventing further reaction of GGBFS [47]. Therefore, a continuous increase in storage modulus of NH-AAS could be observed. It could be considered that the

setting process of NH-AAS shared a similar mechanism as that of Portland cement [343].

However, the evolution of structural build-up of SS-AAS was significantly different from the case of NH-AAS. The initial storage modulus started from a very low value as compared to NH-AAS. In the first 20 min, almost no structural formation could be observed for the mixture SS-AAS. However, afterwards, the storage modulus of SS-AAS steeply increased. Some researchers attributed the very low initial storage modulus of SS-AAS to the viscous nature of sodium silicate solution with a great number of aqueous silicates, which prevents the formation of the percolated network [49], [101]. Due to the mild alkaline environment provided by sodium silicate solution allowed a considerable time for dissolution GGBFS, providing sufficient calcium and aluminum. Once these ions reached to their critical concentration, they will interact with the silicates originating from the activator solution, leading to a great number of reaction products in the matrix [20], [47], [49]. Therefore, a rapid increase in storage modulus could be observed for the mixture SS-AAS. Besides, it could be seen that the initial setting times of AAS pastes were also consistent with the trend of the structural build-up. The mixture of SS-AAS showed a short initial setting (45 min) as compared to that of NH-AAS (120 min).

Fig. 10-2 depicts the evolution of heat flow and cumulative heat release of AAS pastes. As well known, there are five distinctive stages for the AAS mixtures: dissolution, induction, acceleration, deceleration and steady-state [51], [81], [152]. As shown in Fig. 10-2a, during the first 20 min a sharp local peak is observed for the AAS mixtures. The heat flow evolved rapidly upon contact between the activator and the GGBFS is mainly associated with the wetting and dissolution of GGBFS particles and partly the interaction of silicate units and sodium with calcium dissolved from GGBFS [207], [272]. After the dissolution stage, the heat flow for the SS-AAS pastes starts to show an induction period, while no distinctive induction period is observed for NH-AAS pastes. The acceleration calorimetric peaks (second peaks) after the induction period for the AAS pastes are usually attributed to the strength and microstructural development [271]. The occurrence of acceleration peaks of SS-AAS is delayed as compared to the NH-AAS mixtures, and the intensity of acceleration peaks in SS-AAS decreased as compare to the NH-AAS mixture, which is also consistent with previous studies [81], [207]. As shown in Table 10-1, sodium hydroxide has a higher pH value than the sodium silicate activator solution. And it was reported that the higher alkaline environment normally enhances the dissolution rate and reaction degree of slag [228]. Additionally, a higher alkalinity also improves the solubility of silica and alumina in solution which could induce more reaction products formation [69], [70].

The cumulative heat release of NH-AAS showed a higher value as compared to that of SS-AAS at the age of 72 h. However, in the first 3.5 h, the SS-AAS in contrast released more heat as compared to NH-AAS. This is due to the interaction between the calcium ions continuously released from GGBFS and the silicates ions originated

from sodium silicate solution, quickly forming large amounts of gel products [43]. This is also consistent with the rapid increase in storage of SS-AAS in the early time. Besides, the NH-AAS and SS-AAS both presented a similar cumulative heat release of about 17J/g at their initial setting time.

To further understand the setting process and nanostructure of AAS, three critical reaction times based on structural build-up results, SS-AAS at 20 min and 45 min and NH-AAS at 120 min, were selected to conduct the NMR analysis. Two more points based on isothermal calorimetric curves of SS-AAS pastes at the beginning of the acceleration stage (16 h) and at the end of the deceleration period (72 h) were also selected to carry out the NMR tests. More details will be discussed in the following sections.

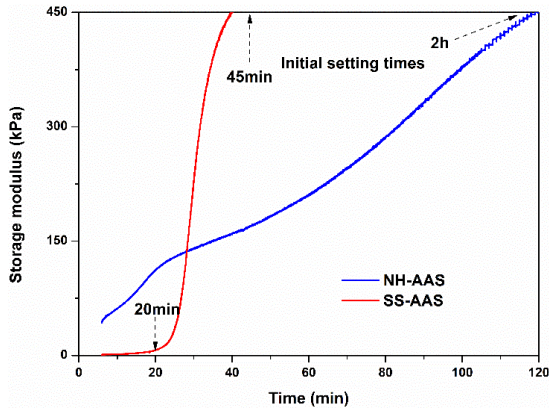
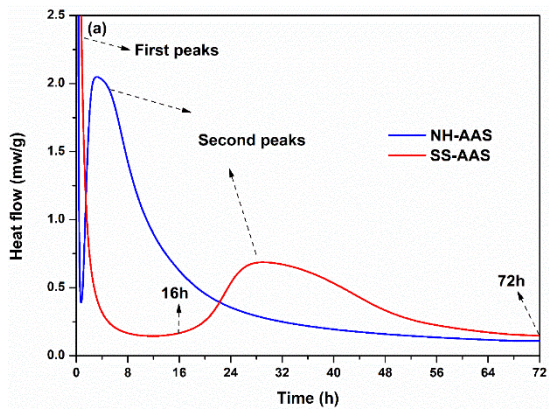


Fig. 10-1 Evolution of structural build-up of sodium hydroxide-activated and sodium silicate-activated GGBFS pastes.



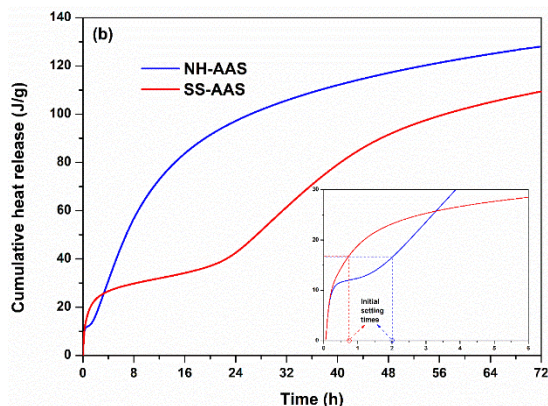


Fig. 10-2 Evolution of heat flow (a) and cumulative heat release (b) of sodium hydroxide-activated and sodium silicate-activated GGBFS pastes.

## 3.2 NMR analysis of AAS pastes.

### 3.2.1 NMR analysis at initial setting times.

As aforementioned it is important to understand the setting process of AAS, therefore the NMR tests were carried out at the age of initial setting times of AAS (at 120 min for NH-AAS and at 45 min for SS-AAS) and one more critical point at the age of 20 min for SS-AAS mixture. The  $^{29}\text{Si}$  Mas NMR spectra for the anhydrous GGBFS and the pastes at different reaction time are given in Fig. 10-3. As shown in Fig. 10-3, the anhydrous slag was the primary sources of the signal at -76.8 ppm in all the spectra. In addition, a shoulder between -80 and -105 ppm was shown at initial setting time for NH-AAS and SS-AAS mixture, reflecting the reaction products formation. These reaction products should be responsible for the initial setting of AAS. While at 20 min there was no difference between the spectra of SS-AAS\_20min and GGBFS, indicating no formation of reaction products. This is also consistent with the results of structural build-up, showing no structural formations at 20 min for the SS-AAS mixture.

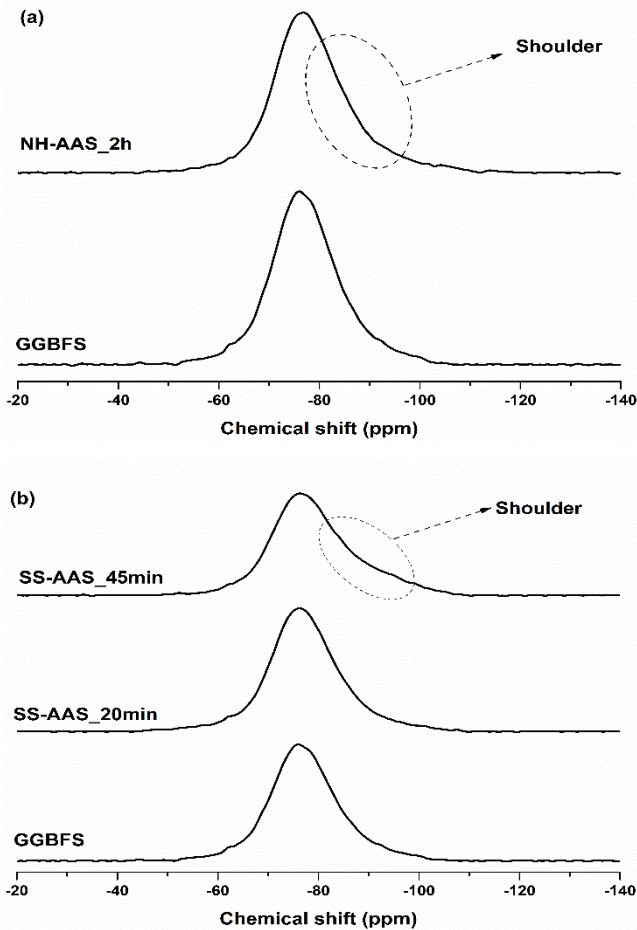


Fig. 10-3 The original spectra of  $^{29}\text{Si}$  MAS NMR spectra of AAS, (a) NH-AAS, (b) SS-AAS.

To better understand the nanostructure of AAS, an accurate deconvolution should be performed on the shoulder region. However, due to the peaks of  $\text{Q}^n$  ( $n=0,1,2,3,4$  and  $m=0,1,2,3,4$ ) units were hidden and overlapped behind the shoulder in the  $^{29}\text{Si}$  MAS NMR spectra [210], a  $^1\text{H}$ - $^{29}\text{Si}$  CP MAS NMR test was performed to find the peaks position prior to the deconvolution of  $^{29}\text{Si}$  MAS NMR spectra. It should be noted that the chemical shift of each resonance was required to be consistent in both the  $^{29}\text{Si}$  MAS NMR and  $^1\text{H}$ - $^{29}\text{Si}$  CP MAS NMR spectral deconvolutions.

Fig. 10-4 and Fig. 10-5 present the differences between the spectra of  $^{29}\text{Si}$  MAS NMR and  $^1\text{H}$ - $^{29}\text{Si}$  CP MAS NMR of the pastes activated by sodium hydroxide and sodium silicate, respectively, as well as their detailed deconvolution. As shown in Fig. 10-4a

and Fig. 10-5a, the resonances observed in the  $^1\text{H}$ - $^{29}\text{Si}$  CP MAS NMR is influenced by their proximity to protons and the Hartmann-Hahn contact period, and so this spectrum particularly shows those Si species present in the hydration reaction products [195]. As a result, the  $^1\text{H}$ - $^{29}\text{Si}$  CP MAS NMR data in the Fig. 10-4a and Fig. 10-5a can confirm that the broad resonance feature observed in the  $^{29}\text{Si}$  MAS NMR is due to the presence of the anhydrous slag in the AAS. It should be noted that although the  $^1\text{H}$ - $^{29}\text{Si}$  CP MAS NMR can provide better resolution of the spectra in terms of hydration reaction products, it can only give qualitative information rather than quantitative information. Therefore, the combined use of  $^1\text{H}$ - $^{29}\text{Si}$  CP MAS NMR and  $^{29}\text{Si}$  MAS NMR enable a more complete examination of the variations in the nanostructure of reaction products that formed in the AAS mixtures.

The nanostructure of AAS can be identified by the  $Q^n(mAl)$  structural units, showing various chemical environment of silicon tetrahedral of phases in  $^{29}\text{Si}$  NMR spectra, where  $n$  denotes the number of oxygen bridges between each silicon tetrahedral unit and other silicon atoms, and  $m$  represents the number of aluminum tetrahedral occupying in bridging position [275], [344]. The deconvolution results of the  $Q^n(mAl)$  structural units in the  $^{29}\text{Si}$  MAS NMR spectra are summarized in the Table 10-2. After decomposition, the deconvoluted peak located at around -76.8 ppm of mixtures of NS-AAS and SS-AAS at initial setting times referred to the remnant GGBFS ( $Q^0$ ), and the integration of these peaks reached to 80.04% and 81.28% of the spectra of  $^{29}\text{Si}$  MAS NMR, respectively. This indicates that when the remnant GGBFS reached to approximately 80.6%, and hence the initial setting of AAS would occur. In other words, when both NH-AAS and SS-AAS mixtures tend to set, they both have a similar reaction degree. Combining the results of rheology and setting time, it can be concluded that the solidification of NH-AAS is a continuous process, however the initial set of SS-AAS occurs suddenly in a shorter period of time.

As shown in Fig. 10-4c, the peak position for the mixture NH-AAS\_120 min at  $\delta = -79.2$  is attributed to  $Q^1$  site, which was the end of chain silicate tetrahedral within C-A-S-H gels [194], [345]. The  $Q^2(1Al)$  and  $Q^2$  site located at -83.5 ppm and -86 ppm are associated to the middle-of-chain silicate within C-A-S-H gels [275], [346]. The peak at -89.2 corresponds to  $Q^3(1Al)$  and  $Q^4(4Al)$  sites due to the overlap of resonances in this area [194], [248], [304]. Herein, it should be noted that the  $Q^3(1Al)$  site denoted a high extent of cross-linking with the C-(N-)A-S-H gel [194], [195], while  $Q^4(4Al)$  site refers to the Al-rich N-A-S-H gel [309]. Besides, three additional sites at around -96 to -110 ppm are assigned to  $Q^4(2Al)$ ,  $Q^4(1Al)$  and  $Q^4(0Al)$ , respectively. These  $Q^4(mAl)$  environment is attributed to a polymerized Si-rich N-A-S-H gel [20], [195], [347].

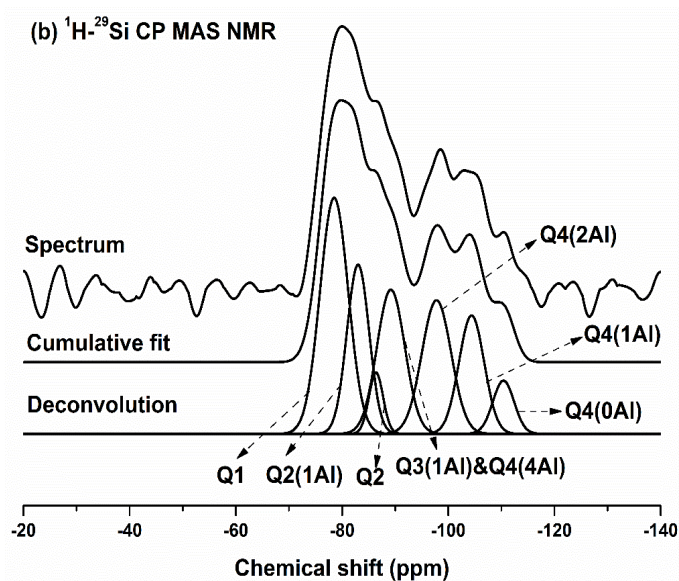
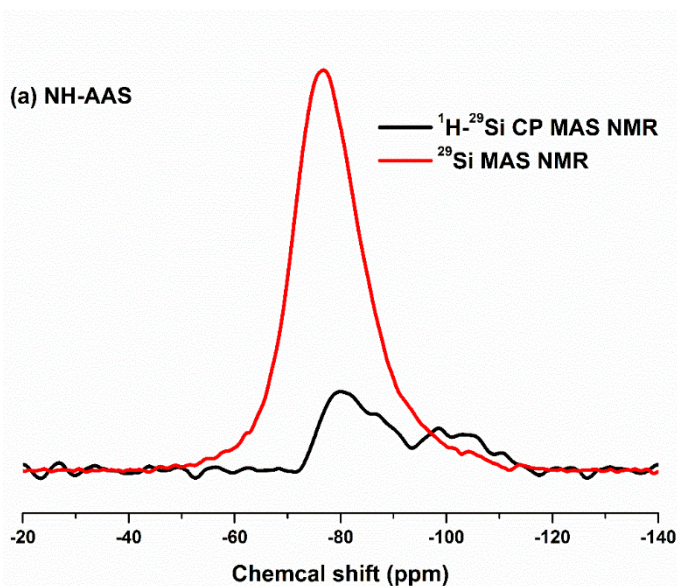
Similarly, three resonances as shown in Fig. 10-5c for the mixture SS-AAS at  $\delta = -78.5$  ppm, -83.0 ppm and -86 ppm are attributed to  $Q^1$ ,  $Q^2(1Al)$  and  $Q^2$  sites, respectively, indicating the formation of C-A-S-H. The  $Q^3(1Al)$  and  $Q^4(4Al)$  sites are located at -88.6 ppm, which is the formation of high crosslinking C-(N-)A-S-H and N-A-S-H, respectively. While the alumino-silicate gel N-A-S-H can be confirmed by

three additional peak at  $\delta$  between -93 and -106 ppm, indicating the  $Q^4(3Al)$ ,  $Q^4(2Al)$  and  $Q^4(1Al)$  sites, respectively.

As shown in Table 10-2, it could be found that SS-AAS mixture showed a higher percentage of N-A-S-H formation ( $Q^4(mAl)$ ) as compared to C-A-S-H ( $Q^1$ ,  $Q^2(1Al)$  and  $Q^2$ ), while C-A-S-H ( $Q^1$ ,  $Q^2(1Al)$  and  $Q^2$ ) was the most dominating reaction product in the NH-AAS mixture. Here, it is very difficult to distinguish  $Q^3(1Al)$  and  $Q^4(4Al)$  due to their overlapped resonance. However, it is still believed that the SS-AAS mixture contained more percentage of N-A-S-H as compared to NH-AAS mixture at initial setting time. In literature [105], [142], the authors have elucidated that sodium silicate solution in general contained high Q Si species. Due to the condensed silicates in the activator of SS-AAS, these higher-Q Si is more likely to condense with Al and Ca to form 3D Ca-modified gel at early ages [74], [348]. While regarding the NaOH-activated mixture, due to the presence of numerous phases within the precursors and previous observations of Al dissolving preferentially over Si from aluminosilicate precursors, it is unlikely that congruent dissolution of the various Si coordination environments within the precursor will occur during alkali activation. Rather, it is expected that the depolymerised calcium silicate phase observed in the precursors [309], [349] will dissolve faster than the highly polymerised aluminosilicate phase and these released depolymerised silicates interact with aluminum and calcium ions to form chain-like C-A-S-H gel [69], [71]. This could be the distinctive difference between SS-AAS and NH-AAS in terms of gel composition at early ages.

It is plausible that the hydration products of AAS at initial setting time are composed of the C-A-S-H and N-A-S-H gels. In the meantime, the mixing of C-A-S-H and N-A-S-H resulted in a 3-D Ca-modified gel (N,C)-A-S-H, which was also reported by Garcia-Lodeiro et al. [303]. However, very few studies focused on the gel composition of AAS at initial setting times, only Palacios et al. [20] used the thermodynamic modelling and NMR technique to confirm the presence of the coexistence formation of the alumino-silicate gel and C-A-S-H gel in the sodium silicate-activated slag mixtures at early times. These C-A-S-H and N-A-S-H gels are formed from the reaction of  $Ca^{2+}$  ions and aluminate species dissolved from slag and  $Na^+$  and silicate species originally in the solution. Therefore, the rheological properties and the setting process are dominated by these reaction products.

However, more studies in general pointed out that the main reaction products of AAS at later ages are C-A-S-H gels, it is therefore very worthwhile to investigate when these N-A-S-H gels start to disappear or whether they are converted into C-A-S-H gels as the reaction continues. To investigate the change of the gel composition of AAS, the NMR tests were conducted on two critical points based on isothermal calorimetric curves of SS-AAS pastes (as shown in section 3.2.2).



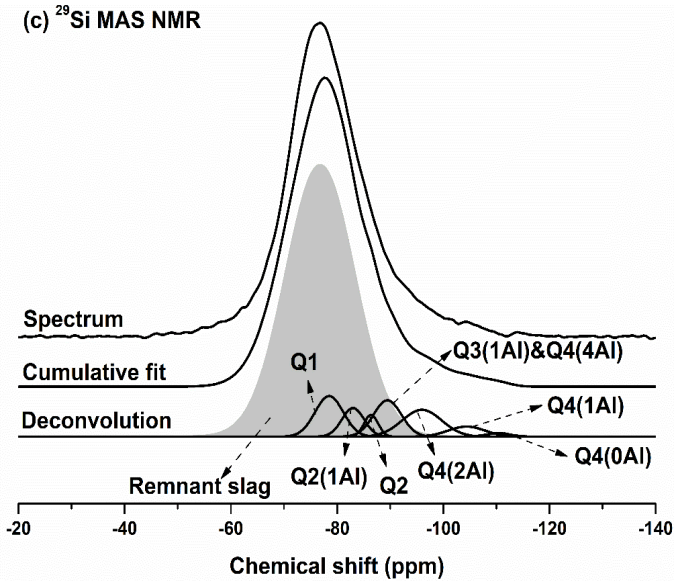
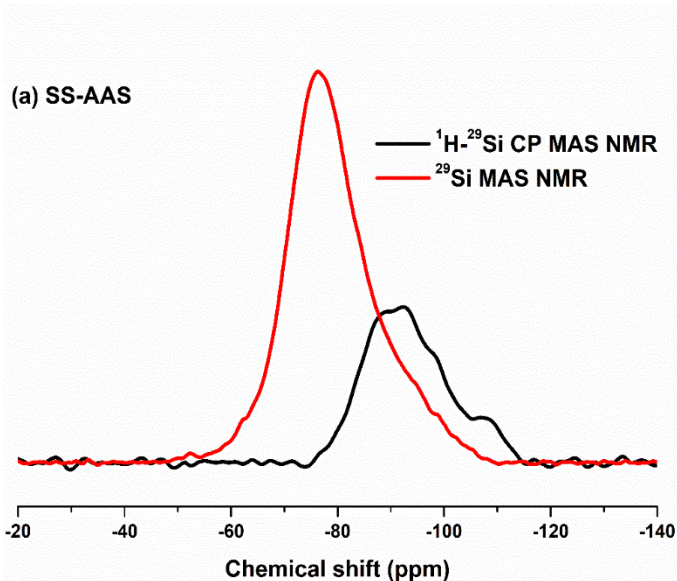


Fig. 10-4 The deconvolution of  $^1\text{H}$ - $^{29}\text{Si}$  CP MAS NMR and  $^{29}\text{Si}$  MAS NMR spectra of NH-AAS at initial setting time (2h), (a) Comparison between the original spectra of  $^1\text{H}$ - $^{29}\text{Si}$  CP MAS NMR and  $^{29}\text{Si}$  MAS NMR, (b) The deconvolution of  $^1\text{H}$ - $^{29}\text{Si}$  CP MAS NMR, (c) The deconvolution of  $^{29}\text{Si}$  MAS NMR.



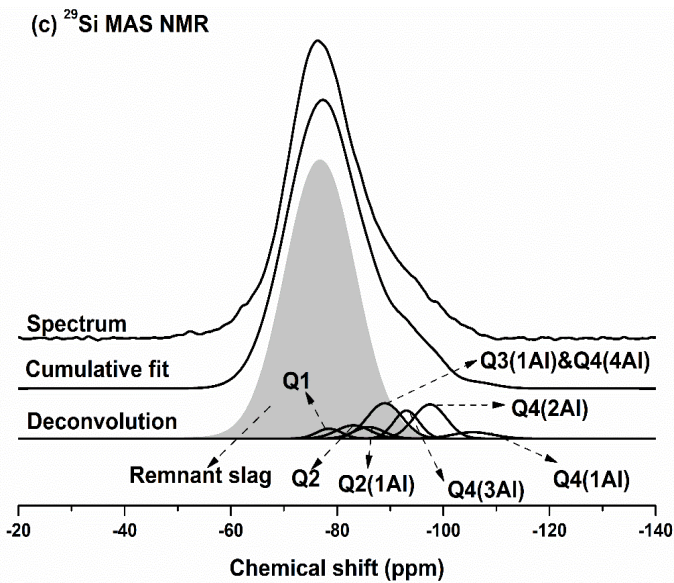
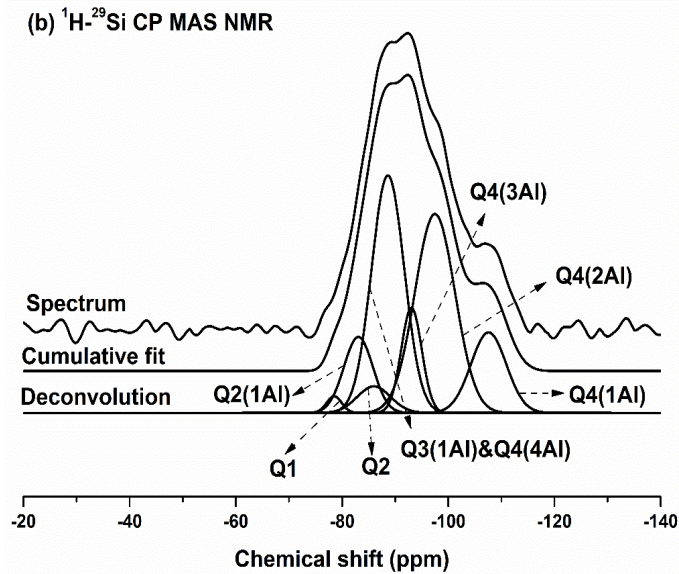


Fig. 10-5 The deconvolution of  $^1\text{H}$ - $^{29}\text{Si}$  CP MAS NMR and  $^{29}\text{Si}$  MAS NMR spectra of SS-AAS at initial setting time (45 min), (a) Comparison between the original spectra of  $^1\text{H}$ - $^{29}\text{Si}$  CP MAS NMR and  $^{29}\text{Si}$  MAS NMR, (b) The deconvolution of  $^1\text{H}$ - $^{29}\text{Si}$  CP MAS NMR, (c) The deconvolution of  $^{29}\text{Si}$  MAS NMR.

Table 10-2 The deconvolution results of the <sup>29</sup>Si MAS NMR spectra of AAS mixtures over time based on area percentage (%).

Mixtures	Unreacted slag		Reaction Products						
			C-A-S-H/C-(N-)A-S-H				N-A-S-H		
	Q0	Q1	Q2(1Al)	Q2	Q3(1Al) & Q4(4Al)	Q4(3Al)	Q4(2Al)	Q4(1Al)	Q4(0Al)
NH-AAS_120min	80.04	4.93	2.74	1.34	4.38	-	4.59	1.62	0.38
	(-76.8 ppm)	(-78.5 ppm)	(-83.0 ppm)	(-86.4 ppm)	(-89.3 ppm)		(-96.5 ppm)	(-104.4 ppm)	(-110.4 ppm)
SS-AAS_45min	81.28	1.07	1.93	1.51	5.32	2.99	4.75	1.14	-
	(-76.8 ppm)	(-78.5 ppm)	(-83.1 ppm)	(-86.0 ppm)	(-89.0 ppm)	(-93.1 ppm)	(-97.2 ppm)	(-105.6 ppm)	
SS-AAS_16h	68.68	2.45	3.80	4.65	7.63	5.34	4.85	2.60	-
	(-76.8 ppm)	(-78.5 ppm)	(-83.1 ppm)	(-86 ppm)	(-88.9 ppm)	(-93.1 ppm)	(-97.3 ppm)	(-105.6 ppm)	
SS-AAS_72h	47.76	10.71	19.52	8.48	6.75	3.76	3.03	-	-
	(-76.8 ppm)	(-78.8 ppm)	(-83.6 ppm)	(-86.2 ppm)	(-89.1 ppm)	(-93.6 ppm)	(-97.5 ppm)		

### 3.2.2 NMR analysis of SS-AAS pastes based on calorimetric curves

Fig. 10-6 illustrates the <sup>29</sup>Si MAS NMR of SS-AAS pastes over time. As the curing age increases from the beginning to 16 h, the broad peak did not shift a lot, while the shoulder area between -80 and -105 ppm was enhanced. With time elapsing from 16 h to 72 h, the broad peak started to shift to a higher value, the shoulder area between -90 and 105 ppm significantly decreased. This is possibly due to the increase of polymerization degree and cross-linking of gels over time and the disappearance of the alumino-silicate gel.

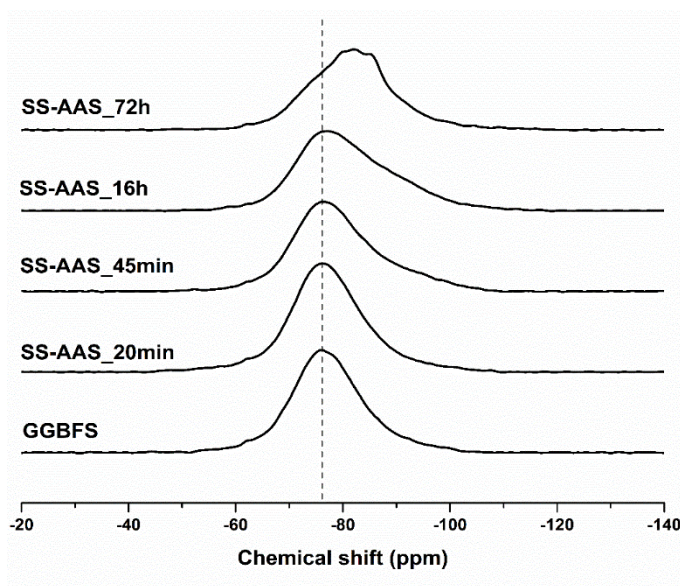


Fig. 10-6 The  $^{29}\text{Si}$  MAS NMR spectra of SS-AAS pastes over time.

To further understand the change of the nanostructure of SS-AAS pastes, Fig. 10-7 presents  $^{29}\text{Si}$  MAS NMR decomposition results at around the starting point of acceleration peak and the end of the deceleration peak based on isothermal calorimetric curves. The area percentage of various  $\text{Q}^n(\text{mAl})$  structural units are quantified and summarized in Table 10-2. It could be seen that the  $\text{Q}^1$  and  $\text{Q}^2$  sites within C-A-S-H increased from 2.45 % to 10.71 % and from 4.65 % to 8.48 % with the increasing curing time from 16 h to 72 h, respectively. In particular, the content of  $\text{Q}^2(1\text{Al})$  significantly increased from 3.80 % to 19.52 % with time elapsing, and became the most dominated  $\text{Q}^n(\text{mAl})$  structural units for SS-AAS pastes at the age of 72 h. This is also consistent with previous studies, reporting the dissolved calcium and aluminum from slag will enhance the gel polymerization and result the chain in C-A-S-H gels with more links [194]. As the reaction time started from the initial setting time (45 min), to 16 h and then to 72 h, the content of  $\text{Q}^3(1\text{Al})$  &  $\text{Q}^4(4\text{Al})$  gradually increased from 5.32 % to 7.63 %, and then decreased to 6.75 %. Meanwhile, the content of N-A-S-H gel (including  $\text{Q}^4(\text{mAl})$ ,  $m=3, 2, 1, 0$ ) first increased from 8.88 % to 12.79 % when the age increased from 45 min to 16 h, and then decreased to 6.79 % when the age increased from 16 h to 72 h. This indicates that the system is continuously enriched with N-A-S-H until the end of the induction period, but as the reaction progresses, the N-A-S-H in the system gradually disappears or depolymerises to form C-A-S-H when reaching to the end of the second exothermic peak of SS-AAS.

Based on the NMR results in this study and the compatibility between C-A-S-H and N-A-S-H gel [303], the activation process of SS-AAS pastes in the early times can be

explained. After mixing the GGBFS with sodium silicate solution, the process begins with the dissolution of the GGBFS particles in the alkaline solution via rupture of the T-O-T bonds (T: Si or Al) and Ca-O bonds in the slag, resulting in a wide variety of dissolved species. This can be confirmed by various previous studies, which use the ICP-OES technique to observe the change of different ion concentrations [47], [69]–[71], [110], [142]. When the ions reaches their oversaturation, a great number of C-A-S-H and N-A-S-H gels precipitates. These gels in general contains a high aluminum content (as shown in NMR results in this study). As the alkaline reaction proceeds, the silicates from original activator solution has been consumed and more bonds Si-O start to dissolve from GGBFS, keeping the silicon concentration at a high level and with it the silicon uptake in both gels. In this study from the initial setting time to 16h, Si uptake will enhance the gel reaction process in terms of C-A-S-H, leading a higher  $Q^2(1A)$  as compared  $Q^1$ . In the meantime, the percentage of N-A-S-H gel also increases when the age increases from the initial setting time to 16h.

Furthermore, with time elapsing, the calcium and aluminum ions present in the aqueous solution start to diffuse across the cementitious matrix and a certain level of Ca ions react with N-A-S-H to form (N,C)-A-S-H. Due to the identical ionic radius and electronegative potential of sodium and calcium ions, calcium replaces the sodium ions via ion exchange in a mechanism similar to that observed in clay and zeolites [350], hence preserving the 3D structure of the (N,C)-A-S-H type gel. Where adequate calcium is available, it diffuses into pores in the matrix and interacts with the (N,C)-A-S-H gel. The  $Ca^{2+}$  polarising effect (which results in the formation of Si-O-Ca bonds) distorts the Si-O-Al bonds, resulting in tension and eventually breakage. As aluminum is released from the N-A-S-H gel, fewer polymerised structures such as C-A-S-H gels form. Simultaneously, the C-A-S-H gel formed in earlier phases is capable of absorbing a greater amount of silicon and aluminum ions in bridge positions [274]. Besides, Puertas et al. [71] also found that at the age of 24h the calcium concentration and pH value of the waterglass-activated slag mixtures reached the peak value in their measurements. This also supports that the N-A-S-H gel will degrade to C-A-S-H due to its low stability in the presence of high pH and high calcium concentrations, which is reported by Garcia-Lodeiro et al. [303]. Eventually, the chain-like C-A-S-H gels will form and dominate in the reaction products, which is also consistent with this study where  $Q^2(1Al)$  is the main reaction products at the age of 72h.

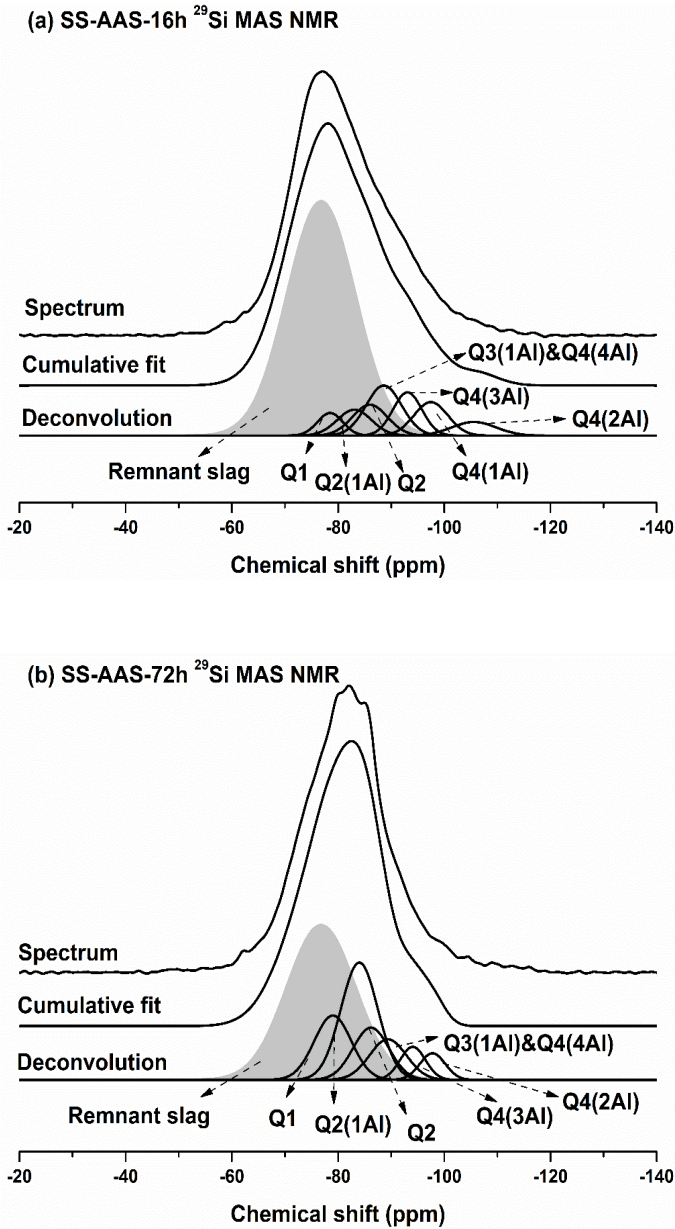


Fig. 10-7 The deconvolution of  $^{29}\text{Si}$  MAS NMR spectra of SS-AAS at around: (a) starting point of acceleration period (16h) and (b) the end of deceleration period based on isothermal calorimetric curves (72 h).

### 3.2.3 Quantitative assessment of C-A-S-H/C-(N-)A-S-H and N-A-S-H

Richardson and Groves [56] have proposed a conceptual model named “substituted general model” (SGM) to describe the C-(N-)A-S-H product, which is a mixture of 14 Å tobermorite, jennite, and  $\text{Ca}(\text{OH})_2$  structures. However, in recent studies, more formation of cross-linked Si sites, such as  $\text{Q}^3$  and  $\text{Q}^3(1\text{Al})$ , is identified by the high-resolution  $^{29}\text{Si}$  MAS NMR [26], [37], [41], [43]. As reported by Myers et al. [26], in tobermorite structural models,  $\text{Q}^3$  type silica bonding environments can only be described by cross-linking between bridging sites in the silicate chains, and another conceptual model “Cross-linked substituted tobermorite model” (CSTM) has been proposed to support the description of the C-(N-)A-S-H gel as a mixture of cross-linked (11 Å tobermorite) and non-cross-linked (14 and/or 9 Å tobermorite) chains. And it should be noted that there are some structural constraints included in the CSTM model: (i) ( $\text{Q}^2 + \text{Q}^2(1\text{Al})$ ) silicate species are twice as many as ( $\text{Q}^3 + \text{Q}^3(1\text{Al}) + \text{Al}[4]$ ). (ii) the fraction of aluminum substitution into  $\text{Q}^3$  type sites is equal to the ratio of  $\text{Q}^2(1\text{Al})$  to  $\text{Q}^2$  sites in cross-linked tobermorite, since aluminum is only substituted into bridging sites; and (iii) the substitution of one  $\text{Al}[4]$  species into cross-linked tobermorite introduces one  $\text{Q}^3(1\text{Al})$  and two  $\text{Q}^2(1\text{Al})$  Si species. Regarding the structural model of N-A-S-H, unfortunately, no acknowledged conceptual model has been proposed due to its complicated 3D structures.

To further investigate the structure of the investigated samples in this study, two extreme scenarios are considered. In this study, as the  $\text{Q}^3(1\text{Al})$  and  $\text{Q}^4(4\text{Al})$  are overlapped at around -89 ppm, it was assumed as a first case that all the signals came from  $\text{Q}^4(4\text{Al})$  and there was no  $\text{Q}^3(1\text{Al})$  in the nanostructure, which means all C-(N-)A-S-H structures consist of non-cross-linked gel as defined by the SGM model. In the second extreme case, it was assumed that the C-(N-)A-S-H had the maximum crosslinking degree (maximum content of  $\text{Q}^3(1\text{Al})$ , and the remaining part is  $\text{Q}^4(4\text{Al})$ ), considering the aforementioned structural constraints. This indicates that the C-(N-)A-S-H is a mixture of cross-linked and non-cross-linked tobermorite-like structures as defined by CSTM.

Table 10-3 presents the C-A-S-H/C-(N-)A-S-H and N-A-S-H gel amounts considering the two extreme scenarios of above. As shown in Table 4, the calculated amounts of C-A-S-H/C-(N-)A-S-H and N-A-S-H vary in a narrow band for these two extreme scenarios. For example, NH-AAS\_120 min exhibited a range of C-A-S-H/C-(N-)A-S-H between 9.01 and 9.68, and N-A-S-H was between 10.30 and 10.97. It can be found that in both two scenarios the relative amount of C-A-S-H/C-(N-)A-S-H is more close to N-A-S-H gel for the mixture of NH-AAS\_120 min, while the N-A-S-H gel is much more dominant in the mixture of SS-AAS\_45 min. With time elapsing, the C-A-S-H/C-(N-)A-S-H amount increased rapidly, while the amount of N-A-S-H firstly increased until the end of induction period based on calorimetric curves, and then started to decrease.

Table 10-3 Nanostructure of investigated pastes in this study considering the two extreme scenarios.

Mixture	Q1	Q2(1A)	Q2	Q3(1A)	Q4(4A)	Q4(3A)	Q4(2A)	Q4(1A)	Q4(0A)	C-A-S-H/C-(N)-A-S-H	N-A-S-H
No cross link in C-A-S-H/C-(N)-A-S-H											
NH-AAS_120min	4.93	2.74	1.34	-	4.38	-	4.59	1.62	0.38	9.01	10.97
SS-AAS_45min	1.07	1.93	1.51	-	5.32	2.99	4.75	1.14	-	4.51	14.20
SS-AAS_16h	2.45	3.80	4.65	-	7.63	5.34	4.85	2.60	-	10.90	20.42
SS-AAS_72h	10.71	19.52	8.48	-	6.75	3.76	3.03	-	-	38.71	13.54
Maximum Cross link in C-A-S-H/C-(N)-A-S-H											
NH-AAS_120min	4.93	2.74	1.34	0.67	3.71	-	4.59	1.62	0.38	9.68	10.30
SS-AAS_45min	1.07	1.93	1.51	0.27	5.05	2.99	4.75	1.14	-	4.78	13.93
SS-AAS_16h	2.45	3.80	4.65	0.61	7.02	5.34	4.85	2.60	-	11.51	19.81
SS-AAS_72h	10.71	19.52	8.48	2.68	4.07	3.76	3.03	-	-	41.39	10.86

### 3.3 FTIR analysis of AAS pastes

Infrared spectroscopy can be used to monitor the evolution of reaction products with time in the AAS samples. The FTIR spectra of AAS samples at initial setting time is given in Fig. 10-8. The FTIR spectrum of anhydrous GGBFS is formed by a broad band at  $970\text{ cm}^{-1}$ , assigned to  $\nu_3(\text{Si-O})$  stretching modes, and another located at  $508\text{ cm}^{-1}$ , ascribed to  $\nu_4(\text{O-Si-O})$  bending modes of  $\text{SiO}_4$  tetrahedra. In AAS pastes activated by sodium silicate solution at initial setting times,  $\nu_3(\text{Si-O})$  band shifted towards higher values (at  $988\text{ cm}^{-1}$ ) and  $\nu_4(\text{O-Si-O})$  band shifts towards lower values (at  $494\text{ cm}^{-1}$ ). The trend is also similar to the case of NH-AAS pastes, a  $\nu_3(\text{Si-O})$  band shifted towards higher values (at  $987\text{ cm}^{-1}$ ) and  $\nu_4(\text{O-Si-O})$  band shifted towards lower values (at  $493\text{ cm}^{-1}$ ). These bands narrowed and shifted to a higher value due to the continuous reaction, indicating the formation of more highly polymerized reaction products [20], [71]. Besides, the similar value of  $\nu_3(\text{Si-O})$  bands between NH-AAS and SS-AAS denotes the similar reaction degree of GGBFS at initial setting times, which is also consistent with NMR results. In the vibration region of Al-O bonds, a displacement of the wide band at  $671\text{ cm}^{-1}$  in the anhydrous GGBFS moves towards  $709\text{ cm}^{-1}$  for SS-AAS and  $698\text{ cm}^{-1}$  for NH-AAS mixture, respectively.

Fig. 10-9 exhibits the FTIR spectra of SS-AAS mixture over time. It could be seen

that the  $\nu_3(\text{Si-O})$  band shifted towards higher values with time elapsing, indicating the formation of more highly polymerized reaction products. At the age of 16h and 72h, the bands appearing at  $1006\text{ cm}^{-1}$  and  $1020\text{ cm}^{-1}$  represent the stretching vibration of the silicate-based gels bound with Na (i.e. the formation of C-(N-)A-S-H) [351], [352], which is also consistent with the findings of the previous studies [210], [353]. However, FTIR data are difficult to interpret since the Si-O-T (T=Al, Si) vibrations of the unreacted GGBFS, aluminosilicate hydrate and calcium silicate hydrate all produce an overlapping spectrum [354].

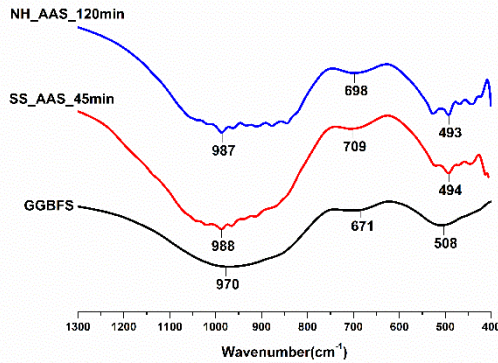


Fig. 10-8 The FTIR spectra of AAS samples at initial setting times.

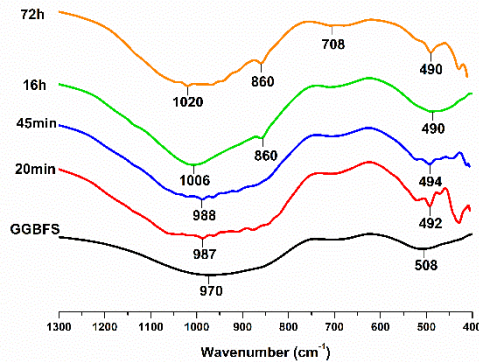


Fig. 10-9 The FTIR spectra of SS-AAS samples over time.

### 3.4 SEM/EDX analysis of AAS pastes

Scanning electron microscopy (SEM) was used to study the microstructural surface of the GGBFS particles and energy-dispersive X-ray spectroscopy was applied to analyze the gel composition [20], [248]. Fig. 10-10 presents the SEM images of AAS pastes during the reaction process. At the age of 120 min for NH-AAS and 45 min for

SS-AAS, the GGBFS particles surface became rough due to the precipitation of reaction products, thereby leading to the initial set of AAS pastes.

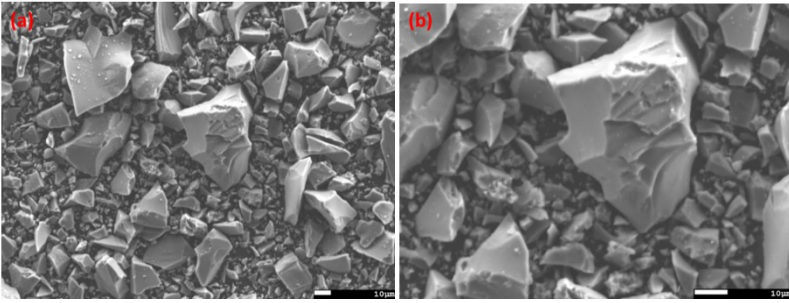
As shown in Fig. 10-10e and f, the surface of the GGBFS particles of the SS-AAS mixture at the age of 20 min was very smooth, indicating no formation of reaction products. This is also consistent with the structural build-up and NMR results in this study. With time elapsing, the dissolved calcium and aluminum ions from the GGBFS reached oversaturation and interacted with the silicates originating from the activator solution, forming more reaction products. Therefore, the surface of GGBFS particles became increasingly rough, and more particles would accumulate on each other due to the formation of reaction products (as shown in Fig. 10-10k and l) [20].

To analyze the composition of reaction products, at least 15 points have been selected from the roughened surface. The results of the energy dispersive x-ray spectroscopy (EDX) are shown in Table 10-4 for the AAS pastes over time. At the age of initial setting times of the AAS pastes, NH-AAS showed a higher Ca/Si ratio as compared to that of SS-AAS pastes. With time elapsing, the Ca/Si in the SS-AAS mixture gradually increased to 1.49 and the age of 16h, indicating more calcium ions starting to be incorporated into the reaction products. Besides, it could be seen that the Al/Si ratio in the SS-AAS mixture decreased with curing time increasing. This is also consistent with the NMR results, showing that the chain-like C-A-S-H was dominated at the later ages, while the 3D aluminosilicate gel started to disappear. The Na/Al ratio in the SS-AAS also increased over time, reflecting that the Na ions played as a charge balancer to form the C-(N)-A-S-H gel in the mixture [247]. While the presence of Mg in the AAS mixture possibly indicated the formation of hydrotalcite, which is a common reaction products in AAS for magnesium-rich precursor [246].

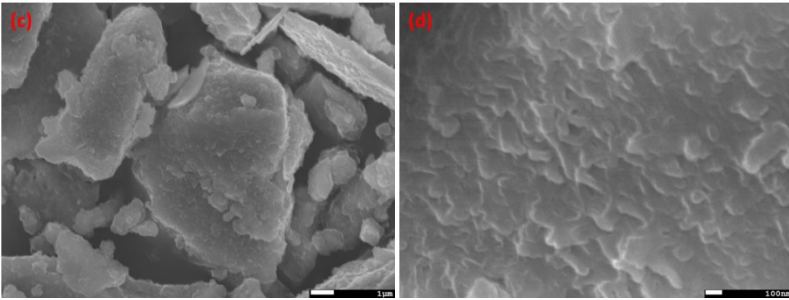
Table 10-4 Atomic ratios of the AAS pastes over time.

Mixture	Ca/Si	Al/Si	Na/Al	Mg/Al
NH-AAS- 120min	1.05 ± 0.1	0.43 ± 0.1	0.09 ± 0.2	0.75 ± 0.2
SS-AAS- 20min	1.02 ± 0.08	0.28 ± 0.1	0.47 ± 0.1	0.76 ± 0.3
SS-AAS- 45min	0.94 ± 0.04	0.35 ± 0.1	0.17 ± 0.1	0.73 ± 0.3
SS-AAS-16h	1.49 ± 0.7	0.31 ± 0.4	0.34 ± 0.2	0.47 ± 0.1
SS-AAS-72h	0.73 ± 0.2	0.27 ± 0.3	1.15 ± 0.1	0.66 ± 0.3

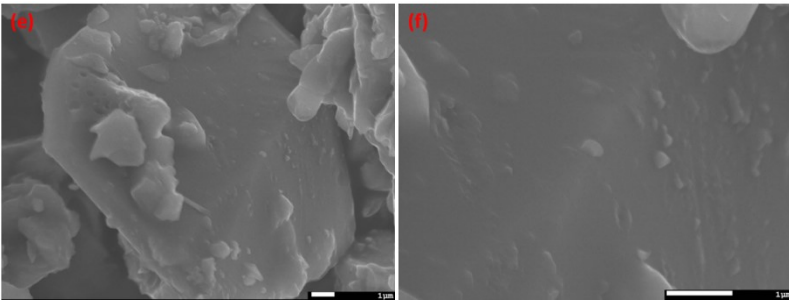
Nanostructure of AAS mixtures



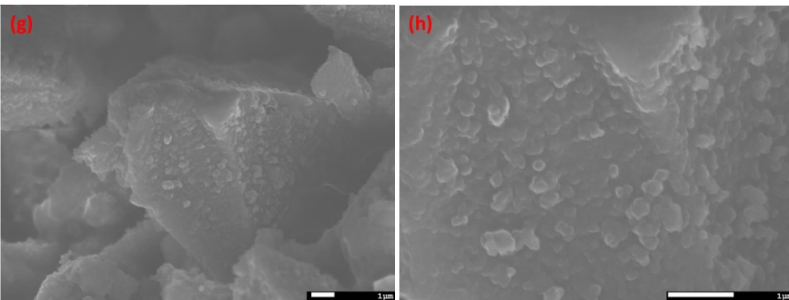
Original GGBFS



NH-AAS\_120min



SS-AAS\_20min



SS-AAS\_45min

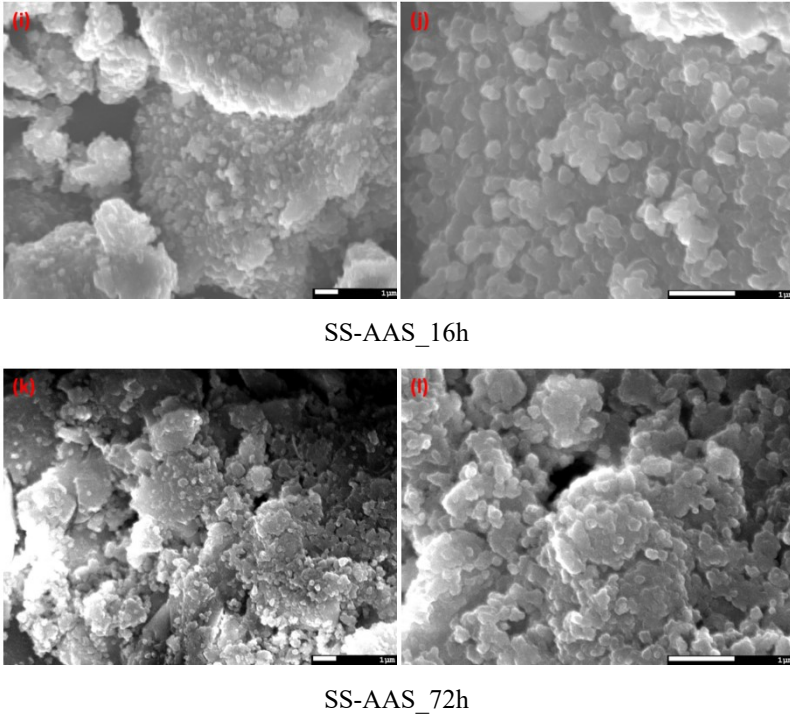


Fig. 10-10 SEM images of AAS pastes over time; (a, b) anhydrous GGBFS; (c, d) NH-AAS at 120 min; (e, f) SS-AAS at 20 min; (g, h) SS-AAS at 45 min; (i, j) SS-AAS at 16 h; (k, l) SS-AAS at 72 h;

#### **4. Conclusion**

---

In this Chapter, a series of tests including SAOS, isothermal calorimetry, NMR, FTIR and SEM/EDX were conducted to investigate the rheological behaviour and nanostructure change of AAS pastes. Based on the experimental results, the main conclusions can be drawn as follows:

1. The structural build-up and setting time results indicated that the setting of NH-AAS is a continuous process. While SS-AAS showed a lower initial storage modulus, followed by an abrupt increase in structural build-up, showing that the initial set occurred suddenly. At initial setting time, NH-AAS and SS-AAS both release similar heat and reach a similar reaction degree.
2. At initial setting times, the C-A-S-H and N-A-S-H gels are both formed in the NH-AAS and SS-AAS mixtures. The difference, however, is that the C-A-S-H gel is more dominating in NH-AAS, while SS-AAS contains more N-A-S-H gel.
3. With time elapsing, more N-A-S-H gel in the mixture SS-AAS precipitates up to the end of the induction period. However, these 3D N-A-S-H gel will degrade to chain-like C-A-S-H gel after the acceleration peak of the isothermal calorimetric curves.

## **Part VII**

---

### **Conclusions and Perspectives**



## **Chapter 11 Conclusions and perspectives**

---

An overview of the results and findings of this thesis is summarized in this concluding chapter. Some further research perspectives are also presented.

## 1. General conclusions

---

The influences of activator solution, precursors, mineral addition and chemical admixture properties on rheology and structural formation of alkali-activated cements were comprehensively investigated. The rheological behaviour of AAS was significantly influenced by the concentration of sodium hydroxide activator. A strong relationship between the Vicat initial setting time and ultrasonic pulse wave for sodium hydroxide-activated slag mixtures identifying the characteristic points or inflection points in the ultrasonic curves and reaching a specific value in the ultrasonic velocity. The early reaction process of the sodium hydroxide-activated slag pastes determined by ultrasonic pulse wave and calorimeter consists of three stages: dissolution, acceleration/condensation and deceleration stages. The yield stress and apparent viscosity of the pastes increase by the addition of sodium hydroxide, and the pastes start to show shear-thickening behaviour when sodium hydroxide concentration reaches 8M. It was also revealed that Si, Al and Ca ion concentrations in the pore solution increase with an increase in sodium hydroxide concentration, and the pore solution of the pastes is dominated by Na and OH<sup>-</sup>. No significant influence of sodium hydroxide concentrations upon 4M on the compressive strength of the mortar samples was observed.

The effects of slag/fly ash ratio, mass ratio of SiO<sub>2</sub> to Na<sub>2</sub>O (Ms) of sodium silicate activator solution and sodium silicate dosage on structural build-up, flow properties and setting characteristics of AAC mixtures were investigated. The solid-like behaviour becomes more dominant with increasing Slag/FA ratio. The Ms value had significant effect on the structural build-up. Significantly higher initial storage modulus with a low increasing rate was observed for the Ms values lower than 0.8. However, for higher Ms values, a sudden increase in storage modulus was observed after negligible initial structuration. An increase in sodium silicate dosage caused a considerable delay in the abrupt increase in the structural formation. ICP-OES tests revealed the lower release of Al and Ca into the pore solution of slag/FA mixtures with low Ms values. A relationship between pore solution chemistry and structural build-up of AAC has been established.

To obtain a more sustainable and economic alkaline activator, silica fume activator (SFA) was introduced and compared with common commercial sodium silicate activator (SSA). The setting time of AAS activated by SFA prolonged significantly with an increase of Ms value opposite to SSA activation case. From the rheological point of view, SFA-activated mixtures exhibited a slower structural build-up in the early stage and better workability retention than SSA-activated mixtures. In addition, SFA mixtures showed lower drying shrinkage and slightly higher mechanical properties as compared to SSA mixtures. Microstructure analysis revealed that the mixture produced by SFA with Ms value of 1.2 had less micro-cracks and a well-packed microstructure as compared to the mixtures produced by SSA. The overall evaluation of the test results revealed that SFA could be a more economical and sustainable alternative to SSA with its lower cost, much lower CO<sub>2</sub> emissions, and

more favorable engineering properties

Regarding the effect of supplementary materials on the structural build-up of AAC mixtures, the pastes incorporating Portland cement or silica fume have a potential to be used in the practical engineering requiring a high structural build-up rate, such as the reduction of formwork pressure, slip form paving, stability and 3D printing concrete. While the early lower structural build-up rate for the mixture with the addition of fly ash and limestone powder activated by Ms1.2 are preferred for the application of multi-layer casting. By the investigation of SEM/EDX, it is found that the AAC pastes present the similar gel C-(N)-A-S-H/C-(A)-S-H and C-S-H at the early age regardless of the type of supplementary materials used.

The utilization potential of citric acid, sodium tetraborate decahydrate and sodium triphosphate pentabasic to control fresh state properties of sodium silicate-activated slag pastes has also been studied. The early structural build-up, reaction kinetics, pore solution chemistry, setting behaviour, and hardened properties such as microstructure, pore structure, and mechanical properties of AAS with these chemicals were investigated. It was found that early structural build-up, reaction kinetics and setting behaviour of AAS can be well controlled by using these chemicals. The citric acid was found the most effective admixture to prolong the setting time of AAS; however, it caused a dramatic decrease in mechanical properties. On the other hand sodium triphosphate pentabasic could provide a slight delay in setting time, while sodium tetraborate decahydrate prolonged the setting time significantly without any detrimental effect on the mechanical properties.

To further understand the difference of rheological behaviour between sodium hydroxide- and sodium silicate-activated slag mixtures, a deeper and comprehensive investigation was performed. The sodium silicate-activated slag mixtures exhibited a lower yield stress and a higher plastic viscosity than sodium hydroxide-activated slag mixtures. The small-amplitude oscillatory shear (SAOS) tests indicated a negligible colloidal interaction between slag particles in sodium silicate-activated system; therefore, the early increase in structuration was associated with the formation of reaction products due to the interaction between the dissolved calcium ions and the silicates originating from the activator solution. On the other hand, the stiffness and the early increase in structural build-up of sodium hydroxide-activated slag system were attributed to the formation of well-percolated network.

Nuclear magnetic resonance (NMR) was also used to determine the nanostructure of AAS at initial setting times. It was found that the C-A-S-H and N-A-S-H gel were the main reaction products for the AAS pastes at the initial setting times. Furthermore, the N-A-S-H gel will gradually degrade to C-A-S-H during the period of the acceleration peaks within isothermal calorimetry curves for the AAS mixtures.

## 2. Main contributions

---

The main contributions of this thesis can be summarized in the following aspects:

1. The influences of activators, precursors, mineral addition and chemical retarders on structural build-up and rheology is systematically investigated. ICP-OES was used to investigate the pore solution chemistry, and the concentration of various ions was correlated with the structuration of AAC pastes.
2. A more sustainable and economic activator, silica fume activator, is evaluated and compared with commercial sodium silicate activator.
3. The setting process of sodium hydroxide- and sodium silicate-activated mixtures was evaluated by a series of rheological measurements. The presence of a percolation network was confirmed by SAOS tests. Physical contributions from the percolated network and chemical contributions from the reaction have been identified.
4. The relationship between early structural build-up and reaction products determined by NMR is found. The nanostructure of AAS at initial setting time has been determined.

## 3. Perspectives

---

The relationship between composition variables and inter-particle forces, as well as hydration kinetics in AAC, should be studied in more detail. This will result in a comprehensive knowledge of the interaction mechanisms and the impact of the various components.

Greater attention should be devoted to various research gaps and restricted research, such as the method of activator addition, sodium hydroxide-metakaolin-based systems or systems employing a greener activator (such as  $\text{Na}_2\text{CO}_3$  or a blend thereof) and so on.

Robust formulations and pertinent chemicals to fulfill the rheological and mechanical specifications of AAMs. To enhance the poor workability of AAC, for instance, the development of organic plasticizers specialized for AAC or the inclusion of inorganic plasticizers is necessary.

While the AAC paste has been rheologically tuned at laboratory scale, its performance should be assessed in real-world systems, such as concrete. Based on this thesis' findings, one can first pick a meaningful mixing technique for concrete systems, integrating the real shear rate regimes that binder particles experience between concrete aggregates. Then, AAC paste investigations must be validated on AAC concrete scale, and the shear technique will be revalidated in AAC concrete systems. If specific shear rates cannot be attained in the planetary concrete mixer, for instance, high shear mixing on the concrete scale or alternate aggregate grading will be explored. The accumulated expertise facilitates the assessment of new properties with both

quantitative (e.g. ConTec Visco 5 rheometer, Sliding pipe rheometer) and empirical (slump flow, V-funnel, L-Box, etc.) approaches.

## References

---

- [1] J. G. J. Olivier, M. Muntean, and J. A. H. W. Peters, "Trends in global CO<sub>2</sub> emissions: 2015 Report Background Study," *PBL Netherlands Environ. Assess. Agency Eur. Comm. Jt. Res. Cent.*, pp. 1–78, 2015, [Online]. Available: [http://edgar.jrc.ec.europa.eu/news\\_docs/jrc-2015-trends-in-global-co2-emissions-2015-report-98184.pdf](http://edgar.jrc.ec.europa.eu/news_docs/jrc-2015-trends-in-global-co2-emissions-2015-report-98184.pdf).
- [2] M. C. G. Juenger, F. Winnefeld, J. L. Provis, and J. H. Ideker, "Advances in alternative cementitious binders," *Cem. Concr. Res.*, vol. 41, no. 12, pp. 1232–1243, 2011, doi: 10.1016/j.cemconres.2010.11.012.
- [3] A. Palomo, P. Krivenko, I. Garcia-Lodeiro, E. Kavalerova, O. Maltseva, and A. Fernández-Jiménez, "A review on alkaline activation: New analytical perspectives," *Mater. Constr.*, vol. 64, no. 315, 2014, doi: 10.3989/mc.2014.00314.
- [4] E. Gartner, "Industrially interesting approaches to 'low-CO<sub>2</sub>' cements," *Cem. Concr. Res.*, vol. 34, no. 9, pp. 1489–1498, 2004, doi: 10.1016/j.cemconres.2004.01.021.
- [5] P. Duxson, J. L. Provis, G. C. Lukey, and J. S. J. van Deventer, "The role of inorganic polymer technology in the development of 'green concrete,'" *Cem. Concr. Res.*, vol. 37, no. 12, pp. 1590–1597, 2007, doi: 10.1016/j.cemconres.2007.08.018.
- [6] J. L. Provis, "Geopolymers and other alkali activated materials : why , how , and what ?," *Mater. Struct.*, pp. 11–25, 2014, doi: 10.1617/s11527-013-0211-5.
- [7] L. Kopecky, "Micromechanical multiscale model for alkali activation of fly ash and metakaolin," *J. Mater. Sci.*, no. January 2014, 2011, doi: 10.1007/s10853-011-5601-x.
- [8] P. Duxson, A. Fernández-Jiménez, J. L. Provis, G. C. Lukey, A. Palomo, and J. S. J. Van Deventer, "Geopolymer technology: The current state of the art," *J. Mater. Sci.*, vol. 42, no. 9, pp. 2917–2933, 2007, doi: 10.1007/s10853-006-0637-z.
- [9] RILEM-TC 224-AAM, *Alkali Activated Materials*. 2014.
- [10] S. A. Bernal and J. L. Provis, "Durability of alkali-activated materials: Progress and perspectives," *J. Am. Ceram. Soc.*, vol. 97, no. 4, pp. 997–1008, 2014, doi: 10.1111/jace.12831.
- [11] C. K. Yip and J. S. J. Van Deventer, "Microanalysis of calcium silicate hydrate gel formed within a geopolymeric binder," *J. Mater. Sci.*, vol. 38, no. 18, pp. 3851–3860, 2003, doi: 10.1023/A:1025904905176.
- [12] A. Palomo, M. W. Grutzeck, and M. T. Blanco, "Alkali-activated fly ashes: A cement for the future," *Cem. Concr. Res.*, vol. 29, no. 8, pp. 1323–1329, 1999, doi: 10.1016/S0008-8846(98)00243-9.
- [13] S. Puligilla and P. Mondal, "Role of slag in microstructural development and

- hardening of fly ash-slag geopolymer,” *Cem. Concr. Res.*, vol. 43, no. 1, pp. 70–80, 2013, doi: 10.1016/j.cemconres.2012.10.004.
- [14] W. K. W. Lee and J. S. J. Van Deventer, “The effect of ionic contaminants on the early-age properties of alkali-activated fly ash-based cements,” *Cem. Concr. Res.*, vol. 32, no. 4, pp. 577–584, 2002, doi: 10.1016/S0008-8846(01)00724-4.
- [15] R. J. Thomas and S. Peethamparan, “Alkali-activated concrete: Engineering properties and stress-strain behaviour,” *Constr. Build. Mater.*, vol. 93, pp. 49–56, 2015, doi: 10.1016/j.conbuildmat.2015.04.039.
- [16] D. R. Shi, Caijun, Pavel V, Krivenko, *Alkali-Activated Cements and Concretes*. 2006.
- [17] D. M. Roy, W. Jiang, and M. R. Silsbee, “Chloride diffusion in ordinary, blended, and alkali-activated cement pastes and its relation to other properties,” *Cem. Concr. Res.*, vol. 30, no. 12, pp. 1879–1884, 2000, doi: 10.1016/S0008-8846(00)00406-3.
- [18] R. E. Lyon, P. N. Balaguru, A. Foden, U. Sorathia, J. Davidovits, and M. Davidovics, “Fire-resistant aluminosilicate composites,” *Fire Mater.*, vol. 21, no. 2, pp. 67–73, 1997, doi: 10.1002/(SICI)1099-1018(199703)21:2<67::AID-FAM596>3.0.CO;2-N.
- [19] F. Pacheco-Torgal, Z. Abdollahnejad, A. F. Camões, M. Jamshidi, and Y. Ding, “Durability of alkali-activated binders: A clear advantage over Portland cement or an unproven issue?,” *Constr. Build. Mater.*, vol. 30, pp. 400–405, 2012, doi: 10.1016/j.conbuildmat.2011.12.017.
- [20] M. Palacios *et al.*, “Early reactivity of sodium silicate-activated slag pastes and its impact on rheological properties,” *Cem. Concr. Res.*, vol. 140, no. July 2020, p. 106302, 2021, doi: 10.1016/j.cemconres.2020.106302.
- [21] D. S. Perera, O. Uchida, E. R. Vance, and K. S. Finnie, “Influence of curing schedule on the integrity of geopolymers,” *J. Mater. Sci.*, vol. 42, no. 9, pp. 3099–3106, 2007, doi: 10.1007/s10853-006-0533-6.
- [22] C. Kuenzel, L. J. Vandeperre, S. Donatello, A. R. Boccaccini, and C. Cheeseman, “Ambient temperature drying shrinkage and cracking in metakaolin-based geopolymers,” *J. Am. Ceram. Soc.*, vol. 95, no. 10, pp. 3270–3277, 2012, doi: 10.1111/j.1551-2916.2012.05380.x.
- [23] M. Palacios and F. Puertas, “Effect of shrinkage-reducing admixtures on the properties of alkali-activated slag mortars and pastes,” *Cem. Concr. Res.*, vol. 37, no. 5, pp. 691–702, 2007, doi: 10.1016/j.cemconres.2006.11.021.
- [24] M. Chi, “Effects of modulus ratio and dosage of alkali-activated solution on the properties and micro-structural characteristics of alkali-activated fly ash mortars,” *Constr. Build. Mater.*, vol. 99, pp. 128–136, 2015, doi: 10.1016/j.conbuildmat.2015.09.029.
- [25] K. Kovler and N. Roussel, “Properties of fresh and hardened concrete,” *Cem.*

## References

- Concr. Res.*, vol. 41, no. 7, pp. 775–792, 2011, doi: 10.1016/j.cemconres.2011.03.009.
- [26] N. Roussel, A. Lemaître, R. J. Flatt, and P. Coussot, “Steady state flow of cement suspensions: A micromechanical state of the art,” *Cem. Concr. Res.*, vol. 40, no. 1, pp. 77–84, 2010, doi: 10.1016/j.cemconres.2009.08.026.
- [27] Q. Yuan, D. Zhou, K. H. Khayat, D. Feys, and C. Shi, “On the measurement of evolution of structural build-up of cement paste with time by static yield stress test vs. small amplitude oscillatory shear test,” *Cem. Concr. Res.*, vol. 99, no. September 2016, pp. 183–189, 2017, doi: 10.1016/j.cemconres.2017.05.014.
- [28] Q. Yuan, D. Zhou, B. Li, H. Huang, and C. Shi, “Effect of mineral admixtures on the structural build-up of cement paste,” *Constr. Build. Mater.*, vol. 160, pp. 117–126, 2018, doi: 10.1016/j.conbuildmat.2017.11.050.
- [29] D. Feys, J. E. Wallevik, A. Yahia, K. H. Khayat, and O. H. Wallevik, “Extension of the Reiner – Rivlin equation to determine modified Bingham parameters measured in coaxial cylinders rheometers,” *Mater. Struct.*, pp. 289–311, 2013, doi: 10.1617/s11527-012-9902-6.
- [30] M. Palacios, P. F. G. Banfill, and F. Puertas, “Rheology and setting of alkali-activated slag pastes and mortars: Effect of organic admixture,” *ACI Mater. J.*, vol. 105, no. 2, pp. 140–148, 2008, doi: 10.14359/19754.
- [31] F. Puertas, C. Varga, and M. M. Alonso, “Rheology of alkali-activated slag pastes. Effect of the nature and concentration of the activating solution,” *Cem. Concr. Compos.*, vol. 53, pp. 279–288, 2014, doi: 10.1016/j.cemconcomp.2014.07.012.
- [32] D. Zhang, K. Zhao, F. Xie, H. Li, and D. Wang, “Effect of water-binding ability of amorphous gel on the rheology of geopolymers fresh pastes with the different NaOH content at the early age,” *Constr. Build. Mater.*, vol. 261, p. 120529, 2020, doi: 10.1016/j.conbuildmat.2020.120529.
- [33] N. Roussel, G. Ovarlez, S. Garraul, C. Brumaud, “The origins of thixotropy of fresh cement pastes,” *Cem. Concr. Res.*, no. 42, pp. 148–157, 2012, doi: 10.1016/j.cemconres.2011.09.004.
- [34] L. J. Struble and M. A. Schultz, “Using creep and recovery to study flow behaviour of fresh cement paste,” *Cem. Concr. Res.*, vol. 23, no. 6, pp. 1369–1379, 1993, doi: 10.1016/0008-8846(93)90074-J.
- [35] N. Roussel and F. Cussigh, “Distinct-layer casting of SCC: The mechanical consequences of thixotropy,” *Cem. Concr. Res.*, vol. 38, no. 5, pp. 624–632, 2008, doi: 10.1016/j.cemconres.2007.09.023.
- [36] N. Roussel, H. Bessaies-Bey, S. Kawashima, D. Marchon, K. Vasilic, and R. Wolfs, “Recent advances on yield stress and elasticity of fresh cement-based materials,” *Cem. Concr. Res.*, vol. 124, no. June, p. 105798, 2019, doi: 10.1016/j.cemconres.2019.105798.

- [37] N. Roussel, "Understanding the Rheology of Concrete," *Woodhead Publ. Ltd.*, 2011.
- [38] P. H. Billberg *et al.*, "Field validation of models for predicting lateral form pressure exerted by SCC," *Cem. Concr. Compos.*, vol. 54, pp. 70–79, 2014, doi: 10.1016/j.cemconcomp.2014.02.003.
- [39] A. Perrot, D. Rangeard, and A. Pierre, "Structural built-up of cement-based materials used for 3D-printing extrusion techniques," *Mater. Struct.*, vol. 49, no. 4, pp. 1213–1220, 2016, doi: 10.1617/s11527-015-0571-0.
- [40] *BS EN 196-3:2005 +A1:2008 Methods of testing cement — Part 3: Determination of setting times and soundness*, vol. 3, no. August. 2003.
- [41] ASTM C191-08, "Standard Test Methods for Time of Setting of Hydraulic Cement by Vicat Needle," vol. i, 2008, doi: 10.1520/C0191-08.2.
- [42] X. Dongyu, H. Shifeng, Q. Lei, L. Lingchao, and C. Xin, "Monitoring of cement hydration reaction process based on ultrasonic technique of piezoelectric composite transducer," *Constr. Build. Mater.*, vol. 35, pp. 220–226, 2012, doi: 10.1016/j.conbuildmat.2012.02.094.
- [43] R. Cao, S. Zhang, N. Banthia, Y. Zhang, and Z. Zhang, "Interpreting the early-age reaction process of alkali-activated slag by using combined embedded ultrasonic measurement , thermal analysis , XRD , FTIR and SEM," *Compos. Part B*, vol. 186, no. November 2019, p. 107840, 2020, doi: 10.1016/j.compositesb.2020.107840.
- [44] S. Uppalapati, L. Vandewalle, and Ö. Cizer, "Monitoring the setting process of alkali-activated slag-fly ash cements with ultrasonic P-wave velocity," *Constr. Build. Mater.*, vol. 271, p. 121592, 2021, doi: 10.1016/j.conbuildmat.2020.121592.
- [45] L. Hertwig and K. Holschemacher, "Setting Time and Strength Monitoring of Alkali-Activated," *Materials (Basel)*, vol. 1889, no. 14, 2021.
- [46] L. Nachbaur, J. C. Mutin, A. Nonat, and L. Choplin, "Dynamic mode rheology of cement and tricalcium silicate pastes from mixing to setting," *Cem. Concr. Res.*, vol. 31, no. 2, pp. 183–192, 2001, doi: 10.1016/S0008-8846(00)00464-6.
- [47] X. Dai, S. Aydın, M. Y. Yardımcı, K. Lesage, and G. De Schutter, "Effects of activator properties and GGBFS/FA ratio on the structural build-up and rheology of AAC," *Cem. Concr. Res.*, vol. 138, no. October, p. 106253, 2020, doi: 10.1016/j.cemconres.2020.106253.
- [48] Y. Rifaai, A. Yahia, A. Mostafa, S. Aggoun, and E. H. Kadri, "Rheology of fly ash-based geopolymer: Effect of NaOH concentration," *Constr. Build. Mater.*, vol. 223, pp. 583–594, 2019, doi: 10.1016/j.conbuildmat.2019.07.028.
- [49] M. F. Alnahhal, T. Kim, and A. Hajimohammadi, "Distinctive rheological and temporal viscoelastic behaviour of alkali-activated fly ash / slag pastes : A comparative study with cement paste," *Cem. Concr. Res.*, vol. 144, no. March,

## References

- p. 106441, 2021, doi: 10.1016/j.cemconres.2021.106441.
- [50] A. Poulesquen, F. Frizon, and D. Lambertin, “Rheological behaviour of alkali-activated metakaolin during geopolymerization,” *Cem. Mater. Nucl. Waste Storage*, vol. 357, no. 21, pp. 225–238, 2013, doi: 10.1007/978-1-4614-3445-0\_20.
- [51] X. Dai, S. Aydin, M. Y. Yardımcı, K. Lesage, and G. De Schutter, “Influence of water to binder ratio on the rheology and structural Build-up of Alkali-Activated Slag / Fly ash mixtures,” *Constr. Build. Mater.*, vol. 264, p. 120253, 2020, doi: 10.1016/j.conbuildmat.2020.120253.
- [52] J. Rouyer and A. Poulesquen, “Evidence of a Fractal Percolating Network During Geopolymerization,” *Am. Ceram. Soc.*, vol. 1587, 2015, doi: 10.1111/jace.13480.
- [53] J. J. Thomas *et al.*, “Modeling and simulation of cement hydration kinetics and microstructure development,” *Cem. Concr. Res.*, vol. 41, no. 12, pp. 1257–1278, 2011, doi: 10.1016/j.cemconres.2010.10.004.
- [54] S. Dittrich and J. Neubauer, “The influence of fly ash on the hydration of OPC within the first 44 h —A quantitative in situ XRD and heat flow calorimetry study,” *Cem. Concr. Res.*, vol. 56, pp. 129–138, 2014, doi: 10.1016/j.cemconres.2013.11.013.
- [55] D. Ravikumar and N. Neithalath, “Reaction kinetics in sodium silicate powder and liquid activated slag binders evaluated using isothermal calorimetry,” *Thermochim. Acta*, vol. 546, pp. 32–43, 2012, doi: 10.1016/j.tca.2012.07.010.
- [56] S. Alonso and A. Palomo, “Calorimetric study of alkaline activation of calcium hydroxide ± metakaolin solid mixtures,” *Cem. Concr. Res.*, vol. 31, 2001.
- [57] M. L. Granizo and M. . Blanco, “Alkaline activation of metakaolin: An isothermal conduction calorimetry study,” *J. Therm. Anal. Calorim.*, pp. 957–965, 1998.
- [58] A. Buchwald, R. Tatarin, and D. Stephan, “Reaction progress of alkaline-activated metakaolin-ground granulated blast furnace slag blends,” *J. Mater. Sci.*, vol. 44, no. 20, pp. 5609–5617, 2009, doi: 10.1007/s10853-009-3790-3.
- [59] Y. Zuo and G. Ye, “Preliminary Interpretation of the Induction Period in Hydration of Sodium Hydroxide / Silicate,” *Materials (Basel)*, 2020.
- [60] P. G. Falkowski *et al.*, “Variation of Crystal Dissolution Rate Based on a Dissolution Stepwave Model,” *Science (80- )*, vol. 291, no. March, pp. 2400–2405, 2001.
- [61] P. M. Dove, N. Han, and J. J. De Yoreo, “Mechanisms of classical crystal growth theory explain quartz and silicate dissolution behaviour,” *Proc. Natl. Acad. Sci. U. S. A.*, vol. 102, no. 43, 2005, doi: 10.1073/pnas.0507777102.
- [62] P. Juilland, E. Gallucci, R. Flatt, and K. Scrivener, “Dissolution theory applied to the induction period in alite hydration,” *Cem. Concr. Res.*, vol. 40, no. 6,

- pp. 831–844, 2010, doi: 10.1016/j.cemconres.2010.01.012.
- [63] P. Steins, A. Poulesquen, O. Diat, and F. Frizon, “Structural evolution during geopolymerization from an early age to consolidated material,” *Langmuir*, vol. 28, no. 22, pp. 8502–8510, 2012, doi: 10.1021/la300868v.
- [64] N. V. Y. Scarlett and I. C. Madsen, “Quantification of Phases with Partial or No Known Crystal Structures Quantification of phases with partial or no known crystal structures,” *Powder Diffr.*, no. December 2006, 2014, doi: 10.1154/1.2362855.
- [65] B. Haha, S. A. Bernal, N. De Belie, E. Gruyaert, P. T. Durdzin, and L. P. Axel, “Outcomes of the RILEM round robin on degree of reaction of slag and fly ash in blended cements,” *Mater. Struct.*, 2017, doi: 10.1617/s11527-017-1002-1.
- [66] R. Snellings, A. Salze, and K. L. Scrivener, “Use of X-ray diffraction to quantify amorphous supplementary cementitious materials in anhydrous and hydrated blended cements,” *Cem. Concr. Res.*, vol. 64, pp. 89–98, 2014, doi: 10.1016/j.cemconres.2014.06.011.
- [67] Z. Sun and A. Vollpracht, “Isothermal calorimetry and in-situ XRD study of the NaOH activated fly ash, metakaolin and slag,” *Cem. Concr. Res.*, vol. 103, no. November 2017, pp. 110–122, 2018, doi: 10.1016/j.cemconres.2017.10.004.
- [68] A. Hajimohammadi, T. Ngo, and P. Mendis, “How does aluminium foaming agent impact the geopolymer formation mechanism?,” *Cem. Concr. Compos.*, vol. 80, pp. 277–286, 2017, doi: 10.1016/j.cemconcomp.2017.03.022.
- [69] S. Song and H. M. Jennings, “Pore solution chemistry of alkali-activated ground granulated blast-furnace slag,” *Cem. Concr. Res.*, vol. 29, no. 2, pp. 159–170, 1999, doi: 10.1016/S0008-8846(98)00212-9.
- [70] Y. Zuo, M. Nedeljković, and G. Ye, “Pore solution composition of alkali-activated slag/fly ash pastes,” *Cem. Concr. Res.*, vol. 115, no. October 2018, pp. 230–250, 2019, doi: 10.1016/j.cemconres.2018.10.010.
- [71] F. Puertas, A. Fernández-Jiménez, and M. T. Blanco-Varela, “Pore solution in alkali-activated slag cement pastes. Relation to the composition and structure of calcium silicate hydrate,” *Cem. Concr. Res.*, vol. 34, no. 1, pp. 139–148, 2004, doi: 10.1016/S0008-8846(03)00254-0.
- [72] R. TC-238, “RILEM TC - 238 SCM Recommendation on hydration stoppage by solvent exchange for the study of hydrate assemblages,” *Mater. Struct.*, no. December 2018, 2019, doi: 10.1617/s11527-018-1298-5.
- [73] X. Chen, A. Meawad, and L. J. Struble, “Method to stop geopolymer reaction,” *J. Am. Ceram. Soc.*, vol. 97, no. 10, pp. 3270–3275, 2014, doi: 10.1111/jace.13071.
- [74] X. Chen, A. Sutrisno, and L. J. Struble, “Effects of calcium on setting mechanism of metakaolin-based geopolymer,” *J. Am. Ceram. Soc.*, vol. 101,

## References

- no. 2, pp. 957–968, 2018, doi: 10.1111/jace.15249.
- [75] S. D. Wang and K. L. Scrivener, “<sup>29</sup>Si and <sup>27</sup>Al NMR study of alkali-activated slag,” *Cem. Concr. Res.*, vol. 33, no. 5, pp. 769–774, 2003, doi: 10.1016/S0008-8846(02)01044-X.
- [76] J. Davidovits, *Geopolymer chemistry and applications*, no. January 2008. 2008.
- [77] G. Fang and M. Zhang, “Multiscale micromechanical analysis of alkali-activated fly ash-slag paste,” *Cem. Concr. Res.*, vol. 135, no. May, p. 106141, 2020, doi: 10.1016/j.cemconres.2020.106141.
- [78] A. Favier, G. Habert, N. Roussel, and J. B. D’Espinosede Lacaillerie, “A multinuclear static NMR study of geopolymerisation,” *Cem. Concr. Res.*, vol. 75, pp. 104–109, 2015, doi: 10.1016/j.cemconres.2015.03.003.
- [79] X. Dai, S. Aydın, M. Y. Yardımcı, K. Lesage, and G. De Schutter, “Effect of Ca(OH)<sub>2</sub> Addition on the Engineering Properties of Sodium Sulfate Activated Slag,” *Materials (Basel)*, vol. 14, p. 4266, 2021.
- [80] S. Aydın and B. Baradan, “Effect of activator type and content on properties of alkali-activated slag mortars,” *Compos. Part B Eng.*, vol. 57, pp. 166–172, 2014, doi: 10.1016/j.compositesb.2013.10.001.
- [81] B. S. Gebregziabiher, R. Thomas, and S. Peethamparan, “Very early-age reaction kinetics and microstructural development in alkali-activated slag,” *Cem. Concr. Compos.*, vol. 55, pp. 91–102, 2015, doi: 10.1016/j.cemconcomp.2014.09.001.
- [82] N. R. Rakhimova *et al.*, “Marl-based geopolymers incorporated with limestone: A feasibility study,” *J. Non. Cryst. Solids*, vol. 492, no. February, pp. 1–10, 2018, doi: 10.1016/j.jnoncrysol.2018.04.015.
- [83] N. K. Lee, J. G. Jang, and H. K. Lee, “Shrinkage characteristics of alkali-activated fly ash/slag paste and mortar at early ages,” *Cem. Concr. Compos.*, vol. 53, pp. 239–248, 2014, doi: 10.1016/j.cemconcomp.2014.07.007.
- [84] Y. Sun *et al.*, “Rheology of alkali-activated slag pastes: New insight from microstructural investigations by cryo-SEM,” *Cem. Concr. Res.*, vol. 157, no. April, p. 106806, 2022, doi: 10.1016/j.cemconres.2022.106806.
- [85] R. J. Myers, S. A. Bernal, and J. L. Provis, “A thermodynamic model for C-(N-)A-S-H gel: CNASH<sub>ss</sub>. Derivation and validation,” *Cem. Concr. Res.*, vol. 66, pp. 27–47, 2014, doi: 10.1016/j.cemconres.2014.07.005.
- [86] R. J. Myers, E. L’Hôpital, J. L. Provis, and B. Lothenbach, “Composition-solubility-structure relationships in calcium (alkali) aluminosilicate hydrate (C-(N,K-)A-S-H),” *Dalt. Trans.*, vol. 44, no. 30, pp. 13530–13544, 2015, doi: 10.1039/c5dt01124h.
- [87] R. J. Myers, B. Lothenbach, S. A. Bernal, and J. L. Provis, “Applied Geochemistry Thermodynamic modelling of alkali-activated slag cements,” *Appl. GEOCHEMISTRY*, vol. 61, pp. 233–247, 2015, doi:

- 10.1016/j.apgeochem.2015.06.006.
- [88] Y. Zuo, M. Nedeljković, and G. Ye, “Coupled thermodynamic modelling and experimental study of sodium hydroxide activated slag,” *Constr. Build. Mater.*, vol. 188, pp. 262–279, 2018, doi: 10.1016/j.conbuildmat.2018.08.087.
- [89] R. J. Myers, S. A. Bernal, and J. L. Provis, “Phase diagrams for alkali-activated slag binders,” *Cem. Concr. Res.*, vol. 95, pp. 30–38, 2017, doi: 10.1016/j.cemconres.2017.02.006.
- [90] L. Gomez-Zamorano, M. Balonis, B. Erdemli, N. Neithalath, and G. Sant, “C–(N)–S–H and N–A–S–H gels: Compositions and solubility data at 25°C and 50°C,” *J. Am. Ceram. Soc.*, vol. 100, no. 6, pp. 2700–2711, 2017, doi: 10.1111/jace.14715.
- [91] G. D. Miron, T. Wagner, D. A. Kulik, and C. A. Heinrich, “Internally consistent thermodynamic data for aqueous species in the system Na-K-Al-Si-O-H-Cl,” *Geochim. Cosmochim. Acta*, vol. 187, pp. 41–78, 2016, doi: 10.1016/j.gca.2016.04.026.
- [92] M. U. Okoronkwo, M. Balonis, L. Katz, M. Juenger, and G. Sant, “A thermodynamics-based approach for examining the suitability of cementitious formulations for solidifying and stabilizing coal-combustion wastes,” *J. Environ. Manage.*, vol. 217, pp. 278–287, 2018, doi: 10.1016/j.jenvman.2018.02.095.
- [93] R. J. Flatt, “Dispersion forces in cement suspensions,” *Cem. Concr. Res.*, vol. 34, no. 3, pp. 399–408, 2004, doi: 10.1016/j.cemconres.2003.08.019.
- [94] R. J. Flatt and P. Bowen, “Electrostatic repulsion between particles in cement suspensions: Domain of validity of linearized Poisson-Boltzmann equation for nonideal electrolytes,” *Cem. Concr. Res.*, vol. 33, no. 6, pp. 781–791, 2003, doi: 10.1016/S0008-8846(02)01059-1.
- [95] D. Feys, *Interacties tussen de reologische eigenschappen en het verpompen van zelfverdichtend beton Interactions between Rheological Properties and Pumping of Self-Compacting Concrete*. 2009.
- [96] P. Billberg, *Form Pressure Generated by Self-Compacting Concrete — Influence of Thixotropy and Structural Behaviour at Rest*. 2006.
- [97] C. Based, “Interparticle Potential and Sedimentation Behaviour of Cement Suspensions,” *Advn Cem Bas Mat*, vol. 7355, no. 96, 1997.
- [98] B. Ersoy, S. Dikmen, and T. Kavas, “Effect of mixing water types on the time-dependent zeta potential of Portland cement paste,” *Eng Compos Mater*, vol. 20, no. 3, pp. 285–292, 2013, doi: 10.1515/secm-2012-0099.
- [99] A. Nonat, J. C. Mutin, X. Lecoq, and S. P. Jiang, “Physico-chemical parameters determining hydration and particle interactions during the setting of silicate cements,” *Solid state ionics*, vol. 103, pp. 923–930, 1997.
- [100] S. P. Jiang, J. C. Mutin, and A. Nonat, “Studies on mechanism and physico-chemical parameters at the origin of the cement setting. I. The fundamental

## References

- processes involved during the cement setting,” vol. 25, no. 4, pp. 779–789, 1995.
- [101] A. Favier, J. Hot, G. Habert, N. Roussel, and J. B. D’Espinoze De Lacaille, “Flow properties of MK-based geopolymer pastes. A comparative study with standard Portland cement pastes,” *Soft Matter*, vol. 10, no. 8, pp. 1134–1141, 2014, doi: 10.1039/c3sm51889b.
- [102] A. Kashani, J. L. Provis, G. G. Qiao, and J. S. J. Van Deventer, “The interrelationship between surface chemistry and rheology in alkali activated slag paste,” *Constr. Build. Mater.*, vol. 65, pp. 583–591, 2014, doi: 10.1016/j.conbuildmat.2014.04.127.
- [103] M. Torres-Carrasco and F. Puertas, “Alkaline activation of different aluminosilicates as an alternative to Portland cement: alkali activated cements or geopolymers,” *Rev. Ing. Constr.*, vol. 32, no. 2, pp. 5–12, 2017, doi: 10.4067/s0718-50732017000200001.
- [104] S. E. Wallah and B. V. Rangan, “Low-calcium fly ash-based geopolymer concrete: Long-term properties,” *Res. Rep. GC*, 2006, [Online]. Available: [http://www.geopolymer.org/fichiers\\_pdf/curtin\\_flyash\\_GC-2.pdf](http://www.geopolymer.org/fichiers_pdf/curtin_flyash_GC-2.pdf).
- [105] J. Aupoil, J. B. Champenois, J. B. d’Espinoze de Lacaille, and A. Poulesquen, “Interplay between silicate and hydroxide ions during geopolymerization,” *Cem. Concr. Res.*, vol. 115, no. May 2018, pp. 426–432, 2019, doi: 10.1016/j.cemconres.2018.09.012.
- [106] A. Mobili, A. Belli, C. Giosuè, T. Bellezze, and F. Tittarelli, “Metakaolin and fly ash alkali-activated mortars compared with cementitious mortars at the same strength class,” *Cem. Concr. Res.*, vol. 88, pp. 198–210, 2016, doi: 10.1016/j.cemconres.2016.07.004.
- [107] C. Lu, Z. Zhang, C. Shi, N. Li, D. Jiao, and Q. Yuan, “Rheology of alkali-activated materials : A review,” *Cem. Concr. Compos.*, vol. 121, no. February, p. 104061, 2021, doi: 10.1016/j.cemconcomp.2021.104061.
- [108] H. Mehdizadeh and E. Najafi Kani, “Rheology and apparent activation energy of alkali activated phosphorous slag,” *Constr. Build. Mater.*, vol. 171, pp. 197–204, 2018, doi: 10.1016/j.conbuildmat.2018.03.130.
- [109] M. Mohan and A. Apurva, “Rheological and mechanical properties of alkali-activated brick powder based pastes : effect of amount of alkali activator,” *IOP Conf.*, 2018, doi: 10.1088/1757-899X/379/1/012011.
- [110] X. Dai, S. Aydin, M. Y. Yardımcı, R. Qiang, K. Lesage, and G. De Schutter, “Rheology, early-age hydration and microstructure of alkali-activated GGBFS-Fly ash-limestone mixtures,” *Cem. Concr. Compos.*, vol. 124, no. May, p. 104244, 2021, doi: 10.1016/j.cemconcomp.2021.104244.
- [111] X. Dai, S. Aydin, M. Y. Yardımcı, K. Lesage, and G. De Schutter, “Rheology and microstructure of alkali-activated slag cements produced with silica fume activator,” *Cem. Concr. Compos.*, vol. 125, no. September 2021, p. 104303, 2022, doi: 10.1016/j.cemconcomp.2021.104303.

- [112] X. Dai, S. Aydin, M. Y. Yardimci, K. Lesage, and G. de Schutter, “Influence of water to binder ratio on the rheology and structural Build-up of Alkali-Activated Slag/Fly ash mixtures,” *Constr. Build. Mater.*, vol. 264, Dec. 2020, doi: 10.1016/j.conbuildmat.2020.120253.
- [113] A. Gadkar and K. V. L. Subramaniam, “An evaluation of yield and Maxwell fluid behaviours of fly ash suspensions in alkali-silicate solutions,” *Mater. Struct.*, vol. 52, no. 6, pp. 1–10, 2019, doi: 10.1617/s11527-019-1429-7.
- [114] A. Aboulayt *et al.*, “Stability of a new geopolymer grout: Rheological and mechanical performances of metakaolin-fly ash binary mixtures,” *Constr. Build. Mater.*, vol. 181, pp. 420–436, 2018, doi: 10.1016/j.conbuildmat.2018.06.025.
- [115] T. Yang, H. Zhu, Z. Zhang, X. Gao, C. Zhang, and Q. Wu, “Effect of fly ash microsphere on the rheology and microstructure of alkali-activated fly ash/slag pastes,” *Cem. Concr. Res.*, vol. 109, no. April, pp. 198–207, 2018, doi: 10.1016/j.cemconres.2018.04.008.
- [116] J. L. Provis, P. Duxson, and J. S. J. van Deventer, “The role of particle technology in developing sustainable construction materials,” *Adv. Powder Technol.*, vol. 21, no. 1, pp. 2–7, 2010, doi: 10.1016/j.apt.2009.10.006.
- [117] K. Vance, A. Kumar, G. Sant, and N. Neithalath, “The rheological properties of ternary binders containing Portland cement, limestone, and metakaolin or fly ash,” *Cem. Concr. Res.*, vol. 52, pp. 196–207, 2013, doi: 10.1016/j.cemconres.2013.07.007.
- [118] P. Rovnaník, P. Rovnaníková, M. Vyšvařil, S. Grzeszczyk, and E. Janowska-Renkas, “Rheological properties and microstructure of binary waste red brick powder/metakaolin geopolymer,” *Constr. Build. Mater.*, 2018, doi: 10.1016/j.conbuildmat.2018.08.150.
- [119] M. Romagnoli, C. Leonelli, E. Kamse, and M. Lassinantti Gualtieri, “Rheology of geopolymer by DOE approach,” *Constr. Build. Mater.*, vol. 36, pp. 251–258, 2012, doi: 10.1016/j.conbuildmat.2012.04.122.
- [120] P. Koutník, A. Soukup, P. Bezucha, J. Šafař, and J. Kohout, “Low viscosity metakaolinite based geopolymer binders,” *Constr. Build. Mater.*, vol. 230, 2020, doi: 10.1016/j.conbuildmat.2019.116978.
- [121] Y. S. Wang, J. L. Provis, and J. G. Dai, “Role of soluble aluminum species in the activating solution for synthesis of silico-aluminophosphate geopolymers,” *Cem. Concr. Compos.*, vol. 93, no. May, pp. 186–195, 2018, doi: 10.1016/j.cemconcomp.2018.07.011.
- [122] V. Benavent *et al.*, “Impact of aluminum on the structure of geopolymers from the early stages to consolidated material,” *Cem. Concr. Res.*, vol. 90, pp. 27–35, 2016, doi: 10.1016/j.cemconres.2016.09.009.
- [123] K. Vance, A. Dakhane, G. Sant, and N. Neithalath, “Observations on the rheological response of alkali activated fly ash suspensions: the role of activator type and concentration,” *Rheol. Acta*, vol. 53, no. 10–11, pp. 843–

## References

- 855, 2014, doi: 10.1007/s00397-014-0793-z.
- [124] E. Nagele and U. Schneider, "The zeta-potential of blast furnace slag and fly ash," *Cem. Concr. Res.*, vol. 19, pp. 811–820, 1989.
- [125] E. Nagele, "The zeta-potential of cement Part II: Effect of pH-value," *Cem. Concr. Res.*, vol. 16, pp. 853–863, 1986.
- [126] A. Fernández-Jiménez, A. Fernández-Jiménez, and F. Puertas, "Effect of Activator Mix on the Hydration and Strength Behaviour of Alkali-Activated Slag Cements," *Adv. Cem. Res.*, vol. 15, no. 2003, pp. 129–136, 2003, doi: 10.1680/adcr.15.3.129.36623.
- [127] M. Palacios, M. M. Alonso, C. Varga, and F. Puertas, "Influence of the alkaline solution and temperature on the rheology and reactivity of alkali-activated fly ash pastes," *Cem. Concr. Compos.*, vol. 95, no. July 2018, pp. 277–284, 2019, doi: 10.1016/j.cemconcomp.2018.08.010.
- [128] M. M. Alonso, S. Gismera, M. T. Blanco, M. Lanzón, and F. Puertas, "Alkali-activated mortars: Workability and rheological behaviour," *Constr. Build. Mater.*, vol. 145, pp. 576–587, 2017, doi: 10.1016/j.conbuildmat.2017.04.020.
- [129] N. Li, C. Shi, Q. Wang, Z. Zhang, and Z. Ou, "Composition design and performance of alkali-activated cements," *Mater. Struct. Constr.*, vol. 50, no. 3, pp. 1–11, 2017, doi: 10.1617/s11527-017-1048-0.
- [130] Z. Li, M. Nedeljković, B. Chen, and G. Ye, "Mitigating the autogenous shrinkage of alkali-activated slag by metakaolin," *Cem. Concr. Res.*, vol. 122, no. March, pp. 30–41, 2019, doi: 10.1016/j.cemconres.2019.04.016.
- [131] M. Almahadmeh and A. M. Soliman, "Effects of mixing water temperatures on properties of one-part alkali-activated slag paste," *Constr. Build. Mater.*, vol. 266, p. 121030, 2021, doi: 10.1016/j.conbuildmat.2020.121030.
- [132] S. A. Bernal, J. L. Provis, V. Rose, and R. Mejía De Gutierrez, "Evolution of binder structure in sodium silicate-activated slag-metakaolin blends," *Cem. Concr. Compos.*, vol. 33, no. 1, pp. 46–54, 2011, doi: 10.1016/j.cemconcomp.2010.09.004.
- [133] Z. Jiao, Y. Wang, W. Zheng, and W. Huang, "Effect of Dosage of Alkaline Activator on the Properties of Alkali-Activated Slag Pastes," *Adv. Mater. Sci. Eng.*, vol. 2018, pp. 10–12, 2018, doi: 10.1155/2018/8407380.
- [134] M. Nedeljković, Z. Li, and G. Ye, "Setting, strength, and autogenous shrinkage of alkali-activated fly ash and slag pastes: Effect of slag content," *Materials (Basel)*, vol. 11, no. 11, 2018, doi: 10.3390/ma11112121.
- [135] S. Choi and K. M. Lee, "Influence of Na<sub>2</sub>O content and Ms (SiO<sub>2</sub>/Na<sub>2</sub>O) of alkaline activator on workability and setting of alkali-activated slag paste," *Materials (Basel)*, vol. 12, no. 13, 2019, doi: 10.3390/ma12132072.
- [136] A. S. S. S. Nedunuri and S. Muhammad, "Fundamental understanding of the setting behaviour of the alkali activated binders based on ground granulated blast furnace slag and fly ash," *Constr. Build. Mater.*, vol. 291, p. 123243,

- 2021, doi: 10.1016/j.conbuildmat.2021.123243.
- [137] X. Ouyang, Y. Ma, Z. Liu, J. Liang, and G. Ye, "Effect of the Sodium Silicate Modulus and Slag Content on Fresh and Hardened Properties of Alkali-Activated Fly Ash/Slag," *minerals*, vol. 10, no. 15, 2020.
- [138] G. Ishwarya, B. Singh, S. Deshwal, and S. K. Bhattacharyya, "Effect of sodium carbonate/sodium silicate activator on the rheology, geopolymerization and strength of fly ash/slag geopolymer pastes," *Cem. Concr. Compos.*, vol. 97, no. December 2018, pp. 226–238, 2019, doi: 10.1016/j.cemconcomp.2018.12.007.
- [139] S. A. Bernal, J. L. Provis, R. J. Myers, R. San Nicolas, and J. S. J. van Deventer, "Role of carbonates in the chemical evolution of sodium carbonate-activated slag binders," *Mater. Struct. Constr.*, vol. 48, no. 3, pp. 517–529, 2014, doi: 10.1617/s11527-014-0412-6.
- [140] A. Fernández-Jiménez and F. Puertas, "Setting of alkali-activated slag cement. Influence of activator nature," *Adv. Cem. Res.*, vol. 13, no. 3, pp. 115–121, 2001, doi: 10.1680/adcr.2001.13.3.115.
- [141] B. Yuan, Q. L. Yu, and H. J. H. Brouwers, "Time-dependent characterization of Na<sub>2</sub>CO<sub>3</sub> activated slag," *Cem. Concr. Compos.*, vol. 84, pp. 188–197, 2017, doi: 10.1016/j.cemconcomp.2017.09.005.
- [142] N. Li, C. Shi, and Z. Zhang, "Understanding the roles of activators towards setting and hardening control of alkali-activated slag cement," *Compos. Part B Eng.*, vol. 171, no. January, pp. 34–45, 2019, doi: 10.1016/j.compositesb.2019.04.024.
- [143] V. Živica, "Effectiveness of new silica fume alkali activator," *Cem. Concr. Compos.*, vol. 28, no. 1, pp. 21–25, 2006, doi: 10.1016/j.cemconcomp.2005.07.004.
- [144] Z. V I, Rousekova Bajza, A, "Silica fume-basic blast furnace slag systems activated by an alkali silica fume activator," *Cem. Concr. Res.*, pp. 1825–1828, 1997.
- [145] E. Luga and C. D. Atiş, "Strength properties of slag/fly ash blends activated with sodium metasilicate and sodium hydroxide+silica fume," *Period. Polytech. Civ. Eng.*, vol. 60, no. 2, pp. 223–228, 2016, doi: 10.3311/PPci.8270.
- [146] S. A. Bernal, E. D. Rodríguez, R. M. De Gutiérrez, and J. L. Provis, "Performance at high temperature of alkali-activated slag pastes produced with silica fume and rice husk ash based activators," *Mater. Constr.*, vol. 65, no. 318, 2015, doi: 10.3989/mc.2015.03114.
- [147] R. H. Geraldo, L. F. R. Fernandes, and G. Camarini, "Water treatment sludge and rice husk ash to sustainable geopolymer production," *J. Clean. Prod.*, vol. 149, pp. 146–155, 2017, doi: 10.1016/j.jclepro.2017.02.076.
- [148] H. K. Tchakouté, C. H. Rüscher, S. Kong, E. Kamseu, and C. Leonelli, "Geopolymer binders from metakaolin using sodium waterglass from waste

## References

- glass and rice husk ash as alternative activators: A comparative study,” *Constr. Build. Mater.*, vol. 114, pp. 276–289, 2016, doi: 10.1016/j.conbuildmat.2016.03.184.
- [149] K. T. Tong, R. Vinai, and M. N. Soutsos, “Use of Vietnamese rice husk ash for the production of sodium silicate as the activator for alkali-activated binders,” *J. Clean. Prod.*, vol. 201, pp. 272–286, 2018, doi: 10.1016/j.jclepro.2018.08.025.
- [150] M. F. Alnahhal, A. Hamdan, A. Hajimohammadi, and T. Kim, “Effect of rice husk ash-derived activator on the structural build-up of alkali activated materials,” *Cem. Concr. Res.*, vol. 150, no. May, p. 106590, 2021, doi: 10.1016/j.cemconres.2021.106590.
- [151] D. Wang, C. Shi, N. Farzadnia, Z. Shi, H. Jia, and Z. Ou, “A review on use of limestone powder in cement-based materials: Mechanism, hydration and microstructures,” *Constr. Build. Mater.*, vol. 181, pp. 659–672, 2018, doi: 10.1016/j.conbuildmat.2018.06.075.
- [152] X. Gao, Q. L. Yu, and H. J. H. Brouwers, “Properties of alkali activated slag-fly ash blends with limestone addition,” *Cem. Concr. Compos.*, vol. 59, pp. 119–128, 2015, doi: 10.1016/j.cemconcomp.2015.01.007.
- [153] J. Xiang, L. Liu, X. Cui, Y. He, G. Zheng, and C. Shi, “Effect of limestone on rheological, shrinkage and mechanical properties of alkali – Activated slag/fly ash grouting materials,” *Constr. Build. Mater.*, vol. 191, pp. 1285–1292, 2018, doi: 10.1016/j.conbuildmat.2018.09.209.
- [154] H. Güllü, A. Cevik, K. M. A. Al-Ezzi, and M. E. Gülsan, “On the rheology of using geopolymer for grouting: A comparative study with cement-based grout included fly ash and cold bonded fly ash,” *Constr. Build. Mater.*, vol. 196, pp. 594–610, 2019, doi: 10.1016/j.conbuildmat.2018.11.140.
- [155] L. Li, J. X. Lu, B. Zhang, and C. S. Poon, “Rheology behaviour of one-part alkali activated slag/glass powder (AASG) pastes,” *Constr. Build. Mater.*, vol. 258, p. 120381, 2020, doi: 10.1016/j.conbuildmat.2020.120381.
- [156] Z. Zhang, J. L. Provis, J. Zou, A. Reid, and H. Wang, “Toward an indexing approach to evaluate fly ashes for geopolymer manufacture,” *Cem. Concr. Res.*, vol. 85, pp. 163–173, 2016, doi: 10.1016/j.cemconres.2016.04.007.
- [157] C. K. Park, M. H. Noh, and T. H. Park, “Rheological properties of cementitious materials containing mineral admixtures,” *Cem. Concr. Res.*, vol. 35, no. 5, pp. 842–849, 2005, doi: 10.1016/j.cemconres.2004.11.002.
- [158] B. Panda, S. Ruan, C. Unluer, and M. J. Tan, “Investigation of the properties of alkali-activated slag mixes involving the use of nanoclay and nucleation seeds for 3D printing,” *Compos. Part B Eng.*, vol. 186, no. January, p. 107826, 2020, doi: 10.1016/j.compositesb.2020.107826.
- [159] X. Dai, Q. Ren, S. Aydin, M. Y. Yardımcı, K. Lesage, and G. De Schutter, “Enhancing thixotropy and structural build-up of alkali- activated slag/fly ash pastes with nano clay,” *Mater. Struct.*, no. 54, p. 163, 2021, doi:

- 10.1617/s11527-021-01760-4.
- [160] S. Kawashima, M. Chaouche, D. J. Corr, and S. P. Shah, “Rate of thixotropic rebuilding of cement pastes modified with highly purified attapulgite clays,” *Cem. Concr. Res.*, vol. 53, pp. 112–118, 2013, doi: 10.1016/j.cemconres.2013.05.019.
- [161] M. . Palacios and F. . Puertas, “Stability of Superplasticizers and Shrinkage-Reducing Admixtures in High Basic Media,” *Mater. Construcción*, vol. 54, pp. 65–86, 2004.
- [162] J. J. Chang, “A study on the setting characteristics of sodium silicate-activated slag pastes,” *Cem. Concr. Res.*, vol. 33, no. 7, pp. 1005–1011, 2003, doi: 10.1016/S0008-8846(02)01096-7.
- [163] S. Yousefi, B. Chen, C. Shakya, M. Riaz, S. Farasat, and A. Shah, “Influence of superplasticizers and retarders on the workability and strength of one-part alkali-activated fly ash / slag binders cured at room temperature,” *Constr. Build. Mater.*, vol. 229, p. 116891, 2019, doi: 10.1016/j.conbuildmat.2019.116891.
- [164] A. Antoni, S. W. Wijaya, J. Satria, A. Sugiarto, and D. Hardjito, “The use of borax in deterring flash setting of high calcium fly ash based geopolymer,” *Mater. Sci. Forum*, vol. 857, pp. 416–420, 2016, doi: 10.4028/www.scientific.net/MSF.857.416.
- [165] C. Gong and N. Yang, “Effect of phosphate on the hydration of alkali-activated red mud-slag cementitious material,” *Cem. Concr. Res.*, vol. 30, no. 7, pp. 1013–1016, 2000, doi: 10.1016/S0008-8846(00)00260-X.
- [166] X. Cong, W. Zhou, X. Geng, and M. Elchalakani, “Low field NMR relaxation as a probe to study the effect of activators and retarders on the alkali-activated GGBFS setting process,” *Cem. Concr. Compos.*, vol. 104, no. April, p. 103399, 2019, doi: 10.1016/j.cemconcomp.2019.103399.
- [167] S. Tong, Z. Yuqi, and W. Qiang, “Recent advances in chemical admixtures for improving the workability of alkali-activated slag-based material systems,” *Constr. Build. Mater.*, vol. 272, p. 121647, 2021, doi: 10.1016/j.conbuildmat.2020.121647.
- [168] N. Garg and C. E. White, “Mechanism of zinc oxide retardation in alkali-activated materials: An: in situ X-ray pair distribution function investigation,” *J. Mater. Chem. A*, vol. 5, no. 23, pp. 11794–11804, 2017, doi: 10.1039/c7ta00412e.
- [169] X. Cong, W. Zhou, X. Geng, and M. Elchalakani, “Low field NMR relaxation as a probe to study the effect of activators and retarders on the alkali-activated GGBFS setting process,” *Cem. Concr. Compos.*, vol. 104, no. August, p. 103399, 2019, doi: 10.1016/j.cemconcomp.2019.103399.
- [170] J. J. Chang, W. Yeih, and C. C. Hung, “Effects of gypsum and phosphoric acid on the properties of sodium silicate-based alkali-activated slag pastes,” *Cem. Concr. Compos.*, vol. 27, pp. 85–91, 2005, doi:

## References

- 10.1016/j.cemconcomp.2003.12.001.
- [171] C. Sun, J. Sun, and D. Wang, "Effect of tartaric acid on the early hydration of NaOH - activated slag paste," *J. Therm. Anal. Calorim.*, vol. 144, no. 1, pp. 41–50, 2021, doi: 10.1007/s10973-020-09466-5.
- [172] L. Xu, F. Matakah, P. Soroushian, N. Darsanasiri, S. Hamadne, and W. Wu, "Effects of citric acid on the rheology, hydration and strength development of alkali aluminosilicate cement," *Adv. Cem. Res.*, vol. 30, no. 2, pp. 75–82, 2018, doi: 10.1680/jadcr.16.00151.
- [173] L. Kalina, V. B. Jr, R. Novotný, and M. Monč, "Effect of Na<sub>3</sub>PO<sub>4</sub> on the Hydration Process of Alkali-Activated Blast Furnace Slag," *Materials (Basel)*, 2016, doi: 10.3390/ma9050395.
- [174] T. Revathi and R. Jeyalakshmi, "XPS, 29Si, 27Al, 11B MAS -NMR, ATR-IR and FESEM characterization of geopolymer based on borax modified water glass activated Fly ash-GGBS blend," *Mater. Res. Express*, vol. 6, no. 8, 2019, doi: 10.1088/2053-1591/ab255e.
- [175] H. Liu, J. G. Sanjayan, and Y. Bu, "The application of sodium hydroxide and anhydrous borax as composite activator of class F fly ash for extending setting time," *Fuel*, vol. 206, pp. 534–540, 2017, doi: 10.1016/j.fuel.2017.06.049.
- [176] A. Kusbiantoro, M. S. Ibrahim, K. Muthusamy, and A. Alias, "Development of Sucrose and Citric Acid as the Natural based Admixture for Fly Ash based Geopolymer," *Procedia Environ. Sci.*, vol. 17, pp. 596–602, 2013, doi: 10.1016/j.proenv.2013.02.075.
- [177] K. Sasaki, K. Kurumisawa, and K. Ibayashi, "Effect of retarders on flow and strength development of alkali-activated fly ash / blast furnace slag composite," *Constr. Build. Mater.*, vol. 216, pp. 337–346, 2019, doi: 10.1016/j.conbuildmat.2019.05.022.
- [178] D. D. Sun and J. H. Tay, "Characterization of mercury- and zinc-doped alkali-activated slag matrix: Part I. Mercury," *Cem. Concr. Res.*, vol. 33, no. 8, pp. 1251–1256, 2003, doi: 10.1016/S0008-8846(03)00045-0.
- [179] N. K. Lee, E. M. Kim, and H. K. Lee, "Mechanical properties and setting characteristics of geopolymer mortar using styrene-butadiene (SB) latex," *Constr. Build. Mater.*, vol. 113, pp. 264–272, 2016, doi: 10.1016/j.conbuildmat.2016.03.055.
- [180] F. Puertas *et al.*, "Alkali-activated slag concrete: Fresh and hardened behaviour," *Cem. Concr. Compos.*, vol. 85, pp. 22–31, 2018, doi: 10.1016/j.cemconcomp.2017.10.003.
- [181] Y. Alrefaei, Y. S. Wang, and J. G. Dai, "Effect of mixing method on the performance of alkali-activated fly ash/slag pastes along with polycarboxylate admixture," *Cem. Concr. Compos.*, vol. 117, no. July 2020, p. 103917, 2021, doi: 10.1016/j.cemconcomp.2020.103917.
- [182] M. Palacios, M. M. Alonso, C. Varga, and F. Puertas, "Influence of the alkaline

- solution and temperature on the rheology and reactivity of alkali-activated fly ash pastes,” *Cem. Concr. Compos.*, vol. 95, no. August 2018, pp. 277–284, 2019, doi: 10.1016/j.cemconcomp.2018.08.010.
- [183] ASTM C 1437-15, “Standard Test Method for Flow of Hydraulic Cement Mortar,” *Annu. B. ASTM Stand.*, pp. 6–7, 2009.
- [184] M. Nehdi and M. A. Rahman, “Estimating rheological properties of cement pastes using various rheological models for different test geometry, gap and surface friction,” *Cem. Concr. Res.*, vol. 34, no. 11, pp. 1993–2007, 2004, doi: 10.1016/j.cemconres.2004.02.020.
- [185] A. Yahia and K. H. Khayat, “Applicability of rheological models to high-performance grouts containing supplementary cementitious materials and viscosity enhancing admixture,” *Mater. Struct. Constr.*, vol. 36, no. 260, pp. 402–412, 2003, doi: 10.1007/bf02481066.
- [186] M. A. Schultz and L. J. Struble, “Use of oscillatory shear to study flow behaviour of fresh cement paste,” *Cem. Concr. Res.*, vol. 23, no. 2, pp. 273–282, 1993, doi: 10.1016/0008-8846(93)90092-N.
- [187] Y. Qian, S. Ma, S. Kawashima, and G. De Schutter, “Rheological characterization of the viscoelastic solid-like properties of fresh cement pastes with nanoclay addition,” *Theor. Appl. Fract. Mech.*, vol. 103, no. April, p. 102262, 2019, doi: 10.1016/j.tafmec.2019.102262.
- [188] A. M. Mostafa and A. Yahia, “New approach to assess build-up of cement-based suspensions,” *Cem. Concr. Res.*, vol. 85, pp. 174–182, 2016, doi: 10.1016/j.cemconres.2016.03.005.
- [189] European Committee for Standardization, “Methods of testing cement —Part 1: Determination of strength,” no. February, 2005.
- [190] N. Alderete, Y. Villagrán, A. Mignon, D. Snoeck, and N. De Belie, “Pore structure description of mortars containing ground granulated blast-furnace slag by mercury intrusion porosimetry and dynamic vapour sorption,” *Constr. Build. Mater.*, vol. 145, pp. 157–165, 2017, doi: 10.1016/j.conbuildmat.2017.03.245.
- [191] J. R. Tenório Filho, E. Mannekens, K. Van Tittelboom, D. Snoeck, and N. De Belie, “Assessment of the potential of superabsorbent polymers as internal curing agents in concrete by means of optical fiber sensors,” *Constr. Build. Mater.*, vol. 238, pp. 1–8, 2020, doi: 10.1016/j.conbuildmat.2019.117751.
- [192] C. A. Mandarim-de-lacerda, “Stereological tools in biomedical research,” *An. Acad. Bras. Cienc.*, vol. 75, pp. 469–486, 2003.
- [193] D. Lee and M. Chen, “An Image-Based Method for Obtaining Pore-Size Distribution of Porous Media,” *Environ. Sci. Technol.*, vol. 43, no. 9, pp. 3248–3253, 2009.
- [194] R. J. Myers, S. A. Bernal, R. San Nicolas, and J. L. Provis, “Generalized structural description of calcium-sodium aluminosilicate hydrate gels: The

## References

- cross-linked substituted tobermorite model,” *Langmuir*, vol. 29, no. 17, pp. 5294–5306, 2013, doi: 10.1021/la4000473.
- [195] B. Walkley, X. Ke, J. L. Provis, and S. A. Bernal, “Activator Anion Influences the Nanostructure of Alkali-Activated Slag Cements,” *J. Phys. Chem. C*, 2021, doi: 10.1021/acs.jpcc.1c07328.
- [196] V. D. Glukhovskiy, *Soil silicates*. Gastroi Publishers, 1959.
- [197] F. Puertas and A. Fernández-Jiménez, “Mineralogical and microstructural characterisation of alkali-activated fly ash/slag pastes,” *Cem. Concr. Compos.*, vol. 25, no. 3, pp. 287–292, 2003, doi: 10.1016/S0958-9465(02)00059-8.
- [198] S. Aydin and B. Baradan, “Mechanical and microstructural properties of heat cured alkali-activated slag mortars,” *Mater. Des.*, vol. 35, pp. 374–383, 2012, doi: 10.1016/j.matdes.2011.10.005.
- [199] M. A. Longhi, Z. Zhang, E. D. Rodríguez, and A. P. Kirchheim, “Efflorescence of Alkali-Activated Cements ( Geopolymers ) and the Impacts on Material Structures : A Critical Analysis,” *Front. Mater.*, vol. 6, no. April, pp. 1–13, 2019, doi: 10.3389/fmats.2019.00089.
- [200] B. Lothenbach *et al.*, “Cement and Concrete Research Cemdata18: A chemical thermodynamic database for hydrated Portland cements and alkali-activated materials,” *Cem. Concr. Res.*, vol. 115, no. April 2018, pp. 472–506, 2019, doi: 10.1016/j.cemconres.2018.04.018.
- [201] B. Lothenbach, “Thermodynamic equilibrium calculations in cementitious systems,” *Mater. Struct.*, pp. 1413–1433, 2010, doi: 10.1617/s11527-010-9592-x.
- [202] G. Trtnik, G. Turk, F. Kavčič, and V. B. Bosiljkov, “Possibilities of using the ultrasonic wave transmission method to estimate initial setting time of cement paste,” *Cem. Concr. Res.*, vol. 38, no. 11, pp. 1336–1342, 2008, doi: 10.1016/j.cemconres.2008.08.003.
- [203] Y. Zhang, W. Zhang, W. She, L. Ma, and W. Zhu, “Ultrasound monitoring of setting and hardening process of ultra-high performance cementitious materials,” *NDT E Int.*, vol. 47, pp. 177–184, 2012, doi: 10.1016/j.ndteint.2009.10.006.
- [204] H. W. Reinhardt and C. U. Grosse, “Continuous monitoring of setting and hardening of mortar and concrete,” *Constr. Build. Mater.*, vol. 18, no. 3, pp. 145–154, 2004, doi: 10.1016/j.conbuildmat.2003.10.002.
- [205] T. Chotard, N. Gimet-Breart, A. Smith, D. Fargeot, J. P. Bonnet, and C. Gault, “Application of ultrasonic testing to describe the hydration of calcium aluminate cement at the early age,” *Cem. Concr. Res.*, vol. 31, no. 3, pp. 405–412, 2001, doi: 10.1016/S0008-8846(00)00446-4.
- [206] J. Zhu, S. H. Kee, D. Han, and Y. Te Tsai, “Effects of air voids on ultrasonic wave propagation in early age cement pastes,” *Cem. Concr. Res.*, vol. 41, no. 8, pp. 872–881, 2011, doi: 10.1016/j.cemconres.2011.04.005.

- [207] X. Gao, Q. L. Yu, and H. J. H. Brouwers, "Reaction kinetics, gel character and strength of ambient temperature cured alkali activated slag-fly ash blends," *Constr. Build. Mater.*, vol. 80, pp. 105–115, 2015, doi: 10.1016/j.conbuildmat.2015.01.065.
- [208] J. Hu, Z. Ge, and K. Wang, "Influence of cement fineness and water-to-cement ratio on mortar early-age heat of hydration and set times," *Constr. Build. Mater.*, vol. 50, no. January 2019, pp. 657–663, 2014, doi: 10.1016/j.conbuildmat.2013.10.011.
- [209] C. Shi and R. L. Day, "Early strength development and hydration of alkali-activated blast furnace slag/fly ash blends," *Adv. Cem. Res.*, vol. 11, no. 4, pp. 189–196, 1999, doi: 10.1680/adcr.1999.11.4.189.
- [210] F. Puertas, M. Palacios, H. Manzano, J. S. Dolado, A. Rico, and J. Rodríguez, "A model for the C-A-S-H gel formed in alkali-activated slag cements," *J. Eur. Ceram. Soc.*, vol. 31, no. 12, pp. 2043–2056, 2011, doi: 10.1016/j.jeurceramsoc.2011.04.036.
- [211] F. Xie, Z. Liu, D. Zhang, J. Wang, and D. Wang, "Understanding the acting mechanism of NaOH adjusting the transformation of viscoelastic properties of alkali activated phosphorus slag," *Constr. Build. Mater.*, vol. 257, p. 119488, 2020, doi: 10.1016/j.conbuildmat.2020.119488.
- [212] G. Trtnik and G. Turk, "Influence of superplasticizers on the evolution of ultrasonic P-wave velocity through cement pastes at early age," *Cem. Concr. Res.*, vol. 51, pp. 22–31, 2013, doi: 10.1016/j.cemconres.2013.04.007.
- [213] Y. Jin and D. Stephan, "The unusual solidification process of alkali activated slag and its relationship with the glass structure of the slag," *Cem. Concr. Res.*, vol. 121, no. October 2018, pp. 1–10, 2019, doi: 10.1016/j.cemconres.2019.04.004.
- [214] D. Feys, R. Verhoeven, and G. De Schutter, "Why is fresh self-compacting concrete shear thickening?," *Cem. Concr. Res.*, vol. 39, no. 6, pp. 510–523, 2009, doi: 10.1016/j.cemconres.2009.03.004.
- [215] P. F. G. Banfill and D. C. Saunders, "On the viscometric examination of cement pastes," *Cem. Concr. Res.*, vol. 11, no. 3, pp. 363–370, 1981, doi: 10.1016/0008-8846(81)90108-3.
- [216] D. Feys, R. Cepuritis, S. Jacobsen, K. Lesage, E. Secrieru, and A. Yahia, "Measuring Rheological Properties of Cement Pastes: Most common Techniques, Procedures and Challenges," *RILEM Tech. Lett.*, vol. 2, pp. 129–135, 2017, doi: 10.21809/rilemtechlett.2017.43.
- [217] H. C. Helgeson, D. H. Kirkham, and G. C. Flowers, "Thermodynamic behaviour of aqueous electrolytes at high pressure and temperature," *American Journal of Science*, vol. 281, pp. 1249–1516, 1981.
- [218] H. Mehdizadeh, E. Najafi Kani, A. Palomo Sanchez, and A. Fernandez-Jimenez, "Rheology of activated phosphorus slag with lime and alkaline salts," *Cem. Concr. Res.*, vol. 113, no. July, pp. 121–129, 2018, doi:

## References

- 10.1016/j.cemconres.2018.07.010.
- [219] J. Ren, Y. Bai, M. J. Earle, and C. Yang, "A preliminary study on the effect of separate addition of lignosulfonate superplasticiser and waterglass on the rheological behaviour of alkali -activated slags," *Sustain. Constr. Mater. Technol.*, vol. 2013-Augus, 2013.
- [220] GRAY DH and LIN YK, "Engineering Properties of Compacted Fly Ash," no. October, 1971.
- [221] P. Nath and P. K. Sarker, "Effect of GGBFS on setting, workability and early strength properties of fly ash geopolymer concrete cured in ambient condition," *Constr. Build. Mater.*, vol. 66, pp. 163–171, 2014, doi: 10.1016/j.conbuildmat.2014.05.080.
- [222] S. Samantasinghar and S. P. Singh, "Fresh and Hardened Properties of Fly Ash-Slag Blended Geopolymer Paste and Mortar," *Int. J. Concr. Struct. Mater.*, vol. 13, no. 1, pp. 1–12, 2019, doi: 10.1186/s40069-019-0360-1.
- [223] P. Chindapasirt, P. De Silva, K. Sagoe-Crentsil, and S. Hanjitsuwan, "Effect of SiO<sub>2</sub> and Al<sub>2</sub>O<sub>3</sub> on the setting and hardening of high calcium fly ash-based geopolymer systems," *J. Mater. Sci.*, vol. 47, no. 12, pp. 4876–4883, 2012, doi: 10.1007/s10853-012-6353-y.
- [224] A. M. Humad, A. Kothari, J. L. Provis, and A. Cwirzen, "The effect of blast furnace slag/fly ash ratio on setting, strength, and shrinkage of alkali-activated pastes and concretes," *Front. Mater.*, vol. 6, no. February, pp. 1–10, 2019, doi: 10.3389/fmats.2019.00009.
- [225] R. J. Flatt, "Towards a prediction of superplasticized concrete rheology," *Mater. Struct. Constr.*, vol. 37, no. 269, pp. 289–300, 2004, doi: 10.1617/14088.
- [226] Q. Yuan, X. Lu, K. H. Khayat, D. Feys, and C. Shi, "Small amplitude oscillatory shear technique to evaluate structural build-up of cement paste," *Mater. Struct. Constr.*, vol. 50, no. 2, pp. 1–12, 2017, doi: 10.1617/s11527-016-0978-2.
- [227] S. Onisei, K. Lesage, B. Blanpain, and Y. Pontikes, "Early Age Microstructural Transformations of an Inorganic Polymer Made of Fayalite Slag," *J. Am. Ceram. Soc.*, vol. 98, no. 7, pp. 2269–2277, 2015, doi: 10.1111/jace.13548.
- [228] A. R. Brough and A. Atkinson, "Sodium silicate-based, alkali-activated slag mortars - Part I. Strength, hydration and microstructure," *Cem. Concr. Res.*, vol. 32, no. 6, pp. 865–879, 2002, doi: 10.1016/S0008-8846(02)00717-2.
- [229] M. Ben Haha, B. Lothenbach, G. Le Saout, and F. Winnefeld, "Influence of slag chemistry on the hydration of alkali-activated blast-furnace slag - Part II: Effect of Al<sub>2</sub>O<sub>3</sub>," *Cem. Concr. Res.*, vol. 42, no. 1, pp. 74–83, 2012, doi: 10.1016/j.cemconres.2011.08.005.
- [230] M. Ben Haha, G. Le Saout, F. Winnefeld, and B. Lothenbach, "Influence of

- activator type on hydration kinetics, hydrate assemblage and microstructural development of alkali activated blast-furnace slags,” *Cem. Concr. Res.*, vol. 41, no. 3, pp. 301–310, 2011, doi: 10.1016/j.cemconres.2010.11.016.
- [231] B. S. Gebregziabihier, R. J. Thomas, and S. Peethamparan, “Temperature and activator effect on early-age reaction kinetics of alkali-activated slag binders,” *Constr. Build. Mater.*, vol. 113, pp. 783–793, 2016, doi: 10.1016/j.conbuildmat.2016.03.098.
- [232] A. A. Kline, T. N. Rogers, M. E. Mullins, B. C. Cornilsen, and L. M. Sokolov, “Sol-gel kinetics for the synthesis of multi-component glass materials - Code: CP13,” *J. Sol-Gel Sci. Technol.*, vol. 2, no. 1–3, pp. 269–272, 1994, doi: 10.1007/BF00486254.
- [233] D. Khale and R. Chaudhary, “Mechanism of geopolymerization and factors influencing its development: A review,” *J. Mater. Sci.*, vol. 42, no. 3, pp. 729–746, 2007, doi: 10.1007/s10853-006-0401-4.
- [234] J. Davidovits, “Properties of Geopolymer Cements,” *First Int. Conf. Alkaline Cem. Concr.*, pp. 131–149, 1994.
- [235] Y. S. Wang, Y. Alrefaei, and J. G. Dai, “Silico-aluminophosphate and alkali-aluminosilicate geopolymers: A comparative review,” *Front. Mater.*, vol. 6, no. May, pp. 1–17, 2019, doi: 10.3389/fmats.2019.00106.
- [236] P. Coussot, “RHEOMETRY OF PASTES, SUSPENSIONS, AND GRANULAR MATERIALS,” *John Wiley Sons*, 2005.
- [237] D. Feys, R. Verhoeven, and G. De Schutter, “Evaluation of time independent rheological models applicable to fresh self-compacting concrete,” *Appl. Rheol.*, vol. 17, no. 5, pp. 1–10, 2007, doi: 10.1515/arh-2007-0018.
- [238] M. Criado, A. Palomo, A. Fernández-Jiménez, and P. F. G. Banfill, “Alkali activated fly ash: Effect of admixtures on paste rheology,” *Rheol. Acta*, vol. 48, no. 4, pp. 447–455, 2009, doi: 10.1007/s00397-008-0345-5.
- [239] C. A. Rees, J. L. Provis, G. C. Lukey, and J. S. J. van Deventer, “The mechanism of geopolymer gel formation investigated through seeded nucleation,” *Colloids Surfaces A Physicochem. Eng. Asp.*, vol. 318, no. 1–3, pp. 97–105, 2008, doi: 10.1016/j.colsurfa.2007.12.019.
- [240] E. H. Oelkers, “General kinetic description of multioxide silicate mineral and glass dissolution,” *Geochim. Cosmochim. Acta*, vol. 65, no. 21, pp. 3703–3719, 2001, doi: 10.1016/S0016-7037(01)00710-4.
- [241] R. K. Iler, “Effect of adsorbed alumina on the solubility of amorphous silica in water,” *J. Colloid Interface Sci.*, vol. 43, no. 2, pp. 399–408, 1973, doi: 10.1016/0021-9797(73)90386-X.
- [242] S. Chithiraputhiran and N. Neithalath, “Isothermal reaction kinetics and temperature dependence of alkali activation of slag, fly ash and their blends,” *Constr. Build. Mater.*, vol. 45, pp. 233–242, 2013, doi: 10.1016/j.conbuildmat.2013.03.061.

## References

- [243] A. Hajimohammadi, J. L. Provis, and J. S. J. Van Deventer, “The effect of silica availability on the mechanism of geopolymerisation,” *Cem. Concr. Res.*, vol. 41, no. 3, pp. 210–216, 2011, doi: 10.1016/j.cemconres.2011.02.001.
- [244] S. Y. Hong and F. P. Glasser, “Alkali sorption by C-S-H and C-A-S-H gels: Part II. Role of alumina,” *Cem. Concr. Res.*, vol. 32, no. 7, pp. 1101–1111, 2002, doi: 10.1016/S0008-8846(02)00753-6.
- [245] E. L’Hôpital, B. Lothenbach, K. Scrivener, and D. A. Kulik, “Alkali uptake in calcium alumina silicate hydrate (C-A-S-H),” *Cem. Concr. Res.*, vol. 85, pp. 122–136, 2016, doi: 10.1016/j.cemconres.2016.03.009.
- [246] B. Walkley, R. San Nicolas, and S. Bernal, “Effect of MgO incorporation on the structure of synthetic alkali-activated calcium aluminosilicate binders,” *Conf. 27th Bienn. Natl. Conf. Concr. Inst. Aust.*, no. August 2015, 2015, [Online]. Available: [https://www.researchgate.net/publication/303968983\\_Effect\\_of\\_MgO\\_incorporation\\_on\\_the\\_structure\\_of\\_synthetic\\_alkali-activated\\_calcium\\_aluminosilicate\\_binders](https://www.researchgate.net/publication/303968983_Effect_of_MgO_incorporation_on_the_structure_of_synthetic_alkali-activated_calcium_aluminosilicate_binders).
- [247] N. K. Lee and H. K. Lee, “Reactivity and reaction products of alkali-activated, fly ash/slag paste,” *Constr. Build. Mater.*, vol. 81, pp. 303–312, 2015, doi: 10.1016/j.conbuildmat.2015.02.022.
- [248] I. Ismail, S. A. Bernal, J. L. Provis, R. San Nicolas, S. Hamdan, and J. S. J. Van Deventer, “Modification of phase evolution in alkali-activated blast furnace slag by the incorporation of fly ash,” *Cem. Concr. Compos.*, vol. 45, pp. 125–135, 2014, doi: 10.1016/j.cemconcomp.2013.09.006.
- [249] S. Aydin, “A ternary optimisation of mineral additives of alkali activated cement mortars,” *Constr. Build. Mater.*, vol. 43, pp. 131–138, 2013, doi: 10.1016/j.conbuildmat.2013.02.005.
- [250] A. Fernández-Jiménez, J. G. Palomo, and F. Puertas, “Alkali-activated slag mortars: Mechanical strength behaviour,” *Cem. Concr. Res.*, vol. 29, no. 8, pp. 1313–1321, 1999, doi: 10.1016/S0008-8846(99)00154-4.
- [251] S. Aydın and C. Ç. Kızıltepe, “Valorization of Boron Mine Tailings in Alkali-Activated Mortars,” *J. Mater. Civ. Eng.*, vol. 31, no. 10, pp. 1–12, 2019, doi: 10.1061/(ASCE)MT.1943-5533.0002871.
- [252] A. M. Rashad, Y. Bai, P. A. M. Basheer, N. B. Milestone, and N. C. Collier, “Hydration and properties of sodium sulfate activated slag,” *Cem. Concr. Compos.*, vol. 37, pp. 20–29, 2013, doi: 10.1016/j.cemconcomp.2012.12.010.
- [253] A. Passuello *et al.*, “Evaluation of the potential improvement in the environmental footprint of geopolymers using waste-derived activators,” *J. Clean. Prod.*, vol. 166, pp. 680–689, 2017, doi: 10.1016/j.jclepro.2017.08.007.
- [254] G. Habert and C. Ouellet-Plamondon, “Recent update on the environmental impact of geopolymers,” *RILEM Tech. Lett.*, vol. 1, p. 17, 2016, doi: 10.21809/rilemtechlett.v1.6.

- [255] F. Pacheco-Torgal, *Eco-Efficient Construction and Building Materials: Life Cycle Assessment (LCA), Eco-Labeling and Case Studies*, no. 1985. Woodhead Publishing Limited, 2014.
- [256] A. Wetzlar and B. Middendorf, "Influence of silica fume on properties of fresh and hardened ultra-high performance concrete based on alkali-activated slag," *Cem. Concr. Compos.*, vol. 100, no. March, pp. 53–59, 2019, doi: 10.1016/j.cemconcomp.2019.03.023.
- [257] S. A. Bernal, E. D. Rodríguez, R. Mejía De Gutiérrez, J. L. Provis, and S. Delvasto, "Activation of metakaolin/slag blends using alkaline solutions based on chemically modified silica fume and rice husk ash," *Waste and Biomass Valorization*, vol. 3, no. 1, pp. 99–108, 2012, doi: 10.1007/s12649-011-9093-3.
- [258] J. E. Wallevik and O. H. Wallevik, "Analysis of shear rate inside a concrete truck mixer," *Cem. Concr. Res.*, vol. 95, pp. 9–17, 2017, doi: 10.1016/j.cemconres.2017.02.007.
- [259] H. Jansson, D. Bernin, and K. Ramser, "Silicate species of water glass and insights for alkali-activated green cement," *AIP Adv.*, vol. 5, no. 6, pp. 1–9, 2015, doi: 10.1063/1.4923371.
- [260] X. Yang, P. Roonasi, and A. Holmgren, "A study of sodium silicate in aqueous solution and sorbed by synthetic magnetite using in situ ATR-FTIR spectroscopy," *J. Colloid Interface Sci.*, vol. 328, no. 1, pp. 41–47, 2008, doi: 10.1016/j.jcis.2008.08.061.
- [261] G. Beersaerts, A. Vananroye, D. Sakellariou, and C. Clasen, "Rheology of an alkali-activated Fe-rich slag suspension: Identifying the impact of the activator chemistry and slag particle interactions," *J. Non. Cryst. Solids*, vol. 561, no. March, p. 120747, 2021, doi: 10.1016/j.jnoncrysol.2021.120747.
- [262] L. Vidal *et al.*, "Controlling the reactivity of silicate solutions: A FTIR, Raman and NMR study," *Colloids Surfaces A Physicochem. Eng. Asp.*, vol. 503, pp. 101–109, 2016, doi: 10.1016/j.colsurfa.2016.05.039.
- [263] J. L. Bass and G. L. Turner, "Anion distributions in sodium silicate solutions. Characterization by 29SI NMR and infrared spectroscopies, and vapor phase osmometry," *J. Phys. Chem. B*, vol. 101, no. 50, pp. 10638–10644, 1997, doi: 10.1021/jp9715282.
- [264] S. Lucas, M. T. Tognonvi, J. L. Gelet, J. Soro, and S. Rossignol, "Interactions between silica sand and sodium silicate solution during consolidation process," *J. Non. Cryst. Solids*, vol. 357, no. 4, pp. 1310–1318, 2011, doi: 10.1016/j.jnoncrysol.2010.12.016.
- [265] P. Rovnaník, P. Rovnaníková, M. Vyšvařil, S. Grzeszczyk, and E. Janowska-Renkas, "Rheological properties and microstructure of binary waste red brick powder/metakaolin geopolymer," *Constr. Build. Mater.*, vol. 188, pp. 924–933, 2018, doi: 10.1016/j.conbuildmat.2018.08.150.
- [266] H. Vikan and H. Justnes, "Rheology of cementitious paste with silica fume or

## References

- limestone,” *Cem. Concr. Res.*, vol. 37, no. 11, pp. 1512–1517, 2007, doi: 10.1016/j.cemconres.2007.08.012.
- [267] D. Krizan and B. Zivanovic, “Effects of dosage and modulus of water glass on early hydration of alkali-slag cements,” *Cem. Concr. Res.*, vol. 32, no. 8, pp. 1181–1188, 2002, doi: 10.1016/S0008-8846(01)00717-7.
- [268] J. L. Provis, A. Kilcullen, P. Duxson, D. G. Brice, and J. S. J. Van Deventer, “Stabilization of Low-Modulus Sodium Silicate Solutions by Alkali Substitution,” *Ind. Eng. Chem. Res.*, vol. 51, pp. 2483–2486, 2012, doi: 10.1021/ie202143j.
- [269] D. Jansen, F. Goetz-Neunhoeffler, B. Lothenbach, and J. Neubauer, “The early hydration of Ordinary Portland Cement (OPC): An approach comparing measured heat flow with calculated heat flow from QXRD,” *Cem. Concr. Res.*, vol. 42, no. 1, pp. 134–138, 2012, doi: 10.1016/j.cemconres.2011.09.001.
- [270] K. L. Scrivener and A. Nonat, “Hydration of cementitious materials, present and future,” *Cem. Concr. Res.*, vol. 41, no. 7, pp. 651–665, 2011, doi: 10.1016/j.cemconres.2011.03.026.
- [271] C. Shi and R. L. Day, “A calorimetric study of early hydration of alkali-slag cements,” *Cem. Concr. Res.*, vol. 25, no. 6, pp. 1333–1346, 1995.
- [272] S. A. Bernal, “Effect of the activator dose on the compressive strength and accelerated carbonation resistance of alkali silicate-activated slag/metakaolin blended materials,” *Constr. Build. Mater.*, vol. 98, pp. 217–226, 2015, doi: 10.1016/j.conbuildmat.2015.08.013.
- [273] T. Bakharev, J. G. Sanjayan, and Y. B. Cheng, “Effect of admixtures on properties of alkali-activated slag concrete,” *Cem. Concr. Res.*, vol. 30, no. 9, pp. 1367–1374, 2000, doi: 10.1016/S0008-8846(00)00349-5.
- [274] I. G. Richardson, A. R. Brough, G. W. Groves, and C. M. Dobson, “The characterization of hardened alkali-activated blast-furnace slag pastes and the nature of the calcium silicate hydrate (C-S-H) phase,” *Cem. Concr. Res.*, vol. 24, no. 5, pp. 813–829, 1994, doi: 10.1016/0008-8846(94)90002-7.
- [275] R. J. Myers, S. A. Bernal, J. D. Gehman, J. S. J. Van Deventer, and J. L. Provis, “The role of al in cross-linking of alkali-Activated slag cements,” *J. Am. Ceram. Soc.*, vol. 98, no. 3, pp. 996–1004, 2015, doi: 10.1111/jace.13360.
- [276] S. D. Wang and K. L. Scrivener, “Hydration products of alkali activated slag cement,” *Cem. Concr. Res.*, vol. 25, no. 3, pp. 561–571, 1995, doi: 10.1016/0008-8846(95)00045-E.
- [277] IUPAC, “Manual of symbols and terminology, appendix 2, part 1, Colloid and Surface Chemistry,” *J Pure Appl Chem*, vol. 31, p. 578, 1972.
- [278] F. Collins and J. G. Sanjayan, “Effect of pore size distribution on drying shrinkage of alkali-activated slag concrete,” *Cem. Concr. Res.*, vol. 30, pp. 1401–1406, 2000.
- [279] B. C. McLellan, R. P. Williams, J. Lay, A. Van Riessen, and G. D. Corder,

- “Costs and carbon emissions for geopolymer pastes in comparison to ordinary portland cement,” *J. Clean. Prod.*, vol. 19, no. 9–10, pp. 1080–1090, 2011, doi: 10.1016/j.jclepro.2011.02.010.
- [280] R. Maddalena, J. J. Roberts, and A. Hamilton, “Can Portland cement be replaced by low-carbon alternative materials? A study on the thermal properties and carbon emissions of innovative cements,” *J. Clean. Prod.*, vol. 186, pp. 933–942, 2018, doi: 10.1016/j.jclepro.2018.02.138.
- [281] M. K. Rahman, M. H. Baluch, and M. A. Malik, “Thixotropic behaviour of self compacting concrete with different mineral admixtures,” *Constr. Build. Mater.*, vol. 50, pp. 710–717, 2014, doi: 10.1016/j.conbuildmat.2013.10.025.
- [282] D. E. Angulo-Ramírez, R. Mejía de Gutiérrez, and F. Puertas, “Alkali-activated Portland blast-furnace slag cement: Mechanical properties and hydration,” *Constr. Build. Mater.*, vol. 140, pp. 119–128, 2017, doi: 10.1016/j.conbuildmat.2017.02.092.
- [283] F. A. Hartmann and J. Plank, “Impact of aging on the hydration of tricalcium aluminate (C3A)/gypsum blends and the effectiveness of retarding admixtures,” *Zeitschrift für Naturforsch. - Sect. B J. Chem. Sci.*, vol. 75, no. 8, pp. 739–753, 2020, doi: 10.1515/znb-2020-0087.
- [284] M. R. Meier, M. Sarigaphuti, P. Sainamthip, and J. Plank, “Early hydration of Portland cement studied under microgravity conditions,” *Constr. Build. Mater.*, vol. 93, pp. 877–883, 2015, doi: 10.1016/j.conbuildmat.2015.05.074.
- [285] N. K. Lee, G. H. An, K. T. Koh, and G. S. Ryu, “Improved Reactivity of Fly Ash-Slag Geopolymer by the Addition of Silica Fume,” *Adv. Mater. Sci. Eng.*, vol. 2016, 2016.
- [286] L. Rodrigues *et al.*, “Influence of quartz powder and silica fume on the performance of Portland cement,” *Sci. Rep.*, no. 0123456789, pp. 1–15, 2020, doi: 10.1038/s41598-020-78567-w.
- [287] S. Roy, S. Chanda, S.K. Bandopadhyay, and S. N. Ghosh, “INVESTIGATION OF PORTLAND SLAG CEMENT ACTIVATED BY WATERGLASS,” *Cem. Concr. Res.*, vol. 28, no. 1050, pp. 3–8, 1998.
- [288] E. Acevedo-Martinez, L. Y. Gomez-Zamorano, and J. I. Escalante-Garcia, “Portland cement-blast furnace slag mortars activated using waterglass : – Part 1 : Effect of slag replacement and alkali concentration,” *Constr. Build. Mater.*, vol. 37, pp. 462–469, 2012, doi: 10.1016/j.conbuildmat.2012.07.041.
- [289] M. J. Sánchez-Herrero, A. Fernández-Jiménez, Á. Palomo, and L. Klein, “Alkaline Hydration of C2S and C3S,” *J. Am. Ceram. Soc.*, vol. 99, no. 2, pp. 604–611, 2016, doi: 10.1111/jace.13985.
- [290] A. H. Mahmood, M. Babae, S. J. Foster, and A. Castel, “Continuous Monitoring of the Early-Age Properties of Activated GGBFS with Alkaline Solutions of Different Concentrations,” *J. Mater. Civ. Eng.*, vol. 33, no. 12, pp. 1–10, 2021, doi: 10.1061/(asce)mt.1943-5533.0003997.

## References

- [291] Q. Fu, M. Bu, Z. Zhang, W. Xu, Q. Yuan, and D. Niu, “Hydration Characteristics and Microstructure of Alkali-Activated Slag Concrete: A Review,” *Engineering*, 2021, doi: 10.1016/j.eng.2021.07.026.
- [292] W. Al Makhadmeh and A. Soliman, “Effect of activator nature on property development of alkali-activated slag binders,” *J. Sustain. Cem. Mater.*, vol. 10, no. 4, pp. 240–256, 2020, doi: 10.1080/21650373.2020.1833256.
- [293] R. Mohamed *et al.*, “Heat evolution of alkali-activated materials: A review on influence factors,” *Constr. Build. Mater.*, vol. 314, no. November 2021, 2022, doi: 10.1016/j.conbuildmat.2021.125651.
- [294] F. Xie, Z. Liu, D. Zhang, J. Wang, T. Huang, and D. Wang, “Reaction kinetics and kinetics models of alkali activated phosphorus slag,” *Constr. Build. Mater.*, vol. 237, p. 117728, 2020, doi: 10.1016/j.conbuildmat.2019.117728.
- [295] W. Chen, Y. Li, P. Shen, and Z. Shui, “Microstructural development of hydrating portland cement paste at early ages investigated with non-destructive methods and numerical simulation,” *J. Nondestruct. Eval.*, vol. 32, no. 3, pp. 228–237, 2013, doi: 10.1007/s10921-013-0175-y.
- [296] A. Fernandez-Jimenez and F. Puertas, “Setting of alkali-activated slag cement. Influence of activator nature,” *Adv. Cem. Res.*, vol. 13, no. 3, pp. 115–121, 2001, doi: 10.1680/adcr.13.3.115.39288.
- [297] M. Criado, A. Fernández-Jiménez, A. Palomo, I. Sobrados, and J. Sanz, “Effect of the SiO<sub>2</sub>/Na<sub>2</sub>O ratio on the alkali activation of fly ash. Part II: 29Si MAS-NMR Survey,” *Microporous Mesoporous Mater.*, vol. 109, no. 1–3, pp. 525–534, 2008, doi: 10.1016/j.micromeso.2007.05.062.
- [298] P. Mounanga, V. Baroghel-Bouny, A. Loukili, and A. Khelidj, “Autogenous deformations of cement pastes: Part I. Temperature effects at early age and micro-macro correlations,” *Cem. Concr. Res.*, vol. 36, no. 1, pp. 110–122, 2006, doi: 10.1016/j.cemconres.2004.10.019.
- [299] F. Collins and J. G. Sanjayan, “Effects of ultra-fine materials on workability and strength of concrete containing alkali-activated slag as the binder,” *Cem. Concr. Res.*, vol. 29, no. 3, pp. 459–462, 1999, doi: 10.1016/S0008-8846(98)00237-3.
- [300] T. Yang, H. Zhu, Z. Zhang, X. Gao, C. Zhang, and Q. Wu, “Effect of fly ash microsphere on the rheology and microstructure of alkali-activated fly ash/slag pastes,” *Cem. Concr. Res.*, vol. 109, no. January, pp. 198–207, 2018, doi: 10.1016/j.cemconres.2018.04.008.
- [301] S. Zhang, Z. Li, B. Ghiassi, S. Yin, and G. Ye, “Fracture Properties and Microstructure Formation of Hardened Alkali-activated Slag/Fly ash Paste,” *Cem. Concr. Res.*, vol. 144, no. April, p. (In revision), 2020, doi: 10.1016/j.cemconres.2021.106447.
- [302] M. Nedeljković, B. Šavija, Y. Zuo, M. Luković, and G. Ye, “Effect of natural carbonation on the pore structure and elastic modulus of the alkali-activated fly ash and slag pastes,” *Constr. Build. Mater.*, vol. 161, pp. 687–704, 2018,

- doi: 10.1016/j.conbuildmat.2017.12.005.
- [303] I. Garcia-Lodeiro, A. Palomo, A. Fernández-Jiménez, and D. E. MacPhee, “Compatibility studies between N-A-S-H and C-A-S-H gels. Study in the ternary diagram  $\text{Na}_2\text{O}-\text{CaO}-\text{Al}_2\text{O}_3-\text{SiO}_2-\text{H}_2\text{O}$ ,” *Cem. Concr. Res.*, vol. 41, no. 9, pp. 923–931, 2011, doi: 10.1016/j.cemconres.2011.05.006.
- [304] G. Fang and M. Zhang, “Multiscale micromechanical analysis of alkali-activated fly ash-slag paste,” *Cem. Concr. Res.*, vol. 135, no. May, p. 106141, 2020, doi: 10.1016/j.cemconres.2020.106141.
- [305] B. Walkley, A. Kashani, M. A. Sani, T. D. Ngo, and P. Mendis, “Examination of alkali-activated material nanostructure during thermal treatment,” *J. Mater. Sci.*, vol. 53, no. 13, pp. 9486–9503, 2018, doi: 10.1007/s10853-018-2270-z.
- [306] R. Xiao, X. Jiang, M. Zhang, P. Polaczyk, and B. Huang, “Analytical investigation of phase assemblages of alkali-activated materials in  $\text{CaO}-\text{SiO}_2-\text{Al}_2\text{O}_3$  systems: The management of reaction products and designing of precursors,” *Mater. Des.*, vol. 194, p. 108975, 2020, doi: 10.1016/j.matdes.2020.108975.
- [307] P. Perez-Cortes and J. I. Escalante-Garcia, “Gel composition and molecular structure of alkali-activated metakaolin-limestone cements,” *Cem. Concr. Res.*, vol. 137, no. August, p. 106211, 2020, doi: 10.1016/j.cemconres.2020.106211.
- [308] R. Sun *et al.*, “Chemo-mechanical properties of alkali-activated slag/fly ash paste incorporating white mud,” *Constr. Build. Mater.*, vol. 291, p. 123312, 2021, doi: 10.1016/j.conbuildmat.2021.123312.
- [309] B. Walkley *et al.*, “Phase evolution of C-(N)-A-S-H/N-A-S-H gel blends investigated via alkali-activation of synthetic calcium aluminosilicate precursors,” *Cem. Concr. Res.*, vol. 89, pp. 120–135, 2016, doi: 10.1016/j.cemconres.2016.08.010.
- [310] C. Shi and Y. Li, “Investigation on some factors affecting the characteristics of alkali-phosphorus slag cement,” *Cem. Concr. Res.*, vol. 19, no. c, pp. 527–533, 1989.
- [311] B. John, C. Ian, C. and L. Anne, “Comparative study of the efficiency of various borate compounds as set-retarders of class G oilwell cement,” *Cem. Concr. Res.*, vol. 21, no. c, pp. 663–668, 1991.
- [312] T. Revathi and R. Jeyalakshmi, “Fly ash – GGBS geopolymer in boron environment : A study on rheology and microstructure by ATR FT-IR and MAS NMR,” *Constr. Build. Mater.*, vol. 267, p. 120965, 2021, doi: 10.1016/j.conbuildmat.2020.120965.
- [313] L. Xu, X. Wang, C. Guan, W. Wu, and L. Zhang, “The Effect of Activators on the Mechanical Properties and Microstructure of Alkali-Activated Nickel Slag,” *Adv. Civ. Eng.*, vol. 2020, 2020.
- [314] I. L. Mallphanov, V. K. Vanag, H. Ni, and M. Wang, “Synthesis of silica gel

## References

- from glass waste for adsorption of  $Mg^{2+}$ ,  $Cu^{2+}$ , and  $Ag^{+}$  metal ions,” *IOP Conf. Ser. Mater. Sci. Eng.*, 2019, doi: 10.1088/1757-899X/509/1/012028.
- [315] P. A. J. De Witte *et al.*, “Synthesis and Characterization of Long Perylenediimide Polymer Fibers : From Bulk to the Single-Molecule Level,” *J. Phys. Chem. B*, pp. 7803–7812, 2006.
- [316] D. Sriramulu, S. P. Turaga, A. A. Bettiol, and S. Valiyaveetil, “Oriented perylene incorporated optically anisotropic 2D silica film,” *R. Soc. Chem.*, vol. 7, pp. 32692–32702, 2017, doi: 10.1039/c7ra05036d.
- [317] Z. Shao, F. Luo, X. Cheng, and Y. Zhang, “Superhydrophobic sodium silicate based silica aerogel prepared by ambient pressure drying,” *Mater. Chem. Phys.*, vol. 141, no. 1, pp. 570–575, 2013, doi: 10.1016/j.matchemphys.2013.05.064.
- [318] G. Shao *et al.*, “Thermal shock behaviour and infrared radiation property of integrative insulations consisting of  $MoSi_2$  / borosilicate glass coating and fibrous  $ZrO_2$  ceramic substrate Surface & Coatings Technology Thermal shock behaviour and infrared radiation property of i,” *Surf. Coat. Technol.*, no. May 2015, 2018, doi: 10.1016/j.surfcoat.2015.03.008.
- [319] T. G. V. M. Rao, A. R. Kumar, K. Neeraja, N. Veeraiah, and M. R. Reddy, “Optical and structural investigation of  $Eu^{3+}$  ions in  $Nd^{3+}$  co-doped magnesium lead borosilicate glasses,” *J. Alloys Compd.*, vol. 557, pp. 209–217, 2013, doi: 10.1016/j.jallcom.2012.12.162.
- [320] M. Sitarz, M. Handke, Z. Fojud, and S. Jurga, “Spectroscopic studies of glassy phospho-silicate materials,” *J. Mol. Struct.*, vol. 747, pp. 621–626, 2005, doi: 10.1016/j.molstruc.2004.12.050.
- [321] M. Sitarz, M. Rokita, and K. Bułat, “Infrared spectroscopy of different phosphates structures,” *Spectrochim. Acta Part A Mol. Biomol. Spectrosc.*, vol. 79, pp. 722–727, 2011, doi: 10.1016/j.saa.2010.08.044.
- [322] L. Zhang, Y. Ji, J. Li, F. Gao, and G. Huang, “Effect of retarders on the early hydration and mechanical properties of reactivated cementitious material,” *Constr. Build. Mater.*, vol. 212, pp. 192–201, 2019, doi: 10.1016/j.conbuildmat.2019.03.323.
- [323] W. K. W. Lee and J. S. J. Van Deventer, “Effects of anions on the formation of aluminosilicate gel in geopolymers,” *Ind. Eng. Chem. Res.*, vol. 41, no. 18, pp. 4550–4558, 2002, doi: 10.1021/ie0109410.
- [324] C. Dupuy, A. Gharzouni, I. Sobrados, N. Texier-Mandoki, X. Bourbon, and S. Rossignol, “ $^{29}Si$ ,  $^{27}Al$ ,  $^{31}P$  and  $^{11}B$  magic angle spinning nuclear magnetic resonance study of the structural evolutions induced by the use of phosphor-based boron-based additives in geopolymer mixtures,” *J. Non. Cryst. Solids*, vol. 521, no. August, p. 119541, 2019, doi: 10.1016/j.jnoncrysol.2019.119541.
- [325] A. Nazari, A. Maghsoudpour, and J. G. Sanjayan, “Characteristics of boroaluminosilicate geopolymers,” *Constr. Build. Mater.*, vol. 70, pp. 262–268, 2014, doi: 10.1016/j.conbuildmat.2014.07.087.

- [326] A. Nazari, A. Maghsoudpour, and J. G. Sanjayan, “Flexural strength of plain and fibre-reinforced boroaluminosilicate geopolymer,” *Constr. Build. Mater.*, vol. 76, pp. 207–213, 2015, doi: 10.1016/j.conbuildmat.2014.12.002.
- [327] W. Kunther, S. Ferreira, and J. Skibsted, “Influence of the Ca/Si ratio on the compressive strength of cementitious calcium-silicate-hydrate binders,” *J. Mater. Chem. A*, vol. 5, no. 33, pp. 17401–17412, 2017, doi: 10.1039/c7ta06104h.
- [328] F. Pelisser, P. J. P. Gleize, and A. Mikowski, “Effect of the Ca/Si molar ratio on the micro/nanomechanical properties of synthetic C-S-H measured by nanoindentation,” *J. Phys. Chem. C*, vol. 116, no. 32, pp. 17219–17227, 2012, doi: 10.1021/jp302240c.
- [329] L. S. Du and J. F. Stebbins, “Nature of silicon-boron mixing in sodium borosilicate glasses: A high-resolution  $^{11}\text{B}$  and  $^{17}\text{O}$  NMR study,” *J. Phys. Chem. B*, vol. 107, no. 37, pp. 10063–10076, 2003, doi: 10.1021/jp0340481.
- [330] L. S. Du and J. F. Stebbins, “Solid-state NMR study of metastable immiscibility in alkali borosilicate glasses,” *J. Non. Cryst. Solids*, vol. 315, no. 3, pp. 239–255, 2003, doi: 10.1016/S0022-3093(02)01604-6.
- [331] G. Tricot, B. Doumert, B. Revel, M. Bria, J. Trebosc, and H. Vezin, “Non-homogeneous distribution of  $\text{Al}^{3+}$  in doped phosphate glasses revealed by  $^{27}\text{Al}/^{31}\text{P}$  solid state NMR,” *Solid State Nucl. Magn. Reson.*, vol. 84, no. November 2016, pp. 137–142, 2017, doi: 10.1016/j.ssnmr.2017.02.003.
- [332] R. Dupree, D. Holland, M. G. Mortuza, J. A. Collins, and M. W. G. Lockyer, “Magic angle spinning NMR of alkali phospho-alumino-silicate glasses,” *J. Non. Cryst. Solids*, vol. 112, no. 1–3, pp. 111–119, 1989, doi: 10.1016/0022-3093(89)90504-8.
- [333] R. A. Fletcher, K. J. D. MacKenzie, C. L. Nicholson, and S. Shimada, “The composition range of aluminosilicate geopolymers,” *J. Eur. Ceram. Soc.*, vol. 25, no. 9, pp. 1471–1477, 2005, doi: 10.1016/j.jeurceramsoc.2004.06.001.
- [334] S. Song, D. Sohn, H. M. Jennings, and T. O. Mason, “Hydration of alkali-activated ground granulated blast furnace slag,” *J. Mater. Sci.*, vol. 35, no. 1, pp. 249–257, 2000, doi: 10.1023/A:1004742027117.
- [335] B. Panda, S. Ruan, C. Unluer, and M. Jen, “Improving the 3D printability of high volume fly ash mixtures via the use of nano attapulgite clay,” *Compos. Part B*, vol. 165, no. June 2018, pp. 75–83, 2019, doi: 10.1016/j.compositesb.2018.11.109.
- [336] G. De Schutter, K. Lesage, V. Mechtcherine, V. Naidu, G. Habert, and I. Agusti-juan, “Vision of 3D printing with concrete — Technical, economic and environmental potentials,” *Cem. Concr. Res.*, vol. 112, no. August, pp. 25–36, 2018, doi: 10.1016/j.cemconres.2018.06.001.
- [337] W. W. S. Fung and A. K. H. Kwan, “Role of water film thickness in rheology of CSF mortar,” *Cem. Concr. Compos.*, vol. 32, no. 4, pp. 255–264, 2010, doi: 10.1016/j.cemconcomp.2010.01.005.

## References

- [338] A. Favier, G. Habert, J. B. Espinose, D. Lacaillerie, and N. Roussel, “Mechanical properties and compositional heterogeneities of fresh geopolymer pastes,” *Cem. Concr. Res.*, vol. 48, pp. 9–16, 2013, doi: 10.1016/j.cemconres.2013.02.001.
- [339] D. W. Zhang, K. F. Zhao, H. Li, D. min Wang, L. lin Wang, and G. fang Zhang, “Dispersion properties of fly ash–slag powders under the different environment,” *Constr. Build. Mater.*, vol. 296, p. 123649, 2021, doi: 10.1016/j.conbuildmat.2021.123649.
- [340] F. K. Crundwell, “On the Mechanism of the Dissolution of Quartz and Silica in Aqueous Solutions,” *Am. Chem. Soc.*, 2017, doi: 10.1021/acsomega.7b00019.
- [341] W. Chen, B. Li, J. Wang, and N. Thom, “Effects of alkali dosage and silicate modulus on autogenous shrinkage of alkali-activated slag cement paste,” *Cem. Concr. Res.*, vol. 141, no. February 2020, 2021, doi: 10.1016/j.cemconres.2020.106322.
- [342] A. M. Mostafa and A. Yahia, “Physico-chemical kinetics of structural build-up of neat cement-based suspensions,” *Cem. Concr. Res.*, vol. 97, pp. 11–27, 2017, doi: 10.1016/j.cemconres.2017.03.003.
- [343] X. Dai, S. Aydin, M. Y. Yardımcı, and G. De Schutter, “Rheology and structural build-up of sodium silicate- and sodium hydroxide-activated GGBFS mixtures,” *Cem. Concr. Compos.*, vol. 131, no. May, p. 104570, 2022, doi: 10.1016/j.cemconcomp.2022.104570.
- [344] P. S. Singh, T. I. M. Bastow, M. Trigg, and C. S. Mdc, “Structural studies of geopolymers by 29 Si and 27 Al MAS-NMR,” vol. 0, pp. 3951–3961, 2005.
- [345] X. Gao, Q. L. Yu, and H. J. H. Brouwers, “Apply 29 Si , 27 Al MAS NMR and selective dissolution in identifying the reaction degree of alkali activated slag- fly ash composites,” *Ceram. Int.*, vol. 43, no. May, pp. 12408–12419, 2017, doi: 10.1016/j.ceramint.2017.06.108.
- [346] E. L. Hôpital, B. Lothenbach, G. Le Saout, D. Kulik, and K. Scrivener, “Incorporation of aluminium in calcium-silicate-hydrates,” *Cem. Concr. Res.*, vol. 75, pp. 91–103, 2015, doi: 10.1016/j.cemconres.2015.04.007.
- [347] G. Fang and M. Zhang, “Multiscale micromechanical analysis of alkali-activated fly ash-slag paste,” *Cem. Concr. Res.*, vol. 135, no. June, p. 106141, 2020, doi: 10.1016/j.cemconres.2020.106141.
- [348] X. Chen, A. Sutrisno, L. Zhu, and L. J. Struble, “Setting and nanostructural evolution of metakaolin geopolymer,” *J. Am. Ceram. Soc.*, vol. 100, no. 5, pp. 2285–2295, 2017, doi: 10.1111/jace.14641.
- [349] B. Walkley, R. San, M. Sani, J. D. Gehman, J. S. J. Van Deventer, and J. L. Provis, “Synthesis of stoichiometrically controlled reactive aluminosilicate and calcium-aluminosilicate powders,” *Powder Technol.*, vol. 297, pp. 17–33, 2016, doi: 10.1016/j.powtec.2016.04.006.

- [350] A. Palomo, D. E. Macphee, and A. Ferna, “Effect of Calcium Additions on N–A–S–H Cementitious Gels,” vol. 1940, pp. 1934–1940, 2010, doi: 10.1111/j.1551-2916.2010.03668.x.
- [351] N. Li, N. Farzadnia, and C. Shi, “Microstructural changes in alkali-activated slag mortars induced by accelerated carbonation,” *Cem. Concr. Res.*, vol. 100, no. July, pp. 214–226, 2017, doi: 10.1016/j.cemconres.2017.07.008.
- [352] I. García Lodeiro, D. E. Macphee, A. Palomo, and A. Fernández-Jiménez, “Effect of alkalis on fresh C-S-H gels. FTIR analysis,” *Cem. Concr. Res.*, vol. 39, no. 3, pp. 147–153, 2009, doi: 10.1016/j.cemconres.2009.01.003.
- [353] A. Fernandez-Jimenez and F. Puertas, “Structure of Calcium Silicate Hydrates Formed in Alkaline-Activated Slag: Influence of the Type of Alkaline Activator,” *J. Am. Ceram. Soc.*, vol. 94, pp. 1389–1394, 2003.
- [354] S. Puligilla and P. Mondal, “Co-existence of aluminosilicate and calcium silicate gel characterized through selective dissolution and FTIR spectral subtraction,” *Cem. Concr. Res.*, vol. 70, pp. 39–49, 2015, doi: 10.1016/j.cemconres.2015.01.006.

## Curriculum Vitae

---

### Personal information

---

Name: Xiaodi DAI

Email: [Xiaodi.dai@ugent.be](mailto:Xiaodi.dai@ugent.be), [daixiaodi0902@gmail.com](mailto:daixiaodi0902@gmail.com);

Date of Birth: March, 1994

Place of Birth: Xiangtan Hunan, China

Research interest: Cementitious materials design; Low-carbon building materials (Alkali-activated materials); Rheology; 3D printing cementitious materials; Hydration and microstructural development; Machine learning.

Skills: Materials design & synthesis; Materials characterization (Rheometer, Mechanical tests, NMR, XRD, FTIR, TGA, SEM/EDX, ICP-OES); Data analysis and academic writing/presentation. Machine learning (Python).

### Education

---

Ghent University (GU) Mar 2019 - Nov 2022	Ph.D. Civil Engineering Gent, Belgium
National University of Singapore (NUS) Dec 2018 - Mar 2019	M.S. Civil Engineering Singapore
Central South University (CSU) Sep 2012 - Jun 2016	B.Eng. Civil Engineering Changsha, China

### Research experience

---

INTERACT Project

Research Fellow Mar 2019 - Nov 2022

- Design alkali-activated materials for low carbon emission.
- Explore rheological and mechanical properties.
- Develop concrete mixtures.
- Investigate the setting mechanism (reaction mechanisms and kinetics, phase formations and binder structure).

RILEM Technical Committee 294-MPA

Research member

Jan 2021 - present

- Conduct round robin tests regarding the rheological and mechanical properties.
- Draft state-of-the-art report on rheological properties of alkali-activated materials.

National University of Singapore (NUS)

Research Assistant

Dec 2018 - Mar 2019

- Design cementitious materials for offshore engineering.
- Set up a fatigue testing system.

### **Honors & Awards**

---

National Scholarship of Undergraduate student. (China's Ministry of Education)  
2013, 2014, 2015

### **Publication list**

---

Journal papers

1. X.Dai, S.Aydin, G.De Schutter, et al. Early structural build-up, setting behavior, reaction kinetics and microstructure of sodium silicate-activated slag mixtures with different retarder chemicals. *Cement and Concrete Research*. 2022, 159:106872.
2. X.Dai, S.Aydin, G.De Schutter, et al. Effects of activator properties and GGBFS/FA ratio on the structural build-up and rheology of AAC. *Cement and Concrete Research*. 2020, 138: 106253.
3. X.Dai, S.Aydin, G.De Schutter, et al. Rheology, early-age hydration and microstructure of alkali-activated GGBFS-Fly Ash mixtures blended with limestone powder. *Cement & Concrete Composite*, 2021, 124: 104244.
4. X.Dai, S.Aydin, G.De Schutter, et al. Rheology and microstructure of alkali-activated slag cements produced with silica fume activator. *Cement & Concrete Composite*. 2022, 125: 104303.
5. X.Dai, S.Aydin, G.De Schutter, et al. Rheology and Structural Build-up of Sodium Silicate- and Sodium Hydroxide-Activated GGBFS Mixtures. *Cement & Concrete Composite*. 2022, 131: 104570.
6. X.Dai, S.Aydin, G.De Schutter, et al. Early age reaction, rheological properties and pore solution chemistry of NaOH-activated slag mixtures. *Cement & Concrete Composite*. 2022, 133: 104715.
7. X.Dai, S.Aydin, G.De Schutter, et al. Influence of water to binder ratio on the

## Curriculum Vitae

rheology and structural build-up of alkali-activated slag/fly ash mixtures. *Construction and Building Materials*. 2020, 264: 120253.

8. X.Dai, Q. Ren, G.De Schutter, et al. Enhancing thixotropy and structural build-up of alkali-activated slag/fly ash pastes with nano clay. *Materials and Structures*. 2021, 54 :163.

9. X.Dai, S.Aydin, G.De Schutter, et al. Effect of Ca(OH)<sub>2</sub> addition on the engineering properties of sodium sulfate activated slag. *Materials*. 2021, 14, 4266.

10. Y.Sun, X.Dai, G.De Schutter, G. Ye, et al. Evaluation on rheology and strength development of alkali-activated slag synthesized from different silicate sources. *Cement & Concrete Composite*. 2022, 128: 104415.

11. Q.Ren, L.Ding, X.Dai, G.De Schutter, et al. Prediction of compressive strength of concrete with manufactured sand by ensemble classification and regression tree method. *Journal of Materials in Civil Engineering*. 2021, 33(7):040211135.

12. Q.Ren, L.Ding, X.Dai, G.De Schutter, et al. Determination of specific surface area of irregular aggregate by random sectioning and its comparison with conventional methods. *Construction and Building Materials*. 273(2021) 122019.

## Oral Presentations

1. X.Dai, S.Aydin, G.De Schutter, et al. Effects of Ms ratio of activator solution on rheological properties of alkali-activated cements. Sheffield, United Kingdom, 74th RILEM Annual Week 2020.

2. X.Dai, S.Aydin, G.De Schutter, et al. Rheological response of alkali-activated cements under elevated temperature. Delft, The Netherlands, Microdurability 2021.

3. X.Dai, G.De Schutter. Early reaction process of alkali-activated cements monitored by ultrasonic wave technology. Kyoto, Japan, 76th RILEM Annual Week 2022.





Low-carbon and sustainable alkali-activated cement in the flow state.